Radio Propagation in Fire Environments

by

Jonathan Alexander Boan

Bachelor of Engineering,

University of Western Australia

Thesis submitted for the degree of

Doctor of Philosophy

in

Department of Electrical and Electronic Engineering,
School of Engineering,
Computer and Mathematical Sciences

University of Adelaide, Australia

2009

Typeset in LaTeX 2_ε
Jonathan Alexander Boan

Abstract

Radio propagation in the presence of fire is known to be problematic to communications. In this thesis we use both experimental and theoretical approaches to examine and understand radio propagation in fire environments. Propagation is examined for three small scale fires with broadband equipment operating from 50MHz to 1GHz. Results for line of sight propagation show a strong interaction of fire with electromagnetic propagation. The next section develops electromagnetic modelling of the fire environment. A model of the combustion induced plasma is developed, as well as a refractive index model of the surrounding atmosphere of a fire. Simple propagation calculations are undertaken, using the developed fire models, to provide an intial understanding of propagation in fire environments. The next portion of the thesis considers propagation using a more rigorous electromagnetic simulation technique. A modified Finite Difference Time Domain method is presented and is utilised to examine three dimensional propagation in the small scale fire experiments. The outcome is a more solid understanding of propagation and the contributing factors. The last portion of the thesis is the application of the above electromagnetic modelling and simulation methods to bushfire scenarios. Various scenarios that are problematic to radio communication are examined. Discussion and recommendations are made concerning radio communication frequency selection and considerations for propagation in fire environments.

This page is blank

Statement of Originality

This work contains no material which has been accepted for the award of any other degree or diploma in any university or other tertiary institution to Jonathan Boan and , to the best of my knowledge and belief, contains no material previously published or written by another person, except where due reference has been made in the text.

I give consent to this copy of my thesis, when deposited in the University Library, being made available for loan and photocopying, subject to the provisions of the Copyright Act 1968.

I also give permission for the digital version of my thesis to be made available on the web, via the University's digital research repository, the Library catalogue, the Australasian Digital Theses Program (ADTP) and also through web search engines, unless permission has been granted by the University to restrict access for a period of time.

Signed

Date

This page is blank

Acknowledgements

The author would like to thank:

- Associate Professor Chris Coleman, for his academic guidance, financial support and encouragement.
- Claire Boan, for her loving encouragement and emotional support.
- School of Electrical and Electronic Engineering of the University of Adelaide for the opportunity to undertake post-graduate study.
- All those involved in experimental work including, the Freeman family of Pipers Creek and the Raukkan Farm and manager.

Jonathan Boan

This page is blank

BIBLIOGRAPHY

[1] J.A. Boan. FDTD for Tropospheric Propagation. *IEEE Antennas and Propagation Symposium, Albuquerque, New Mexico*, 2006.

[2] J.A. Boan. Radio propagation in fire environments. *Workshop Applications of Radio Science, WARS'06, Luera, Australia*, 2006. Awarded Best Student Paper.

[3] J.A. Boan. Radio Experiments with fire. *IEEE Antennas and Wireless Propagation Letters*, 6:411 – 414, 2007.

[4] C. J. Coleman and J. A. Boan. A kirchoff integral approach to radio wave propagation in fire. *IEEE Antennas and Propagation Symposium, Hawaii, Honolulu*, 2007.

This page is blank

TABLE OF CONTENTS

LIST OF ILLUSTRATIONS

LIST OF TABLES

LIST OF TABLES

SECTION 1

Introduction

Australia is a dry continent with extremely hot temperatures during Summer, or a dry season. Every Summer, countless numbers of fires start throughout the country: in the last few decades Australians have seen a number of major fire disasters. In 1983, the Ash Wednesday fires burned 4000km^2 of land in two states. Seventy five people lost their lives during these bushfires. Estimated losses were $320 million[123]. During this time, Melbourne was completely surrounded by fire and much of the Adelaide Hills were alight. In 2003, the majority of the Australian Capital Territory was burnt. The estimated insurance costs were $250 million[123][79]. In 2005, 8000km^2 of rural land in Eyre Peninsula, South Australia was burnt, killing 9 people and injuring 110 people. Bushfire or Wildfire is a global problem. Internationally, many regions suffer from large wildfires including the continents of North and South America, Africa and Mediterranean Countries.

Amongst this huge destruction, fire fighters put there lives in danger to protect people and properties. Modern radio communication equipment has given fire fighters the capability to coordinate and cooperate their efforts to extinguish and control bushfire outbreaks. However, since the introduction of radio communications to emergency services little attention has been paid to considering the propagation of radio waves in extreme fire environments. Fire fighters have testified that radio communications can be severely degraded by being in the proximity of a fire[45]. There have been situations where people are able to see each other but not communicate on radio.

Issues with radio communications in fire environments have been known by the Australian community for over 30 years. The problem was brought to the attention of the public and of radio-engineers, following the 'Lara' fires in Victoria, in early 1969. Shortly after, the Department of Supply performed the 'Euroka' mass fire experiment in Queensland. The Euroka report states that 'over recent years, many country fire-fighters have come to suspect that their radio-communication systems will not always function reliably under bushfire conditions'[124]. More recently, reports have come forward from the Country Fire Association (CFA) following the Linton fire disaster in 1998[17] [45]. During this fire, failure of radio communication was identified as a contributor to the death of five fire fighters. Anecdotal evidence is growing but conclusive scientific research is scarce and has found the effect fickle and very hard to demonstrate how and when problems will arise.

To meet some of the growing concern of the fire fighting community, the research seeks to address this problem and give it a foundation to explain what is occurring to radio propagation in fire environments. The research is limited to common radio frequency bands. The frequency range of interest for this study is 50MHz to 1GHz, which encompasses VHF, UHF and Mobile (GSM-400, GSM-450, GSM-850, GSM-900, AMPS) communication bands. This is a fairly large slab of spectrum to consider and includes a large array of propagation phenomena. The conclusions and models that are developed in this work are designed to be as flexible as possible and widely applicable beyond the designated spectrum of interest.

Radio communication amongst fire fighting personnel occurs between a ground based transmitter and receiver. Radio wave propagation through a horizontal environment is very complex; being a function of frequency, ground characteristics, surrounding atmosphere and vegetation characteristics (species, density and distribution). Problems with radio communication exist when smoke and fire are present on the path of radio propagation[45].

To give some basic insight into the problem, consider the illustration in Figure 1. This figure demonstrates that while all three fire personnel are in the vicinity of the fire, communication problems are exhibited when one communicates through the fire front. Although the illustration is a gross simplification of the overall radio wave propagation, it highlights the region of the fire front that is problematic to radio propagation.

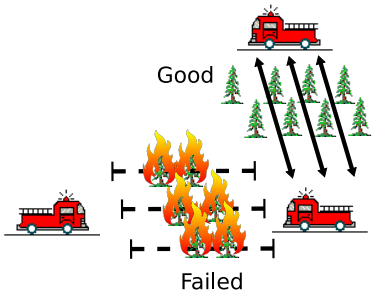

Figure 1.1: Radio Communications Illustration

In this thesis we seek to address the problem of radio communications in fire environments. A number of key goals of this research are:

- Experimentally validate whether fire has an effect on radio propagation.
- Identify propagation factors that will affect radio communication.
- Provide models and numerical simulation for propagation factors. With the ability to model and simulate propagation through these environments one can begin to understand what contributes and how it contributes to degrade communication ability. Computer modelling also limits the need for dangerous experiments.
- Explore the various propagation factors numerically and consider their implications in different scenarios.

Section 2 explores the results from a number of radio experiments with small scale fires. These results provide a measurement of the attenuation of radio waves over a broad range of frequencies.

Section 3 presents the modelling of the fire environment in terms of its refractive index and combustion induced plasma. Mathematical models are presented that are used later to provide a means to calculate propagation characteristics.

Section 4 provides some simple propagation calculations that focus on the combustion induced plasma. Attenuation is considered and the various parameters that control propagation through and around a combustion region.

Section 5 presents the Finite Difference Time Domain algorithm that is used as a full electromagnetic simulator of the fire environment. Various key features are identified

and extensions of the algorithm are presented that are necessary for simulating these environments.

Section 6 explores the small scale fire experiments from a modelling point of view. Explanation is provided for the propagation of radio waves around a fuel and combustion region. Dynamics of the fire environment changing over time are also considered with a qualitative explanation of the phenomena seen in the experimental results of Section 2.

Section 7 includes a digression into the future work of large scale bushfire simulations. A two dimensional Finite Difference Time Domain algorithm is used to explore a number of scenarios that involve propagation over large distances.

The final chapter includes a summary and conclusion for future work.

The remainder of this chapter will introduce the propagation elements that are important for this work. A literature review is included in the background material.

1.1 Background and Literature

Specific research that addresses radio propagation in fire environments is scarce. There are three independent studies that should be mentioned. One study is the Euroka experiment by the Department of Supply in 1969 [124]. This was a mass fire-firestorm experiment at Langley, Queensland measuring general fire conditions whilst monitoring radio communication channel. A 400m x 400m section of land containing heaps of wood was burnt with radio recordings taken at 2MHz , 5MHz , 150MHz , 450MHz and 4GHz . The radio measurements showed a loss in radio signal strength during the fire but was rather small (typically 0.7dB with sub-refraction being identified as the main cause of radio strength).

A second study was at the James Cook University in Queensland [48]. Here, a study was undertaken to look into the presence of ionised particles in the combustion zone of a fire. This is quite recent research, and results from experiments are still reaching the public arena. However, within their controlled experiment of different fuel types some results are tangible with theory.

The third observation to mention is radar measurement of a smoke stack, in Montreal 1996 [92]. Radar data of an industrial smoke plume showed abnormal scattering as a result of turbulent air movement.

Following the Linton fires of 1998, the Country Fire Authority of Victoria issued a number of investigations into radio communications following the death of a number of fire fighters[45].

There is no conclusive study that investigates this problem experimentally and theoretically. What follows is a collection of various areas that contribute to understanding this problem.

1.2 Propagation

Electromagnetic radiation encompasses a large array of phenomena, from radio waves to heat to visible light to X-rays. Mathematically all these forms of electromagnetic radiation obey Maxwell's equations. Electromagnetic waves consist of an electric field and magnetic field that are coupled together, which oscillate in time (frequency) and space (wavelength). The product of wavelength and frequency is the speed of light ($c = \lambda f$). The speed of light in a medium is related to the material characteristics ($c = 1/\sqrt{\mu\epsilon}$), where μ is the permeability and is related to medium's magnetic characteristics and ϵ is the permittivity and is related to the medium's electrical characteristics. When the medium changes due to a sudden change, like an object, or a slight change due to pressure or temperature, the propagation of radio energy changes. The change in propagation is dependent on the relationship between the wavelength (λ) of the wave and size of the object. In a vacuum, radio waves at 50MHz have a wavelength of approximately 6m , and 1GHz have a wavelength of approximately 30cm .

1.2.1 Refraction in Fire Environments

Refraction is the redirection of electromagnetic waves due to slight or slow changes in the propagation medium. In a fire environment, electromagnetic waves are not travelling in a vacuum but through an atmosphere which is changing. For normal atmospheric conditions radio waves bend slightly toward the earth's surface. This is due to the atmospheric

pressure and temperature profile causing a higher refractive index (a measure of the electromagnetic characteristics) at ground level. Heat generated from regions where fire is present cause changes in the atmosphere's temperature and gas makeup. As the temperature increases the refractive index lowers. Because the hottest part of the atmosphere in a fire is near ground level the refractive increases with height. This is called subrefractive conditions and causes the radio energy to bend away from the ground, decreasing the signal strength of ground based units. An illustration of this is given in Figure 1.2. Results from the Euroka[124] experiment suggest sub-refractive conditions, caused by a fire, contributed to signal loss for ground based communication. It requires a certain distance for the refractive effects to accumulate. For longer wavelengths, the distance can be substantial. Where as, for smaller wavelengths it is shortened and therefore refractive effects are more prominent at higher frequencies.

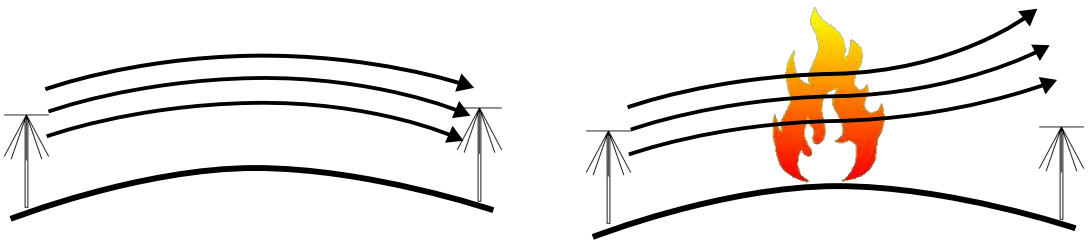

(a) Normal (b) Fire

Figure 1.2: Refraction Illustration

In order to consider propagation through a fire's atmosphere a model of the refractive index is necessary. Formulations of the refractive index of the Earth's atmosphere consider changes in the temperature, pressure and humidity. A mathematical expression to calculate the refractive index for general atmospheric conditions is the Debye equation[68].

$$N_r = (n_r - 1) \times 10^6 = 77.695\frac{P_{Dry}}{T} + 71.97\frac{P_{H_2O}}{T^2} + 375406\frac{P_{H_2O}}{T} \tag{1.1}$$

where N_r is the refractivity, n_r the refractive index, T is temperature in Kelvin, P_{Dry} is the partial pressure of the 'dry air' gases in the atmosphere and P_{H_2O} is the water vapour partial pressure in hPa . The dry air component consists of atmospheric pressure minus P_{H_2O}, or the gases that do not change in consistency, such as nitrogen, oxygen, carbon

dioxide and trace gases including He, Ar, H, Na etc. As carbon dioxide levels continue to rise the constant for the dry air term needs to be recalculated. Alternatively, one can separate out carbon dioxide from dry air. A general formula which separates the CO_2 term is shown in equation 1.2 [93].

$$N_r = K_1 \frac{P_{Dry-CO_2}}{T} + K_2 \frac{P_{H_2O}}{T} + K_3 \frac{P_{H_2O}}{T^2} + K_4 \frac{P_{CO_2}}{T} \tag{1.2}$$

where $K_1 = 77.694$°K /hPa ,$K_2 = 71.97$°K /hPa , $K_3 = 375406$°K ^{2}/hPa and $K_4 = 133.484$°K /hPa are constants derived from experimental measurement[94] and P_{Dry-CO_2} is dry carbon dioxide free air. It is easily understood that the refractive index is sensitive to the partial pressures of each constituent gas of the atmosphere.

In the fire atmosphere, the gas constituents are changing in concentration as they under-go combustion. Obvious examples are the change from oxygen to carbon dioxide but additionally the oxidation of nitrogen. Water vapour is generated as a product of the combustion. This undermines our usage of a dry air term with assumptions of a 70% nitrogen, 20% oxygen atmosphere. The other problem is the lack of experimental evaluation under the conditions of investigation, such as high temperatures (current atmospheric models are limited to $-50°C \ - \ +40°C$ [93]). In order to overcome these difficulties a more general formulation of the refractive index is required. One can extend the process of separating the dry air term to include other gases. Such a technique has been shown in [21].

Generally, the refractivity (N_r) term is taken to be constant for all frequencies. At radio frequencies, care is needed to account of molecular resonances in the atmosphere. Liebe has done some extensive work in the modelling of air at frequencies below 1000GHz [69, 3]. Certain atmospheric gases, such as water and oxygen, will resonate when an electromagnetic wave impinges causing a dramatic change in the refractive index. In this case the refractive index becomes a complex variable that includes the lossless N_r component; an absorption component, denoted $(jN_{abs}(f))$, and a dispersive $D(f)$ component. Millimetre-wave Propagation Model [33] is a computer routine used to calculate the complex refractive index from 1Hz to 1THz . It uses a fixed carbon dioxide value model and includes all molecular resonances in the specified frequency range 1Hz - 1THz . Figure 1.3 gives a view of the refractive index attenuation in its variation over a large array of

frequencies for a waterless atmosphere (Rel. Hum. 0%) and relative humidity of 10%. A smaller range of frequencies from 1Hz to 10GHz has also been included in Figure 1.4.

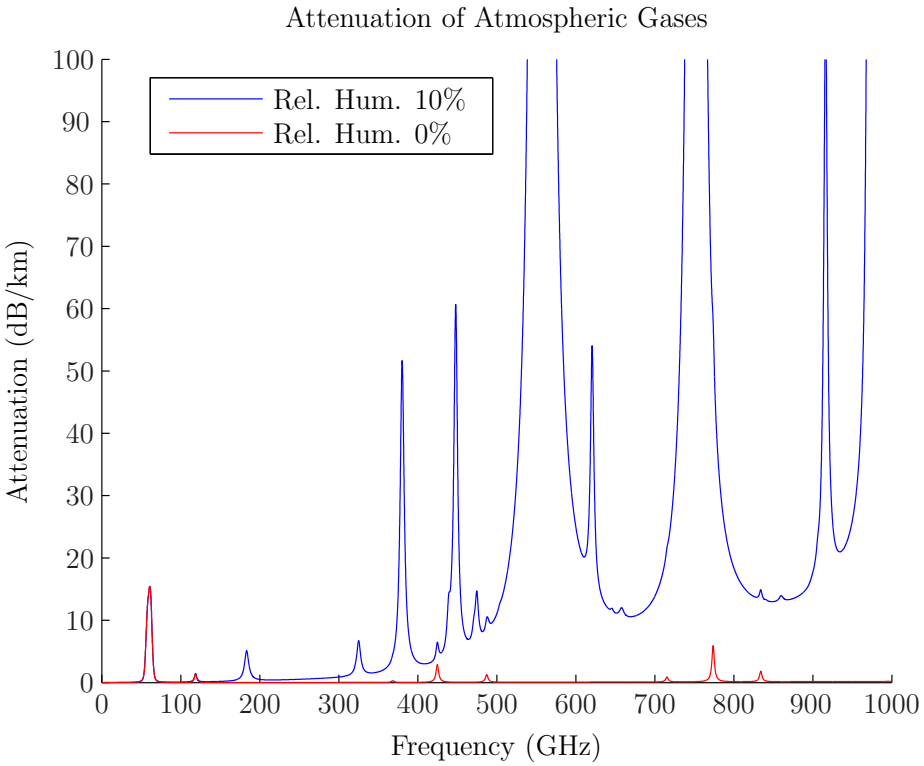

Figure 1.3: Attenuation of the Atmosphere 1Hz-1THz

By inspecting the frequency range of interest (50MHz - 1GHz) for this study we can see that we are well away from any resonances and a non-dispersive model is adequate. Only the frequency independent term N_r is necessary for modelling the refractive index in a fire environment from 50MHz - 1GHz .

1.2.2 Scattering

Scattering is caused by sudden changes in the propagation medium. These changes cause radio energy to be scattered in all or non-preferred directions. In a fire environment, particle scatter occurs from airborne debris or particles swept up by the convection currents of the combustion region.

Jones has considered particles scattering for carbon particles[57] and long chains of carbon agglomerates [56]. Particles can function as individual objects or when their

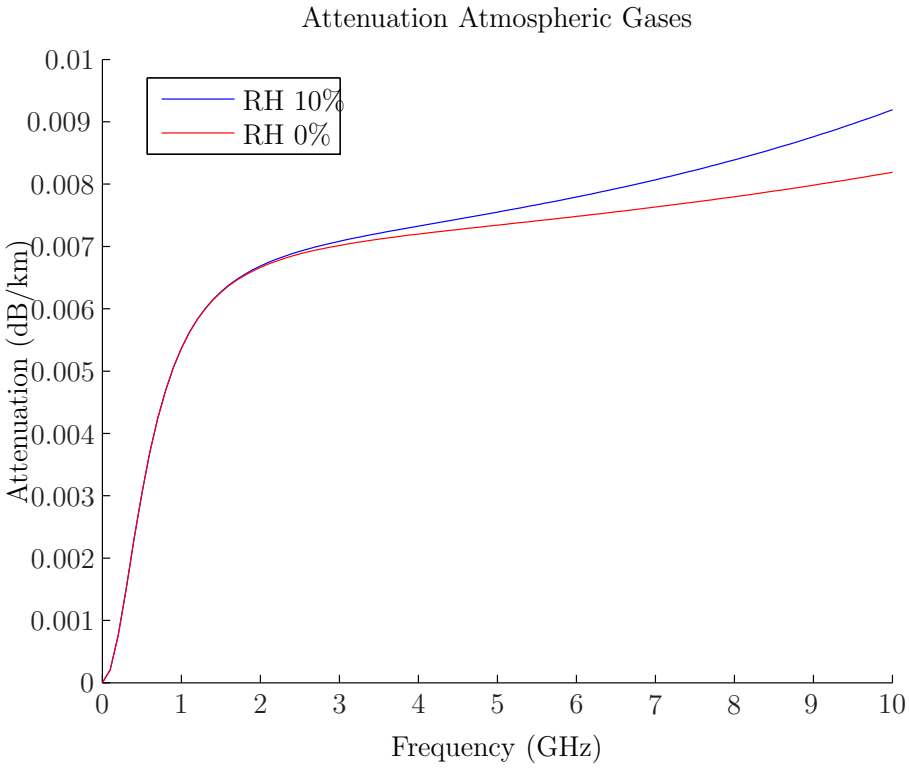

Figure 1.4: Attenuation of the Atmosphere 1Hz-10GHz

density is high enough to function as a single larger body[5] and be treated as the larger object. Carbon agglomeration and formation is affected by the presence of an electric field and has been an area of intense research in the laboratory flames[78][66] . Particle scattering obeys the Rayleigh approximation when the size of the particle is much smaller than the wavelength. Rayleigh scattering is proportional to the λ^{-4}, as such at the lower frequencies, such as 50MHz , the contribution from particle scattering will be very small. As the wavelength becomes smaller, the scattering efficiency increases. When a particle's size is proportional to the wavelength, scattering becomes more complex and obeys Mie's theory.

Another form of scattering present is caused by air movements in the atmosphere surrounding a fire. Inconsistencies occur in the refractive index and results in Bragg scattering[92]. The reflectivity from Bragg scattering is proportional $\lambda^{-1/3}$ and is a function of Reynolds number; a measure of vorticity in a fluid. Radar observations demonstrate that this type of scatter is prevalent in smoke plumes and turbulent air movement[92]. Fire modelling and fire weather has long seen the connection of convection as a major contributor to a wildfire's development[22]. Clark et al. show the development

of a fire front is related to the surrounding weather which is often induced by the fire. Heskestad[49] considers the dynamics of the plume in a fire. Computational fluid dynamics are increasingly being used for modelling the turbulent aspects of fire[25]. In many cases however full computational fluid dynamics is not possible on large wildfires[120].

1.2.3 Diffraction

When an object blocks a wave it causes a shadow region behind the object. Some radio energy exists in this region due to diffraction. This phenomena is proportional to wavelength such that longer wavelengths exhibit greater diffractive recovery in the shadow region of the object. Diffraction for lower frequencies is one of the reasons they are chosen for long range propagation and communication. Diffraction is an important phenomena because where propagation is obstructed, for example by a fire or tree, radio energy will still propagate into the shadow region.

1.2.4 Plasma in Fire Environments

A plasma is a state of matter that contains charged particles that freely move. When an electromagnetic wave impinges on a plasma, energy is imparted to the charge particles, tracking the oscillation of the electric and magnetic fields. The higher the density of free charged particles, the more energy that is coupled into the plasma and particle motion. The flame region of a fire consists of free electrons and charged particles, which are generated by the combustion process. The positive ions have a mass which is generally 2000

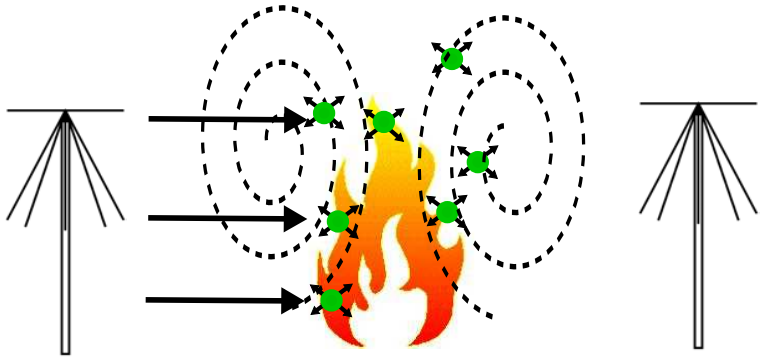

Figure 1.5: Scattering Illustration - Particle and Turbulent air movement

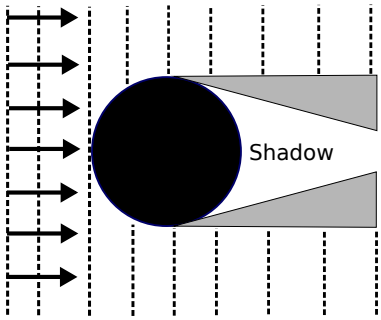

Figure 1.6: Diffraction Illustration

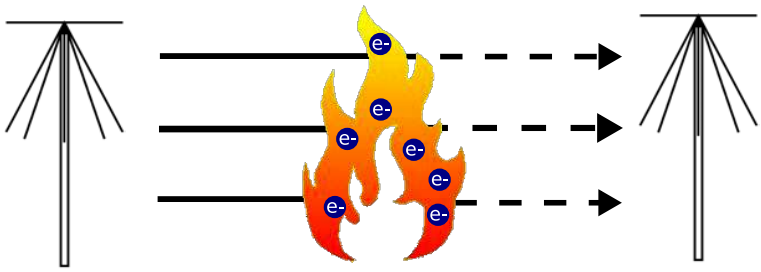

Figure 1.7: Plasma/Ionisation Illustration

times greater than an electron and because of this, electrons are dominant in interactions with electromagnetic radiation[13]. The formation of a combustion induced plasma will be discussed in a section on combustion.

Whilst the particle is moving with the field, if a collision occurs momentum is lost and electromagnetic energy transferred and dissipated. This results in attenuation of the electromagnetic wave. Attenuation and dispersion of microwaves for ionised gases has been studied by Margenau[77]. Schneider and Holfmann [96] applied Margenau's theory to ionised gases in flames. Using an experimental technique involving the attenuation of microwaves, Sugden et al. studied the electron concentration of alkali and alkaline salts in coal-air flames[6, 7] and hydrogen-air flames [106, 107]. The number collision of electrons with neutral particles per second is referred to as the collision frequency (denoted ν).

When an electron is met by an oscillating electric field its mean displacement r is mathematically expressed by equation 1.3 [13].

$$m\frac{\partial^2 \mathbf{r}}{\partial t^2} + m\nu\frac{\partial \mathbf{r}}{\partial t} = e\mathbf{E} \tag{1.3}$$

where m is the particles mass, e is electronic charge ($\sim 1.6\times10^{-19}C$) and ν is the collision frequency. When we sum together the interactions over a volume of electron density the coefficient for the right hand side is defined as the plasma frequency. The plasma frequency is defined as $\omega_P = Ne^2/(\epsilon_0 m)$, where N is the density of charged particles in m^{-3} , e is the charge at $1.6 \times 10^{-19}C$ and m is the mass of the particle. The plasma frequency of positive charges is very low due to the much larger mass. Flame investigations have tried using low frequency radio waves to identify the positive charges in flames[10]. The plasma frequency of electrons is substantially larger and strongly interact with electromagnetic waves.

As can seen from equation 1.3, the collision frequency has the effect of dampening the electron oscillation. Mathematically, it can be calculated using the relationship shown in equation 1.4 [54].

$$\langle\nu_{eff}\rangle = \frac{8}{3\sqrt{\pi}}N\left(\frac{m_e}{2kT_e}\right)^{5/2}\int_0^\infty v^5 Q^{(m)}(v)\exp\left(-\frac{m_e v^2}{2kT_e}\right)dv \tag{1.4}$$

where k is boltzmann's constant, T_e is the electron temperature, m_e is the mass of an electron and Q is the momentum-transfer cross section for elastic collisions. This calculation can be quite complex but Itikawa[54] has calculated the effective collision frequency for a number of gases over a large temperature range. Vidmar has explored the generation, attenuation and properties of plasma in the lower atmosphere[119]. Vidmar has applied Itikawa's collision frequency data to the earth's atmosphere and reduced the features to pressure, temperature and gas make-up. At low altitudes the collision frequency increases, resulting in a collision dominant plasma with very broadband characteristics.

In addition to this, a number of indirect measurements of the collision frequency have been recorded from experiments with various flames and conditions. Table 1.2.4 is a summary of collision frequencies found in the literature concerning flames.

1.2.5 Propagation in Forest Environments

The propagation of radio waves through a fire inherently includes propagation through a background medium. In a bushfire, this background medium encompasses some form of

Conditions	ν_{eff}	Ref.
Acetylene - air 760mm Hg, 2480°K	2.6×10^{11}	[14, 96]
Acetylene - O_2 7.5mm Hg, 2300°K	3.7×10^{9}	[14, 96]
Coalgas - air 760mm Hg, 2200°K	8.8×10^{10}	[106]
Pine Needles - 1013.25hPa , ∼1100°K	$3.43 - 5.97 \times 10^{10}$	[61, 82]

Table 1.1: Flame collision frequency

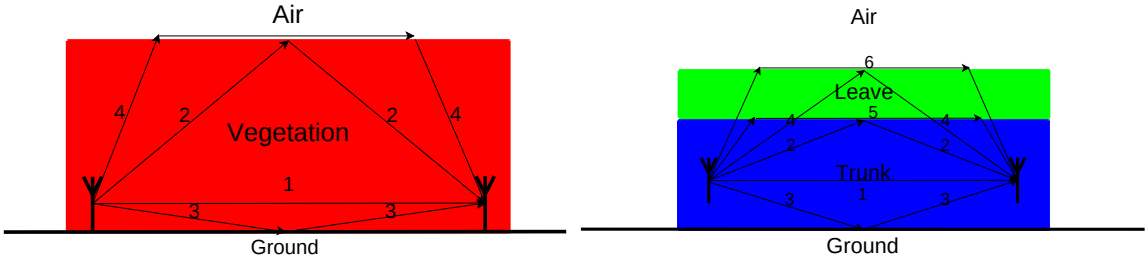

(a) Single Slab (b) Multi-Slab

Figure 1.8: Slab Model

vegetation. It is therefore important to consider the propagation of radio waves through a forested environment.

Radio propagation in forests is approached from two perspectives. From low frequencies the forest is treated as a uniform slab and from high frequencies the forest is treated as a randomly placed medium. Hill[50] considers HF propagation in a forest environment. Tamir [115] examined forest propagation for 1-100MHz using a slab model. Tamir and Dence identified the lateral wave on the air-forest interface as the dominant propagation path in lossy forests and examined its loss characteristics[30]. Interfaces of the forest and more complex propagation was studied for 2-200MHz in [30]. A lossy dielectric slab model is still deemed sufficient at these frequencies. A depiction of the slab model is shown in Figure 1.8. Each ray path has been numbered. Ray paths on the air-forest interface have been identified as the dominant propagation in a lossy forest. In the single model this is ray number 4, in the multi-slab model this is path 6.

Seker [98] introduced a multi-layered slab model to examine stratified forest for frequencies above 200MHz to 2GHz [72]. The stratified forest considers a trunk, branch and leaf layers as seperate layers in the forest (as shown in Figure 1.8(b)). Later work [99]

introduces anisotropy in the dielectric to better model trunk, branch and leaf orientation. Seker also introduced an extension of the slab model by separating coherent fields (slab related) with incoherent fields (scatter related). This work was experimentally validated on S-Band (2-4GHz)[100]. Stochastic approaches can also been found in [53].

As the frequency increases, the incoherent or scatter aspect of the forest becomes greater. Chauhan et al. [84] has investigated a Boreal forest with an extended slab model with randomly distributed cylinders in the slab to represent branch and leaf orientation. Chauhan's work considers P-, L-, C- bands with an airborn Synthetic Aperture Radar (SAR) platform. Similar SAR modelling and experimentation work has been performed on Australian mixed species forests in Queensland by Lucas et. al[90]. Australian forests are problematic due to their low density and variability in plant life.

Dielectric properties are invaluable to accurately model the forest environments. The most extensively used work is the El-Rayes and Ulaby model for vegetation[31, 118]. It is valid from 200MHz to 20GHz and includes dispersion characteristics related to free and bound water. The strong dependence of water distribution and movement in the plant requires some idea of the water relations in the plant. Gates[73] provides some insight into this with data for American conifers and hardwoods. Australian eucalypt data can be found in [4].

1.3 Combustion

Combustion consists of a series of complex exothermic reactions between fuel and oxygen, accompanied by the production of heat and light. For a chemical reaction to occur it requires suitable reactants (fuel and oxygen), the activation energy (the energy required to begin the reaction) which produces products (CO_2 , H_2O ...). A simple representation of the overall chemical reaction for a simple and general hydrocarbon is shown below.

$$CH_4 + 2O_2 \longrightarrow 2H_2O + CO_2 \tag{1.5}$$

$$C_xH_y + \nu_{O_2}O_2 \longrightarrow \nu_{CO_2}CO_2 + \nu_{H_2O}H_2O + \nu_{CO}CO \tag{1.6}$$

where CH_4 is methane, the simplest of hydrocarbons, and C_xH_y represents a general hydrocarbon. In this example, the fuel (C_xH_y) is burnt in the presence of oxygen. If

oxygen is not abundant, greater proportions of carbon-monoxide (CO) will be produced as well as unburnt reactants.

When considering the different steps that occur in combustion, the chemical process becomes very complex. Taking methane as an example of the simplest hydrocarbon (CH_4), Figure 1.9 shows the reaction flow and intermediate products involved [71]. Loo[71] states, 'in reality several hundreds of reversible elementary reactions are needed to describe in detail the combustion process of even light hydrocarbons, such as methane, which is an important intermediate in biomass combustion'. As the size of the hydrocarbon chain increases the complexity of the chemical process also increases.

NOTE:
This figure is included on page 15 of the print copy of the thesis held in the University of Adelaide Library.

Figure 1.9: Methane Reaction Flow [71]

1.3.1 Flames

Flames are a visible indication of combustion. Flame colour and temperature are determined by the reactants and combustion conditions. A representative diagram of a flame is shown in Figure 1.10. There are a number of areas that are important to consider in the flame. At the base of the flame, which is closest to the fuel source, there is the C_2 and CH zone [41]. In this region, a complex molecule fuel is broken into simple easily combustible molecules. The main reaction zone is where the actual combustion reaction takes place. This is on the edge of the luminous part of the flame. Flames in bushfires are diffusion flames, which require the oxygen to be diffused into the combustion zone. The maximum temperatures of the combustion process is limited to a small region of space where the oxygen is present and is quickly exhausted. Above these two zones is the luminous zone, where activated carbon is present. The activated carbon is what radiates light (generally yellow for carbon).

The region of combustion activity is a very small area of the whole structure of the flame. Turbulence or air movement allows the reactants to mix, increasing the combustion surface area. In large scale fires, the atmosphere surrounding the fire contains convective currents that bring oxygen into the combustion zone.

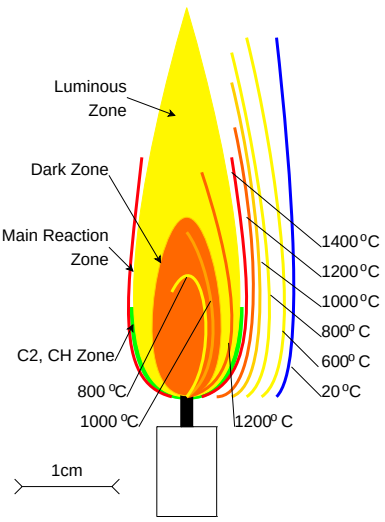

Figure 1.10: Flame Regions and Temperature [14]

1.3.2 Electrical Aspects of Combustion

It has been known for a long time that flames possess a high electrical conductivity and can be distorted by an electric field. In 1802, G. Erman obtained currents from flames by inserting two wires in them[14]. Early experiments utilised DC voltages to understand the currents induced by flames[125]. Later, Payne and Weinberg investigated flame distortion and ion movement in ethylene flames under strong DC voltage fields (7-13kV) in diffusion and premixed flames[89]. This is an interesting phenomena as products of combustion are electrically neutral and reactants are generally similar.

Further electrical interactions have been seen with electromagnetic waves, such as microwaves [96] [6] and HF [10] [106] in flames. Microwaves have been used primarily for the detection of electrons and HF to detect positive and negative ions, which have a much greater mass and therefore lower resonant frequency. Belcher and Sugden [6] show that the collision frequency, which is related to attenuation, is inversely proportional to weight of the charged particle. These experimental observations present a precedent of interactions with electromagnetic waves in our frequency range of interest (50MHz - 1GHz).

In 1957, Calcote [14] summarised a number of possible mechanisms for ionisation in flames. Since that time, two major mechanisms have been identified [101]; chemi-ionisation, which involves the chemical creation of intermediatory charged particles and thermal ionisation, which involves the stripping of electrons from an atom by thermal excitation.

Both chemi-ionisation and thermal ionisation are included in this discussion due to there importance in flora fuelled fires. Chemi-Ionisation is attributed to hydrocarbon reactions, where as thermal ionisation requires the presence of low ionisation energy elements in the fuel.

1.3.3 Chemi-Ionisation

Chemi-ionisation is the temporary generation of ionised particles in hydrocarbon chemical reactions. As shown above, in Equation 1.6 and Figure 1.9, combustion is a complex chemical reaction. Long hydrocarbon molecules are broken into ‘simpler’ chemical units

prior to or in the reaction zone. During the combustion process, temporary intermediary charged particles are created.

The ions produced by chemi-ionisation have been an element of conjecture. Mobility studies have shown that positive ions are low in mobility (typically 1V cm $\sec^{-1}$), compared to negative elements (typically 10^3V cm $\sec^{-1}$) indicating electrons are the main mechanism of negative charge transportation [14]. Probe studies at atmospheric pressure showed the concentration of electrons exceeds the concentration of positive ions in the reaction zone. The reverse situation applies outside the reaction zone[9][15]. A representative diagram for the distribution of flame conductivity is shown below.

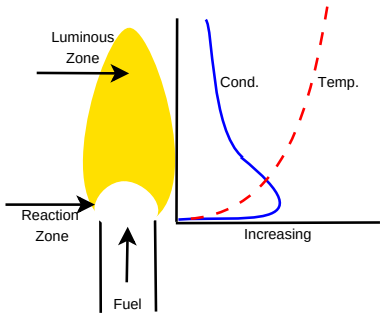

Figure 1.11: Chemi-Ionisation Zone[15]

The conductivity is indicative of chemi-ionisation being concentrated around the reaction zone. The actual size of these ion and electron populations depends on the characteristics of the fuel, flame, stoichiometric balance and additives to the fuel. Ion concentrations in flames is of the order of $4.5 \times 10^{10} ions$ cm^3 for hydrocarbon-air flames [14] and for acetylene at atmospheric pressure electron concentrations of the order $7 \times 10^9 \text{cm}^3$ [96]. Estimations show concentration should be approximately $10^{12} ions$ cm^3 [14].

Conclusive experimental evidence first appeared through the mass spectrometric work of Green and Sugden [44] and Calcote [15] as to what reactions occur in the chemi-ionisation process. This process consists of three stages. The electron creation stage, the proton exchange and electron attachment.

$$CH + O \longrightarrow CHO^+ + e^- \tag{1.7}$$

$$CHO^+ + H_2O \longrightarrow H_3O^+ + CO \tag{1.8}$$

$$H_3O^+ + e^- \longrightarrow H_2O + H \tag{1.9}$$

Further generalisation was made by Klemm and Blades [62] and Hayhurst[46] to include other possible reactions in longer hydrocarbon molecules than those used by Green and Sugden.

Being a chemical process, the population of ions and electrons in the flame is largely concentrated in the reaction zone. Electron populations are extremely localised as the population is generally higher in the combustion zone and then quickly decreases outside. This results from quick attachment of the electrons to form negative ions in the other parts of the flame [9] [14].

Chemi-ionisation has been studied by measuring the generation and recombination rates in flames. One experimental method to measure these rates is the saturation method outlined by Lawton and Weinberg[67]. This procedure measures the generation rate of ions. Boothman et al. has measured the generation rate for a number of fuels and flame types[27]. Saturation currents for woody fuels can be found in [65]. Other flames have been examined in[101] [15].

In application to plant life and bushfires, it is probable that significant electron populations are generated by chemi-ionisation. Chemi-ionisation is known to increase for larger hydrocarbon molecules and plant life is known to consist of reasonably large molecules, lignin ($C_{40}H_{40}O_6$) and cellulose ($C_6H_{10}O_5$).

1.3.4 Alkali-Alkaline Thermal Ionisation

Thermal ionisation occurs when an electron attached to an atom in its ground state is thermally excited to a free electron. Compared to chemi-ionisation, which is seen to be purely chemical, thermal ionisation is strongly dependent on the temperature. For an element M, the ionisation equation is described in equation 1.10.

$$M \longrightarrow M^+ + e^- \tag{1.10}$$

Mathematically, this chemical process is modelled using the Saha equation [76].

$$\frac{N_{M^+}N_{e^-}}{N_M} = \frac{2P_{M^+}}{P_M}\left(\frac{2\pi m_e kT}{h^2}\right)^{\frac{3}{2}} \exp\left(\frac{-E_i}{kT}\right) \tag{1.11}$$

where N is the respective number of particles, P is the respective internal partition function, k is Boltzmann's constant, T is temperature (°K) and E_i is the ionisation

potential. According to the Saha equation, the electron population is greatly controlled by the ionisation potential of the element M. The lower the ionisation potential, the more dominant the element will be in releasing electrons. Group I and II metals are known to have relatively low ionisation potentials. Ionisation data has been collated in Table 1.2. Calcote [14] notes that the conductivity is substantially larger for flames containing metal salts than for those that do not. Furthermore, because the main ionisation mechanism is thermal and not chemical, the conductivity profile generally extends further into the flame above the reaction zone[14], resulting in a greater surface area being ionised. This implies that where thermal ionisation is present it will be a dominant mechanism for electron generation in terms of population and surface area. One way to experimentally establish

Element	**Symbol**	**Group**	**Ionisation Potential**
Potassium	K	I	4.33eV
Sodium	Na	I	5.15eV
Calcium	Ca	II	6.11eV
Magnesium	Mg	II	7.65eV
Silicon	Si	IV	8.16eV
Zinc	Zn	IIB	9.41eV

Table 1.2: Ionisation Potential

the electron population in flames is to use microwaves. Margenau [77] first considered the attenuation and dispersion of microwaves in high temperature gases. Schneider and Holfmann [96] then went on to apply Margenau's theory to flames. Using this experimental technique of microwaves, Sugden et al. studied the electron concentration of alkali and alkaline salts in coal-air flames[6, 7] and hydrogen-air flames [106, 107]. Sugden et al. notes in these studies that the Saha equation does not adequately describe the levels of ionisation in the flame. Sugden et al. concludes the ionisation process is not in equilibrium. He proposed a more complex process involving alkali hydroxyl and oxide attachment. This more accurate chemical process is shown in equation 1.12.

$$M + OH \longrightarrow MOH^+ + e^- \tag{1.12}$$

or

$$MO + H \longrightarrow MOH^+ + e^- \tag{1.13}$$

Sugden's studies show in general the level of ionisation is one-fifth of that calculated by the Saha equation [106]. This was further supported by [106] [47] [97]. Furthermore, Schofield and Sugden[97] demonstrated that Group II metals (Ba , Sr,Ca, Mg) , which have higher ionisation potentials, produce greater electron populations than Group I metals (Na,K,). There are however, a number of factors that affect the amount of ionisation, such as the fuel, stoichiometric balance, salt used and flame type.

All work cited above considers hydrocarbon fuels seeded artificially with metal salts. The next section considers plant life as fuel and the implications on ionisation.

Plant Life as Fuel

So far we have only considered hydrocarbons as a source of fuel. This is because they have a chemical reaction that is understandable with simple chemistry. When we look at plant life, its molecular structure consists mainly of carbon, hydrogen and oxygen [116]. The major chemical constituents of plant life are cellulose, hemicelluloses and lignin. Cellulose ($C_6H_{10}O_5$) is a condensed form of glucose ($C_6H_{12}O_6$) and makes up 40 to 45% of wood[71]. Hemicellulose is a molecule that is less complex than cellulose and consists of other sugars[71]. It makes up 20 to 35% of wood. Lignin ($C_{40}H_{44}O_6$) is a non-sugar molecule that gives strength to wood and makes up 15 to 30% of wood [71]. It is commonly referred to as the glue of wood[116]. The chemical make up of wood and plant life is substantially more complex than simple hydrocarbons. In addition, there exists trace elements of a range of minerals that are important to a plant's health. Trace elements are important in association with radio propagation through fire as highlighted by Mphale and Heron[48]. These elements have the potential to be present in the combustion zone and undergo thermal ionisation.

For a non-gaseous fuel to reach the combustion zone it undergoes a number of changes. There are two main processes, drying and pyrolysis, prior to actual combustion. Plant life inherently contains a large amount of water. Plant life should always be dried prior to burning in a combustion furnace or pot-belly. In a bushfire a large amount of thermal energy is used in drying the fuel load. A hot dry summer aids the drying process and therefore increases the occurrence and spread of bushfires. The process of drying occurs at temperatures below 100°C .

Once the wood or a section of wood is in a dry state, pyrolysis takes place. This process is the delivery of solid fuel into a gaseous state that then enters the combustion zone. It is defined as "the thermal degradation in the absence of an externally supplied oxidising agent" [71]. Pyrolysis occurs for any fuel that is not in a gaseous state. Pyrolysis is an endothermic process and requires thermal energy. Different parts of the plant undergo pyrolysis at different temperatures. Hemicellulose starts when temperatures are above 200°C. Cellulose and lignin start at substantially higher temperatures above 400°C . Hardwoods are known to have greater proportions of hemicellulose than cellulose, which explains a hardwoods greater burning efficiency.

Once pyrolysis has occurred, combustion occurs and the majority of the wood is burnt into water, carbon dioxide, carbon monoxide and ash. Considering the large presence of hydrogen and carbon in plant life, we can already see that chemi-ionisation will be present in the combustion of plant life. As noted above, if thermal ionisation is possible it will be a dominant mechanism for producing electron populations with a large surface area. To investigate this we need to understand what ash is.

Ash, a by product of combustion consists of oxidised trace elements that are caught up in combustion. A breakdown of ash is shown in Table 1.3 for different woods and Table 1.4 for different plants.

Ash Analysis	**Pine**	**Oak**	**Spruce**	**Redwood**
SiO_2	39.0	11.1	32.0	14.3
Fe_2O_3	3.0	3.3	6.4	3.5
TiO_3	0.2	0.1	0.8	0.3
Al_2O_3	14.0	0.1	11.0	4.0
Mn_3O_4	Trace	Trace	1.5	0.1
CaO	25.5	64.4	25.3	6
MgO	6.5	1.2	4.1	6.6
Na_2O	1.3	8.9	8.0	18.0
K_2O	6	0.2	2.4	10.6
SO_3	0.3	2.0	2.1	7.4
Cl	Trace	Trace	Trace	18.4

Table 1.3: Ash Analysis for Different Woods [116]

Ash wt % (d.b)	Wood chips (spruce)	Bark (spruce)	Straw (wheat,rye,barley)	Cereals (wheat,triticale)
Si	4.0 - 11.0	7.0 - 17.0	16.0 - 30.0	16.0 - 26.0
Ca	26.0 - 38.0	24.0 - 36.0	4.5 - 8.0	3.0 - 7.0
Mg	2.2 - 3.6	2.4 - 5.6	1.1 - 2.7	1.2 - 2.6
K	4.9 - 6.3	2.4 - 5.6	1.1 - 2.7	1.2 - 2.6
Na	0.3 - 0.5	0.5 - 0.7	0.2 - 1.0	0.2 - 0.5
Zn	0.026 - 0.05	0.03 - 0.094	0.006 - 0.009	0.012 - 0.02

Table 1.4: Plant Minerals

As can be seen in the tables, the majority of ash is made of trace metals in plant life. Here, we have some indication that these elements are present in plant life and more importantly are transported into the combustion zone and undergo chemical change. Particular elements important in ionisation are calcium (due to its abundance as a trace element), magnesium and potassium (due to its low ionisation potential).

The pyrolysis of alkali-alkaline elements such as potassium, magnesium, and calcium has been studied by [63] [60] [88] [55] [117] [32] [28]. Alkali metals cause corrosion and deterioration in boilers, reducing their lifetime[88]. Therefore, they receive a great deal of attention in biomass literature. Okuno [117] has shown that potassium is one of the first elements to undergo pyrolysis and begins pyrolysis at approximately 400°C , compared to calcium and magnesium, begin at approximately 600°C . As a result, less potassium is retained in the wood compared to the other two. Additionally, under fast pyrolysis conditions almost all potassium is pyrolysised.

As indicated by Mphale and Heron[81], these trace elements are present in plant life and have the potential to produce substantial electron populations. This is due to thermal ionisation.

Australian forests consist mainly of plants from the eucalypt family. Heron[48] has summarised a number of key features of alkali concentrations in Australian forests. However, little attention has been paid by Heron to the distribution of trace elements in the plant itself. Alkali trace elements are known to exist in plants but if they are not accessible as a fire passes through little ionisable material will be available. This is important because a fire front does not burn the entire tree: there is always a structure present

after, and burning of the entire structure occurs well after the fire front has passed. What is necessary for a substantial electron population to be generated is accessibility of the ionizable material during flaming of the plant. When we consider the distribution of trace metals in plant life we see that there is indeed great accessibility of alkali elements to the combustion zone.

There is a number of data available in Attiwill's *Nutrition of Eucalypts* [4]. Two tables have been taken from to illustrate the distribution of alkali elements in a tree's structure.

Table 1.5: Range of measure concentrations of macro-nutients various components of eucalypts[4]

Table 1.5 shows the concentration of alkali metals is greater in the foilage and bark compared with the internal wood and branches. This is true for potassium and magnesium

	K			Ca		
Eucalypts	H[a]	S[b]	B[c]	H	S	B
E. cameronii	0.002	0.037	0.529	0.003	0.0024	0.58
E. campuanulata	0.003	0.016	0.410	0.002	0.006	5.25
E. oleosa	0.054	0.160	0.625	0.270	0.160	2.00
E. saligna	0.004	0.100	0.970	0.010	0.050	0.65
E. saligna	0.006	0.075	0.440	0.025	0.064	3.88
E. maculata	0.022	0.080	0.190	0.237	0.124	2.93
E. diversicolor	0.018	0.105	0.145	0.018	0.064	0.31
E. sieberi	0.016	0.090	0.070	0.075	0.095	0.1
E. grandis	0.020	0.125	0.175	0.075	0.065	3.15
E. viminalis	0.007	0.115	0.160	0.020	0.073	2.24
E. obliqua	0.001	0.065	0.090	0.002	0.051	0.1
E. obliqua	0.006	0.059	0.266	0.008	0.022	0.43
E. diversicolor	0.009	0.12	0.35	-	0.069	2.08
E. calophylla	0.05	0.10	0.32	-	0.14	0.47
E. marginata	0.023	0.051	0.234	0.007	0.024	0.43
Other Species						
Tristania conferta	0.105	0.105 0.220	0.175	0.080	0.67	
Syncarpia glomulifera	0.004	0.095	0.016	0.013	0.060	0.13
Acacia aneura	0.002	0.059	0.191	0.580	0.250	2.35
Ackama paniculata	0.210	0.110	0.265	0.049	0.061	0.32
Ceratopetalum apetalum	0.170	0.120	0.100	0.270	0.260	0.48
Tarreita actinophylla	0.090	0.290	0.166	0.075	0.076	0.88
Pinus radiata	0.028	0.094	0.073	0.115	0.090	0.56

Table 1.6: Trunk distribution

[a]Heartwood
[b]Sapwood
[c]Bark

with calcium showing some variation of different plant species. Table 1.6 shows a higher concentration of mineral content in the bark section of the trunk.

This information is particularly important when considering values for a plant's mineral concentration. A single value for mineral concentration over the entire plant will underestimate the actual amount available to a fire. Concentration varies over the entire plant structure, with a greater proportion existing in the extremities of the plant. In combustion, it is self evident that during initial flaming from a fire front a substantial proportion of a plant's trace minerals are accessible and transported to the combustion zone. Hence, significant thermal ionisation with naturally occurring trace metals is very possible in a bushfire or any biomass based fuel.

SECTION 2

Experimental Investigations

Experimental investigation of radio propagation through bushfire environments is a current shortfall in scientific studies and literature. Only one such large scale fire (450m by 450m) experiment, known as the Euroka experiment, has been conducted that was by the Department of Supply in Queensland in 1970 [124]. Frequencies 2, 5, 160, 450 and 4000MHz were monitored over a short path of 700m and a long path of 24km. The major focus in monitoring radio propagation was to investigate sub-refractive conditions caused by the fire. Measurements showed the signal rarely fell 5dB below 'pre-burn' levels during the experiment and the final consensus was no substantial propagation effects were observed.

On the micro scale, attenuation and phase shift in electromagnetic propagation has been used in laboratory flames to measure flame characteristics [96]. The attenuation of microwaves was a popular method for measuring electron concentrations in flames[105],[107] [39] and will be further explored in another section. More recently, Mphale and Heron[61][82] have experimented with pine needle fires in a small combustion chamber. Microwave attenuation at 8-10GHz was observed, demonstrating attenuation can occur with biomass fuel. Between these two extremes, the literature is silent. It is unknown what is occurring as we move from laboratory flame studies to large scale bushfire. This intermediate range of propagation over short paths of 10-100m has never been considered.

The experimental campaign of this current work is aimed at filling this gap and considers small scale fire, typically 1-10m in size (the order of a wavelength). This is an

important step in taking some of the micro-scale findings of laboratory work and seeing whether they transfer to larger scale fire. This scale of fire is beneficial as it represents a pocket of fire present in a large fire front. Additionally, the ability to control the fire allows observation at close proximity to the flame. This observation allows a better understanding of the propagation characteristics around the combustion region. Furthermore, small fires give one the ability to control the fire, hence safely experiment without large amounts of manpower. As a consequence, smaller manageable fires also allow a greater number of experiments, and a means to assess for consistency of observations.

Two sets of equipment are utilised in the experimental campaign. One set involves broadband radio equipment, which considers propagation through simple small-scale fires over a range of frequencies. The second set of apparatus operates on a single frequency band and uses multiple transmitters separated by a slight difference in frequency to track different paths of propagation. This apparatus is designed for longer propagation studies and bushfire deployment.

The primary interest of this work is to consider frequencies below 1GHz. This encompasses the main emergency services communication bands. Particular interest is paid to VHF band communications (100-180MHz), UHF band communications (400-500MHz) and common mobile communication bands from 800-1000MHz. Broadband equipment is used to monitor this entire frequency range. The idea is to identify particular frequency bands or propagation phenomena that are particularly sensitive to the presence of fire. This experimental work is however, indicative and needs further elucidation with modelling. Later chapters provide a more vigorous understanding by means of electromagnetic modelling.

2.1 Broadband Experiments

Broadband experimentation provides us with a number of tools. Firstly, it helps deduce whether particular areas of the spectrum are affected. Preliminary experiments have already pin-pointed problematic frequency bands and directed where to concentrate future work. Secondly, factors that affect propagation are generally frequency dependent; therefore it is hoped that particular contributing factors can be identified by looking at broadband experimental results.

2.1.1 Broadband Apparatus

The broadband equipment consists of a transmitter and receiver that sweep over a large range of frequencies. The spectrum analyser used was the HAMEG HM5014, which comes with a built-in signal generator. From the signal generator, a power amplifier (Mini-Circuits ZHL-2-8) was used to increase the power at the antenna. Discone antennas, which are designed for operation from 100MHz to 980MHz , were used to transmit and receive. After propagating through the fire, the signal is received via one of the antennas, fed back into the spectrum analyser and downloaded onto a computer. Using this setup, we obtain a sample every 7-12 seconds from 100MHz to 1GHz with 0.5MHz resolution. Whilst collecting propagation data the system also collects WebCam pictures of the fire every 1-2 seconds. These pictures help to identify physical events that might correlate with propagation events. A MATLAB GUI was used to display the webcam pictures and propagation measurements. The GUI allows real time analysis of the signal and correlation of propagation anomalies with a visual picture of the fire.

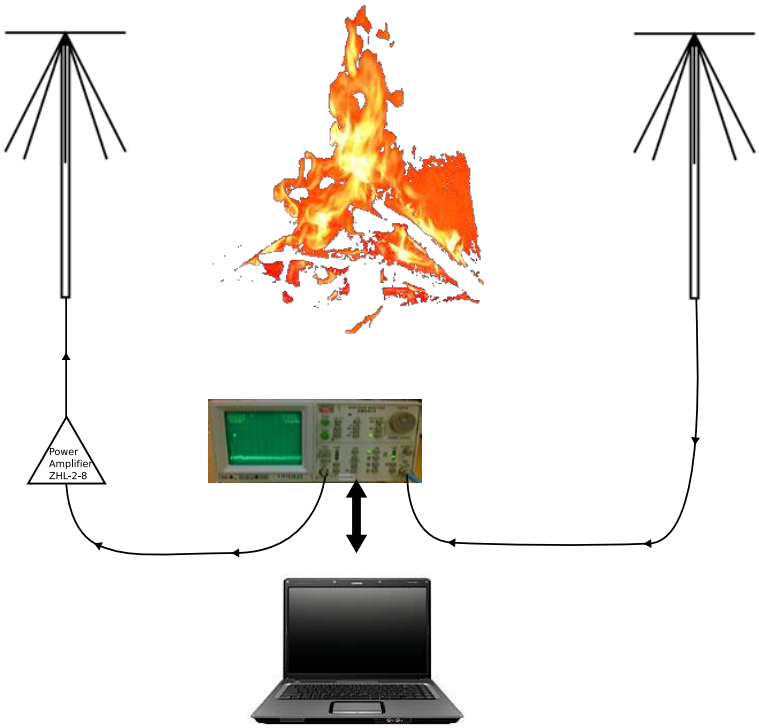

Figure 2.1: Overall Setup, Antennas, HAMEG, MATLAB GUI

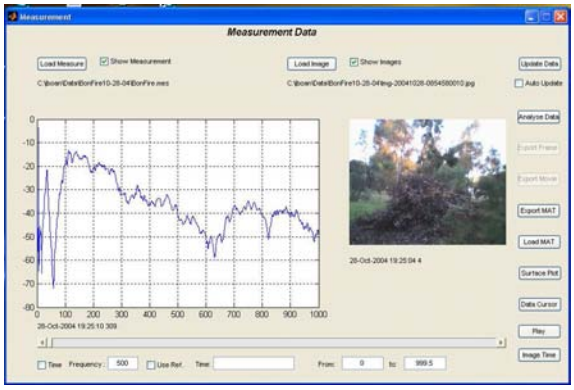

Figure 2.2: Measurement GUI

2.2 Small Scale Fires

Measurements for three fires, denoted Fire A, B and C, are presented in this section. A summary of the dimensions is given in Table 2.1 and a representative picture is shown in Figure 2.3. To help summarise the plethora of data, we will concentrate on three bands of frequencies. Band 1 represents a typical VHF communications band, encompassing frequencies from 160MHz to 180MHz . Band 2 represents a UHF communications band and encompasses frequencies from 400MHz to 450MHz . Band 3 considers a popular band for mobile communications with frequencies from 850MHz to 950MHz .

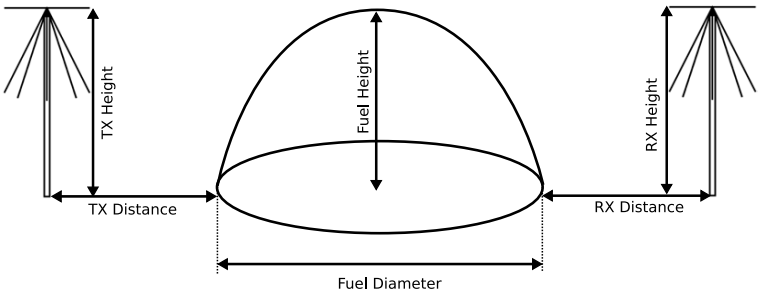

Figure 2.3: Fire Dimensions

2.2.1 Fire A

Fire A was located on a private property in Lyndoch of the Barossa Valley, in late October, 2004. It was the first fire of the campaign. The ambient temperature was approximately

	TX/RX Height	*TX/RX Distance*	*Fuel Height*	*Fuel Diameter*	*Additives*
Fire A	1.6m	1.5m	1.5m	3.0m	-
Fire B	1.8m	5.0m	3.6m	7.5m	-
Fire C	1.8m	5.0m	2.8m	7.0m	K_2SO_4

Table 2.1: Fire Dimensions

16°C, with very minimal wind. The fire was small in radius, with fuel consisting of eucalyptus leaves and branches from the surrounding area. An accelerant was used to aid in even ignition of the fuel heap. Ignition occurred at approximately 6:40pm. In this experiment, antennas were placed 1.5m from the base of the fuel heap.

A selection of webcam photos are displayed in Figure 2.4(a) - 2.4(l). As can be seen, the fire builds in intensity very quickly but subsides after about 3 minutes of burning. Due to safety concerns, water was applied to the fire to dampen it out about 2 minutes after ignition. In Figure 2.4(j),2.4(i) there is an observable stream of water from the left. Time series plots of each Band is shown in Figure 2.5 - 2.7. An entire spectrum plot is shown in Figure 2.8 for three key time samples; pre-burn, maximum attenuation and post-burn. A noticeable characteristic of these plots is the sudden drop in the signal strength on Band 1 and Band 2. By inspecting the photos, it can be seen that the sudden drop in signal strength correlates with the presence of the fire. It is noticeable that the fuel heap reduces as the fire burns. The deterioration in height of the fuel masks the effect of the fire on propagation and will be discussed in Section 2.2.5.

2.2.2 Fire B

Fires B and C were performed on a farming property near Pipers Creek, Victoria. The experiments took place during April 2005, just after the fire ban had ended. Fire B was the largest of the three fires used in these experiments. The fuel was composed of eucalypt branches and leaves from the surrounding region. The ground around the fuel heap was mowed and suitably prepared. Regions around the antennas were sprayed with water for protection of equipment. A lot of this activity is seen as disturbance in the signal strength; particularly visible on Band 1 in Figure 2.9. An accelerant was not used to assist ignition but the fuel heap was evenly ignited around the base with a flame torch.

(a) 2sec (b) 11sec (c) 23sec

(d) 36sec (e) 52sec (f) 67sec

(g) 85sec (h) 105sec (i) 145sec

(j) 219sec (k) 305sec (l) 1156sec

Figure 2.4: Fire A. Photos - Time after Ignition

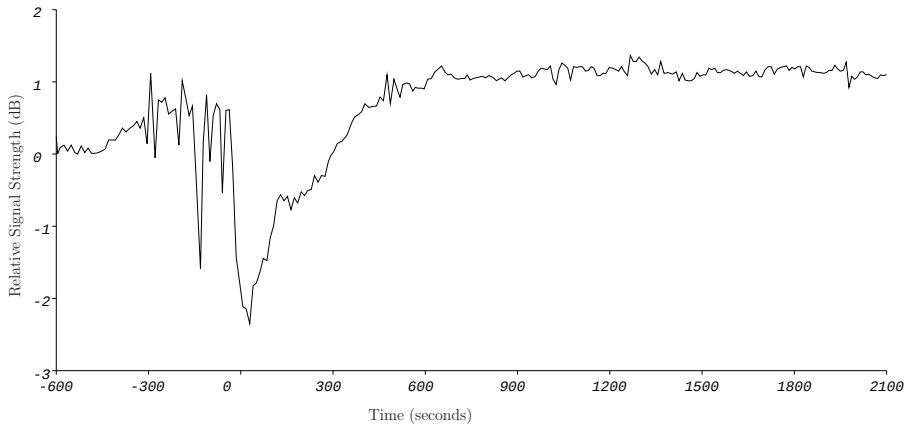

Figure 2.5: Fire A. Band 1 160MHz - 180MHz

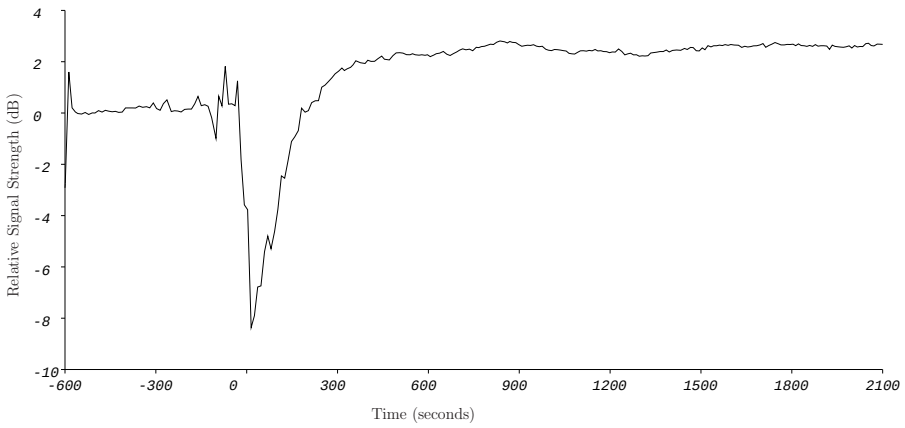

Figure 2.6: Fire A. Band 2 400MHz - 450MHz

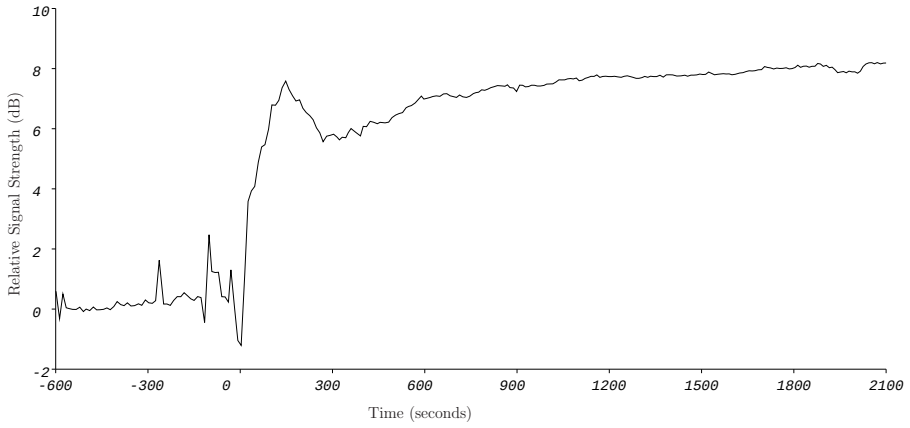

Figure 2.7: Fire A. Band 3 850MHz - 950MHz

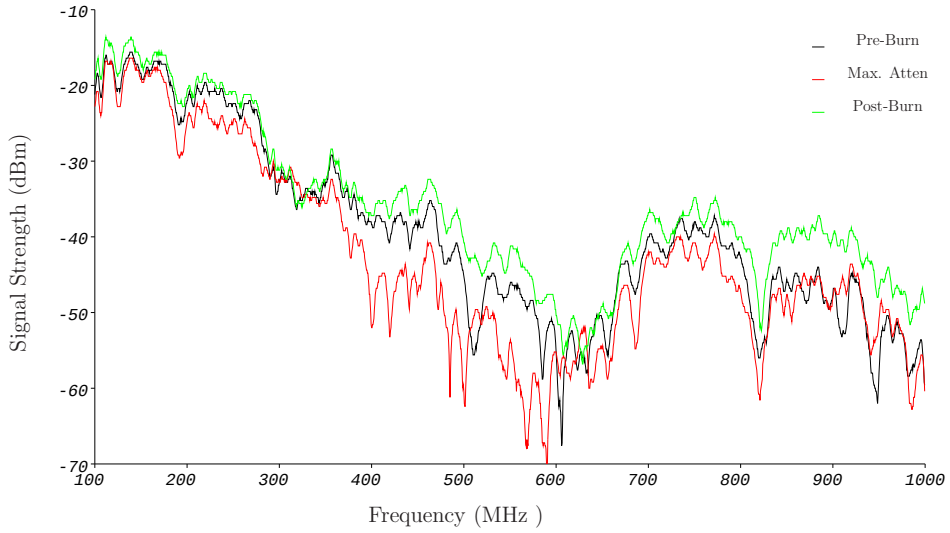

Figure 2.8: Fire A Spectrum Plot

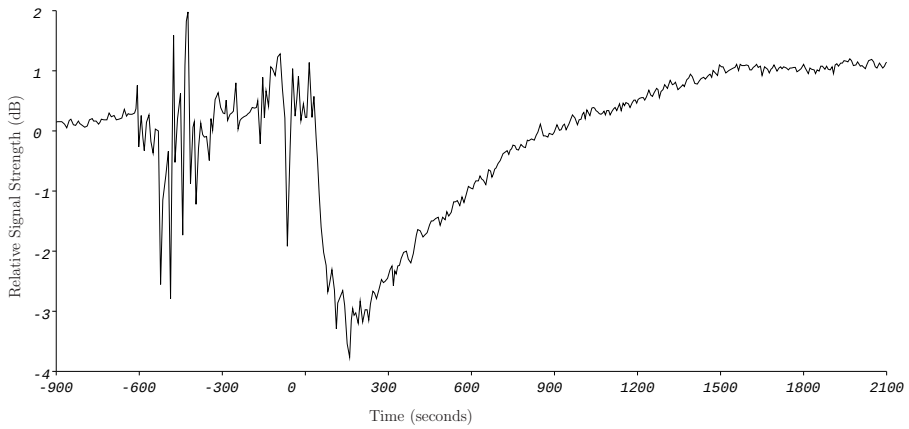

Figure 2.9: Relative Signal Strength - Fire B. Band 1 160MHz - 180MHz

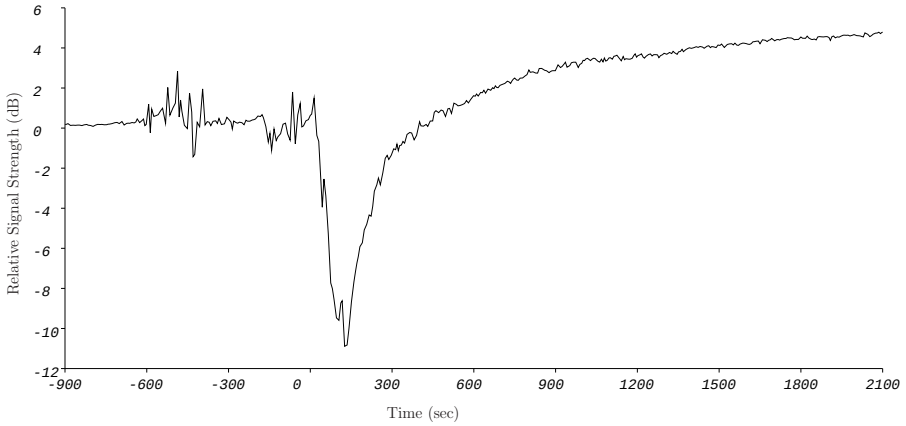

Figure 2.10: Relative Signal Strength - Fire B. Band 2 400MHz - 450MHz

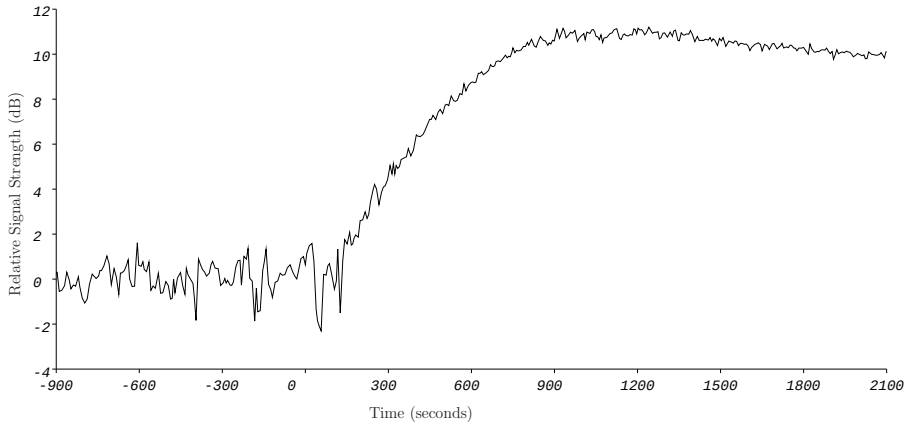

Figure 2.11: Relative Signal Strength - Fire B. Band 3 850MHz - 950MHz

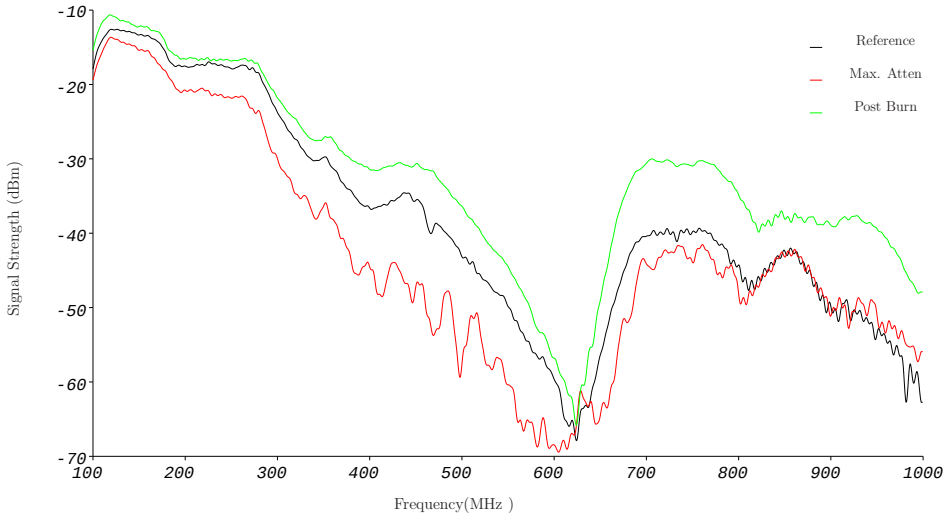

Figure 2.12: Fire B Spectrum Plot

Signal strength plots in time for Band 1 - 3 are shown from Figure 2.9 - 2.11. Compared to Fire A, Fire B was a much larger fire and measures propagation over a larger distance.

2.2.3 Fire C

Fire C was performed on the same day as Fire B, and under similar conditions. The fuel consists of eucalypt branches and leaves, although after burning it was observed that this fire contained a number of larger logs in the base of the fuel heap. An additive of 2.5kg of K_2SO_4 was added to the fuel heap in the form of small pellets. The additive artificially increased the potassium content of the fuel. This was designed to increase the electron concentration and plasma frequency in the flames. As such, it provided a means of investigating the effect of ionisation upon propagation. Due to its similar size and condition to Fire B, Fire C provides a means of directly observing the effects of increased ionisation without adjusting other effects. Time series plots of the signal strength are shown in Figure 2.13 - 2.15. Three measurement samples for the entire measured spectrum is shown in Figure 2.16.

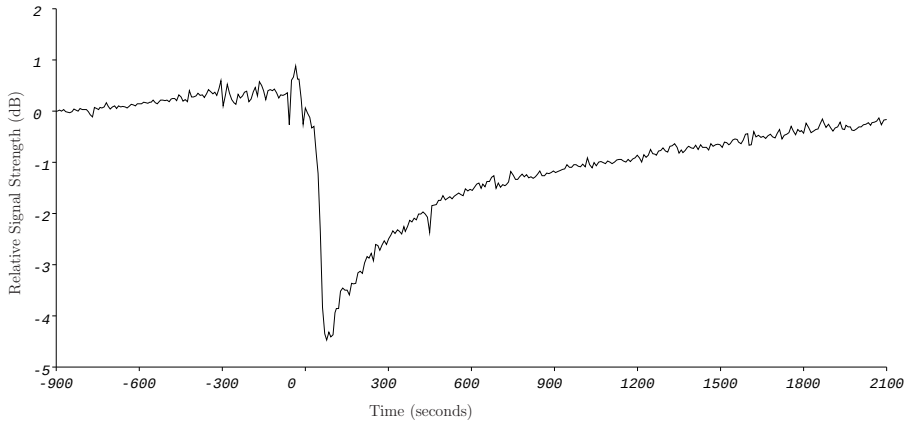

Figure 2.13: Relative Signal Strength - Fire C. Band 1 160MHz - 180MHz

2.2.4 Processing of Results

To aid in clarity, some processing has been applied to the raw measurements. The figures above show a plot of the time series for a band of frequencies. Three operations have

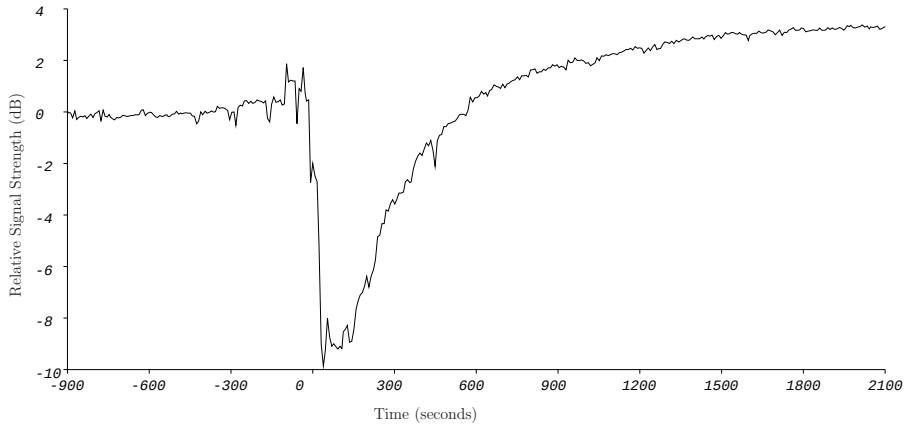

Figure 2.14: Relative Signal Strength - Fire C. Band 2 400MHz - 450MHz

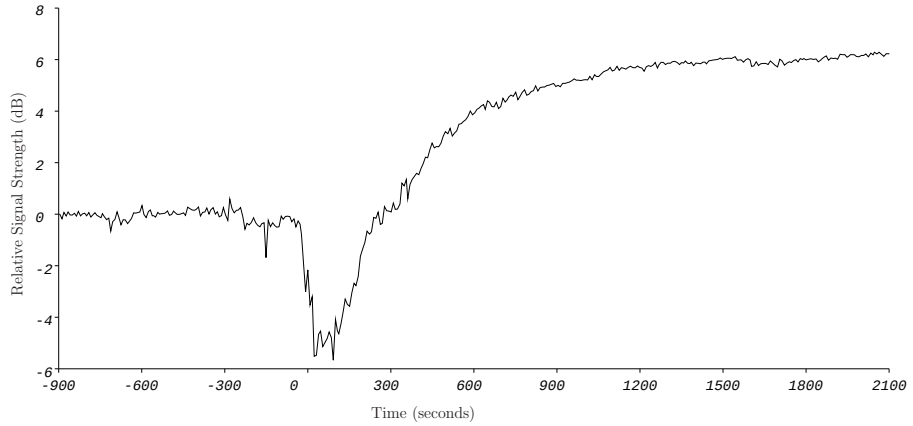

Figure 2.15: Relative Signal Strength - Fire C. Band 3 850MHz - 950MHz

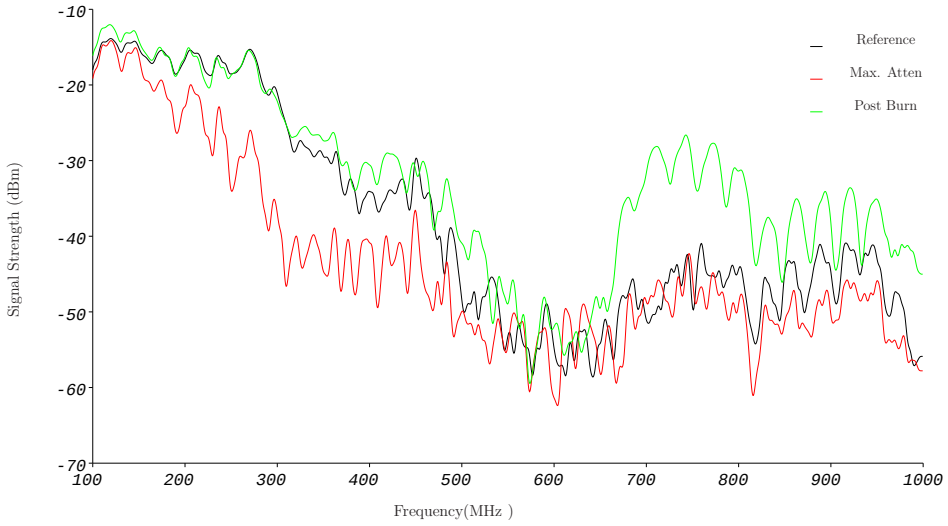

Figure 2.16: Fire C Spectrum Plot

been performed on the data to obtain those plots. Firstly, the time and date of each time sample are made relative to the time of ignition. This breaks our plots into a 'pre-burn' level (negative seconds) and a 'post-ignition' level (positive seconds). Secondly, a reference sample is taken from a stable period of time in the 'pre-burn' period. This reference sample is used to calculate relative signal strengths of each band of frequencies measurement. Lastly, the relative signal strength is averaged over the whole band to provide a representative value of the relative signal strength and to help negate selective frequency fading.

2.2.5 Discussion

One of the first observations from these experiments is their consistency with each other. All experiments show a reduction in signal strength caused by the fire. The general trend for Bands 1 and 2 is a quick drop in signal strength after ignition (at zero seconds), continuing to a point of maximum attenuation. After the point of maximum attenuation, the signal recovers until it eventually reaches its post-burn level. A number of tables have been included to summarise these results. Table 2.2 summarises the maximum attenuation for each band and over the entire measured frequency range. Table 2.3 includes a measure of the fire attenuation duration and is the duration of time it takes for each band to recover to its 'pre-burn' level after ignition.

	Fire A	**Fire B**	**Fire C**
Band 1	-3.30dB (180MHz)	-3.70dB (180MHz)	-6.00dB (180MHz)
Band 2	-12.5dB (418MHz)	-14.4dB (446MHz)	-15.4dB (408MHz)
Band 3	-0.70dB (947MHz)	-4.70dB (921MHz)	-7.20dB (874MHz)
Worst[a]	-17.7dB (577MHz)	-17.0dB (497MHz)	-21.4dB (309MHz)

Table 2.2: Maximum Attenuation

[a]Worst recorded frequency in measurement data

Pre-Post Burn Levels and Fuel Heap Interactions

Each time series plot, shown in Figure 2.5 to 2.15, displays a greater level of signal strength at 'post-burn' compared to 'pre-burn'. A summary of this characteristic is given in Table

	Fire A	Fire B	Fire C
Band 1	402sec	849sec	2477sec
Band 2	235sec	401sec	570sec
Band 3	<10sec	<10sec	254sec

Table 2.3: Fire Attenuation Duration

2.4. This increase in signal strength is not related to the fire but is an interaction of propagation with the fuel heap. As the fuel is burnt the fuel heap diminishes, presenting less of an obstacle on the propagation path and thus allowing more signal at the receiver. The stronger post-burn signal level is simply due to the destruction of the fuel heap. This explains the higher post-burn signal level in general but it does not address the differences of frequency, as shown in Table 2.4. To understand Table 2.4 we need to consider diffraction. Diffraction causes power to propagate into the shadow region of an

	Fire A	Fire B	Fire C
Band 1	1.7dB	1.3dB	0.5dB
Band 2	3.3dB	4.9dB	4.2dB
Band 3	8.6dB	11.2dB	6.4dB

Table 2.4: 'Pre - Post' Burn Signal Level Difference

object, where a line of sight propagation path does not exist. Diffraction is dependent on the wavelength with longer wavelengths displaying stronger diffraction. Consequently, lower frequencies (Band 1) show a smaller difference in the pre-post burn levels, compared to Band 2 and Band 3. If we consider the fuel heap to be perfectly absorbing (a gross approximation), a simple diffraction calculation can be made for the difference in the signal between the different frequency Bands. A simple diffraction calculation for a purely absorbing screen, about 2.5m - 3m high, shows the difference in the signal strengths for each band is approximately 4dB . That is, 4dB between Band 1 and Band 2 and 4dB between Band 2 and Band 3. This 4dB estimation of diffraction puts us in the region of the pre-post burn levels shown in Table 2.4. Further exploration of fuel heap interactions will be undertaken with more sophisticated propagation modelling to be introduced in a later chapter.

The diminishing of the fuel heap introduces a complication in identifying what effect the fire has on the attenuation of the signal. The attenuation caused by the fire is masked

by the dynamic deterioration of the fuel heap. This is one problem of experimenting with fire, as fire burns it will modify the objects in a propagation medium. Having considered some of the interactions of the background medium and how it changes, it is now appropriate to consider the region of attenuation that occurs just after ignition.

Attenuation Causes

The attenuation of the signal just after ignition is one of the peculiar aspects of these experiments. As attenuation occurs before the fuel heap undergoes significant deterioration, the loss can only be explained by an interaction with the fire and flames. It is known from laboratory flame experiments that charged particles exist in the combustion zone. Charged particles will interact with electromagnetic waves, causing attenuation. Consequently, if charged particles are present in the fire, some consideration is required as to why attenuation occurs and how this attenuation can be observed in the spectrum.

Plant life presents a very diverse fuel when it burns. It is made up mainly of carbon, hydrogen and oxygen and a mixture of trace elements. When plant life burns it undergoes pyrolysis, this causes the solid wood to be gasified. As the wood breaks down, different materials and minerals get drawn into the combustion zone. Some of these minerals, presenting as trace elements, have low ionisation energies. By releasing free electrons, a plasma of electrons and ions is generated in the flame. When an electromagnetic wave impinges on the plasma it causes the electrons to oscillate with the electric field. During this oscillation, electrons will collide with neutral particles and therefore lose momentum in the direction of the electric field. These collisions result in attenuation as the wave travels through the plasma medium.

Cold Plasma Model

A good approximation to the combustion induced ionisation is a cold plasma. At this stage we will not consider the intricacies of the plasma generation but only consider a very crude approximation in terms of collision frequency (denoted ν) and plasma frequency (denoted ω_p, f_p). The collision frequency is the number of collisions per second of an electron with neutral particles. The plasma frequency is related to the square root of the density of the electrons ($N_e\ m^{-3}$). For simplicity, consider a slab of plasma and the attenuation as

a wave travels through that slab. Cold plasmas generally have very frequency dependent behaviours, controlled by the interactions between the collision frequency and the plasma frequency. Due to atmospheric pressure and flame conditions, the collision frequency is quite high, in the vicinity of 10^{11}sec^{-1} [119]. If this is the case, the collision frequency is substantially higher than the plasma frequency and frequency dependence is controlled by the collision frequency. For a typical eucalypt mineral concentration of potassium, calcium and magnesium, reaching temperatures between 1300K to 1600K in the combustion zone, the electron concentration will be in the region of 10^{15}m^{-3} to 10^{16}m^{-3} . This represents a plasma frequency in the range of 300MHz to 700MHz . A plot of varying collision frequency is shown in Figure 2.17, and of varying electron concentration shown in Figure 2.18 A high collision frequency causes the electrons to become more rigid and therefore

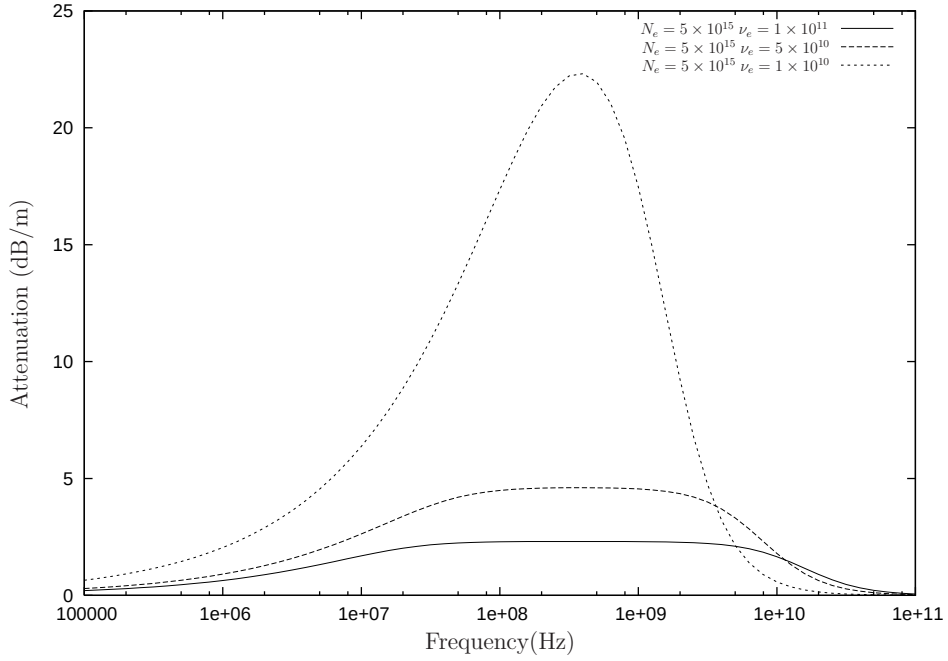

Figure 2.17: Cold Plasma Attenuation - Constant electron density (N_e m^{-3}), Varying collision frequency(ν_e Hz)

they do not gain momentum from the impinging electromagnetic wave. Consequently, as the collision frequency reduces, more energy gets coupled into the electron movement resulting in increased attenuation. Noticeably, as the collision frequency and plasma frequency come closer together a very frequency dependent behaviour results, as seen on the third trace of Figure 2.17. A collision frequency as low as 10^{10}sec^{-1} is not realistic in the current scenario, judging from calculations using given data, modelling

and measurement of the collision frequency in laboratory flames. Calculations of flame conditions put the collision frequency in the region of $1 \times 10^{11}\text{sec}^{-1}$. The flames studies of Sugden et al measured collision frequencies of $8.8 \times 10^{10}\text{sec}^{-1}$. This suggests the traces for the higher collision frequency are more realistic in the current situation. If this is the case, attenuation is slight and it becomes important to consider changes in the electron concentration. For the next plot (Figure 2.18), consider the attenuation as it varies with electron concentration. As the electron concentration increases more electrons couple energy into their movement. Therefore, as the electron concentration increases the attenuation will also increase. As can be seen from the figure, the attenuation becomes

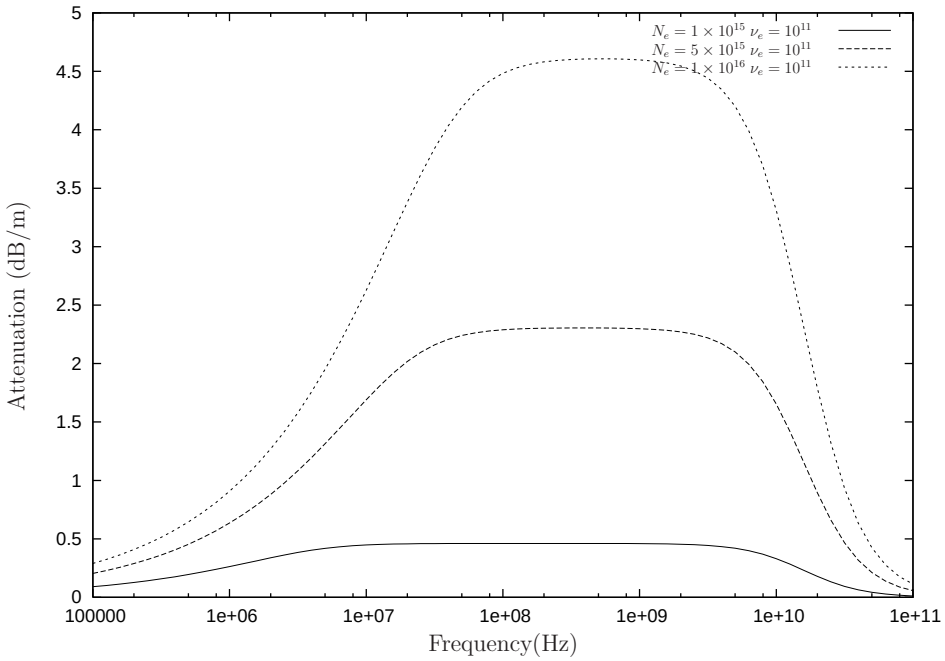

Figure 2.18: Cold Plasma Attenuation - Constant Collision Frequency(ν_e Hz , Varying Electron Concentration ($N_e\text{m}^{-3}$)

broadband. As the electron concentration increases, the attenuation does also but the broadband behaviour is maintained. The cold plasma model demonstrates that broadband attenuation is the expected result from the experimental work.

As the fire ignites and intensity builds more plant material gets swept into the combustion zone therefore increasing the electron concentration. From the cold plasma model, this causes broadband attenuation to occur and increase until the point of maximum attenuation from which it depreciates as the amount of ionisation decreases. So, for the

attenuation to be maintained, it requires (1) increased temperature to ionise electrons and/or (2) fresh biomass material. Notably, in Fire C, where the mineral content was artificially increased, broadband attenuation was seen on Band 3. In addition, this also correlates with the longer duration times for Fire B and Fire C. As more fuel is present, the time for which fresh plant material is available will be a longer duration.

At higher frequencies, the effect of the heap is to shorten the duration of the period where attenuation is greater than the initial value (i.e. pre-burn). This is due to the fact that attenuation is due to the heap is minimal at low frequencies, but is quite strong at the higher frequencies. Consequently, the reduction in heap size as the burn progresses will cause a far greater increase in signal at the higher frequencies and hence a quicker return to pre-burn levels. Bringing all this together, the experiments shows Band 2 suffers the worst of both phenomena, attenuation is strong on this band with little recovery by diffraction. Band 1 suffers from attenuation from the combustion plasma but has better diffractive recovery, reducing the severity of the plasma and influence of the fuel heap. Band 3 is estimated to suffer considerable attenuation but generally the attenuation is not sufficient to overcome changes in the fuel heap. When the electron concentration is artificially increased this attenuation is observed. Fire C supports the above notion as it contains a considerable increase in ionisable material, which results in a longer time before the effects of a reducing fuel heap become obvious.

2.3 Multi-Transmitter Investigations

One of the problems apparent with the broadband experiments above, although they are extremely insightful, is that they fail to help us understand what is happening over the structure of the fire. Spatial information and identification of critical paths of propagation is hard to be discerned. This may not present much of a problem on small scale fuel heaps but over a larger fire front in a bushfire different propagation paths will exist and show variation in propagation characteristics. Additionally, the bushfire destroys the propagation medium and static conditions can not be reproduced for measurements at different locations. Consequently, in order to build an overall picture of the propagation in a bushfire scenario, different paths must be monitored simultaneously.

A method that was considered was the use of multiple stand alone transmitters, located at different positions before the fire front and a single or multiple receiver located behind the fire front. An illustration is shown in Figure 2.19. Consistent propagation conditions are ensured by considering a single band of frequencies. Each transmitter however, is differentiated by a slight change in frequency representing a channel in the band of frequencies. Building from the results of the broadband experiments, one can see that the UHF band of frequencies are very sensitive to the presence of a fire. It was decided to develop a measurement system for this frequency band and to make this a focus for multi-transmitter investigation (these frequencies are part of the Citizen Band or ISM Band). Transmitters have been designed around the radio band allocated from 430MHz to 450MHz [122].

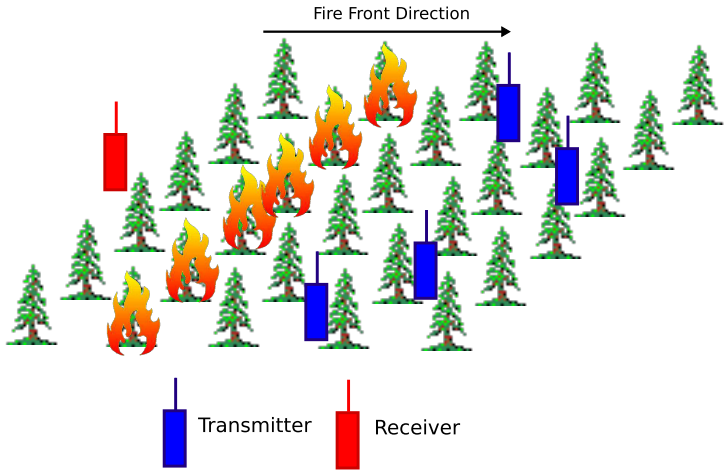

Figure 2.19: Bushfire Experimental Deployment

2.3.1 Transmitters

The transmitters are designed to be cheap and easy to deploy. They consist of a battery power supply, a radio frequency transmitter module and a monopole antenna. The radio frequency module components include a frequency synthesiser and modulator, a power amplifier and an output low-pass filter. The module is capable of an output power in the vicinity of 38dBm . Future versions will likely include temperature sensing capabilities and monitoring facilities where data can be modulated onto the carrier signal. As yet, no opportunity has arisen to deploy this system, but it is hoped to deploy these devices in a controlled fire in future large scale experiments (see Figure 2.19). In particular,

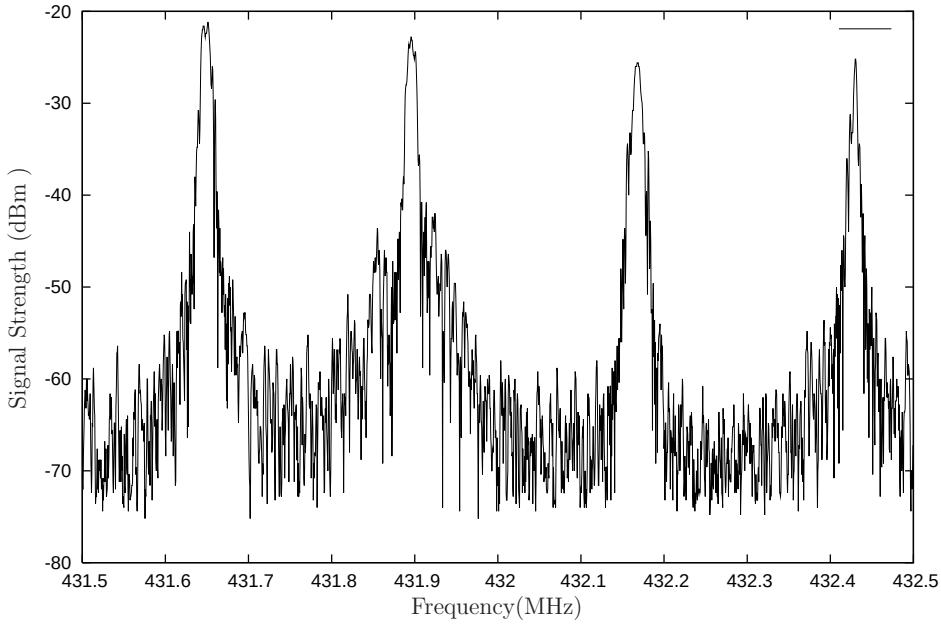

Figure 2.20: Mutli-Transmitter Trial

it is hoped to deploy this system in a future fire service controlled burn exercise. The receiver consists of a single monopole being fed into the HAMEG spectrum analyser and the same setup in the broadband experiments with suitable tuning of the HAMEG to the correct frequency band. A sample of the received spectrum is shown in Figure 2.20. The operation of the system has been proven in some preliminary experiments and is waiting for an opportunity for deployment to occur. It will be noted that the transmitter units operate at slightly different frequencies to aid in identifying each transmitter.

SECTION 3

Electrical Modelling of a Fire Environment

This chapter lays the foundation for considering the fire environment as a propagation medium. In order to consider the propagation of radio waves through an environment, it is important to build an electromagnetic model of that environment. The fire environment is broken into two regions; the combustion region and the fire atmosphere.

The combustion region is where the chemical process occurs and reactants become products. In this region, we focus on the generation of charged particles and hence the formation of a combustion induced plasma. A cold plasma model will be used to represent this region and to study electromagnetic interactions.

The fire atmosphere is considered to be chemically stable. A lossless refractive index model is used, which encompasses the variations in temperature and gas concentration. Although the fire environment is similar to the earth's atmosphere, a number of differences are apparent, which need special consideration.

Before we can consider the electromagnetic modelling however, we need to build physical representation of the fire environment; this leads to an introduction of the Fire Dynamics Simulator.

3.1 Fire Dynamics Simulator - FDS

Fire Dynamics Simulator (FDS), developed by the National Institute of Standards and Technology (NIST), is used in this work to simulate fire conditions. FDS is a three dimensional thermodynamic solver, which includes combustion modelling. The source code and packages are freely available from the NIST website [37]. FDS models the solid phase pyrolysis and the gas phase combustion reaction in finite steps in time. Pyrolysis is concerned with the generation of fuel vapour at a solid or liquid surface, allowing simulation of solid materials, such as wood. Actual combustion occurs in the gaseous state between fuel vapour and oxygen. In the simulations presented here, the gas phase combustion reaction is modelled using the simple mixture fraction model. In the mixture fraction model, an instantaneous reaction occurs when the right conditions are met: fuel vapour, oxygen and temperature. FDS does include additional combustion models but the mixture fraction model is adequate for this application. A full technical explanation can be found in the 'FDS technical guide' on the FDS website (`http://www.fire.nist.gov/fds`). The version used in this work is FDS 5 (see the community website `http://www.fds-smv.net`).

If a greater understanding of the combustion reaction is required beyond the scope the FDS, one can consider chemical kinetics. Cantera[16] and STANJAN[109] are two packages that are freely available which model simple chemical kinetics of reactions. Currently there is no need for a chemical kinetics calculation. FDS is adequate to build a spatial picture of the fire and the gases involved for building a propagation model. Examples of two simple objects that have been developed for this work are shown in Figure 3.1.

To appreciate FDS's part in the modelling pipeline consider Figure 3.2. In the figure: square blocks represent modelling portions, triangles the output that is produced and circle elements represent external information that is required for each model. FDS uses an atmosphere that is composed of nitrogen (N_2), oxygen (O_2), water (H_2O) , carbon dioxide (CO_2) and carbon monoxide (CO). All these gases are important for the formation of the refractive index and collision frequency of the cold plasma model. An additional ionisation model uses fuel data from FDS and traces the ionisation elements through the combustion process. The fuel data of FDS is invaluable as it accounts for the pyrolysis process and transport to the combustion zone. As a supplement to the sophisticated thermo-

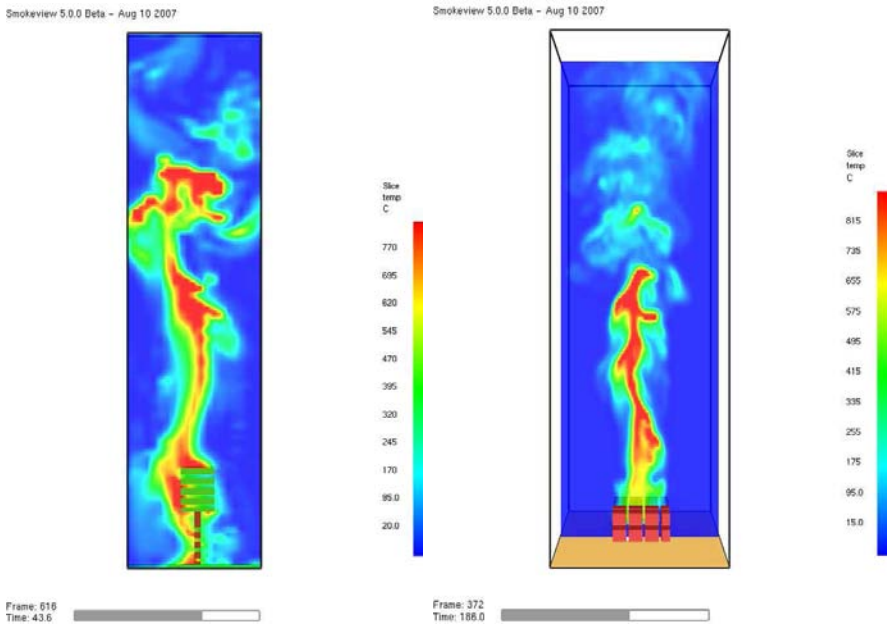

(a) Simple Tree (b) Bonfire

Figure 3.1: FDS Examples

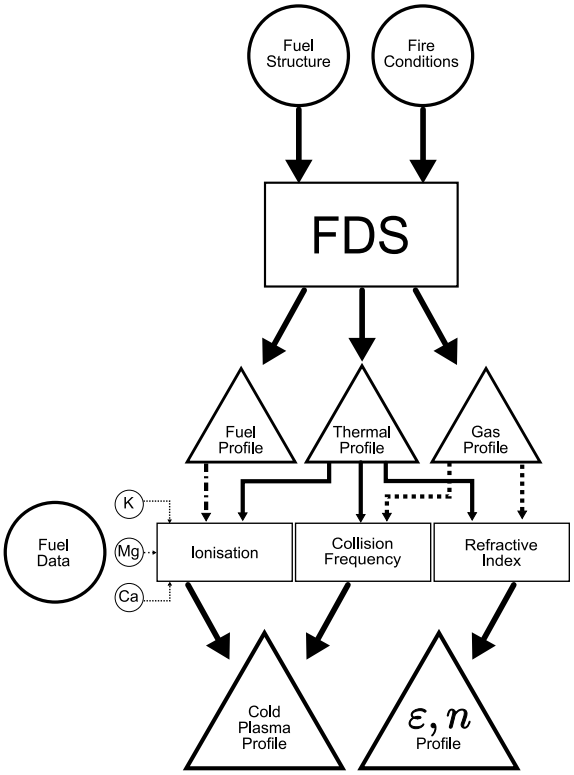

Figure 3.2: Modelling Flow

dynamics simulation of FDS, a mathematical representation of the fire environment has been included towards the end of this chapter. This representation is an extraction from FDS simulations. It is designed to be approximate and allow one to explore propagation phenomena without the need for an expensive detailed fire simulation.

3.1.1 Small Scale Physical Model

In Section 2, a number of small scale fire experiments produced some interesting results related to radio propagation. A FDS model is introduced here, to examine those experiments with electromagnetic modelling.

For the geometry of the small scale fires, a simple block (3.5m x 7m x 7m) of fuel is used for the fuel heap. Slices of the block have been removed to represent the sparsity of the fuel heap and to allow simulation of combustion within the fuel heap. The wood combustion model is an adapted 'spruce' model from the FDS database. The density of this model has been changed to represent a leaf, branch structure and a solid wood or trunk structure. Density values are taken from a collection of biomass data[71][116].

To start ignition, a 'heat vent' is used below the block of fuel. This vent is open for 30 seconds and then closed for the remainder of the simulation. An inert surface is used for the ground. The remaining boundaries are 'open' surfaces, which are used to simulate open air boundary conditions. A cross-section has been taken through the fuel heap and

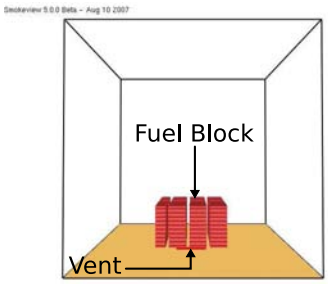

Figure 3.3: Small-Scale Model

various profiles are displayed in Figure 3.4. The profiles are a snapshot of a single frame in time. At this point we are not interested in the fluctuations of the profiles in time, but wish to explore the general effect of the fire on propagation. For this reason, data has been averaged in time when used as input for the propagation models. Time varying

Variable	Min.	Max.	Unit
Temperature	288	1008	°K
Oxygen O_2	0.09	0.19	mol/mol
Nitrogen N_2	0.70	0.80	mol/mol
Carbon Dioxide CO_2	0.00	0.09	mol/mol
Water H_2O	0.00	0.09	mol/mol
Fuel	0.0	0.06	mol/mol
Density	0.39	1.24	kg m^{-3}

Table 3.1: Variables of fire and their extremes

models will be pursued at another place. To aid in the visibility of the gas profiles Table 3.1 has been included with the various bounds of the profiles.

3.1.2 Calculating the Partial Pressures and absolute moles

FDS calculates the concentration of the gases in moles per moles. Unfortunately, this isn't helpful for input into the electrical models. An additional calculation is required for usage in the refractive index and cold plasma models. The only connection to the actual mass or pressure of the element is the through the density (ρ in $kg\ m^{-3}$) in FDS.

$$M_{total} = \frac{[M_{O_2}X_{O_2} + M_{CO_2}X_{CO_2} + \ldots]}{X_{O_2} + X_{CO_2} + \ldots} \tag{3.1}$$

$$N_{total} = \rho / M_{total} \quad \text{moles/m}^3 \tag{3.2}$$

$$N_{O_2} = X_{O_2} N_{total} \quad \text{moles/m}^3 \tag{3.3}$$

$$N_{H_2O} = X_{H_2O} N_{total} \ldots \tag{3.4}$$

where $M_{...}$ is the molar weight, $X_{...}$ is the molar fraction for each gas and $N_{...}$ is the density in moles m^{-3} .

3.2 Fire Atmosphere Refractive Index Model

In the literature review, refractive index models of the Earth's atmosphere have been laid out in detail. It was seen that the refractive index is a summation of different gases and their contribution. For a frequency range of interest, a non-dispersive lossless refractive

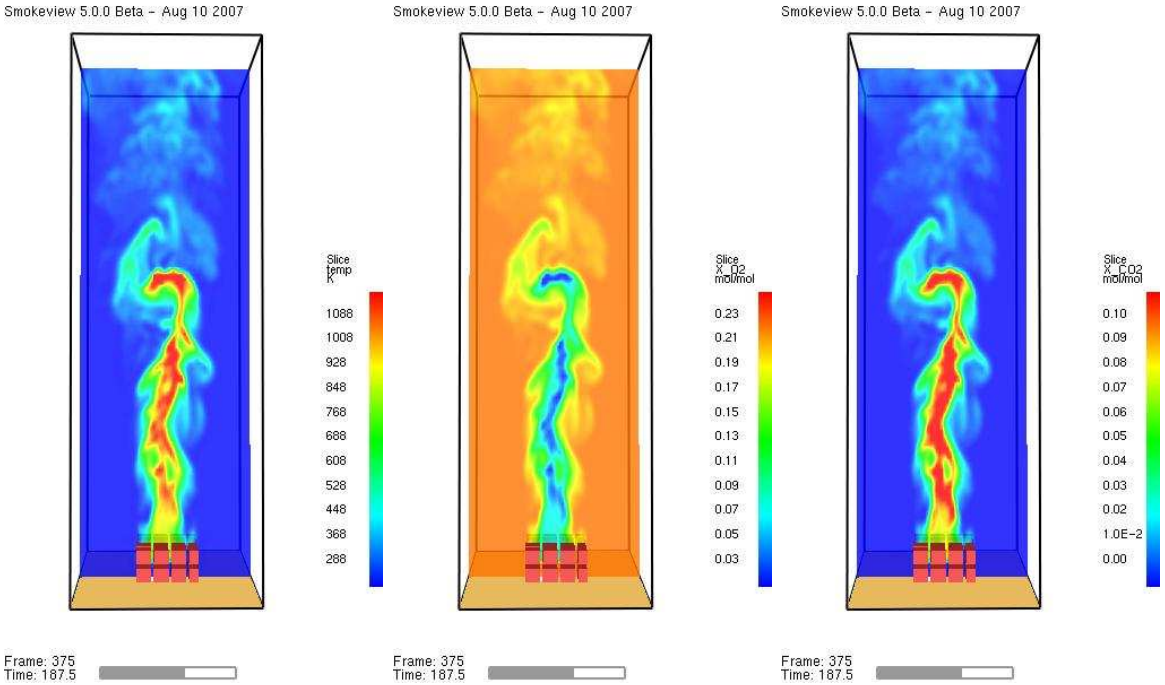

(a) Temperature°C (b) O_2 (c) CO_2

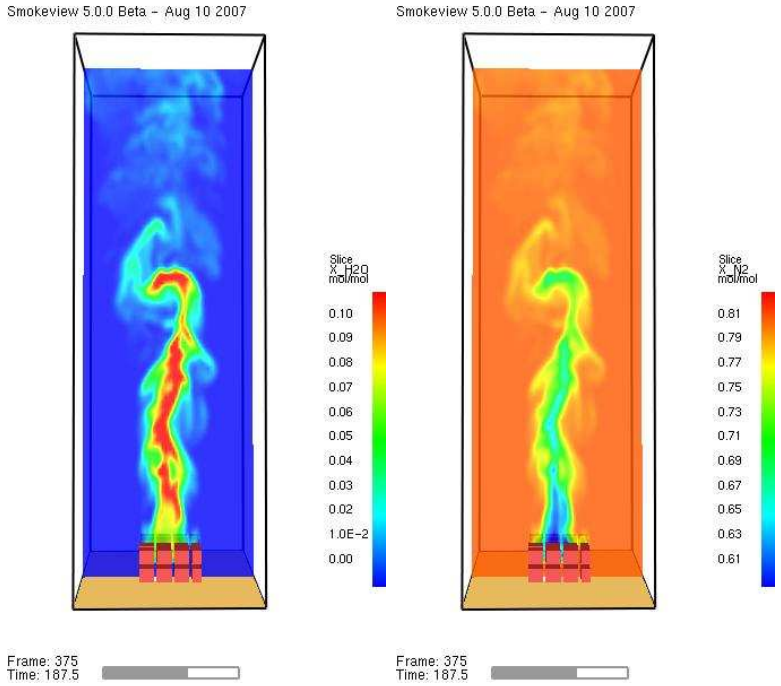

(d) H_2O (e) N_2

Figure 3.4: Selection of FDS Profiles

index model is adequate. In application to fire atmospheres the current atmospheric models have a number of limitations. The dry air component assumes constant partial pressures for nitrogen and oxygen. In addition, carbon dioxide is assumed to be a constant concentration. From the FDS profiles and Table 3.1 above, we know these major gases do not remain constant in the fire atmosphere. For a fire environment atmosphere it would be more desirable if each gas contribution was individually considered in the refractive index.

In the Lorentz-Lorenz model, we consider the contribution of each gas separately. By summing the Lorentz-Lorenz relation of each gas the overall refractive index can be found. For an individual gas the refractive index is described by the Lorentz-Lorenz relation shown in Equation 3.5 [11].

$$\frac{n^2-1}{n^2+2} = \frac{4\pi}{3}\frac{N_A}{M\alpha\rho} \tag{3.5}$$

where, N_A is Avogadro's number, M is the molar weight of the gas molecule or atom, ρ is the density of the gas and α is the molar refractivity of the gas and is a material dependent value. For multi-gas environments, the refractive index becomes the summation of the Lorentz-Lorenz relation for each individual gas [87].

$$\frac{n^2-1}{n^2+2} = \sum_i R_i\rho_i \tag{3.6}$$

where $R_i = \frac{4}{3}\pi N_A/M_i\alpha_i$ is a collection of the Lorentz-Lorenz terms denoted the specific refraction for each gas. Since R_i is a function of molecular constants, and assuming α_i does not vary with frequency or atmospheric conditions, one need not find R_i explicitly but can use the following procedure. Ciddor[19] solves for the specific refraction at a reference refractive index under known 'controlled' conditions and then accounts for the change in actual density of each gas. This is mathematically expressed in Equation 3.7 [87][19].

$$L = \sum_i \left(\frac{\rho_i}{\rho_{is}}\right)\frac{n_{is}^2-1}{n_{is}^2+2} \tag{3.7}$$

where ρ_i is the density for each gas 'i', ρ_{is} is the density at a known reference standard refractive index, and n_{is} is the reference refractive index at a standard known individual gas atmosphere. We now have a solution to the right hand of Equation 3.6 and the refractive index for a multi-gas atmosphere is shown in Equation 3.8[19].

$$n_{LL} = \sqrt{\frac{1+2L}{1-L}} \tag{3.8}$$

Using Equation 3.7 and 3.8 we now have a means to calculate the refractive index for any multi-gas atmosphere. Refractive index data for water and carbon dioxide can be found in the current atmospheric literature [20, 87, 19]. Additional information concerning nitrogen, oxygen and others can be found in references [104, 108]. To calculate the density of each gas one can use the ideal gas law (see Equation 3.9). When calculating the density the compressibility of a water filled atmosphere requires special consideration with inclusion of the BIPM formulae (see [20] [29]).

$$PV = nRT\ Z \tag{3.9}$$

where R is the ideal gas constant $8.314472 m^3 Pa\ K^{\ 1} mol^{\ 1}$, T is in °K and Z is the compressibility of the gas. Gas profile information can be gathered from fire simulations (FDS) or an abstracted mathematical model.

The Lorenz-Lorentz model shows good agreement with other atmospheric refractive models and MPM'93. The flexibility of this model is also shown with the inclusion of additional components into the refractive index. Some possible examples are soot or smoke. A refractive index model [91][38][12] for carbon soot has been incorporated into the model. Smoke inclusion is important for the exploration of inversion layers and the dynamics of the smoke plume to communications[45].

The above model of the refractive index is an initial attempt at building a picture of the unreactive regions of the fire environment. Accuracy of the model is limited by the lack of experimental data at high temperature conditions found in fire.

3.3 Combustion Induced Plasma Model

To electrically represent the combustion induced plasma, a cold plasma model is used. A simple cold plasma model requires knowledge of the electron density profile and the collision frequency. In this section, a description will be given for the calculation of the electron concentration and collision frequency in the fire.

3.3.1 Electromagnetic Field Interactions

An ionised electron has velocity due to thermal energy. When an electromagnetic field impinges upon an electron an additional force is applied to the electron, displacing it from its mean thermal velocity position. From Budden[13] we know the movement of the electron about its mean position is described by the following differential equation.

$$m\frac{\partial^2 \mathbf{r}}{\partial t^2} + m\nu\frac{\partial \mathbf{r}}{\partial t} = e\mathbf{E} \tag{3.10}$$

where $\mathbf{r}$ is the displacement vector from its mean thermal position, m is the mass of the particle and ν is the collision frequency. If we consider the displacement vector and its relationship to the polarisation vector of the medium we need to include the density of particles being affected by the $\mathbf{E}$ field, hence the polarisation vector is $\mathbf{P} = eN_e\mathbf{r}$. When using the time domain, it is helpful to introduce the polarisation current, which is the rate of change in time of the polarisation vector $J_P = \partial\mathbf{P}/\partial t$. This reduces Equation 3.10 to a first order differential equation and represents the entire medium of electrons.

$$\frac{\partial \mathbf{J_P}}{\partial t} + \nu\mathbf{J_P} = \varepsilon_0\omega_P^2\mathbf{E} \tag{3.11}$$

where $\omega_P^2 = N_e e^2/(m_e\varepsilon_0)$ is the plasma frequency. For inclusion in Maxwell's equations only the temporal electro-differential equation needs to include the polarisation current as an additional current source.

$$\nabla \times \mathbf{H} = \varepsilon\frac{\partial \mathbf{E}}{\partial t} + \sigma\mathbf{E} + \mathbf{J_P} \tag{3.12}$$

In the frequency domain Equation 3.10 can be easily be reduced to the following form[13].

$$\mathbf{E}Ne^2 = -\omega^2 m\left(1 - \frac{i\nu}{\omega}\right)\mathbf{P} \tag{3.13}$$

Having this form allows us to express the complex permittivity as:

$$\widehat{\varepsilon} = \varepsilon_0\left[1 + \frac{\omega_P^2}{\omega\left(i\nu - \omega\right)}\right] \tag{3.14}$$

or as seen in the ionospheric literature

$$\varepsilon = 1 - \frac{X}{U} = n^2 \tag{3.15}$$

where $X = \frac{\omega_P^2}{\omega^2} = \frac{Ne^2}{\varepsilon_0 m_e\omega^2}$ and $Z = \frac{\nu_{eff}}{\omega}$, $U = 1 - iZ$. The collision frequency in the fire environment is typically high due to atmospheric pressure and the gases involved. An

approximation for the refractive index of a cold plasma with high collision frequency is shown below[23].

$$n^2 = 1 - i\frac{\sigma}{2\varepsilon_0\omega} \quad \text{where } \sigma = \frac{Ne^2\varepsilon_0}{m_e\nu_{eff}} \tag{3.16}$$

Having outlined some of the mathematical basis for the cold plasma, we now consider the modelling the plasma frequency (ω_P) and the collision (ν) frequency in the flames.

To calculate the attenuation per meter, the propagation constant for the plasma is simply

$$\gamma = j\omega\sqrt{\mu_0\varepsilon_0\varepsilon_r} \tag{3.17}$$

$$\alpha = Re\{\gamma\} \times 8.6 \tag{3.18}$$

where 8.6 is the neper field to decibel power conversion ($20\log_{10}(e)$).

3.3.2 Electron Population

Low ionisation alkali-alkaline elements exist in plant life and are readily accessible due to their distribution in the plant to the combustion zone of a fire. These elements become thermally ionised and, compared to chemi-ionisation, are the dominant source of electrons in terms of quantity and flame surface area. As a result in this section we only consider an electron population which is generated by thermal ionisation of low ionisation energy elements. To consider chemi-ionisation, the chemical kinetics involved need to be considered. As discussed in Section 1.3.2 chemi-ionisation is not the dominant process, the necessity and time has not yet arisen to pursue this area.

In considering thermal ionisation there are a number of stages prior to ionisation that need to be considered. Figure 3.5 is an illustration of the journey of potassium from wood to ash.

3.3.3 Establishing the Fuel Rate, K, Ca, Mg

Establishing the rate at which fuel is swept into the combustion zone is one of the key elements in modelling the combustion related areas. For the thermal ionisation calculation it is important to establish the amount of low ionisation elements entering the combustion

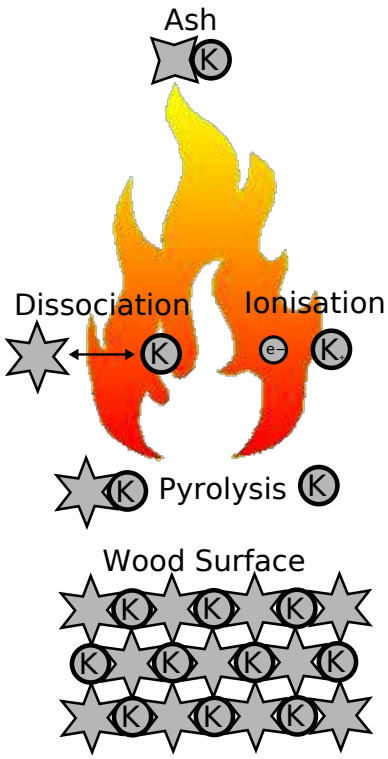

Figure 3.5: Flow of Potassium through the different processes

zone. This amount is related to overall fuel rate coming into the combustion zone and the percentage of the low ionisation element.

Two different approaches have been used in this project. One utilises FDS data, while the other is used for long bushfire fronts. The thermally ionised elements undergo a number of processes prior to reaching the flame region. Originally, these elements exist as trace elements in the solid wood. Pyrolysis is the process of transition from solid fuel to gasified fuel. In pyrolysis, these elements are generally of higher concentration in the extremeties of plant-life and are swept along with the gasified wood. The three most prevalent low-ionisation elements in plant-life are potassium (K), magnesium (Mg) and calcium (Ca). A list of plant related data is collected in the appendix.

The pyrolysis studies of Okuna et al. [117] showed alkali elements K, Ca, Mg pyrolyse by differing amounts. Potassium is a dominant product of pyrolysis. Once gasified it will exist in the form of KCl, KOH or elemental K. As highlighted by Mphale and Heron [81], potassium is a major element in thermal ionisation due to its prevalence in plant life, its low ionisation energy and pyrolysis characteristics.

Once the fuel has become gasified it is transported by air movement into the combustion zone. Up till this point, FDS can be used to model the pyrolysis process of the wood and transport our fuel density N_{fuel}. As an estimation of the amount of each element present, this is simply:

$$N_X = N_{fuel} \cdot \rho_X \cdot \Pi_X \tag{3.19}$$

where ρ_X is the percent of each element (K, Mg, Ca) present in the part of the plant that is burnt, and Π_X is a pyrolysis coefficient encapsulating the ease of pyrolysis by the element. A time plot of N_{fuel} from FDS for a small bonfire is shown in Figure 3.6. Following the pyrolysis data found in [117], a conservative value for the amount of

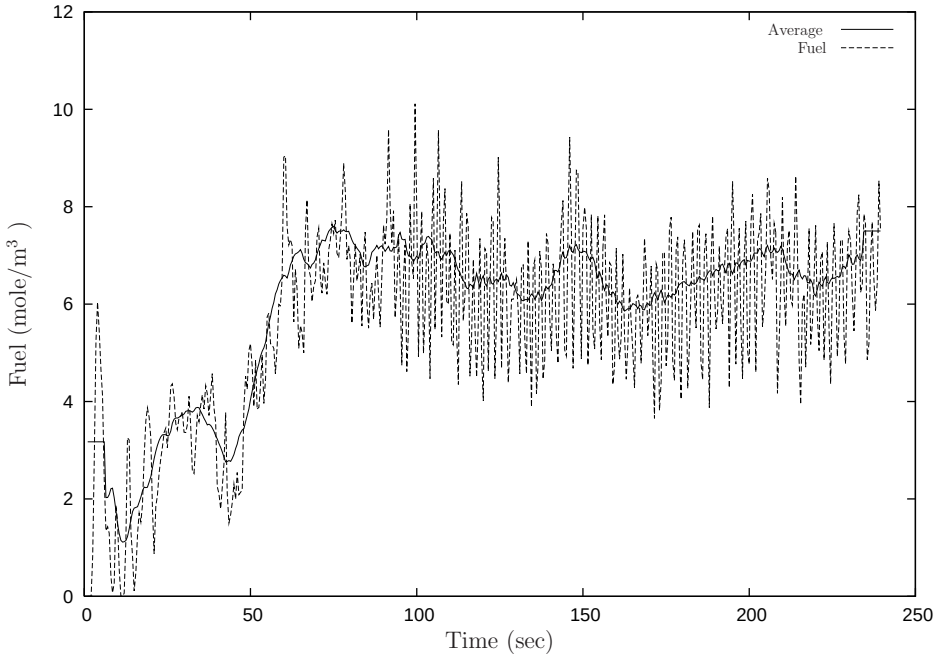

Figure 3.6: Fuel Vapour in moles just above the fuel heap

each element present in plant life that reaches the combustion zone is shown in Table 3.2. These calculations for fuel in the combustion zone are adequate at low levels in the flames.

	Π		
Element	K	Mg	Ca
Fast Pyrolysis	100%	40%	20%
Slow Pyrolysis	60%	20%	10%

Table 3.2: Pyrolysis Coefficient - Π

Some consideration is needed to account for the gases rising in height as turbulence in the entrainment gases. As the ions rise in height they will be spread out over a larger area, hence reducing in density. Added to this it would be prudent to include the rate of rising and higher turbulent effects as the gases cool. As these secondary effects occur well above the flaming region of the fire we assume that insufficient thermal energy is present to sustain adequate thermal ionisation. At this stage of ion modelling, the above model is adequate.

Moving Bushfire Front

For very large bushfires, a computer model of the fire may be unrealistic. An estimation can still be made of the fuel. A moving fire front has a constant amount of fresh plant material being swept into the combustion zone. The amount is controlled by how fast the fire front moves, fuel type and fuel distribution[48]. Parameters that are used to classify bushfires are the rate of spread (m s^{-1}), intensity (kW/m), fuel load (t/ha) and the burning efficiency or percentage of burnt material. Grant et al.[43] has recorded a number of such parameters for fires in rehabilitated bauxite mines of South Western Australia. For an infinitely long fire front moving through the forest the fuel in the combustion zone is simply the rate of spread (ρ_s, m/s) multiplied by the fuel load (F_L, kg/m^2) and percentage burnt during flaming (η) [48].

$$M_{fuel} = F_L \cdot \rho_s \cdot \eta \tag{3.20}$$

where M_{fuel} is the mass of fuel being burnt in ($kg/m/s$). This is an approximate value for a very long fire front. It is useful when examining potential bushfire scenarios with bushfire data. The moving fire can be thought of as a fixed line with the above rate of fuel being fed in.

As shown above a fire can be represented in two ways. One way is a fire fixed in location that changes in time due to the burning and eventual exhaustion of a fuel source. The second is by a fire that spreads and changes in location and therefore has a constant influx of material in time. We can approximate a fire that varies in location and time by one that is fixed with a constant influx of new fuel.

3.3.4 Thermal Ionisation

If the alkali metal is bonded to another element two steps are required for an electron to be ionised. One step is the dissociation process shown in Equation 3.21 and the other is the ionisation process, shown in Equation 3.23.

$$AB \rightarrow A + B \tag{3.21}$$

The dissociation process can be modelled using the Guldberg-Waage relation, shown in equation 3.22.

$$\frac{N_A N_B}{N_{AB}} = \frac{P_A P_B}{P_{AB}} \left(\frac{2\pi kT}{h^2}\right)^{3/2} \left(\frac{m_A m_B}{m_{AB}}\right)^{3/2} \exp\left(\frac{-E_d}{kT}\right) \tag{3.22}$$

where N_X is the density of product X, P_X is the internal partition function of the element X, m_X is the mass of element X, k is Boltzmann's constant, h is Planck's constant, T is the absolute temperature in °K , and E_d is the dissociation energy. Typical values of the dissociation energy for potassium salts range from 0.75eV to 4.51eV [59]. Heron and Mphale[48] estimate that all of the compounds will dissociate without too much energy and assume complete dissociation.

Once the alkali element is in its elemental form it can undergo ionisation. The ionisation calculation involves the process shown by Equation 3.23, which can be modelled using the Saha equation shown in Equation 3.24.

$$M \rightarrow M^+ + e^- \tag{3.23}$$

$$\frac{N_{M^+} N_{e^-}}{N_M} = 2\frac{P_{M^+}}{P_M} \left(\frac{2\pi m_e kT}{h^2}\right)^{3/2} \exp\left(-\frac{E_i}{kT}\right) \tag{3.24}$$

where E_i is the ionisation potential. Typical values of the ionisation potential of the three elements of interest is shown in Table 3.3. To solve for the electron population from the

Element	Ionisation Energy
Potassium (K)	4.34eV
Calcium (Ca)	6.11eV
Magnesium (Mg)	7.64eV

Table 3.3: Ionisation Energy for Elements of interest.

Saha equation, Frost[39] suggests the expression below is a good approximation.

$$N_{e^-} = \sqrt{K_1 N}\left[\sqrt{1+\frac{K_1}{4N}} - \sqrt{\frac{K_1}{4N}}\right] \tag{3.25}$$

where $N = N_{M^+} + N_M$ and encompasses the total number of atoms present being neutral or ionised, K_1 is the right hand side of Equation 3.24. The internal partition function (P) is calculated using Equation 3.26, where ω_j is the weighting coefficients for each j state and E_j is the energy level for that state. Chemical data for each step in this calculation can be found in the NIST-JANAF thermochemical Tables[18].

$$P = \sum_j \omega_j \exp\frac{-E_j}{kT} \tag{3.26}$$

It should be noted that the Saha and Guldberg-Waage equations assume that equilibrium is reached in the chemical reaction. As highlighted by Sugden [44], this may not be the case in flames. It was noted later by Mphale[48] in their discussion of 'local thermal equilibrium' in the flame. Consequently, the calculation outlined above should only be considered as an estimate for the electron population. With the possibility of mathematically estimating the contribution of thermal ionisation to the electron population from incoming fuel it is now important to address how to estimate the fuel present in the combustion zone.

As can be seen from the electron density profile, the electron population is very sensitive to temperature. The maximum electron density is localised to a very small section of the flame.

3.3.5 Collision Frequency

When electrons are set in motion by an electromagnetic field they collide with other particles. Collisions cause the electrons motion to be dampened. The collision frequency is a measure of the average number of collisions per second (ν), or more accurately the effective number of collisions (ν_{eff}) . The calculation of the collision frequency is generally complex, being a function of particle density, electron velocity and momentum. For our environment, Itikawa[54] suggests the usage of Equation 3.27 which includes the integration over the entire Maxwellian velocity distribution.

$$\langle v_{eff}\rangle = \frac{8}{3\sqrt{\pi}} N \left(\frac{m_e}{2kT_e}\right)^{5/2} \int_0^\infty v^5 Q^m(v) \exp\left(-\frac{m_e v^2}{2kT_e}\right) dv \tag{3.27}$$

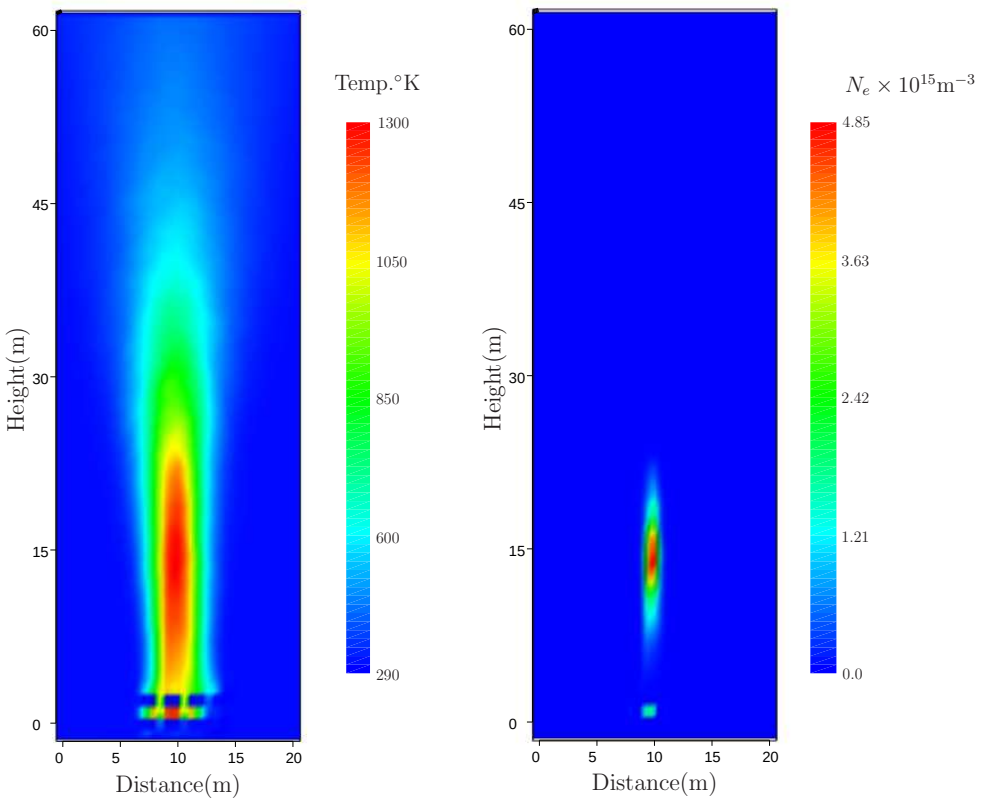

(a) Temperature (b) Electron Profile

where N is the particle number density of the gas, k is Boltzmann's constant, T_e is the electron temperature, m_e is the mass of electrons, v is electron velocity and $Q^m(v)$ is the momentum-cross section for elastic scattering. The electron temperature is assumed to be equal to the temperature of the atmospheric gases. Vidmar[119] has shown that in the earth's atmosphere the collision frequency can be calculated utilising the data of Itikawa[54]. Itikawa has calculated the effective collision frequency for atmospheric gases for temperatures 100°K to 5000°K , providing a helpful look-up table for the collision frequency over the temperature range of our fire. A select listing of various gases is shown in Table 3.4.

The significant gases contributing to the collision frequency are water(H_2O) and carbon dioxide(CO_2). In combustion these two gases are involved and are changing concentration substantially. By implementing the collision frequency data in an interpolated look-up table we can reconstruct the collision frequency using fire data from our FDS simulation. As an example we consider the averaged profiles of our small scale FDS model.

The averaged temperature profile is shown in Figure 3.7(c) and the calculated effective collision frequency profile in Figure 3.7(d).

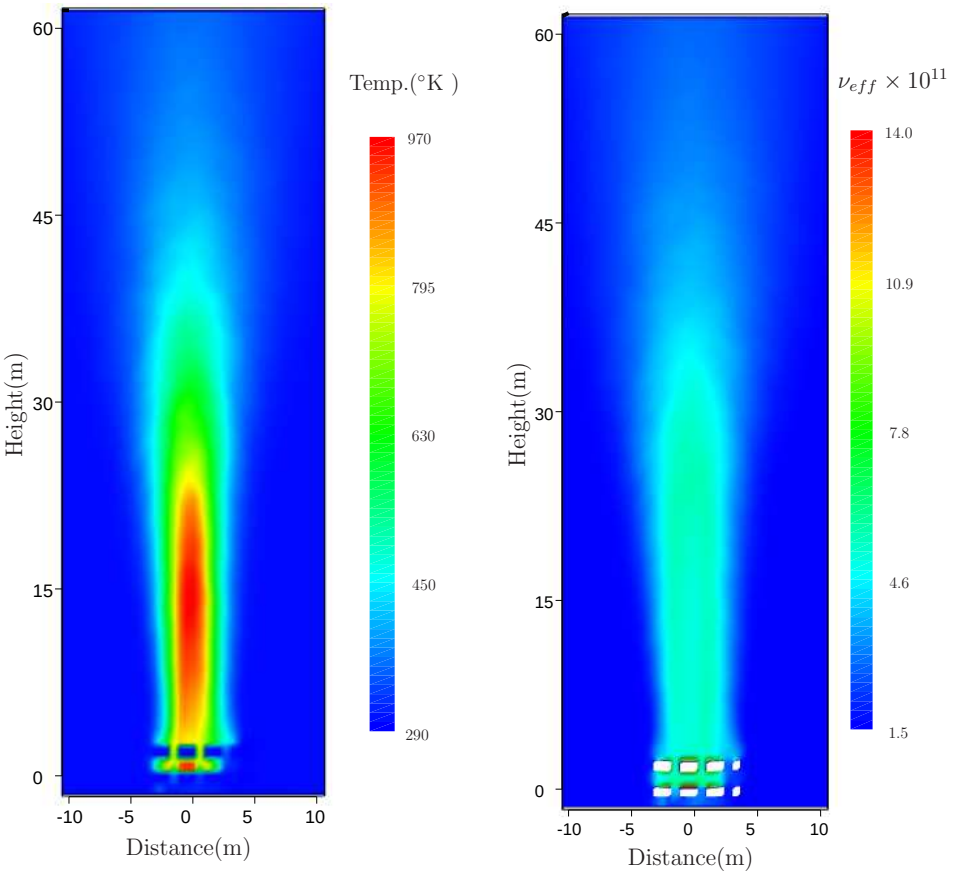

(c) Temperature (d) Collision Frequency

Figure 3.7: Small Scale Collision Frequency Model

	Collision Frequency		
Gas	300°K	1000°K	1500°K
H_2	1.39	3.27	4.40
O_2	0.335	0.956	1.41
CO	0.950	2.79	3.99
H_2O	**84.9**	**39.3**	**29.3**
CO_2	10.1	8.04	6.45

Table 3.4: Effective Collision Frequency $\langle \nu_{eff} \rangle / N$ in 10^{-8}sec^{-1} cm^3

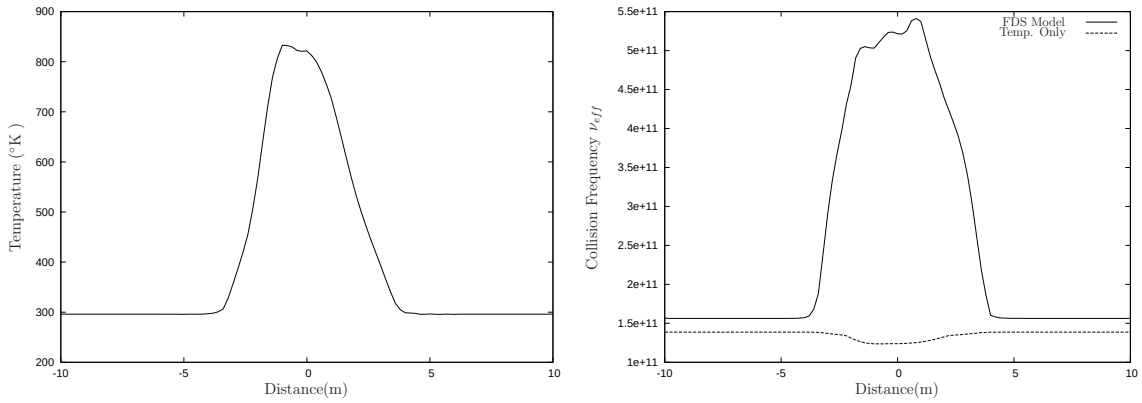

(a) Temperature(°K) (b) Collision Frequency(Hz)

Figure 3.8: Cross Section at Height 5m

As can be seen, the collision frequency increases in the fire. This is an important observation as generally the increase in temperature will cause a decrease in the collision frequency. In the fire however, the pressure is not constant but increases as the combustion products are produced. This is further shown in a cross-section of the collision frequency profile shown in Figure 3.8. An additional calculation is shown in Figure 3.8(b) of the collision frequency calculation with a constant atmospheric pressure. The constant pressure model is consistent with collision frequency calculations in fire by Heron and Mphale [48]. From this comparison, it seems there is no inclusion of the changes in the fire pressure in their work.

Finally, a table has been prepared of measurements of the collision frequency made in flames. In general, the measurement technique was using RF attenuation methods. The ν_{meas} represents the value taken from the given reference and the calculated ν_{calc} represents the effective collision frequency using the given conditions. For the pure oxygen flame the atmospheric conditions were approximated to 50% O_2, 25% H_2O, 25% CO_2, using a standard atmosphere results in a $\nu_{calc} \sim 2 \times 10^9$. Other flames used a representative atmosphere percentage taken from FDS.

From the table we can see that the calculated collision frequencies are within an order of magnitude, which is reasonable considering the lack of information concerning the gas make-up in the flames. As we have outlined in the literature review the high collision frequency found above leads to a collision dominant cold plasma. A variation in the collision frequency of an order of magnitude around 10^{11} will not affect the frequency response of the cold plasma, only the overall attenuation of the plasma.

Conditions	ν_{meas} (Hz)	ν_{calc} (Hz)	Ref.
Acetylene - air 760mm Hg, 2480°K	2.6×10^{11}	1.5×10^{11}	[14, 96]
Acetylene - O_2 7.5mm Hg, 2300°K	3.7×10^{9}	3.1×10^{9}	[14, 96]
Coalgas - air 760mm Hg, 2200°K	8.8×10^{10}	1.7×10^{11}	[106]
Pine Needles - 1013.25hPa , ∼1100°K	$3.43 - 5.97 \times 10^{10}$	3.7×10^{11}	[61, 82]

Table 3.5: Measured Collision Frequency

3.4 Mathematical Generic Modelling

In this section a mathematical model is developed for a fire scenario. The mathematical model is extracted from data based on FDS simulations. The fire environment contains a number of parameters that change such as, temperature, gas profiles and fuel profiles. The most dominant feature in terms of the refractive index and cold plasma modelling is the temperature.

3.4.1 Core Fire Profile

The FDS data was produced using a representative fire, a tree structure. A good mathematical fit for the temperature profile is a gaussian relationship in the horizontal plane and a log-normal distribution in the vertical plane. A mathematical expression for the gaussian relationship is:

$$f(x) = \exp\left[-\left(\frac{x-\mu_x}{\sigma_x}\right)^2\right] \tag{3.28}$$

where μ_x is the centre of the tree in the x dimension, σ_x is related to the spread of the profile. A mathematical expression for the log-normal distribution is:

$$f(z) = \exp - \left(\frac{\ln(z) - \ln(\mu_z)}{\sigma_z}\right)^2 \text{ for } z > 0 \tag{3.29}$$

where μ_z is the vertical point where the variable is a maximum and σ_z is related to the vertical spread of the function. Combining to the two into a function of two dimensions:

$$f(x,z) = (A_{max} - A_{min}) \exp\left[-\left(\frac{x-\mu_x}{\sigma_x}\right)^2\right] \times \exp\left[-\left(\frac{\ln(z) - \ln(\mu_z)}{\sigma_z}\right)^2\right] + A_{min} \tag{3.30}$$

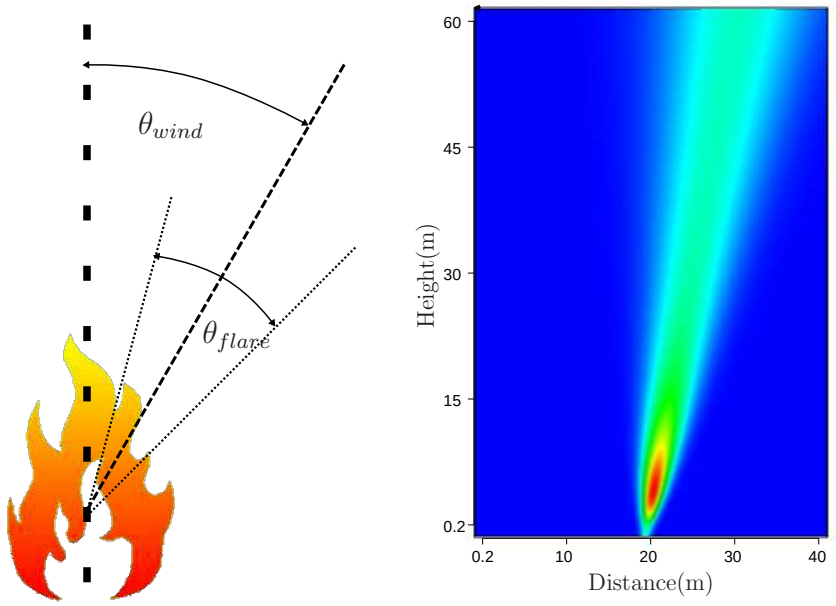

(a) (b)

Figure 3.9: Fire Flare angle

where A_{max} and A_{min} are the maximum and minimum of the variable of interest over the region to be modeled. An appropriate choice of σ_x is to set the width of the burning object to be the point of 10% of the profile. A simple calculation is $\sigma_x = Width/(\sqrt{\ln(10)})$.

Although the vertical temperature profile in Equation 3.29 is reasonably accurate looking directly in the z direction, it does not account for the turbulent mixing that occurs above the fire. This causes the profile to flare out as z increases in height. A simple addition to Equation 3.29 and 3.30 is to allow the σ_x to a function of z. The flare angle can be incorporated by:

$$\sigma_x(z) = \sigma_{x0} + \tan\theta_{flare}\frac{(z-\mu_z)}{\sigma_x} \tag{3.31}$$

where σ_{x0} is the initial profile spread at height μ_z and θ_{flare} is the flare angle as shown in Figure 3.9. In addition a wind component can be added making μ_x a function of height (z).

$$\mu_x(z) = \mu_{x0} + \tan\theta_{wind}[z-\mu_z] \tag{3.32}$$

A comparison of the mathematical temperature profile and FDS has been produced for the small scale experiments. The width (W) of the burning mass represents the 10% value and σ is calculated using the following formula $\sigma_x = W/21/\sqrt{\log_e 10}$. As can be seen in

Parameter	Value
μ_x	4.0m
μ_z	5.0m
Width	4.0m
Flame Height	20.0m
σ_x	1.318
σ_z	6.5901
θ_{flare}	20°
θ_{wind}	0°

Table 3.6: Profile Parameters

Variable	Min.	Max.	Unit
Temperature	288	938	°K
Oxygen O_2	0.09	0.19	mol/mol
Nitrogen N_2	0.70	0.80	mol/mol
Carbon Dioxide CO_2	0.00	0.09	mol/mol
Water H_2O	0.00	0.09	mol/mol
Fuel	0.0	0.06	mol/mol
Density	0.39	1.24	kg m^{-3}

Table 3.7: Fire Variables and the extremes

Figure 3.10(d), quite good agreement is found in the horizontal direction. The flare angle was set to 20° .

Once the basic profile parameters have been selected, a fire's parameter can be found by scaling the profile using the minimum and maximum paramters as listed in Table 3.7. For example, a profile for Carbon Dioxide can be estimated by scaling the basic profile by its maximum (0.09).

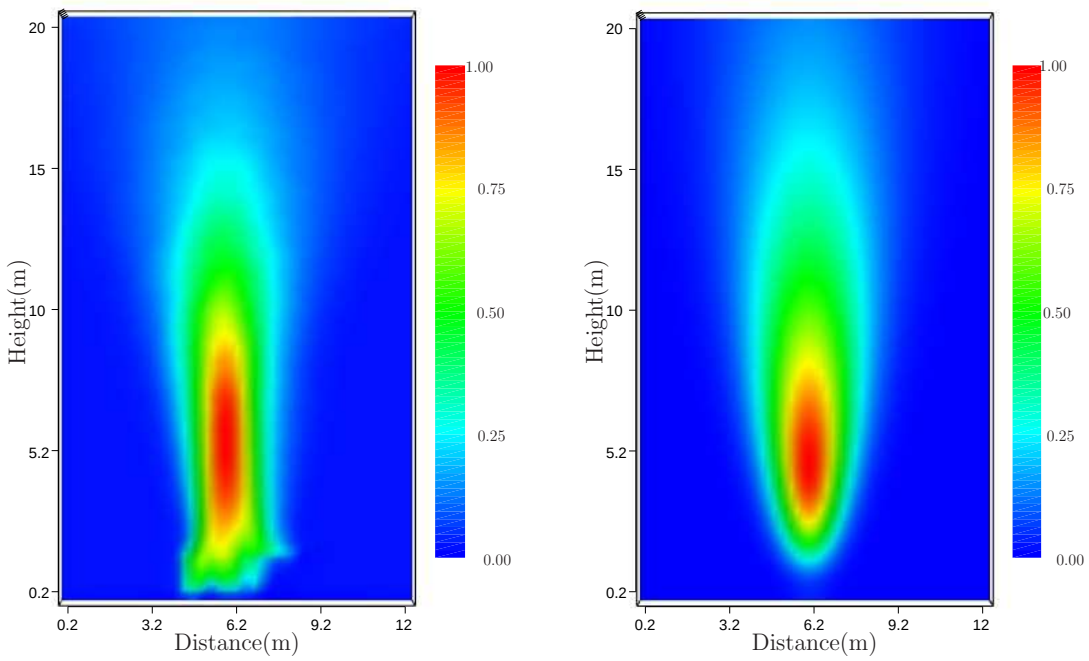

(a) Averaged FDS

(b) Fire Model

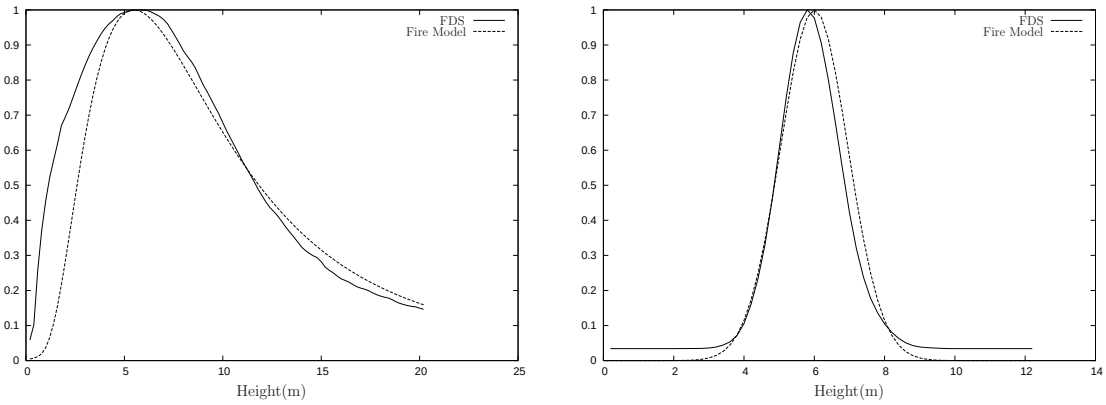

(c) Height Profile at 6m

(d) Width Profile at 5m

Figure 3.10: Comparison FDS , Fire Model

SECTION 4

Simple Propagation Treatment

In this chapter simple propagation modelling is used to examine some of the key mechanisms of the small scale experiments.

Due to the small distances involved in the small scale experiments we can neglect the refractive effects of the fire atmosphere and will focus on the combustion induced plasma as the main propagation mechanism. For the cold plasma, we shall consider contributions from refraction due to the cold plasma, including some rough calculations of attenuation as a wave passes through the plasma. The main objective is to gather engineering insight into the key features of this complex environment. In addition, knife-edge diffraction calculations will be included to examine the effects of the fuel heap collapsing.

4.1 Refraction - Ray Tracing

Ray tracing is a geometric optics approximation of the maxwell's electromagnetic field equations. Individual rays travel normal to the wave front. Ray tracing provides a representation of the wave front and its direction as it travels through a medium that varies in the refractive index.

The combustion induced plasma can cause attenuation or loss of a radio signal at the receiver in two ways. Firstly, energy is lost in the plasma due to collisions and electron movement. The loss results in direct attenuation on the propagation path. Secondly, radio energy can be redistributed in space due to refraction or the path it travels. Radio

energy can be spread due to defocussing or focussing of the wave caused by changes in the propagation medium. We will illustrate this using an extreme and unrealistic example as shown in Figure 4.1. The rays have been reflected by a column electron profile (shown in Figure 4.2(a)), where $N_{e_{max}} = 2 \times 10^{15}$ and an unrealistic constant collision frequency of $\nu_{eff} = 5 \times 10^8$. These parameters, although not found in real fire conditions, have been chosen to demonstrate how ray tracing gives an illustration wave energy distribution. By observing the path the ray takes we can understand how the wave is affected by the changes in the refractive index. Rays are reflected due to refraction above 8m and rays below 8m are defocussed, similarly to passing through a convex lens. To represent

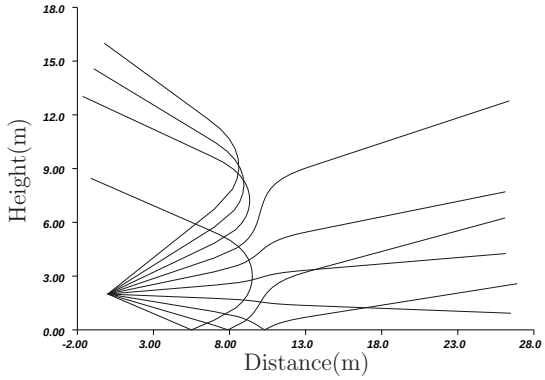

Figure 4.1: Ray Trace - Redistribution of radio energy for an unrealistic scenario using extreme refraction parameters

the combustion plasma in the ray tracing, a simple profile is used. A vertical column represents the combustion in the flames above the fuel heap. The electron profile varies as a cosine function as we approach the centre of the fuel heap. A plot of the electron density is shown in Figure 4.2(a) and its 3D representation.

As shown in the section on fire modelling, the collision frequency is relatively high. In Figure 4.3, three sets of rays have been prepared for the cosine distribution above with varying collision frequency. The refractive index is modelled according to the formulation in Section 3.3.

Initially, with such a large electron population the plasma is highly refractive causing defocusing at lower heights and reflection as the angle of approach increases with height (see Figure 4.3(a)). This is expected because the plasma frequency ($\omega_p \sim 2.5 \times 10^9, f_p \sim 4 \times 10^8$) is in the vicinity of the collision frequency of (1×10^9) and the resulting refractive

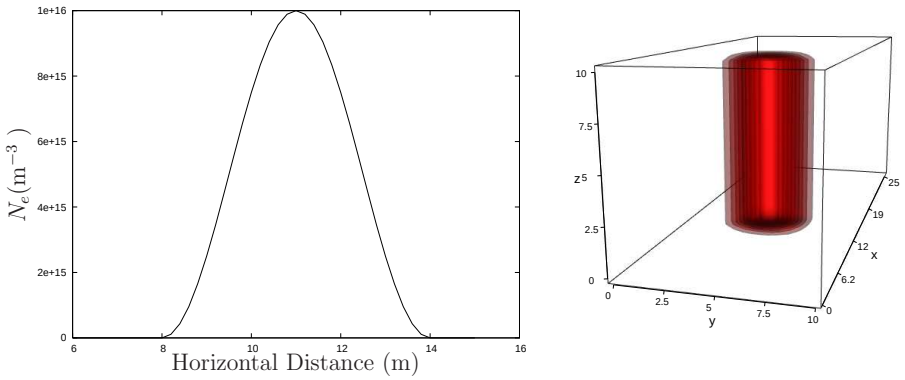

(a) Electron Density (b) 3D Column

Figure 4.2: Column Cosine distribution

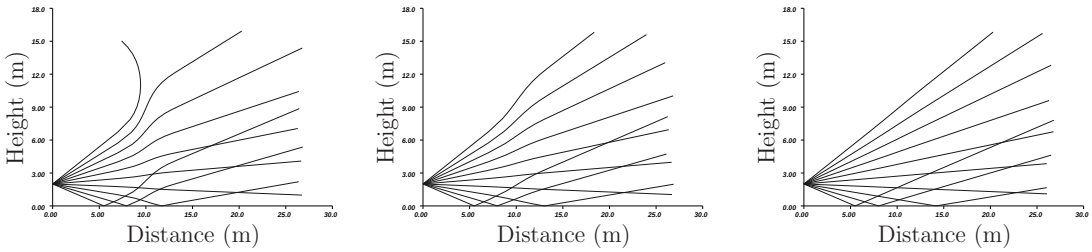

(a) $\nu_{eff} = 1 \times 10^9$ (b) $\nu_{eff} = 2 \times 10^9$ (c) $\nu_{eff} = 1 \times 10^{10}$

Figure 4.3: Ray Trace at 450MHz $N_{e_{max}} = 2 \times 10^{15}\mathrm{m}^{-3}$

index is still strongly refractive being a function of both variables. As the collision frequency increases in Figure 4.3(b)-4.3(c), the refractive index becomes collision frequency dominant and little refraction results. The dominance of the collision frequency leads to a reduction in refraction caused by the plasma. It should be noted that collision frequencies below 1×10^{10} are well below what is calculated in Section 3.3.5. As the collision frequency further increases into a typical range for the combustion induced plasma $(2 \times 10^{10} - 3 \times 10^{11})$ the refractive index becomes collision dominant.

The ray tracing above demonstrates that for fire environments there is not a lot of refraction likely to occur, due to the combustion induced plasma. Consequently, loss of signal strength is not resultant from redistribution of radio energy due to refraction. Attenuation caused by electron-electromagnetic dynamics and diffraction are the main mechanisms in the small scale experiments.

4.2 Attenuation

In the discussion of the small scale experiments we considered the propagation through a block of plasma. Those figures have been reproduced here (see Figure 4.4). The attenuation of a cold plasma can be calculated by taking the real component of the complex propagation constant γ and making an appropriate conversion from nepers to decibels. In the fire environment, the attenuation caused by the plasma becomes broadband as the collision frequency is much higher than the plasma frequency.

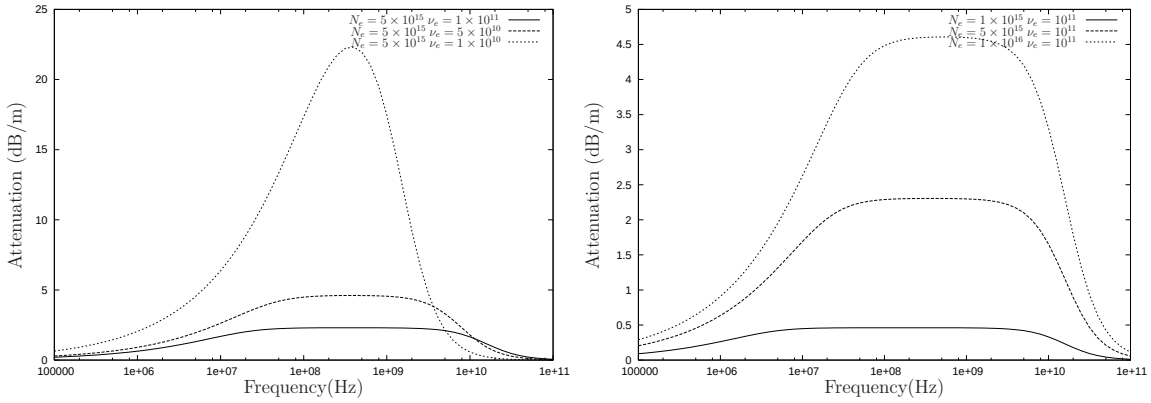

(a) Varying ν_{eff}

(b) Varying N_e

Figure 4.4: Cold Plasma Block - Attenuation

Although a block representation of a plasma provides insight into the attenuation, it does not best represent the profile of a fire. The column profile considered may better represent the plasma profile above the fuel heap and hence give a reasonable estimate of the attenuation experienced in the small scale experiments. To calculate the attenuation of a spatially varying plasma profile the total attenuation is the integration through the path.

$$L_{\text{dB}} = \int_a^b L(\mathbf{r}) d\mathbf{r} \tag{4.1}$$

where L_{dB} is propagtion loss in dB and $L(\mathbf{r})$ is the loss function over space, see [13]. A table has been prepared for different values of collision frequency and electron concentration.

The results of the table show consistency with the frequency plots of the block plasma. The table shows that attenuation is broadband for high collision frequencies. As the collision frequency decreases the attenuation increases, until frequency dependent behaviour is observed for table entries of $\nu_{eff} = 1 \times 10^9$. To obtain a collision frequency

Parameters	**180**MHz	**450**MHz	**950**MHz
$\nu_{eff} = 1 \times 10^{11}$Hz			
$N_{e_{max}} = 1 \times 10^{15}\text{m}^{-3}$	1.38dB	1.38dB	1.37dB
$N_{e_{max}} = 5 \times 10^{15}\text{m}^{-3}$	6.91dB	6.91dB	6.89dB
$N_{e_{max}} = 1 \times 10^{16}\text{m}^{-3}$	13.7dB	13.8dB	13.8dB
$N_{e_{max}} = 2 \times 10^{16}\text{m}^{-3}$	27.1dB	27.6dB	27.6dB
$N_{e_{max}} = 3 \times 10^{16}\text{m}^{-3}$	39.7dB	41.3dB	41.4dB
$\nu_{eff} = 1 \times 10^{10}$Hz			
$N_{e_{max}} = 1 \times 10^{15}\text{m}^{-3}$	13.8dB	12.9dB	10.3dB
$N_{e_{max}} = 5 \times 10^{15}\text{m}^{-3}$	64.1dB	66.2dB	53.5dB
$N_{e_{max}} = 1 \times 10^{16}\text{m}^{-3}$	112dB	131dB	110dB
$\nu_{eff} = 1 \times 10^{9}$Hz			
$N_{e_{max}} = 1 \times 10^{15}\text{m}^{-3}$	88.2dB	17.9dB	3.91dB
$N_{e_{max}} = 5 \times 10^{15}\text{m}^{-3}$	308dB	202dB	23.2dB

Table 4.1: Attenuation Table for Cosine Profile

of $\nu_{eff} = 1 \times 10^{9}$, one requires a temperature of 5000°K (unrealistic in a flame) and atmospheric pressure of 10hPa with no water, carbon dioxide or oxygen present. The table entries have been included here to clearly show that frequency dependent attenuation is not present in the plasma. One should not interpret the signal strength frequency variation of the small scale experiments without an understanding of the combustion plasma. Reasonable values for the collision frequency from calculations and flame measurements are from $5 \times 10^{10} - 5 \times 10^{11}$.

Thus far, there has been no presentation of values for the relationship of the fuel, trace element concentration and temperature, to producing the electron population. This is largely because such a calculation is specific to particular fire data. Table 4.2 is a collection of electron densities for different conditions in the flame. Fuel densities of 1kg m^{-3} and 0.1kg m^{-3} have been used with varying temperature and trace element. Mineral concentrations have been taken for Eucalyptus Marginata (Jarrah).

From the table it is quite apparent that potassium is a particularly dominant element. This dominance is due to the pyrolysis conversion and low ionisation energy, not necessarily the amount present. The temperature is the most dominant parameter with temperatures above 1200°K producing substantial electron populations. Such critical

Temperature	$N_{e_K}(\mathrm{m}^{-3})$	$N_{e_{Mg}}(\mathrm{m}^{-3})$	$N_{e_{Ca}}(\mathrm{m}^{-3})$
$M_{fuel} = 0.1\mathrm{kg\ m}^{-3}$			
1000°K	8.2×10^{12}	4.4×10^{4}	2.5×10^{8}
1100°K	8.7×10^{13}	2.6×10^{6}	6.7×10^{9}
1200°K	1.9×10^{15}	8.1×10^{7}	1.1×10^{11}
1300°K	3.3×10^{15}	1.5×10^{9}	1.1×10^{12}
1400°K	1.4×10^{16}	1.7×10^{10}	8.1×10^{12}
1500°K	4.9×10^{16}	1.5×10^{11}	4.6×10^{13}
$M_{fuel} = 1\mathrm{kg\ m}^{-3}$			
1000°K	2.3×10^{13}	1.4×10^{5}	7.871×10^{8}
1100°K	2.8×10^{14}	8.4×10^{6}	2.1×10^{10}
1200°K	1.9×10^{15}	2.5×10^{8}	3.3×10^{11}
1300°K	1.1×10^{16}	4.7×10^{9}	3.4×10^{12}
1400°K	4.4×10^{16}	5.7×10^{10}	2.6×10^{13}
1500°K	1.5×10^{17}	4.9×10^{11}	1.4×10^{14}

Table 4.2: Electron Density due to Potassium[a]

[a]Eucalyptus Marginata: K=0.52%,Ca=0.58%,Mg=0.28%,Pyrolysis Conversion:$\Pi_K = 100\%$,$\Pi_{Ca} = 20\%$,$\Pi_{Mg} = 40\%$

temperatures are easily obtained in the flames themselves and the overall temperature distribution.

In reality, such high temperatures do not necessarily exist over large regions of space and, in terms of propagation, the effective area relative to wavelength is what is important. A very high electron density may exist at the hottest part of the fire but in order for propagation to be substantially affected a large volume is required.

4.3 Diffraction

To examine the effect of the fuel heap on the measurements a simple knife-edge calculation has been used. For the geometry see Figure 4.5. No attempt has been made to account for the curvature of the fuel heap. The calculation is based on those shown in [95]. The knife edge calculation is an approximation for an infinitely long knife edge and does not

account for diffraction around the object, only over. Diffraction is a wave phenomena and therefore is related to the wavelength.

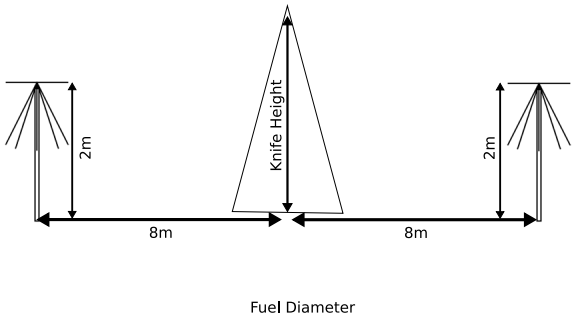

Figure 4.5: Knife Edge Geometry

From simple model calculations we expect to see a difference of 4dB between frequencies. This variation in frequency leads to greater sensitivity to the fuel heap and its height

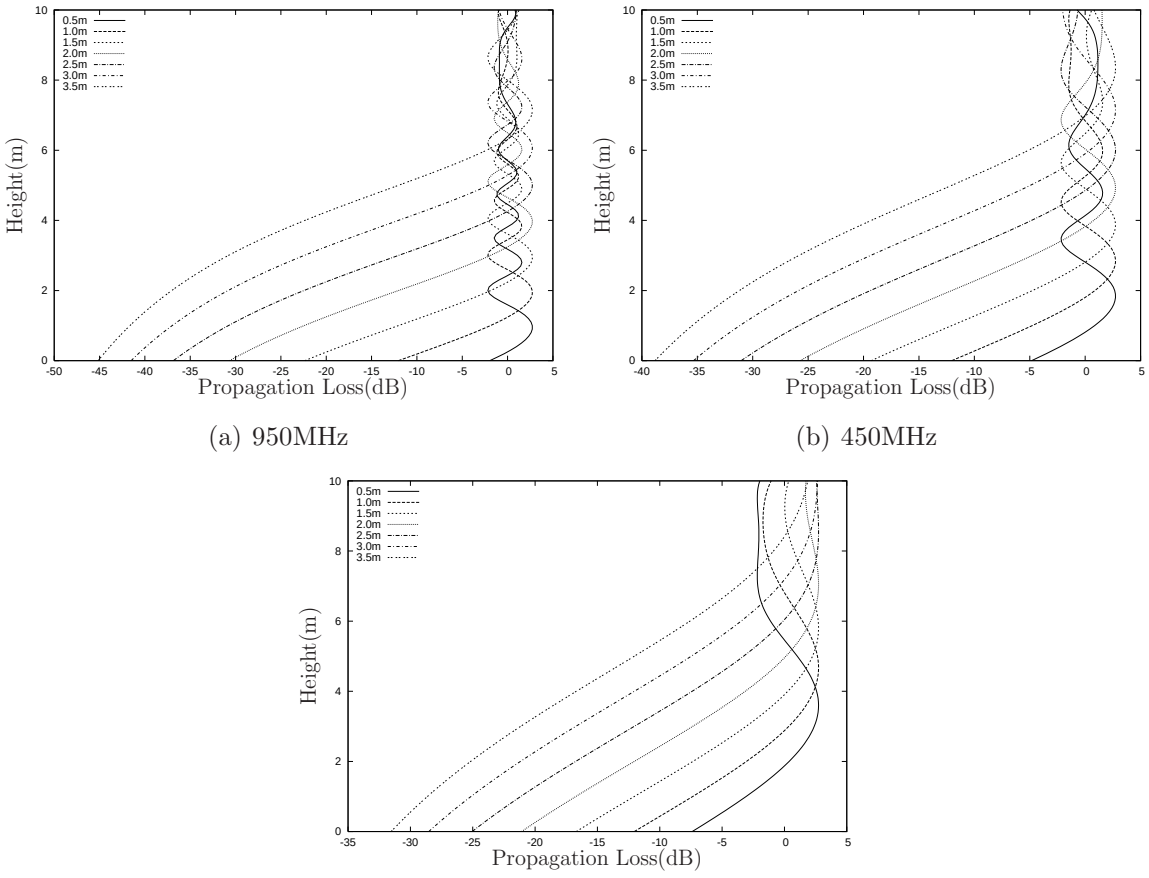

(a) 950MHz

(b) 450MHz

(c) 180MHz

Figure 4.6: Knife Edge Diffraction - Frequency Dependence

for higher frequencies. As the fuel heap changes in height, the recovery/difference in the signal strength will be larger for higher frequencies than low frequencies. This could help explain the observation in the small scale experiments.

All of the above highlight the need for a full electro-magnetic solution of the fire environment in order that plasma and diffractive mechanisms are taken into account. This simple treatment of the propagation problem for small scale fires has shown that attenuation caused by the plasma and complex interactions with diffractive mechanism caused by the fuel heap lead to a complex problem. Although, some general understanding has been the result of this chapter we now have some direction and basis of understanding to pursue the problem using a full electromagnetic solution in later chapters.

SECTION 5

Propagation Algorithms

5.1 Introduction

When studying propagation numerically, there are two classes of problems that the literature has addressed. Scattering algorithms address the solution electromagnetic fields of small or medium size structures, with respect to wavelength. Generally, these algorithms seek a solution of Maxwell's equations, or a derivative such as the Electric Field Integral Equation. Algorithms that fall into this category include Method of Moments (MoM), Finite Difference Time Domain (FDTD), Transmission Line Matrix (TLM), Finite Element Method (FEM) and for larger structures more recently the Multi-Level Fast Multipole Method (MLFMM). Propagation algorithms are a second class that are more interested in longer propagation from a source or transmitter to a receiver. In propagation algorithms there is generally an approximation to Maxwell's equations which allows an efficient solution over long distances. Some examples of propagation algorithms include Parabolic Equation Methods, Ray Tracing and more recently Integral techniques such as Coleman's technique[24].

In application to studying bushfire and fire environments we are confronted with conflicting requirements. The size of the problem varies from small scale experiments of the order of tens of meters to large scale bushfires of the order of kilometers. Over these large distances the medium is very complex in the flame regions and extremely dynamic in the surround air movements and atmospheric interactions. Unfortunately, sudden changes in the propagation medium pose problems for most propagation algorithms. From

experimental work we know that diffraction is a major contributor to propagation around the vicinity of the flame regions. Pure Ray Tracing techniques are therefore not realistic option. With such a complex medium is would be desirable to consider a full solution of Maxwell's equations. The usage of a scattering algorithm, although being highly accurate, has severe computational limitations, hence reducing the size of the problem that can be considered.

The solution of Maxwell's equations can occur in the time domain and the frequency domain. Frequency domain algorithms require a knowledge of the entire problem space to reach a solution. Time domain algorithms examine the development of a time pulse as it travels through the problem space. There are some latent advantages of time domain algorithms that allow them to be applied to long range problems. In this chapter an introduction to the Finite Difference Time Domain method will be presented; several advantages and disadvantages will be highlighted, which can help utilise this method for application to this problem.

Maxwell's Equations

$$\nabla \times \mathbf{E} = -\mu \frac{\partial \mathbf{H}}{\partial t} \tag{5.1}$$

$$\nabla \times \mathbf{H} = \epsilon \frac{\partial \mathbf{E}}{\partial t} + \sigma \mathbf{E} \tag{5.2}$$

5.2 Finite Difference Time Domain (FDTD) Algorithm

The Finite Difference Time Domain Algorithm was first introduced by Yee, in 1966[126]. It utilises finite difference approximations to calculate the space and time derivatives of Maxwell's equations, shown in 5.2. The fields E and H are solved for a volume, which is broken into small cubic cells on a fixed and regular grid. The grid is excited in time and the FDTD algorithm iterates at fixed time steps to calculate the response for E and H fields. The response of the fields over a number of time steps results in the impulse of the field in that cell or location. Fourier analysis is then carried out on each impulse response to acquire the frequency information of the fields in a volume. One large advantage of time domain algorithms is the ability to obtain the solution of a large number of frequency points from one time domain simulation.

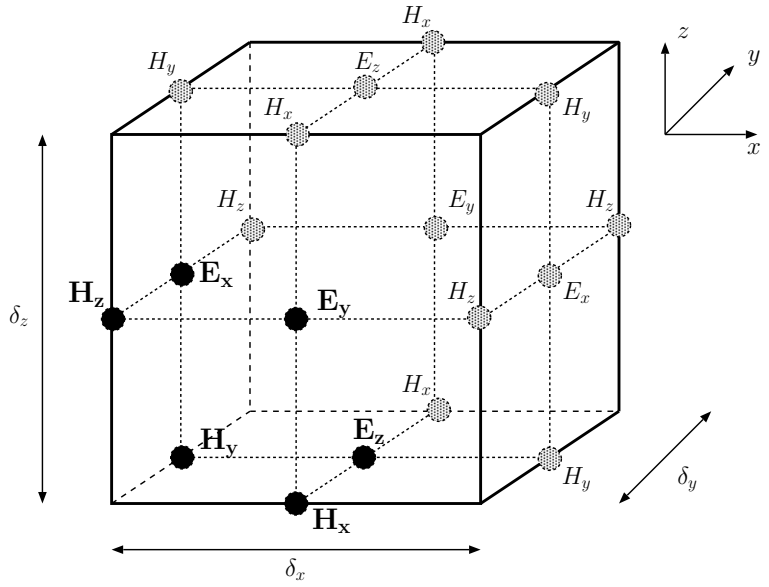

Figure 5.1: Yee Cell. Dark spots represent fields for one cell. Neighbouring fields in shaded spots.

Yee introduced two fundamental components of the FDTD algorithm. The first is the structure of the Yee cell, which represents the location of the electromagnetic fields in a cell on the grid. The **E** fields are offset by half a grid spacing from the **H** fields. This is shown in Figure 5.1, where the fields of one cell are shown in dark spots and the fields from neighbouring cells are shaded spots. One cell is denoted by $(\delta_x, \delta_y, \delta_z)$. The curl operator in Maxwell's equations (see Equation 5.2) is clearly illustrated by looking at one field component; take for example field E_y, and the curl is calculated from the surrounding fields around on its cartesian plane (fields H_y H_x H_y H_x).

The second component that Yee introduced is the separation of evaluation of E and H fields in time; one time iteration consists of the evaluation of the **H** at time $t + 1/2$ and the evaluation of the **E** fields at $t + 1$. Interleaving in time is often called a leapfrog finite difference scheme. Taflove [114] [112] further promoted Yee's algorithm and greatly increased its popularity with exploration of the FDTD algorithm for 2D (TM and TE) and 3D solutions and has been a major contributor to the development and acceptance of FDTD with the publication of one of the main books on the subject[112].

An entire FDTD program consists of three main components; pre-processing, iterative calculation and post-processing. Pre-processing configures the main algorithm, checks for

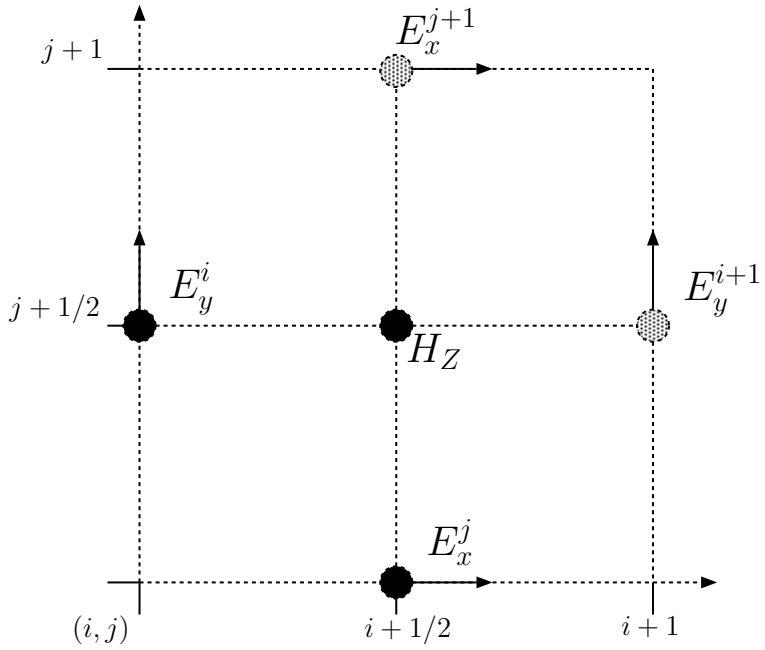

Figure 5.2: TE_z Yee Cell. Dark spots represent fields for one cell. Neighbouring fields in shaded spots.

correct conditions, fills the grid with the appropriate coefficients and acts as a bridge between the physical domain and the discrete numerical domain. The main calculation consists of iteratively updating the fields until the simulation time has been completed. Post-processing is important as it extracts the information into a discernable fashion. Typically this includes a collection of time samples, Fourier transformation of time domain data to the frequency domain and translation of the electric field into a voltage, power, current and acts as a bridge from the discrete numerical domain to the physical. A flow chart of a FDTD program is shown in Figure 5.3.

Maxwell's equations are valid for any co-ordinate system. FDTD can also be evaluated in any co-ordinate system, including, cartesian [126], cylindrical [40], spherical [52] and any general co-ordinate system [51, 74]. Cylindrical and spherical coordinate systems have advantages due to symmetry but also contain singularities at $r = 0$, which can be problematic. For simplicity the cartesian coordinate has been selected as the main algorithm to be used in this work. A cylindrical coordinate algorithm has been developed during this work but has not been widely used and therefore will not be included here.

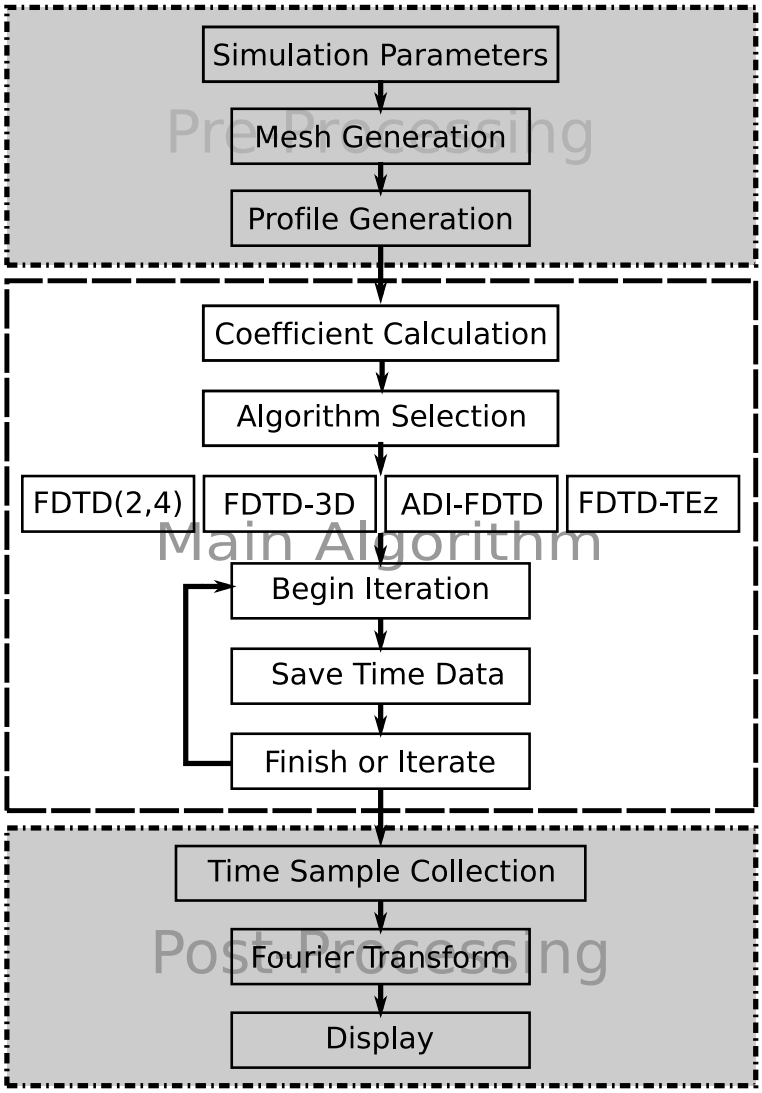

Figure 5.3: Calculation Steps

5.2.1 Cartesian Equations

An expansion of Maxwell's equation in the cartesian system is shown below. In order to evaluate these equations numerically the derivatives of time and space need to be discretised. The discretisation of the partial derivatives follows a particular finite difference scheme.

$$\varepsilon \frac{\partial E_x}{\partial t} = \frac{\partial H_z}{\partial y} - \frac{\partial H_y}{\partial z} - \sigma E_x \tag{5.3}$$

$$\varepsilon \frac{\partial E_y}{\partial t} = \frac{\partial H_x}{\partial z} - \frac{\partial H_z}{\partial x} - \sigma E_y \tag{5.4}$$

$$\varepsilon \frac{\partial E_z}{\partial t} = \frac{\partial H_y}{\partial x} - \frac{\partial H_x}{\partial y} - \sigma E_z \tag{5.5}$$

$$\mu \frac{\partial H_x}{\partial t} = \frac{\partial E_y}{\partial z} - \frac{\partial E_z}{\partial y} \tag{5.6}$$

$$\mu \frac{\partial H_y}{\partial t} = \frac{\partial E_z}{\partial x} - \frac{\partial E_x}{\partial z} \tag{5.7}$$

$$\mu \frac{\partial H_z}{\partial t} = \frac{\partial E_x}{\partial y} - \frac{\partial E_y}{\partial x} \tag{5.8}$$

One can choose to select explicit or implicit finite difference schemes to implement. Explicit schemes are conditionally stable, being constrained by the cell size and time step. Breaking these constraints or conditions results in an unstable solution. The original FDTD algorithm and majority of implementations discussed below are explicit schemes. Implicit schemes are unconditionally stable but are more complex to calculate than the explicit variety. The limiting factor is the accuracy of the solution. The Alternating-Direction Implicit FDTD (ADI-FDTD) [85] is a popular implicit method for FDTD, but there are others such as Crank Nicholson FDTD (CN-FDTD) scheme. A two dimensional ADI-FDTD implementation has been developed for this work but has not been incorporated into the simulation framework and will not be discussed here.

The finite difference schemes that have been used in the implementation of the FDTD algorithm are discussed below. The Leapfrog scheme relates to the partial derivative in time. The others are related to the implementation of the partial derivatives in space.

Leapfrog Scheme - Time.

For a discrete solution, a field v at time iteration $n+1$ is related to past values by the leapfrog scheme shown in Equation 5.9[80].

$$v_j^{n+1} = v_j^n + a(\Delta t/\Delta x)(v_{j+1}^{n+1/2} - v_{j-1}^{n+1/2}) \tag{5.9}$$

In the FDTD algorithm the solutions at $n+1/2$ are included in the magnetic field. Due to the coupling of the electric and magnetic field, each opposing field is updated at the half time step. This allows memory resources to be conserved as only one electric field vector and one magnetic field vector needs to be stored.

Forward and Backward Finite Difference - Space

The discretisation of spatial derivatives are different for each field due to the offset grid. For the electric field a forward difference scheme is used for the spatial partial derivative. The forward finite difference in direction x at time t is shown in Equation 5.10 [80].

Forward

$$\Delta_{2x+}v(x,t) = \frac{1}{\Delta x}\left[v(x+\Delta x,t) - v(x,t)\right] \tag{5.10}$$

For the magnetic fields a backward finite difference scheme is used. This is shown in Equation 5.11.

Backward

$$\Delta_{2x-}v(x,t) = \frac{1}{\Delta x}\left[v(x,t) - v(x-\Delta x,t)\right] \tag{5.11}$$

Both the forward and backward finite difference schemes are second order accurate. The cartesian representation of Maxwell's equations shown in Equation 5.3 can be expressed using forward and backward operators. In Equation 5.12, Δ_{y-} is the backward finite difference operator on the H_z field.

2nd Order Accurate Scheme

$$\varepsilon\Delta_t E_x = \Delta_{y-}H_z - \Delta_{z-}H_y - \sigma E_x \tag{5.12}$$

Similarly the finite difference form of Equation 5.6 is shown in Equation 5.13. Note the direction of the finite difference operator. This notation has been introduced to conveniently demonstrate where different operators have been used in a particular variation of the algorithm

$$\mu\Delta_{t+1/2}H_x = \Delta_{z+}E_y - \Delta_{y+}E_z \tag{5.13}$$

Traditional FDTD notation uses the raw field location in terms of the Yee cell to denote the field equations. Using the FDTD convention Equation 5.3 would be expressed

as:

$$\varepsilon\frac{E_x^{n+1}(i+\frac{1}{2},j,k)-E_x^{n}(i+\frac{1}{2},j,k)}{\Delta t}= \frac{H_z^{n+\frac{1}{2}}(i+\frac{1}{2},j+\frac{1}{2},k)-H_z^{n+\frac{1}{2}}(i+\frac{1}{2},j-\frac{1}{2},k)}{\Delta y} - \frac{H_y^{n+\frac{1}{2}}(i+\frac{1}{2},j,k+\frac{1}{2})-H_y^{n+\frac{1}{2}}(i+\frac{1}{2},j,k-\frac{1}{2})}{\Delta z} - \sigma\frac{E_x^{n+1}+E_x^{n}}{2} \tag{5.14}$$

The traditional representation better encapsulates the offset grid and the time stepping but can lead to confusion when we consider higher order algorithms.

4th Order Scheme

The 4th order scheme is a more accurate representation of the spatial derivatives. It is commonly used in the higher order FDTD(2,4) algorithm, where the 2 represents the second order time derivative and the 4 the higher order spatial derivative. The higher order scheme is necessary for long range algorithms to mitigate against numerical dispersion. It also reduces error in the simulation over time and therefore aids in stability over long simulation times. The 4th order scheme is shown in Equation 5.15 for the forward implementation and Equation 5.16 for the backward scheme.

$$\Delta_{4x+}v(x,t)=\frac{1}{\Delta x}a\left[v(x+\Delta x,t)-v(x,t)\right]+\frac{1}{\Delta x}b\left[v(x+2\Delta x,t)-v(x-\Delta x,t)\right] \tag{5.15}$$

$$\begin{aligned}\Delta_{4x-}v(x,t)=&\frac{1}{\Delta x}a\left[v(x,t)-v(x-\Delta x,t)\right]\\&+\frac{1}{\Delta x}b\left[v(x+\Delta x,t)-v(x-2\Delta x,t)\right]\end{aligned} \tag{5.16}$$

The coefficients a and b are weighting coefficients for the differential stencil. Liu[70] was one of the first to introduce this type of discretisation in application to FDTD algorithms and chose values for $a = 9/8$ and $b = 1/24$. Further improvements in dispersion and stability can be made by selecting different values as shown by Tsiboukis[131].

Additionally higher order schemes exist for the FDTD. As can be seen above, the higher order schemes generally come at the price of a greater computational burden. One

technique that takes a slight different tact and has attracted some recent attention is Multi-Resolution Time Domain (MRTD)[64] which make use of wavelets to calculate a dispersionless differential operator. As MRTD highlights, by using a higher order scheme larger grid size can be utilised therefore reducing memory requirements. MRTD maintains good accuracy close to the Nyquist sampling limit.

5.2.2 Stability

Having introduced the explicit finite difference schemes for the FDTD algorithm it is now important to examine the stability requirements. The FDTD algorithm obeys the Courant Friedrichs Levy condition for stability and convergence of the FDTD solution. The condition is shown in Equation 5.17, where c is the maximum speed of light and is related to the dielectric properties of the propagation medium [114]. Included in this formula is the variable q which is the Courant number often found in the literature. This is a number to describe where a simulation is with respect to its maximum stability and is always less than 1.

$$\Delta t_{Yee} \leq q \left(c \sqrt{\frac{1}{\Delta x^2} + \frac{1}{\Delta y^2}} + \frac{1}{\Delta z^2} \right)^{-1} \tag{5.17}$$

For the long range simulations the FDTD(2,4) algorithm is quite often used. The general stability criteria is shown in Equation 5.18 and using the choice of $a = 9/8$ and $b = 1/24$ the reduced form shown in Equation 5.19.

$$\Delta t_{(2,4)} \leq \left(c \sqrt{\frac{\left(|a_x| + |b_x|\right)^2}{\Delta x^2} + \frac{\left(|a_y| + |b_y|\right)^2}{\Delta y^2}} + \frac{\left(|a_z| + |b_z|\right)^2}{\Delta z^2} \right)^{-1} \tag{5.18}$$

$$\Delta t_{(2,4)} \leq \frac{6}{7} \left(c \sqrt{\frac{1}{\Delta x^2} + \frac{1}{\Delta y^2}} + \frac{1}{\Delta z^2} \right)^{-1} \tag{5.19}$$

As can be seen for the FDTD(2,4) algorithm the courant number is less than its maximum value. So to ensure stability, the time step needs to be reduced by the value of 6/7. This is not a severe limitation when the benefits of the dispersion are taken into account for long range simulations.

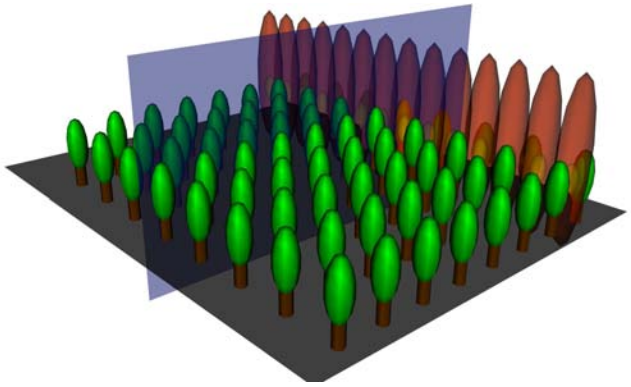

Figure 5.4: A representation of the bushfire symmetry

5.2.3 TE_z formulation

When encompassing all fields in the FDTD algorithm there are three electric field components and three magnetic field components. As the size of a problem increases in three dimensions the memory requirements quickly become very large. One way to reduce the computational burden of problems is to consider whether the problem has any form of symmetry. If symmetry exists in one or two dimensions of the problem, these dimensions can be removed, hence reducing the total number of cells.

Bushfires generally have a very long fire front, which extends over a large distance. An approximation can be made which reduces the problem to the cross-sectional plane of the fire front. This is shown in Figure 5.4.

By using symmetry to reduce the 3D problem into a 2D problem we should also consider the field selection. It is not necessary to calculate all 6 field components on this reduced space. We can further reduce the requirements by setting the $E_z = 0$ which reduces the required calculation fields to E_x, E_y, H_z which forms a Transverse Electric field solution (TE_z). The Yee cell for a TE_z formulation is shown in Figure 5.5. Similarly, we could use the duality principle by setting $H_z = 0$ and the reduced components are H_x, H_y, E_z, which is referred to as Transverse Magnetic field (TM_z).

Using symmetry however, can limit the types of sources that can be represented. In this case, a point source cannot be represented and only a line source can be simulated.

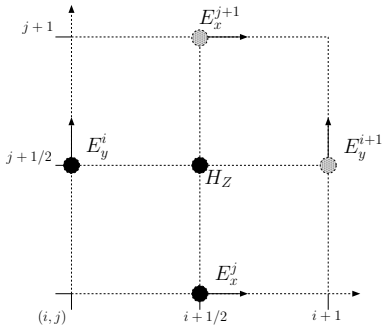

Figure 5.5: 2D TE_z FDTD Cell

5.2.4 Boundary Conditions

In a finite difference environment it is important to truncate the calculation on a grid correctly so no artificial solution occurs. If a grid does not have correct boundary conditions the solution will become contaminated by undesired reflections at the boundaries. Typically, to simulate free space conditions the grid is truncated with an absorbing boundary condition. This boundary condition ideally gives no reflection. In 1994, Berenger [8] introduced the perfectly matched layer(PML), which revolutionised absorbing boundary conditions for FDTD. Prior to the PML, radiation boundary conditions were used such as Mur [83], Liao [113] and those in [102].

When we model Maxwell's Equations we are simply modelling the differential equations. This does not provide a unique solution to a problem but simply describes the intrinsic coupling of electric and magnetic fields and electromagnetic wave propagation. To provide uniqueness of a solution, boundary conditions are required. Boundary conditions tell you how the fields should behave around a region of space (boundary),which may be an object, wall or antenna and can have various properties such as metal, magnetic, lossy. We will introduce some simple boundary conditions and one important boundary condition, the 'Perfect Matched Layer'.

Perfect Electrical Conductors - PEC

This boundary condition represents a perfect metal conductor with infinite conductivity. When a wave approaches a perfect metal, the electric field causes free electrons to interact and follow or track the electric field. This means the transverse electric field is continuous.

The normal component of E or D is discontinuous and tends to zero. In real metals, a finite amount of conductivity exists, and penetration occurs resulting in the skin effect phenomena. Mathematically, this is expressed as:

$$\mathbf{E} \times \underline{n} = 0, \qquad \mathbf{D} \cdot \underline{n} \propto \rho \tag{5.20}$$

where ρ is the surface charge density.

In the FDTD algorithm, a PEC boundary condition can easily be implemented by forcing the normal electric field component to zero. This is more preferable to a large conductivity because stability is related to changes in time and space. Due to the large conductivity, a large change occurs in the fields at the metal boundary and therefore the entire algorithm will become unstable. Large Finite Conductivities can be modelled through the surface impedance method, which follows the same principle of directly solving the E and H fields for a given conductivity and a specific frequency and forcing the grid into that solution. This however, has the limitation of obtaining frequency accuracy at one specified frequency, which curtails some of the advantages of time domain techniques. To correctly implement the surface impedance method a dispersive material needs to be modelled using convolution techniques or auxiliary methods. For low changes in permittivity and conductivity, inclusion into the FDTD grid is fine.

Perfect Magnetic Conductors - PMC

This is simply the symmetric partner of PECs. A Perfect Magnetic Conductor results in the transverse magnetic field being continuous at the boundary and the normal component being discontinuous. The electric field then follows suit with its normal component being continuous and the transverse component being discontinuous. Although this seems like a fictitious material it is generally used for symmetry where a PMC surface represents symmetry on that plane. Although no material has yet been found that exhibits magnetic conductivity mathematically it is a kind tool for dealing with the symmetry of Maxwell's Equations. A mathematical representation is shown below.

$$\mathbf{H} \times \underline{n} = 0, \qquad \mathbf{B} \cdot \underline{n} \propto K \tag{5.21}$$

where K is the surface current density. A PMC can also be used as a good approximation where the grazing angle is low such as high frequencies propagating over long distances.

Surface Impedance Boundary Conditions

A more general boundary is the impedance boundary condition. The relation between the fields at the boundary is mathematically described as:

$$\overline{E}_{tan}(\omega) = Z(\omega)\left[\widehat{n} \times \overline{H}_{tan}(\omega)\right] \tag{5.22}$$

where $\overline{E}_{tan}$ and $\overline{H}_{tan}$ are the tangential components of the electric and magnetic fields the interface, Z is the surface impendance and $\widehat{n}$ is the normal unit vector pointing out at the interface. One of the problems with Impedance Boundary Conditions in FDTD is the frequency dependence of the eletric and magnetic fields. Various modifications to the algorithm can be made which usually involve costly recursive or convolutional algorithms.

In this work, where an interface exists, both mediums are modelled using their permittivity, conductivity and permeability negating the need for impedance boundary conditions. If a medium requires truncation a perfectly matched layer is used.

Generalised Perfectly Matched Layer - GPML

The Perfectly Matched Layer (PML) was first introduced by Berenger in 1994[8]. The PML is an artificial material that is anisotropic and has magnetic conductivity. Magnetic conductivity in the literature is denoted σ^*. Berenger showed that if a material with a magnetic conductivity and electric conductivity obeys the relationship shown in Equation 5.23, the material will be perfectly absorbing and reflectionless.

$$\frac{\sigma_z}{\epsilon} = \frac{\sigma_z^*}{\mu} \tag{5.23}$$

In order to have a material that perfectly absorbs in one direction, which is used at a boundary of the grid, anisotropy must be introduced into the material. Anisotropy of the material is implemented with the split field concept that Berenger introduced (other implementations do exist which move the field into a stretched complex coordinate space). Individual fields $(E_x, E_y, E_z, H_x, H_y, H_z)$ are split into two auxiliary fields with

components such that $E_x = E_{xy} + E_{xz}$ for example. Maxwell's equation will yield for E_x component

$$\partial_t E_x + \sigma E_x = \partial_y H_z - \partial_z H_y \tag{5.24}$$

becomes two equations

$$\partial_t E_{xy} + \sigma_y E_{xy} = \partial_y H_z \tag{5.25}$$

$$\partial_t E_{xz} + \sigma_z E_{xz} = \partial_z H_y \tag{5.26}$$

This separation allows the anisotropy in the conductivity profile of the σ_y and σ_z directions. By obeying the PML relation (see Equation 5.23) no reflection results at the PML boundary.

In numerical implementation, a PML layer will require a thickness of several cells in order to provide sufficient absorption. The conductivity profile must be slowly introduced, with typical layers compromising of 4 to 16 cells dependent on the problem. The original profile that was introduced by Berenger is shown in Equation 5.27.

$$\sigma_z(z) = \sigma_{max} \left(\frac{z}{\delta}\right)^n \tag{5.27}$$

where σ_{max} is the maximum conductivity, δ the thickness of the layer and n is the order and is generally in the vicinity of 2. Various optimisations for the selection of these values can be found in the literature [8][35] [36] [34]. Fang and Wu introduced the Generalised Perfectly Matched Layer (GPML) in 1996 [35]. The GPML has the advantages of linear time stepping, a centred difference scheme and the flexibility to have background permittivity and conductivity.

$$\nabla \times \mathbf{E} = -\left(\mu \frac{\partial \mathbf{H}}{\partial t} + \sigma^* \mathbf{H}\right) \tag{5.28}$$

$$\nabla \times \mathbf{H} = \epsilon \frac{\partial \mathbf{E}}{\partial t} + \sigma \mathbf{E} \tag{5.29}$$

These are the Maxwell's equations that are used in the PML with suitable splitting of the field to achieve the required anisotropy.

5.2.5 Numerical Dispersion

Dispersion is a phenomena due to the phase velocity of light in a medium, being a function of frequency. Different frequencies travel at different speeds and, over distance the separate frequencies spread out and "disperse". In numerical electromagnetics, a similar phenomena occurs because of the discretisation. A discrete solution suffers from two sources of numerical dispersion. One is the approximation of the continuous partial derivatives in implementation as finite difference schemes. Particular finite difference schemes have different dispersion relations and the introduction of higher order schemes, such as FDTD(2,4), is used to minimise this source of numerical dispersion. The second source of numerical dispersion is related to the sampling of space by the FDTD grid. The phase velocity is related to the wavelength, direction of propagation, grid resolution and aspect ratio (ratio of $\Delta x/\Delta y$)[130]. To reduce dispersion one can simply increase the sampling of the grid relative to wavelength. This is counter-productive, as it increases the computational effort due to the larger grid. To examine numerical dispersion it is helpful to consider the dispersion relation.

Dispersion Relation

For the 3D FDTD algorithm the dispersion relation is shown in Equation 5.30 [130]. The overall wave vector is a function of the direction in which it travels. For the 2D FDTD algorithm the dispersion relation is shown in Equation 5.31 [131], and includes the anisotropy of permittivity.

$$\frac{1}{\Delta x^2}\sin\left(\frac{k_x\Delta x}{2}\right)+\frac{1}{\Delta y^2}\sin\left(\frac{k_y\Delta y}{2}\right)+\frac{1}{\Delta z^2}\sin\left(\frac{k_z\Delta z}{2}\right)=\frac{1}{(c\Delta t)^2}\sin\left(\frac{\omega\Delta t}{2}\right) \quad (5.30)$$

$$\left[\frac{1}{c_0\Delta t}\sin\left(\frac{\omega\Delta t}{2}\right)\right]^2=\frac{\sin^2\left(\frac{k_x\Delta x}{2}\right)}{\epsilon_y\Delta x^2}+\frac{\sin^2\left(\frac{k_y\Delta x}{2}\right)}{\epsilon_x\Delta y^2} \quad (5.31)$$

The FDTD(2,4) algorithm has a slightly more complex dispersion relation, as shown in Equation 5.32 [131], where a_x, a_y and b_x, b_y are the stencil weightings.

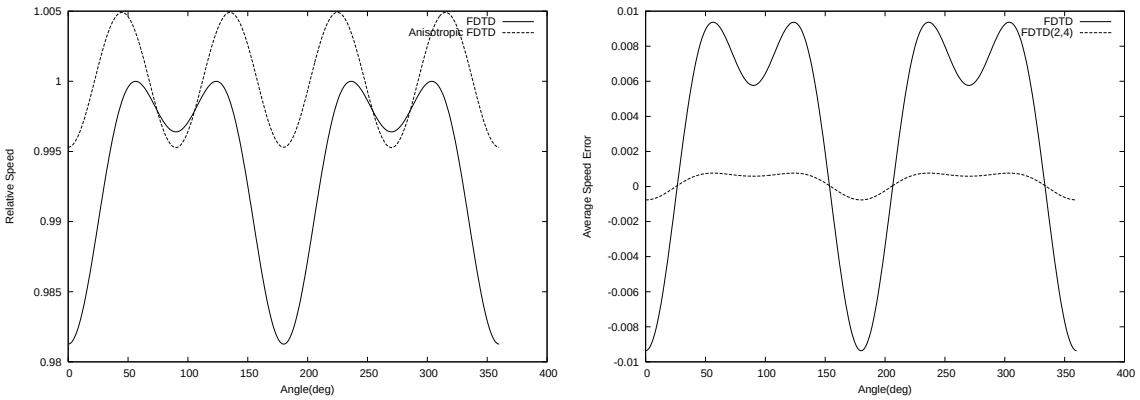

(a) Anisotropy (b) FDTD(2,4)

Figure 5.6: FDTD Dispersion - Direction

$$\left[\frac{\sin\left(\frac{\omega\Delta t}{2}\right)}{c_0\Delta t}\right]^2 = \frac{1}{\epsilon_y}\left[\frac{a_x\sin\left(\frac{k_x\Delta x}{2}\right)+b_x\sin\left(\frac{3k_x\Delta x}{2}\right)}{\Delta x}\right]^2 + \frac{1}{\epsilon_x}\left[\frac{a_y\sin\left(\frac{k_y\Delta y}{2}\right)+b_y\sin\left(\frac{3k_y\Delta y}{2}\right)}{\Delta y}\right]^2 \tag{5.32}$$

Angular Dispersion

Numerical dispersion is a function of propagation direction. A comparison has been made for the different schemes in Figure 5.6. To decrease the angular dispersion one can introduce an artificial anisotropy by modifying relative permittivity ϵ_x and ϵ_y separately[58]. The result is shown in Figure 5.6(a) and demonstrates the reduced dispersion of angle. This method helps maintain phase accuracy over a number of directions. In application to bushfire problems we only consider uni-axial propagation. In this case artificial anisotropy does not result in a large reduction. The only solution is to increase the grid resolution, which is costly to performance, or to use a higher order scheme. A comparison of a higher order scheme and its dispersion of propagation angle is shown in Figure 5.6(b); a reduction in phase error is obvious.

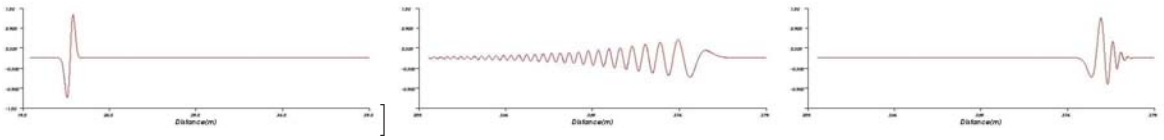

(a) Original Pulse (b) Yee FDTD (c) FDTD(2,4)

Figure 5.7: Dispersion of Pulse after 350m

Frequency Dispersion

Numerical Dispersion is particularly a problem for long range simulation. Simulations involving the wave propagator can result in a dispersed pulse that extends beyond one simulation space. This results in data being lost and requires some form of disperion mitigation. Because the wave propagator is used for propagation in one direction using anisotropic techniques will not help. Therefore, a higher order algorithm must be introduced to provide better dispersion performance. For long simulations the FDTD(2,4) algorithm is used which is 2nd order in time and 4th order in space. As can be seen in Figure 5.7, the FDTD(2,4) algorithm performs far better in terms of numerical dispersion, and results in a more compact pulse after 350m. The pulse with the original FDTD has dispersed and consumes the entire calculation space. As will be seen, this is a major problem for implementing the wave propagator and maintaining accuracy.

5.2.6 Excitation

Excitation is one of the most important elements of computational electromagnetics. If the numerical representation of the problem is not properly excited a correct solution will not be obtained. This is complicated further by the simulation of time domain algorithms. To exploit the time domain feature the excitation should cover the frequency range of interest.

In Maxwell's equations there can be both magnetic and electric field sources. If we consider the Maxwell equation shown in Equation 5.33 and an electric field source. The electric field can be excited using grid input at $\mathbf{E_1}$ or $\mathbf{E_2}$. These two locations are referred to as 'hard' ($\mathbf{E_1}$) and 'soft' ($\mathbf{E_2}$) source respectively[110]. A hard source simply sets the E field. A soft source represents an additive input current source to Maxwell's equation. In the numerical implementation used in this work $\mathbf{E_2}$ is sometimes denoted as current

source $\mathbf{J}$.

$$\nabla \times \mathbf{H} = \frac{\partial \mathbf{E_1}}{\partial t} + \sigma \mathbf{E_2} \tag{5.33}$$

A discrete time function is then fed into the grid at each iteration. The excitation should contain the necessary frequency information as well as be smooth in time and compact to minimise the number of iterations required to fill the grid. Examples of functions that have been used in literature[111] include Gaussian functions, derivatives of Gaussian functions, single sinusoids and a variety of custom excitation functions. One problem that has surfaced in the usage of functions with a DC component, such as a gaussian function, is the resident charge in the grid[121]. This charge resides on the grid over the entire simulation time and has lead us to the use of derivatives of the Gaussian function instead.

The excitation of the grid occurs over space as well as time and the spatial excitation is dependent on the problem. Dual magnetic and electric sources can be used simultaneously where uni-directional propagation is desired, such as the separation of incoming from outgoing waves for S-parameter evaluation[128]. In this work, a very simple excitation of a fictitious Gaussian spatial electric source has been used. For 2D FDTD simulations a plane wave is used.

5.3 Algorithm Additions

Yee's original algorithm lacks certain features, which are necessary in application to the study of bushfire propagation. The combustion induced plasma that exists in the flames of the fire is a dispersive medium. In order to gain the benefits of time domain simulation it must be possible to implement cold plasma materials in the numerical time domain.

The second change is to overcome the computational limitations with long distances for bushfire simulations. A moving window scheme is proposed here. It utilises the inherent advantages of time domain pulses that are localised in time and space.

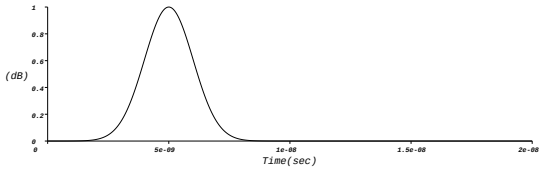

(a) Gaussian Time

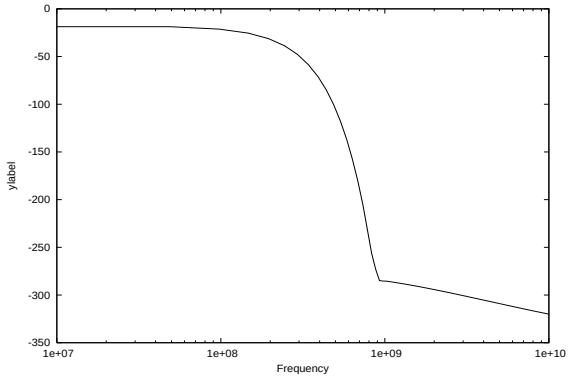

(b) Gaussian Frequency

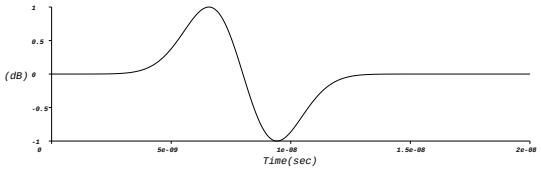

(c) Differential Gaussian Time

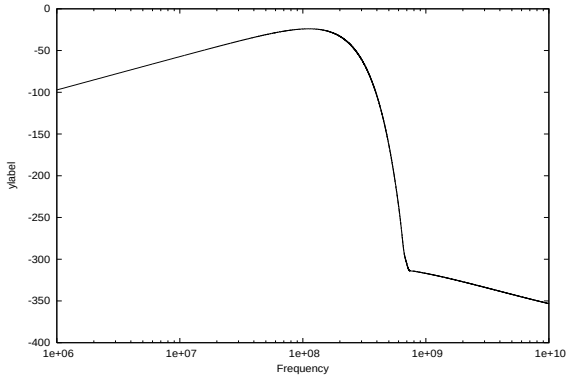

(d) Differential Gaussian Frequency

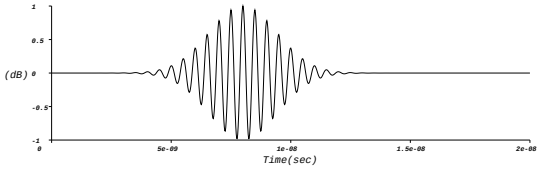

(e) Modulated Gaussian Time

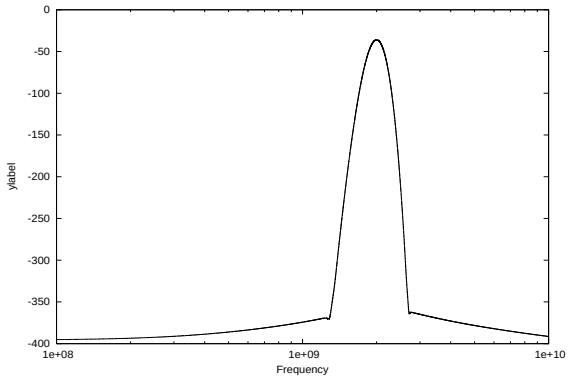

(f) Modulate Gaussian Frequency

Figure 5.8: FDTD Excitation Functions

5.3.1 Cold Plasma Mediums

Cold Plasma represents a frequency dependent medium and this is problematic for time domain algorithms, due to the time dependence of the permittivity and conductivity. There are two main approaches to modelling dispersive media in FDTD. The first is to use convolutional algorithms and the second involves an auxiliary differential equation. A good summary of current techniques can be found in [129].

In this implementation we follow the use of an auxiliary equation. This method was first put forward by Nickisch [86] and was used for modelling cold plasma media. This technique is best explained by following ionospheric physics. Following Budden [13], in the presence of a external magnetic field $\mathbf{B_{ext}}$ the displacement vector $\mathbf{r}$ of a charged particle in a cold plasma medium can be described as:

$$e\mathbf{E} + e\frac{\partial \mathbf{r}}{\partial t} \times \mathbf{B_{ext}} = m\frac{\partial^2 \mathbf{r}}{\partial t^2} + m\nu\frac{\partial \mathbf{r}}{\partial t} \tag{5.34}$$

where ν is the collision frequency and m is the mass of the charged particle. In our application, we simplify the equation by making the assumption that no external magnetic field exists $\mathbf{B_{ext}} = 0$. Defining the polarisation vector for the entire volume as $\mathbf{P} = eN_e\mathbf{r}$, the polarisation vector differential equation becomes:

$$\frac{\partial^2 \mathbf{P}}{\partial t^2} + \nu\frac{\partial \mathbf{P}}{\partial t} = \frac{e^2 N}{m}\mathbf{E} \tag{5.35}$$

A polarisation current can be defined as $\mathbf{J_P} = d\mathbf{P}/dt$, which results in a first order differential equation.

$$\frac{\partial \mathbf{J_P}}{\partial t} = -\nu\mathbf{J_P} + \epsilon_0\omega_P^2\mathbf{E} \tag{5.36}$$

where ω_P^2 is the plasma frequency defined as $\omega_P = \sqrt{e^2N/\epsilon_0 m}$. The final auxiliary equation for implementation in the FDTD algorithm is shown in equation 5.36. Maxwell's equations are modified to include the extra plasma current component in the temporal electric field equation.

$$\epsilon_0\frac{\partial \mathbf{E}}{\partial t} = \nabla \times \mathbf{H} - \sigma\mathbf{E} - \mathbf{J_P} \tag{5.37}$$

In the finite difference scheme, a number of different implementations exist for these equations. Young [127] originally proposed a split update of J and E where J is updated

at the same time as H, or n+1/2. Cummer [26] suggested a exponential time stepping for strongly damped plasma and updating J and E at the same time step, this requires the solution of simultaneous equations. Three implementations have been tried here. The first is Young's split update implementation, however this implementation suffers from stability issues due to the difference in where E and J are updated and has a severe limitation on the time step. The maximum time step is reduced by $\sqrt{1-(\omega_{P_{max}}\Delta t/2)}$. In bushfire plasma $\omega_{P_{max}}$ can be quite large, therefore this is a severe limitation in time step. The split update implementation is shown in Equation 5.38 and 5.39.

$$\frac{\mathbf{J}_P^{n+1/2}-\mathbf{J}_P^{n-1/2}}{\Delta t} = -\nu\left(\frac{\mathbf{J}_P^{n+1/2}+\mathbf{J}_P^{n-1/2}}{2}\right)+\epsilon_0\omega_P^2\mathbf{E}^n \tag{5.38}$$

$$\epsilon_0\left(\frac{\mathbf{E}^{n+1}-\mathbf{E}^n}{\Delta t}\right) = \nabla\times\mathbf{H}^{n+1/2}-\mathbf{J_P}^{n+1/2} \tag{5.39}$$

Therefore, an implementation that simultaneously updates E and J has also been incorporated. Simultaneously evaluating E and J_P removes the maximum time step limitation[129]. One implementation uses linear time stepping and the other exponential time stepping, this is Equation 5.40 - 5.41. The exponential variation, shown in Equation 5.42 - 5.43, is more advantageous where the collision frequency is exceptionally high.

Linear Time Step

$$\frac{\mathbf{J}_P^{n+1}-\mathbf{J}_P^{n}}{\Delta t} = -\nu\left(\frac{\mathbf{J}_P^{n+1}+\mathbf{J}_P^{n}}{2}\right)+\epsilon_0\omega_P^2\left(\frac{\mathbf{E}^{n+1}+\mathbf{E}^n}{2}\right) \tag{5.40}$$

$$\epsilon_0\left(\frac{\mathbf{E}^{n+1}-\mathbf{E}^n}{\Delta t}\right) = \nabla\times\mathbf{H}^{n+1/2}-\left(\frac{\mathbf{J}_P^{n+1}+\mathbf{J}_P^{n}}{2}\right) \tag{5.41}$$

Exponential Time Step

$$\begin{aligned}\mathbf{J}_P^{n+1} = e^{-\nu\Delta t}\mathbf{J}_P^n &+ \frac{\epsilon_0\omega_P^2}{\nu^2\Delta t}\left(\nu\Delta t+e^{-\nu\Delta t}-1\right)\mathbf{E}^{n+1}\\ &+\frac{\epsilon_0\omega_P^2}{\nu^2\Delta t}\left(1-e^{-\nu\Delta t}-\nu\Delta t e^{-\nu\Delta t}\right)\mathbf{E}^{n+1}\end{aligned} \tag{5.42}$$

$$\epsilon_0\left(\frac{\mathbf{E}^{n+1}-\mathbf{E}^n}{\Delta t}\right) = \nabla\times\mathbf{H}^{n+1/2}-\left(\frac{\mathbf{J}_P^{n+1}-\mathbf{J}_P^{n}}{2}\right) \tag{5.43}$$

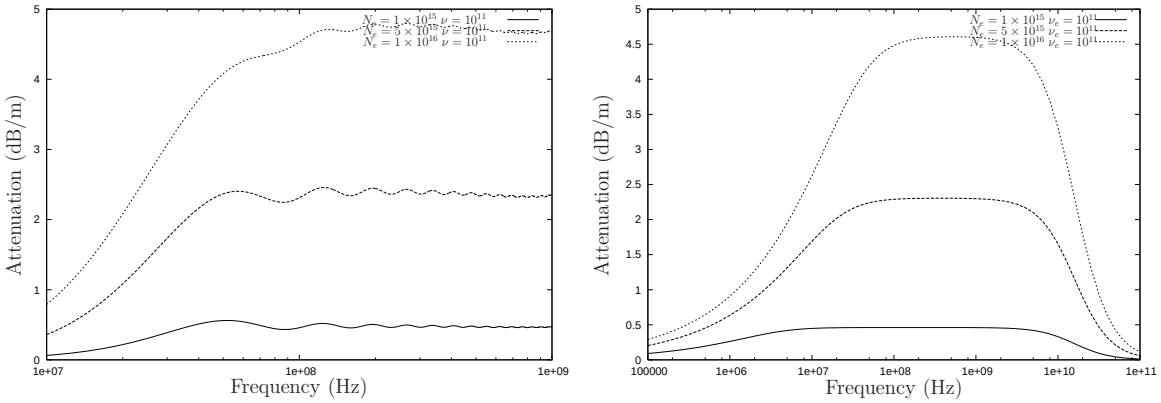

(a) FDTD (b) Analytical

Figure 5.9: Varying Electron concentration

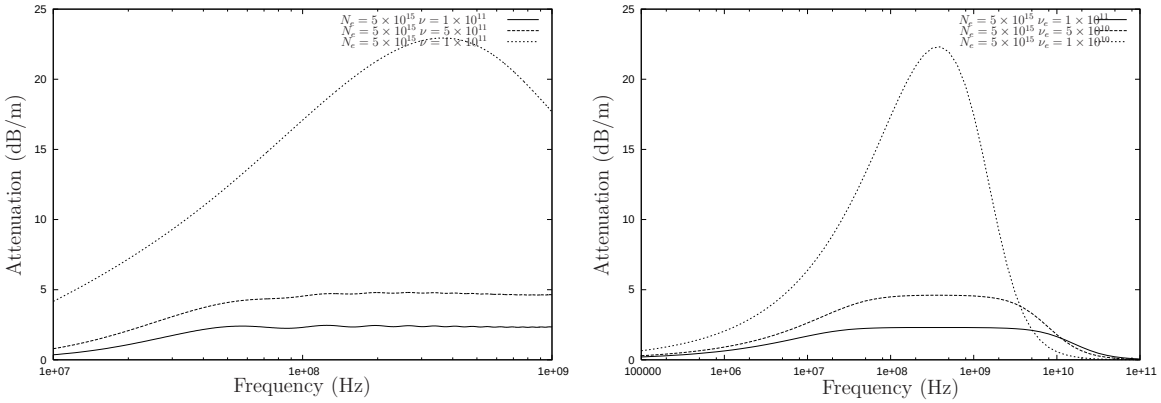

(a) FDTD (b) Analytical

Figure 5.10: Varying Collision Frequency

Plasma Plots

A demonstration of plots with the analytical cold plasma model shown in previous chapters (See Section 4.2) is compared with the FDTD numerical solution. Comparisons are shown in Figure 5.9 and Figure 5.10. As can be seen, this verifies that the numerical calculation has provided an accurate representation of the analytic solution.

5.3.2 Moving Grid Wave Propagator

The moving grid wave propagator is a way to limit the calculation grid to a smaller region of the larger problem space. As the grid is excited the pulse will propagate through space.

The pulse, however, is localised in space and time and, because of this, we can limit the actual iteration update to only the segment of space that contains the pulse, greatly reducing the computational burden of the entire problem[103]. A representation of this is shown in Figure 5.3.2. The entire problem space is split up into smaller domains, as indicated by the numbering. The actual computational grid that is iterated contains a limited number of smaller domains and a PML layer on the main computational boundary, indicated by the red surrounding box. The grid is then excited and the pulse tracked as it passes and exits each domain. Once it reaches the edge of the main computational grid a domain to the left is unloaded from memory and a domain to the right is loaded. This allows our pulse to continue throughout the entire problem space. Post-processing is then used to collect the time samples into their respective domains and collect the overall solution.

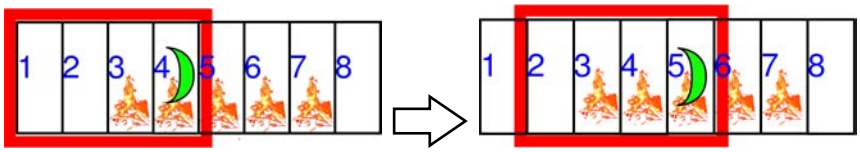

Figure 5.11: FDTD Wave Propagator. Space Numbering and Calculation grids.

The wave propagator is an elegant solution for this particular problem but does have a number of limitations. It only considers electromagnetic propagation in a direction of preference. This is similar to uni-axial algorithms like the Parabolic Equation Methods. In fact Sevgi[1, 75, 2] has implemented a similar technique for FDTD, TLM and conducted comparative studies with parabolic equation methods. Localised back scatter can be evaluated for a limited number of domains as a post-processing step, where the domains of interest are reloaded and continued in iteration until the scatter is evaluated.

A limitation of the wave propagator is solutions that require a long settling time. An example of this is an undamped cold plasma. A long settling time is problematic as the information will be spread out in time and space resulting in larger computational grids required to encapsulate the required information. Increasing the computational grid negates some of the computational savings of using the sliding window technique. For bushfire plasma this does not present much of a problem as the plasma are very heavily damped due to the very high collision frequency.

Due to numerical dispersion there is an upper limit upon how long one simulation can be run. As shown in Figure 5.7, dispersion causes the pulse to spread out in space. It is therefore important to use a higher order algorithm where possible. If longer distances are required, post-processing and reinjection of the pulse can be used to restart the simulation and make the pulse more compact. Alternatively, it can be seen from Figure 5.7(b) that the original FDTD algorithm is positively dispersive, meaning higher frequencies travel slower than lower frequencies. Also as seen in Figure 5.7(c) the FDTD(2,4) algorithm is negatively dispersive, i.e. higher frequencies travel faster than lower frequencies. By coupling these two algorithms together it would be possible to maintain the pulse shape for longer simulation distances.

SECTION 6

Numerical Experiments

In this chapter, the Finite Difference Time Domain (FDTD) method is used to explore the electromagnetic propagation in a simulated environment of the small scale fire experiments. A number of factors will be explored. Initially, fuel heap interactions will be examined, with emphasis on the fuel heap properties and sensitivity to the geometry and height. Following this, the combustion induced plasma will be considered. Different profiles are examined to understand the effects of geometry, electron density and temperature upon propagation. In conclusion, dynamics with the fuel heap and plasma will be considered together.

This portion of work hopes to explain the major features of the experimental work in Section 2. The features include, the difference between pre-burn and post-burn signal strengths, the fuel heap deterioration and its ramifications concerning masking the effects of ionisation and explain some the characteristics of increasing temperature and its relation to the electron concentration and propagation characteristics.

6.1 Simulation Parameters

The electromagnetic model is based on the dimensions from the small scale experiments. A representative model of the simulation volume is shown in Figure 6.1. The transmitter (green ball) is located at height 1.8m and slightly inside the $X = 0$ boundary. The fuel heap is the large red hemispherical object. The ground ($Z = 0$) is a perfectly electrically

conducting (PEC) plane. The PEC plane simplifies simulation and above 100MHz - 150MHz is fairly good representation of the ground (an alternative is a surface impedance model of the ground[103]). Additionally, the ground characteristics are largely unknown and are subject to change during the duration of a fire, due to heating of the ground and evaporation of water. Other boundaries of the simulation domain are truncated with a Perfectly Matched Layer (PML).

FDTD simulations produce a huge amount of data for a single simulation. To minimise the storage requirements, field monitors have been located on vertical lines. These are represented by small dark blue balls and, on the boresight of the antenna, represented by the small light blue balls. These monitors record the E_z field or a vertically oriented receiving antenna. The majority of results displayed use recorded data on the vertical line 20m from the transmitter.

6.1.1 Excitation

To excite the FDTD grid a space-time pulse is used, being a differentiated gaussian pulse in time. The differentiated pulse does not suffer from DC artifacts present in other excitation functions. Parameters have been selected to correctly excite the grid and adequately cover the frequency range of interest, as shown in Figure 6.2. The E_z field is excited to represent a vertical oriented Hertzian dipole.

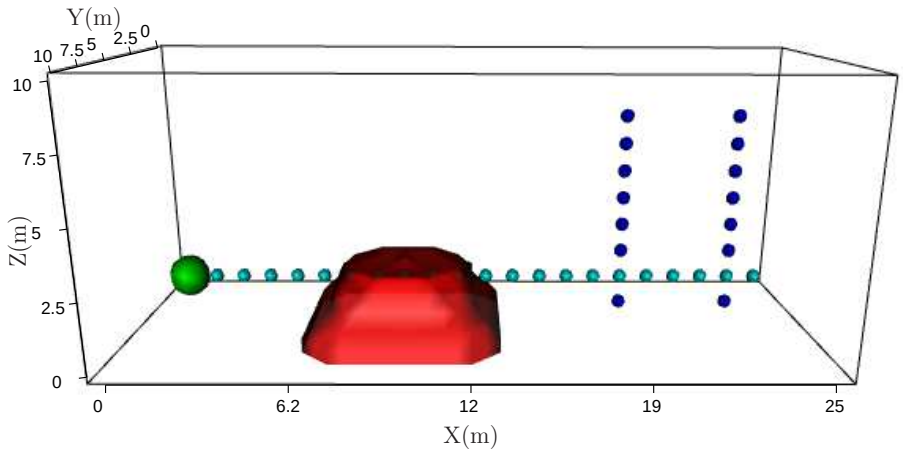

Figure 6.1: Simulation Volume - Location of Source (Green sphere), Fuel Heap (Red Hemi-sphere), Field Sensors (Small spheres)

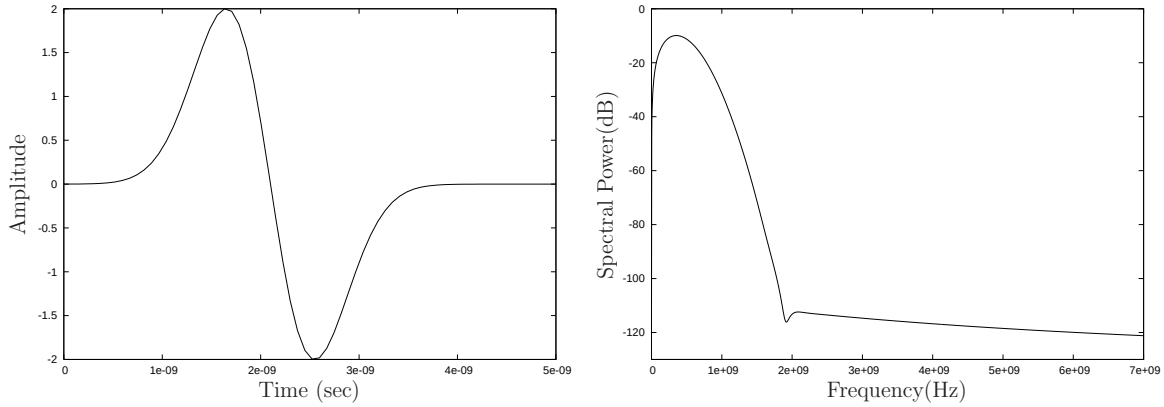

(a) Time Stimulus (b) Frequency Domain

Figure 6.2: Excitation Function

$$S(x,y,z) = e^{-\left(\frac{y-\mu_y}{2\sigma_y}\right)^2} \cdot e^{-\left(\frac{z-\mu_z}{2\sigma_z}\right)^2} \tag{6.1}$$

In the spatial domain, the initial excitation of the FDTD grid was chosen to be a 2D gaussian surface. The mathematical expression is shown in Equation 6.1, where $\mu_y = 5m$, $\sigma_y = 0.05$, $\mu_z = 2m$ and $\sigma_z = 0.1$. An excitation surface is needed to ensure an equivalent excitation occurs as the grid resolutions changes. It is hard to include the antenna pattern in a time domain simulation because it changes with frequency. Instead, a small point source has been used to investigate the propagation effects. A smooth function, such as a Gaussian surface, has been used here as it meets the criteria of excitation (see Figure 6.3).

6.1.2 Grid Resolution

As the grid resolution increases, numerical dispersion decreases. However, the resolution cannot be increased without limit since rounding errors will eventually dominate (due to the finite number of bits in computer number representation) and computational resources are limited. FDTD is a time domain technique and because of this, convergence of a solution always occurs for lower frequencies prior to higher frequencies. This is due to the number of cells in the discretisation grid per wavelength. Generally, a good rule of thumb is to choose a grid resolution such that $\Delta_{x,y,z}$ is approximately $\lambda/10$ for the highest frequency of interest. Figure 6.4 is a plot of the propagation factor at 20m from the source for different grid resolutions.

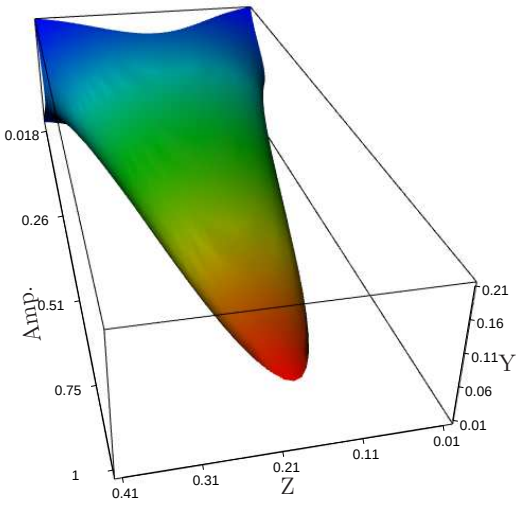

Figure 6.3: Spatial Excitation

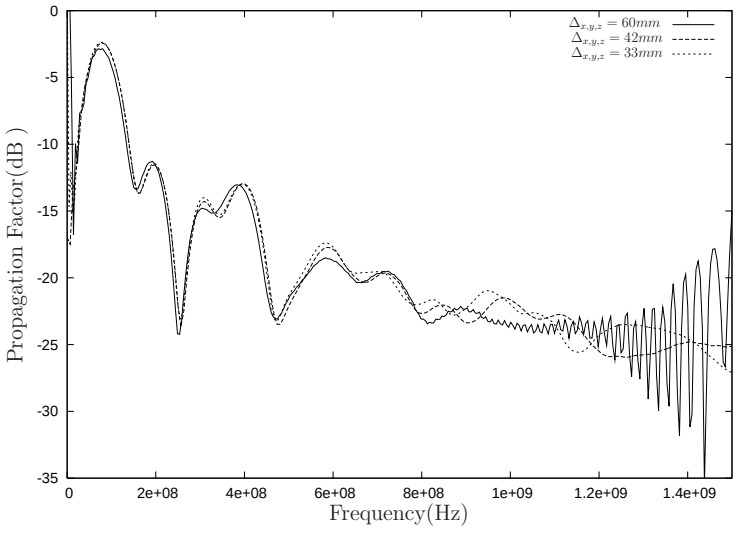

Figure 6.4: Propagation Factor for different discretisation schemes (at 20m from source, height 2m)

As can be seen the lower frequencies maintain a good grouping of consistency in the results, while the higher frequencies show less consistency. When $\Delta_{x,y,z} = 60mm$, the simulation loses representation of the propagation factor above 1GHz with the introduction of numerical inconsistency in the power profile. When $\Delta_{x,y,z} = 42mm$ and $\Delta_{x,y,z} = 33mm$, we begin to see strong convergence up to 800MHz where each profile is within a 1dB of each other. As we increase the grid resolution we find the features of the spectrum become compressed at higher frequencies. This compression is due to numerical dispersion, which introduces a time delay as the pulse spreads out. What is interesting about this is that propagation characteristics above 1GHz are still evident when $\Delta_{x,y,z} = 42mm$ and $\Delta_{x,y,z} = 33mm$, but the profile has shifted in frequency. For our study of propagation, it is important to keep in mind that at higher frequencies the features are present but frequency accuracy diminishes.

Convergence testing aids in choosing an appropriate simulation accuracy. If the discretisation of the simulation is too small, the simulation becomes computationally expensive. If the step size becomes too large, accuracy is sacrificed. We will revisit convergence when we consider plasma materials. For the fuel heap simulations reasonable accuracy can be achieved for $\Delta_{x,y,z} = 42mm$ grid resolution.

6.1.3 Propagation Factor

As we change the environment and examine the change in propagation, we examine this in terms of relative propagation loss. We use the propagation factor, which is the ratio of simulated power loss over that in free space and expressed in decibels (dB).

$$PF = 20 \log_{10} \left(\frac{\mid E_{sim}(f) \mid}{\mid E_{free}(f) \mid} \right) \tag{6.2}$$

To perform this calculation two simulations are required. One is the free space reference ($E_{free}(f)$), which is the same in terms of excitation and grid resolution but with Perfectly Matched Layer for all boundaries. The second simulation ($E_{sim}(f)$) is actually the environment under investigation. All plots included here are the propagation factor, unless specified otherwise.

6.2 Fuel Heap

The fuel heap is a major aspect of the small scale fires. To model its shape a simple hemisphere has been used.

6.2.1 Ulaby and El-Rayes Vegetation Model

To model the dielectric of the fuel heaps the Ulaby and El-Rayes model is used [31][118]. The dielectric properties of vegetation and wood is a function of the free water, bound water and residual permittivity in the plant. Bound water refers to water molecules that are tightly held to organic compounds by physical forces and free water refers to water molecules that can move within the material with relative ease. Due to the dependence of water, the dielectric properties of vegetation are dispersive. Ulaby and El-Rayes model has been found to be valid from 200MHz to 20GHz [118].

$$\varepsilon_r(f) = \varepsilon_{res} + v_f\varepsilon_f(f) + v_b\varepsilon_b(f) \tag{6.3}$$

where ε_{res} is the relative permittivity for the residual component, ε_f is the relative permittivity of the free water component, ε_b for bound water, v_f is the volume fraction of free water and v_b is the volume fraction for bound water. The relative permittivity for the free and bound water components is as follows:

$$\varepsilon_f(f) = 4.9 + \frac{75}{1 + if/18} - i\frac{18\sigma_S}{f} \tag{6.4}$$

$$\varepsilon_b(f) = 2.9 + \frac{55}{1 + \sqrt{if/0.18}} \tag{6.5}$$

$$\tag{6.6}$$

where f is in gigahertz, σ_S is the ionic conductivity of the free water ($\sigma_S \cong 0.16S - 0.0013S^2\ S \cdot m^{-1}$ and S is the salinity assumed to be $S \leq 10\%_\circ$). It is difficult to estimate the volume fraction for the free (v_f) and bound (v_b) water as it changes with plant type, season, water availability and forest distribution. A relation of best fit from vegetation data has been provided in the model by the following set of equations[118].

$$\varepsilon_{res} = 1.7 - 0.74M_g + 6.16M_g^2 \tag{6.7}$$

$$v_f = M_g\,(0.55M_g - 0.076) \tag{6.8}$$

$$v_b = 4.64\frac{M_g^2}{1 + 7.36M_g^2}\sigma_S = 1.27 \tag{6.9}$$

where M_g is the gravimetric moisture content ($Mass_{water}/Mass_{solids}$). Dielectric characteristics for varying gravimetric moisture content (M_g) is shown in Figure 6.5 for high moisture contents ($M_g = 0.7$) to low moisture contents ($M_g = 0.1$). In Figure 6.5 ε' is the real component of the complex relative permittivity and ε'' is the imaginary component of the complex relative permittivity.

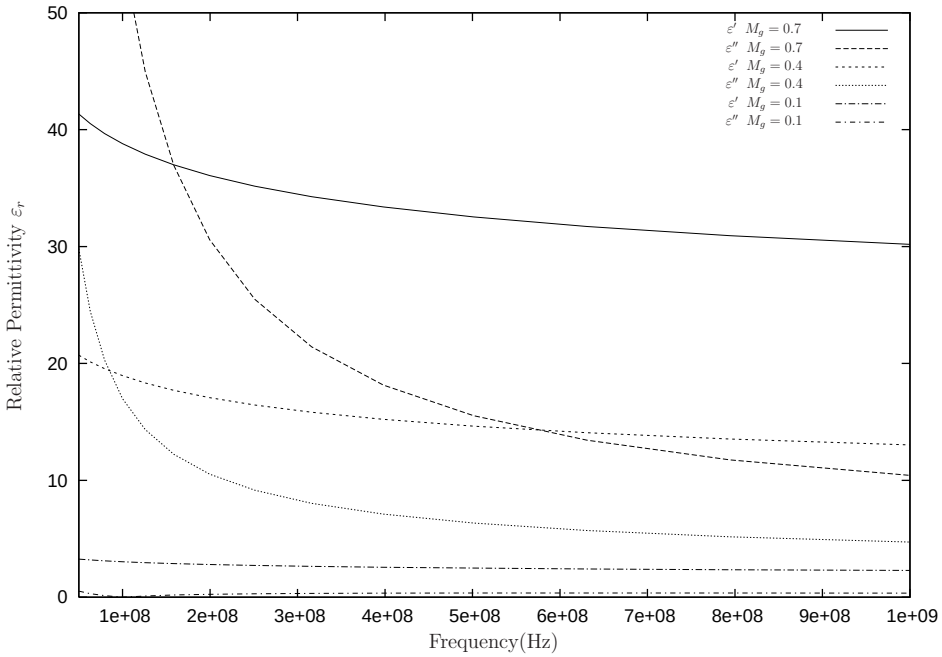

Figure 6.5: Vegetation Dielectric ε' and ε''

As the moisture content increases the dielectric properties become more dispersive. A number of options are available when using this dual-dispersion model for vegetation in a time domain algorithm. One option is to use auxiliary equations, similar to the cold plasma, to simulate the polarisation current of the free water and the polarisation current of the bound water. This results in an exact model of the dielectric. Alternatively, as an approximation one can use a constant dielectric value in the middle of the frequency band of interest and approximate the dielectric properties from the simulation [103]. If greater accuracy is required one can reduce the bandwidth of interest and increase the number of simulations to cover the entire frequency range.

Here, an approximation of the dielectric is sufficient, particularly because as the moisture level reduces the dielectric properties of the vegetation become more uniform in frequency. Low moisture content is expected because a lot of the fire experiments used

fallen branches as fuel and took place after a period of hot weather. In addition to this, as the fire begins the fuel will quickly dry out leaving extremely low moisture content. An appreciation for the changes in propagation due to moisture can be attained from the propagation calculation of Figures 6.6-6.8 for a fuel heap of height 3m .

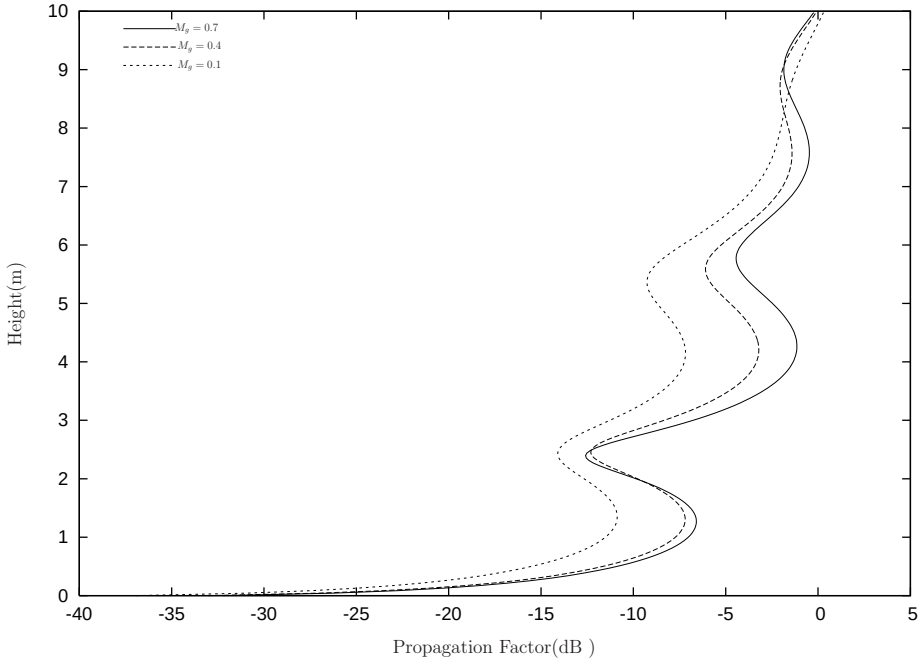

Figure 6.6: Propagation Factor vs Fuel Heap Moisture (Height 3m) - 180MHz

As the moisture content changes the same propagation profile is coming through for all frequencies. The sensitivity of the fuel heap reduces with frequency. In the two lower frequencies the nulls of the propagation remain in the same position and only the peaks increase or decrease. The effect of the fuel heap drying out is to fill in the nulls and decrease the intensity of the peaks. Choosing a lower moisture content will help see more clearly the effect of the fuel heap without the masking effect of interference. Above $M_g = 0.4$, the propagation characteristics are relatively stable because the fuel heap exhibits greater loss and dielectric properties.

With a representative model of the dielectric properties and an understanding of the propagation characteristics, we will now only consider fuel heaps with a moisture content of $M_g = 0.1$. If an adjustment needs to be made for a change in moisture content one can refer to the figures in this section as a guide.

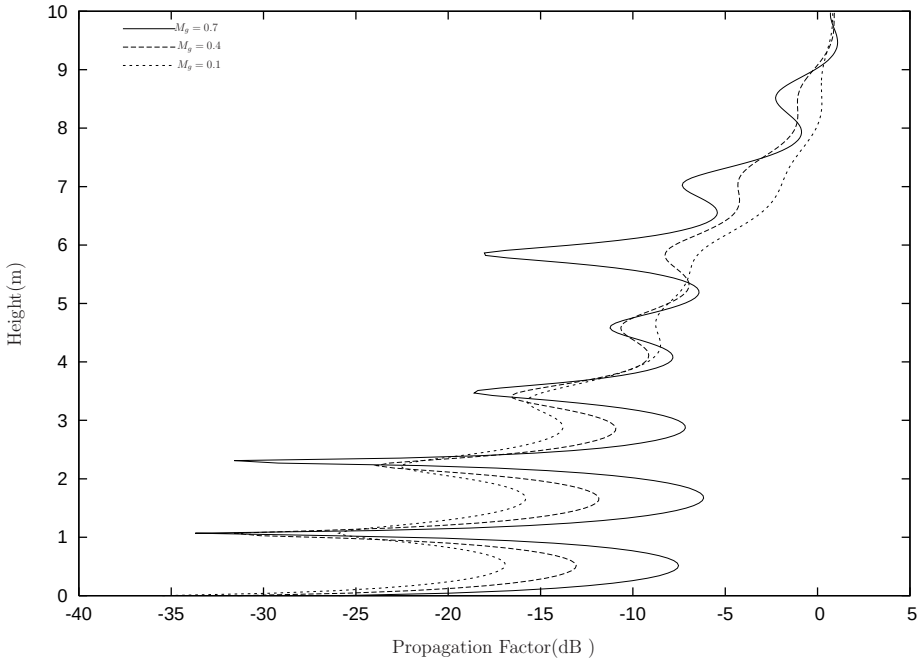

Figure 6.7: Propagation Factor vs Fuel Heap Moisture (Height 3m) - 450MHz

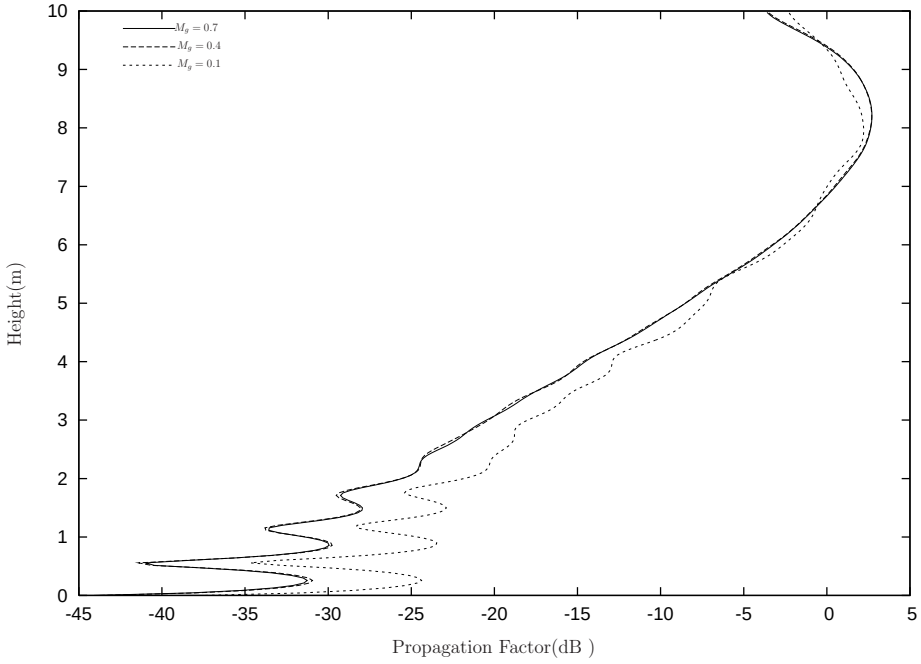

Figure 6.8: Propagation Factor vs Fuel Heap Moisture (Height 3m) - 950MHz

6.2.2 Varying Fuel Height

When discussing the experimental findings of Section 2 it was stipulated that the dynamics of the fuel heap mask the influence of the fire on the attenuation of the radio signal. Later, it was demonstrated with simple diffraction calculations (see Section 4.3) that as the fuel heap reduces the signal strength increases. Here, we explore the same issue but use electromagnetic modelling of the fuel heap and geometry to explore the influence of the fuel heap with variation in height and frequency. The representation of the fuel heap is shown in Figure 6.9. A cylinder representation is also included in Figure 6.10 for comparison.

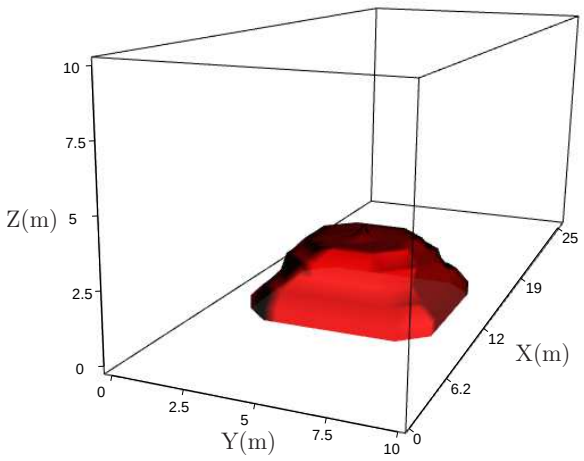

Figure 6.9: Fuel Heap representation - Height 3m . For simulation geometry see Section 6.1, and Figure 6.1

These three comparisons for the fuel cylinder and fuel heap profiles show that little is gained by using 3D geometry for high frequencies but as the frequency decreases 3D geometry becomes quite important. This is attributed to diffraction and its importance as the wavelength becomes longer. Higher frequencies are more disrupted by the fuel heap when compared to the 180MHz plots. As the fuel heap height becomes comparable to wavelength (λ) some deviation is shown in the simulation data. Compared to the diffraction calculations (repeated in Figure 6.17(a)-6.17(c)), the presence of the fuel heap is less obstructive to the signal, particularly for the 450MHz and 180MHz plots. The

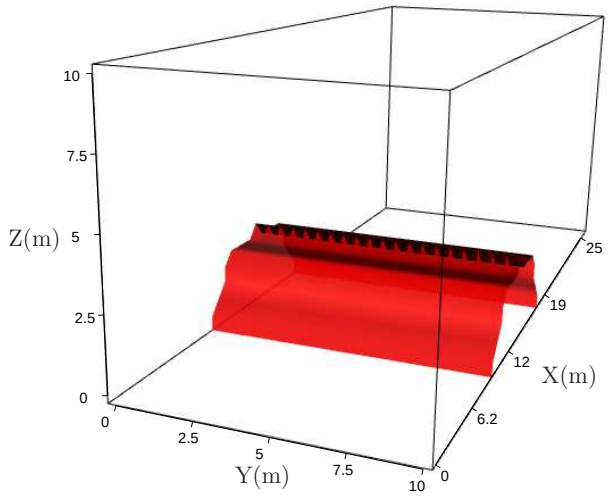

Figure 6.10: Fuel Cylinder representation - Height 3m . For simulation geometry See Section 6.1 and Figure 6.1

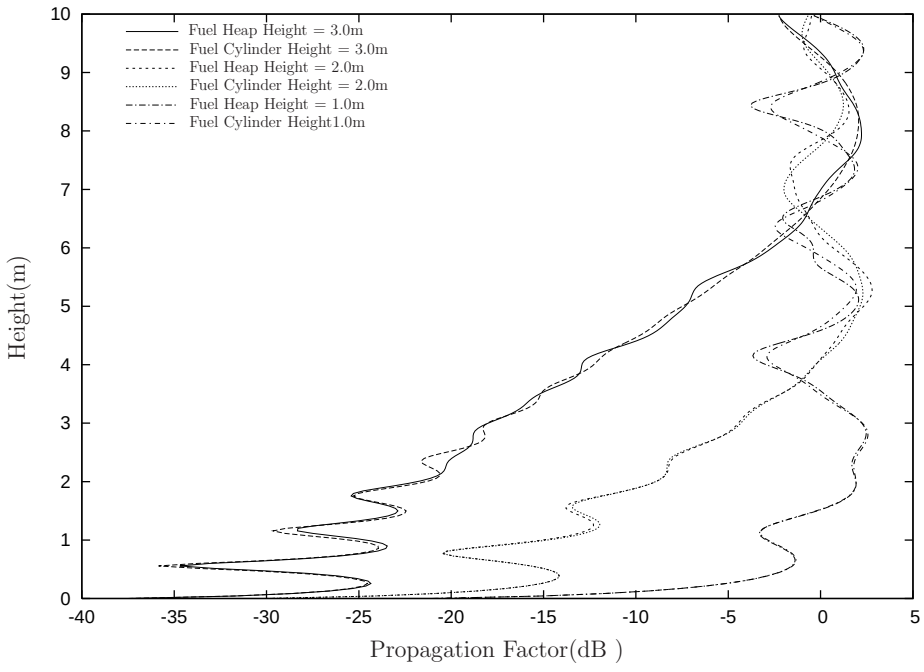

Figure 6.11: Propagation Factor for Fuel Heap and Cylinder Profiles with varying height - 950MHz (20m from Transmitter)

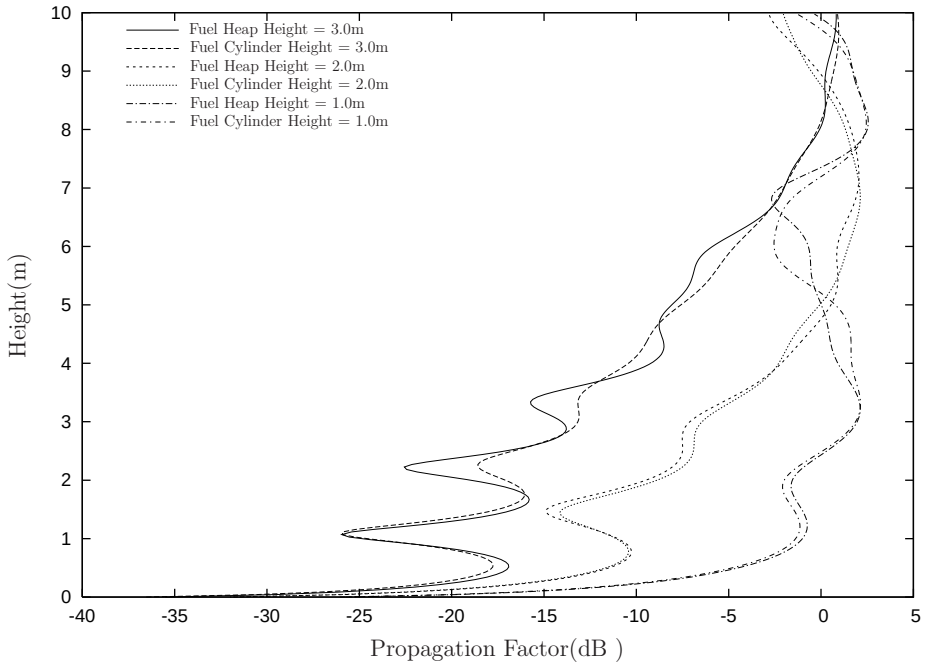

Figure 6.12: Propagation Factor for Fuel Heap and Cylinder Profiles with varying height - 450MHz (20m from Transmitter)

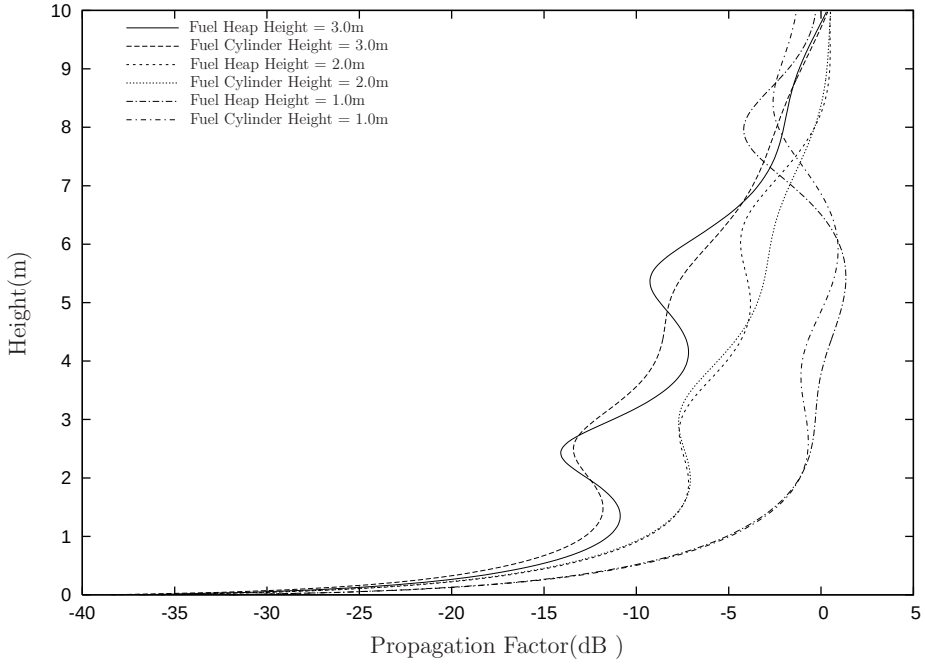

Figure 6.13: Propagation Factor for Fuel Heap and Cylinder Profiles with varying height - 180MHz (20m from Transmitter)

introduction of a lossy dielectric, as opposed to a perfectly absorbing screen, and a ground plane account for the differences between calculations and these simulations.

Varying the fuel height brings up a number of interesting features. Plots have been prepared for frequencies 950MHz (see Figure 6.14), 450MHz (Figure 6.15) and 180MHz (Figure 6.16). All three plots show that propagation is affected both below the fuel heap height and above. This is consistent with the knife-edge diffraction plots. The 950MHz traces show a consistent increase in relative signal strength as the fuel height reduces: this strongly agrees with the diffraction plots.

The 450MHz traces also show a consistent increase in the signal strength as the fuel heap decreases. An interesting feature is observed around the receiver height of 1.8m where the movement of the fuel heap causes a peak in signal trough to become a null. This transformation of peak to null poses an interesting observation over time. The signal strength at the receiver will remain quite constant as the fuel heap decreases. Once the fuel heap reduces below 2.0m a sharp increase in the signal strength will be experienced. The construction of nulls and peaks is due to the presence of a PEC ground plane.

The 180MHz traces show a greater departure from the knife-edge diffraction plots. At the lower frequencies the results are no longer consistent with knife-edge diffraction. This indicates a lack of sensitivity to disturbances caused by the fuel heap. This trend in frequency is an important element in understanding the difference in pre-burn and post-burn signal strengths.

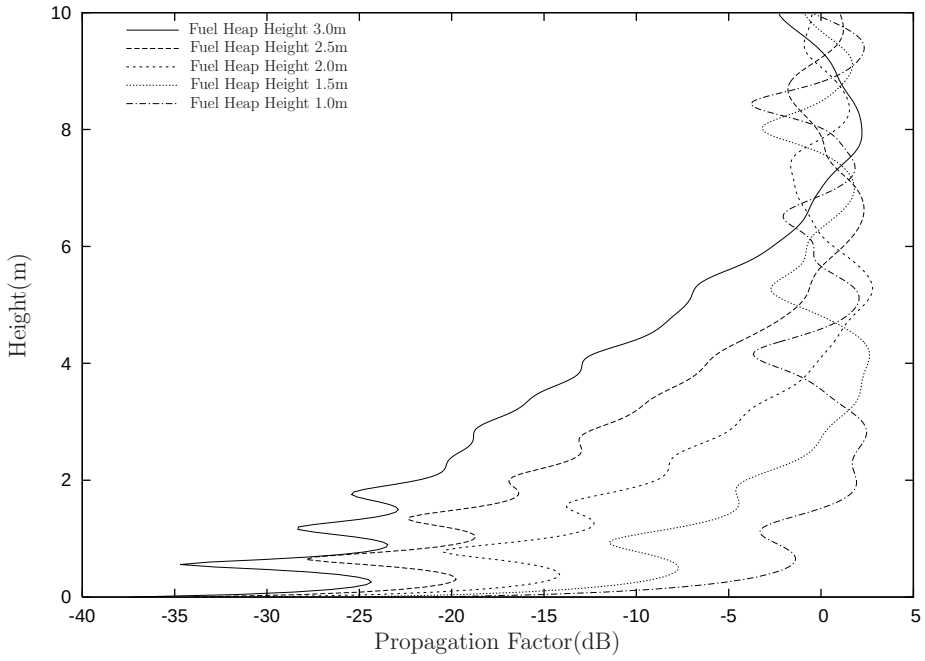

Figure 6.14: Propagation Factor and sensitivity to varying Fuel Heap Height - 950MHz (20m from Transmitter)

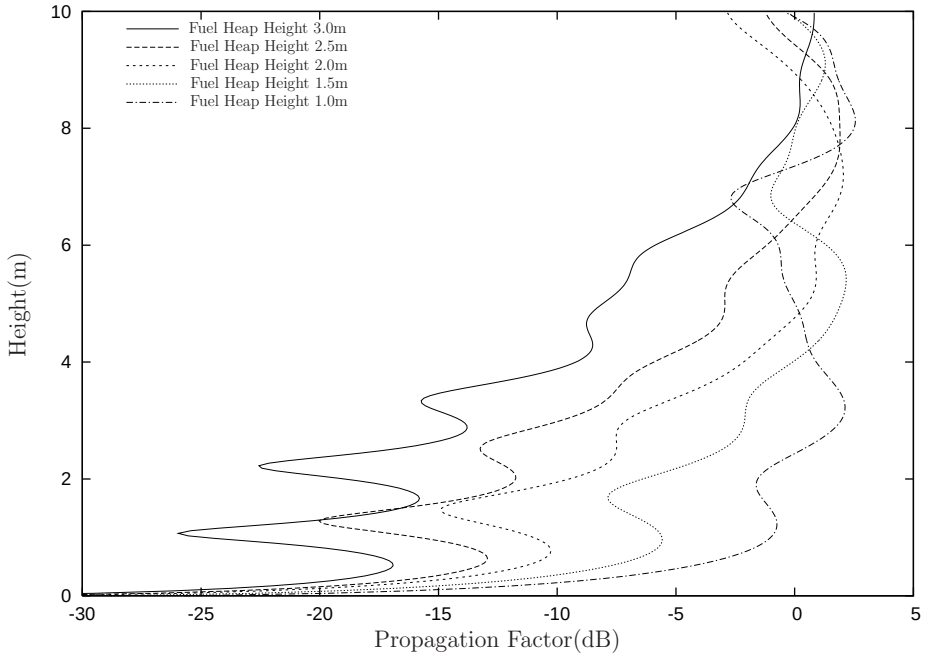

Figure 6.15: Propagation Factor and sensitivity to varying Fuel Heap Height - 450MHz (20m from Transmitter)

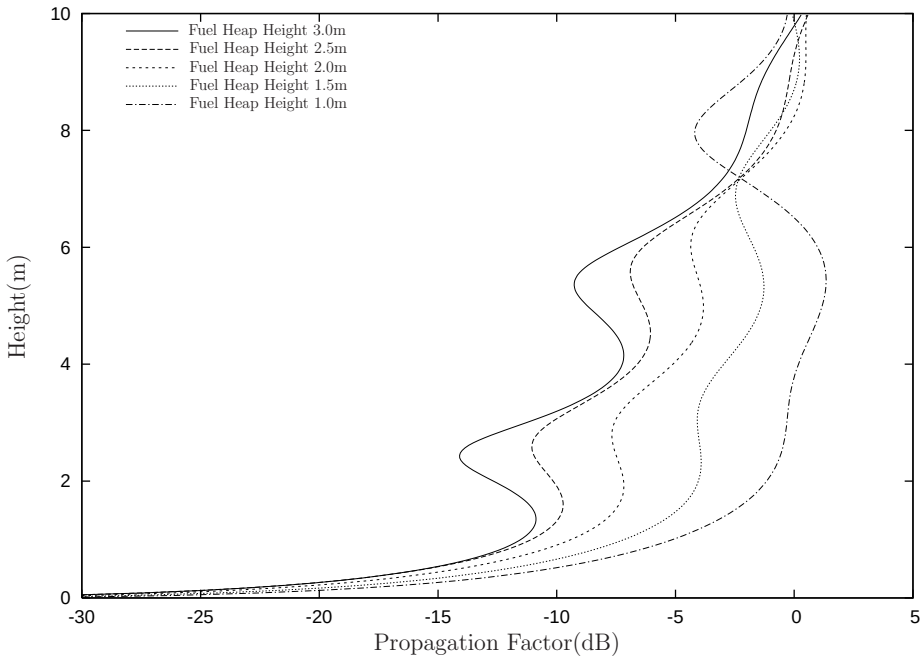

Figure 6.16: Propagation Factor and sensitivity to varying Fuel Heap Height - 180MHz (20m from Transmitter)

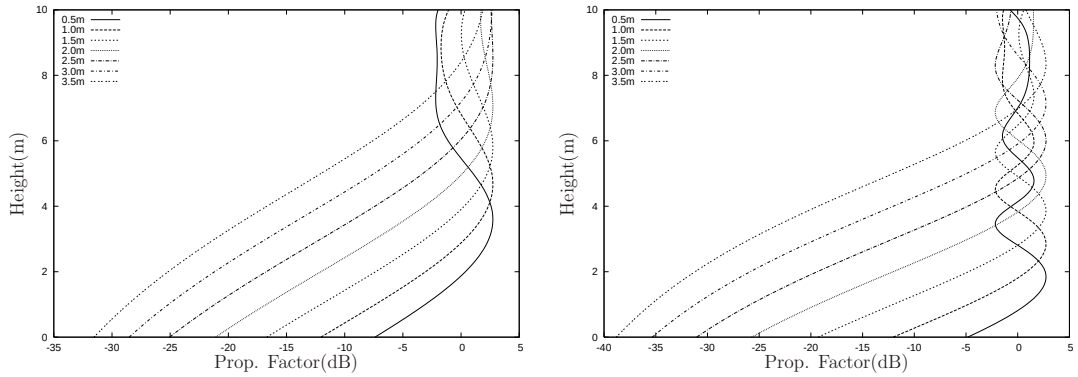

(a) 180MHz

(b) 450MHz

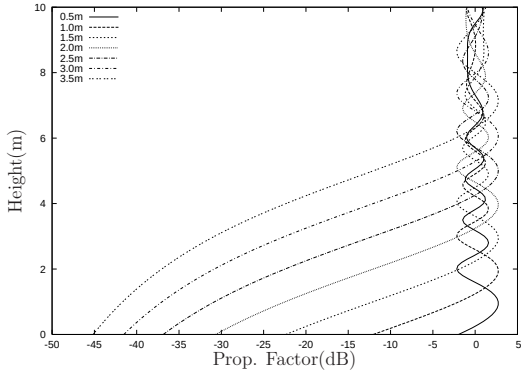

(c) 950MHz

Figure 6.17: Diffraction Plots: Propagation Factor of varying obstruction height - Taken from Section 4.3

6.3 Combustion Induced Plasma

The creation of a plasma of free electrons by the combustion process has been highlighted as a major factor that affects radio propagation in fire environments. Having developed a means to model the combustion induced plasma and provided simple propagation calculations, we now explore the area with a three dimensional FDTD method. Three different profiles will be examined in order to investigate different aspects of the propagation. The first is a vertical column of plasma that has no effective variation along the vertical axis (Z). The column profile is helpful for investigating the effects of propagation around the fire (i.e. propagation effects in the X-Y plane). The next plasma profile will consider variations in height using a representative mathematical model of the fire that introduces dependency on the temperature. At this point we are only considering the effects of the combustion plasma with no fuel heap present. The mathematical model then takes us to the next stage of considering variation in the height of the plasma and connecting the plasma density to the temperature of a fire. The final profile will be generated using a FDS simulation of the fire. The FDS profile is the most realistic model that will be presented here.

In any numerical simulation it is important to assess the convergence of the results and so in Figure 6.18 we present the results of propagation simulations for the column profile for two different discretisations (the simulations will be more thoroughly discussed in the next section). Slight deviation starts to occur above 600MHz and becomes significant above 1GHz . Results of higher frequencies would be desirable, but unfortunately computer memory limitations prevent simulations of higher resolution. Plasma simulation used here is particularly problematic as the plasma properties substantially vary over the simulation volume. This variation requires a substantial amount of material information to be held in computer memory during simulation.

6.3.1 Column Profile

The first plasma profile that will be considered is a vertical column. A vertical column is one of the simplest structures, which encapsulates the flame structure. It is a good starting point as it has no height variation in the electron density profile. The lack of vertical

variation helps transition our understanding from simplistic propagation modelling (see Section 4.2) to the more sophisticated 3D FDTD simulation shown here.

The column profile is a vertical column that varies in electron density according to a sinusoidal function in the X and Y direction. The maximum electron density is found in the centre of the column ($(X, Y) = (10m, 5m)$) and the period of the sinusoid is 6m . Various representations are shown in Figure 6.19. Various Column Electron density Profiles (CEP) are utilised here and a summary of plasma and propagation characteristics are collated in Table 6.1. The collision frequency for each profile is constant throughout entire simulation volume. The simple estimate of propagation loss are results from Section 4.2. Little variation in attenuation was estimated over the three frequencies and attenuation was considered broadband. For the FDTD simulations, the loss is calculated relative to the ground reference in each plot.

The introduction of three dimensional geometry in the FDTD simulations produces some interesting results. Besides direct line of sight propagation through the plasma, there is now the possibility of diffraction around the plasma column. Propagation is least for 450MHz , followed by 180MHz and then 950MHz . This set of simulations show attenuation is dependent on the wavelength due to the geometry of the plasma.

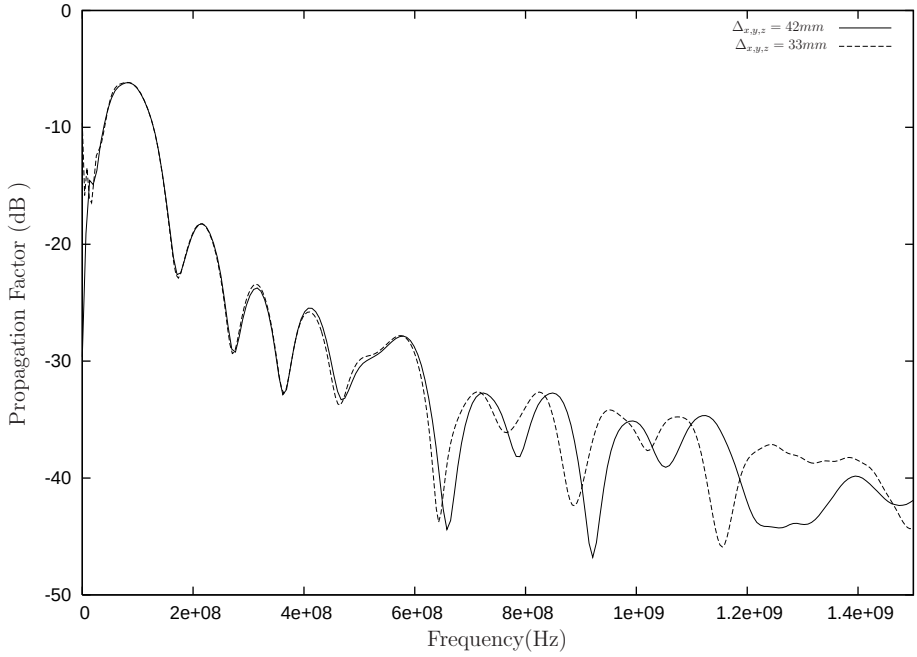

Figure 6.18: Grid Resolution - Column Plasma profile 20m from source at height 2m

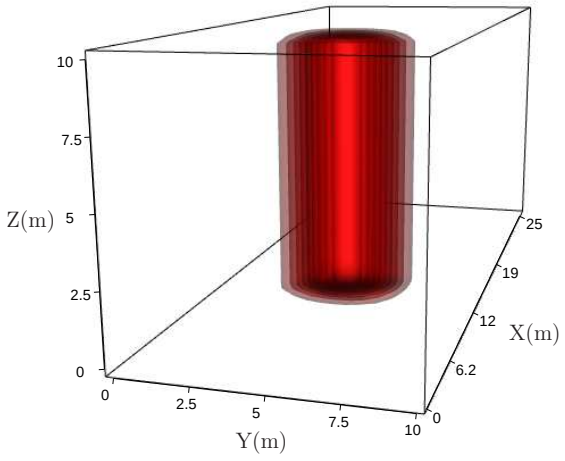

(a) Volume

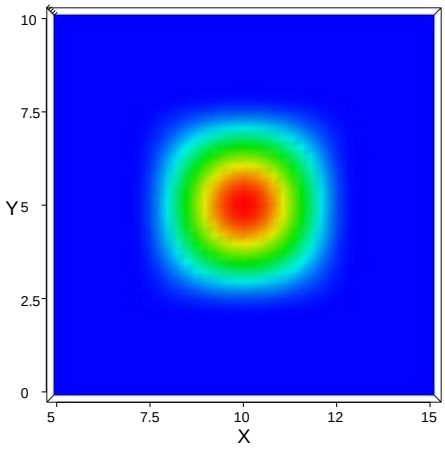

(b) X-Y Plane

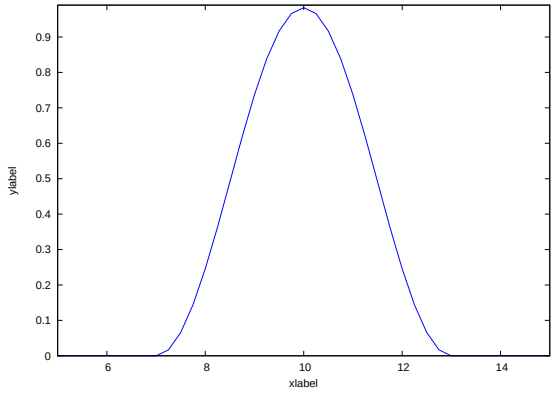

(c) X Line

Figure 6.19: Column Plasma Profile - Various geometries

Parameters	CEP 1	CEP 2	CEP 3	CEP 4
$N_{e_{max}}$ (m^{-3})	1×10^{16}	1×10^{16}	2×10^{16}	2×10^{16}
ν_{eff} (Hz)	10^{11}	10^{10}	10^{11}	10^{10}
Simple Estimated Loss[a]	13.7dB	112dB	27.1dB	231dB
FDTD 180MHz Loss[b]	10.5dB	17.3dB	14.1dB	18.9dB
FDTD 450MHz Loss	11.3dB	30.2dB	21.5dB	28.8dB
FDTD 950MHz Loss	6.59dB	9.95dB	8.36dB	12.1dB

Table 6.1: Column Plasma Profile Characteristics

[a]see Section 4.2

[b]Taken 20m from transmitter at height 2m

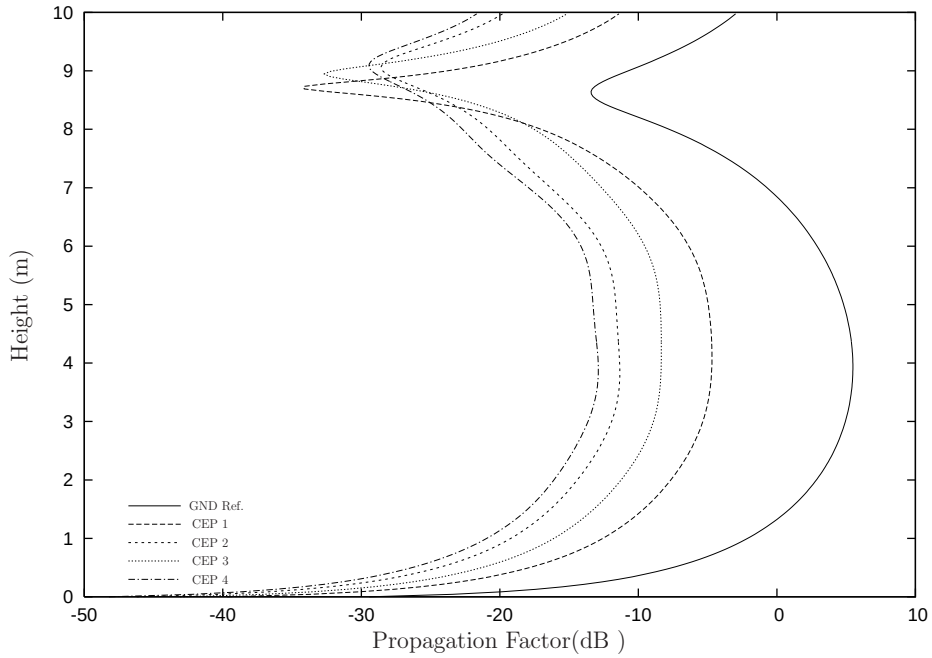

Figure 6.20: Propagation Factor versus Height for Column Plasma Profiles (See Table 6.1) - 180MHz (20m from Transmitter)

A reduction in attenuation is expected due to the introduction of diffraction around the column. For 450MHz the results do show some correlation with the simple estimates propagation loss, particularly for the high collision frequency profiles (CEP 1, CEP 3). For the low collision profiles (CEP 2, CEP 4) attenuation is much lower than the estimated 120dB . As the plasma size reduces, diffraction will become a more important propagation mechanism. Therefore, a maximum amount of loss will be reached where the plasma is totally absorbing and energy is propagated purely by diffraction.

A number of plots showing the variation in propagation factor with height have been prepared for the three frequencies of interest in Figures 6.20- 6.22. The 180MHz and 450MHz traces both show consistent attenuation at every height. The ground interference pattern is maintained, though the difference between peaks and troughs diminishes. For the low collision frequency profiles (CEP 2, CEP 4) the change in electron density shows little increase in attenuation; this is despite an expected increase in energy absorption by the plasma. In fact, for the 450MHz traces there is hardly any difference in the low collision frequency profiles.

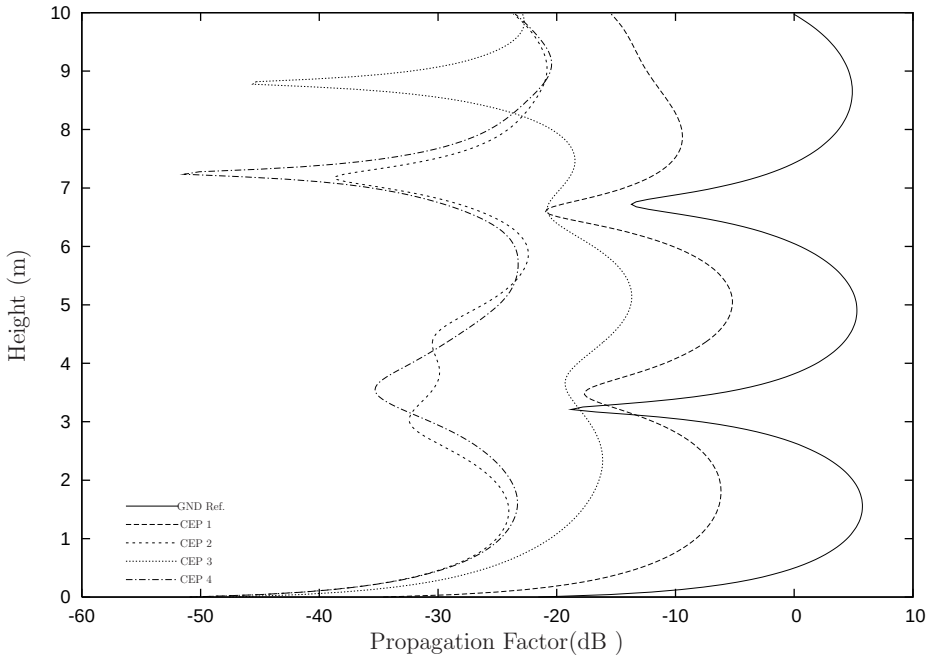

Figure 6.21: Propagation Factor versus Height for Column Profiles (See Table 6.1) - 450MHz (20m from Transmitter)

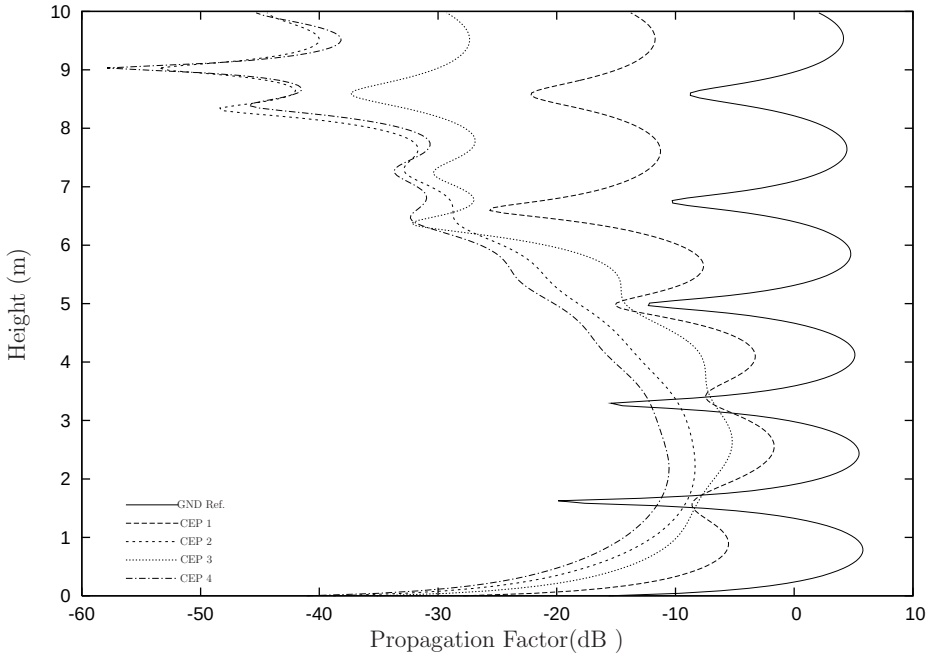

Figure 6.22: Propagation Factor versus Height for Column Plasma Profiles (See Table 6.1) - 950MHz (20m from Transmitter)

The 950MHz plots show strong attenuation at high heights but relatively poor attenuation at low heights. The propagation is obviously becoming more complex. A contributor is the position of the transmitter source and its proximity to the ground. At low heights stronger signal levels are expected from the direct and ground reflected paths. At higher heights reduced signal strength is expected due to the angle of transmission through the plasma, hence a longer path for plasma effects to accumulate.

It is important to note the ground reflection pattern for the 950MHz plot. The rapid changing of the signal strength due to the ground reflection interference increases the complexity of the height profile. In this example, if a receiver exists in the 1.5m null of the ground reflection pattern it will actually experience a rapid rise in signal strength at the initial establishment of such a plasma profile. The plasma disrupts the ground interference pattern and allows more energy into the null. This is counter-intuitive and helps illustrate the increase in complexity of propagation at higher frequencies.

Height Variation

The temperature and FDS plasma models in the next section introduce variation in the plasma profile as a function of Z or height. In preparation, we will examine a variation in the starting height of the plasma column. Profile, CEP 1, from Table 6.1 will start as different heights, as shown in Table 6.2. An illustration is shown in Figure 6.23.

Profile Name	**Start Height**
CEP 1-0m	0m
CEP 1-3m	3m
CEP 1-2m	2m
CEP 1-1m	1m

Table 6.2: Column Electron density Plasma with variation in starting height

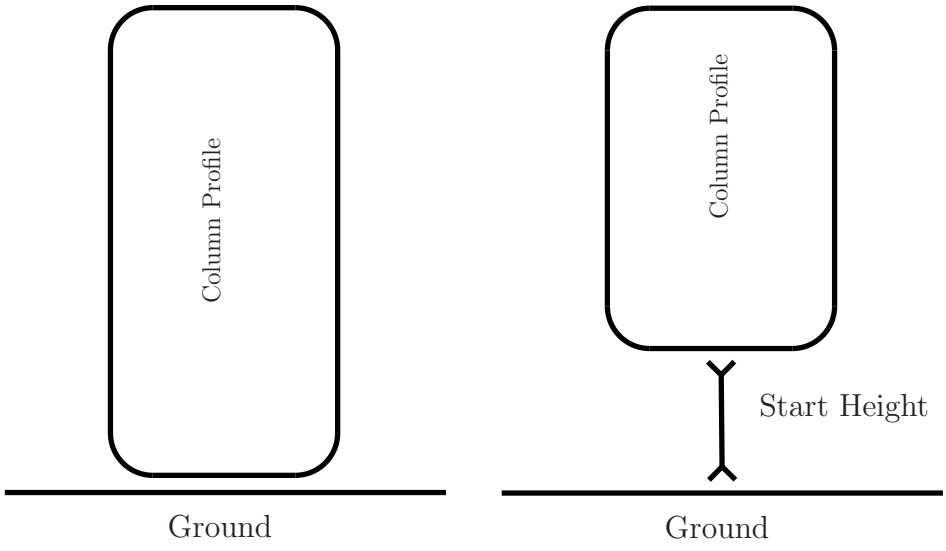

Figure 6.23: Illustration of the starting height of the column, examining the effect of the ground reflection propagation path (See Table 6.2)

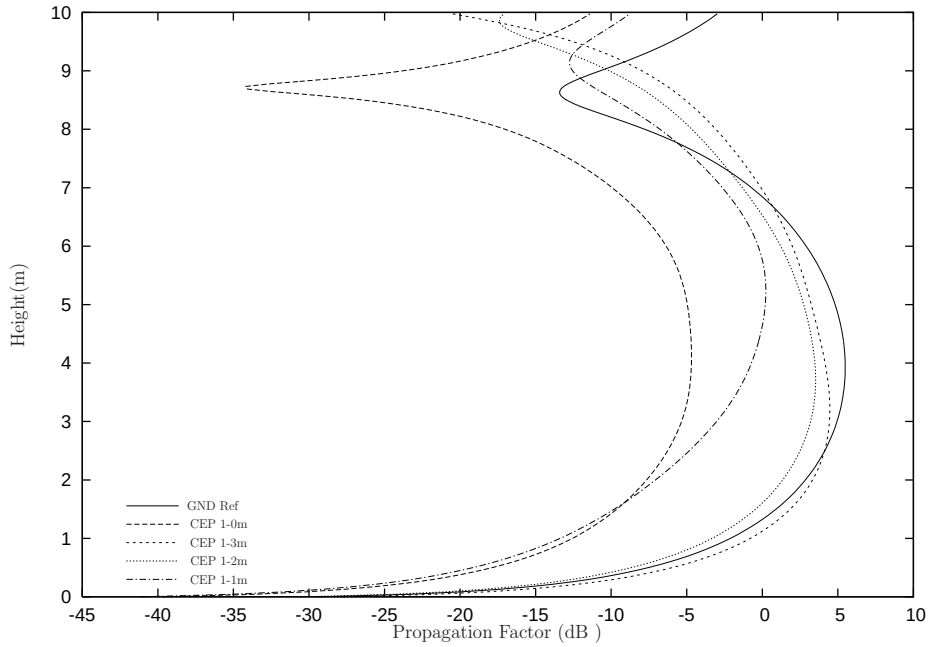

Figure 6.24: Propagation Factor for a Plasma Column with varying starting height - 180MHz (20m from Transmitter)

Quite obviously, as we increase the height at which the plasma begins, a strong propagation path is introduced at low heights. As the starting height of the plasma increases, the propagation factor tends toward the reference ground solution.

The addition of the fuel heap will reduce this ground reflected propagation path and so this effect is indicative of the fuel heap dynamics.

6.3.2 Temperature Profiles

The column profile above consisted of an arbitrary simplistic electron profile and was not related to the underlying temperature profile in a real fire. In this section, we use temperature profiles, derived from fire models, to explore the propagation characteristics in the small scale fire experiments (See Chapter 2). From the experimental work there is very little information regarding the maximum temperature and the temperature profile over the fire. Fire modelling has been used to fill this gap in information. However, there are a number of assumptions and simplifications made to produce those models. As a result of the unknowns, the information presented here is representative, but it is expected

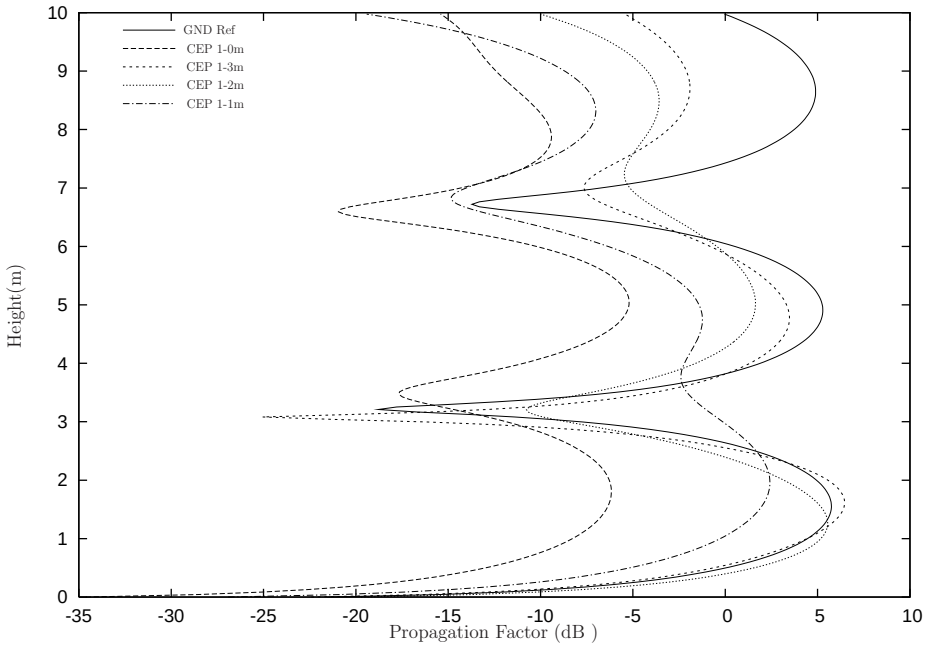

Figure 6.25: Propagation Factor for a Plasma Column with varying starting height - 450MHz (20m from Transmitter)

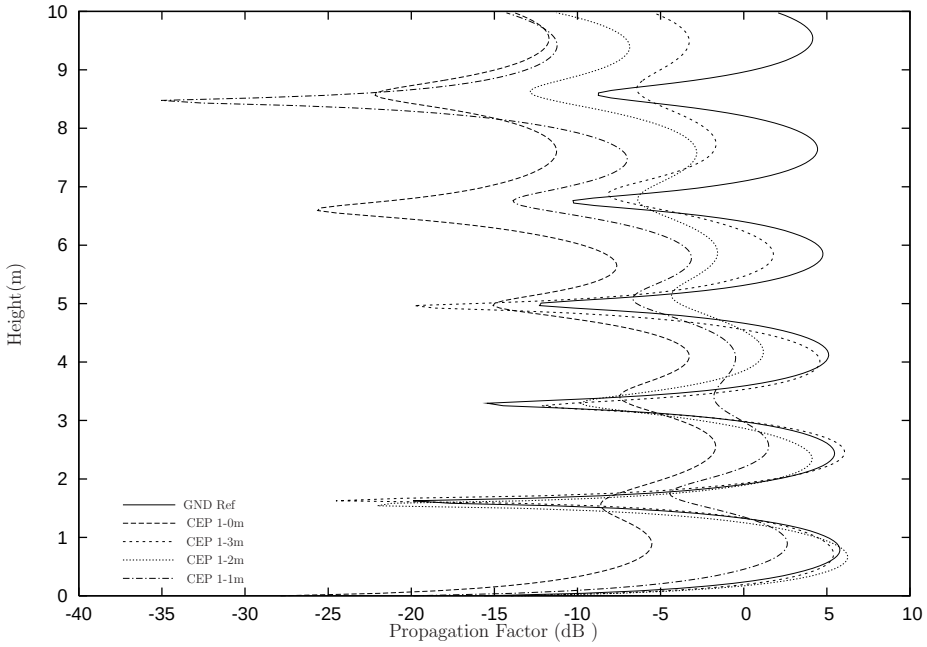

Figure 6.26: Propagation Factor for a Plasma Column with varying starting Height 950MHz (20m from transmitter)

Small Scale fire Model

Temperature °K	1100	1200	1300	1400	1500	1600	1700
$N_e \times 10^{15}$ m^{-3}	0.13	0.95	5.0	21.5	75.1	225	595
Attenuation (dB m^{-1})	0.06	0.4	2.3	9.8	33.4	84	159

Bushfire Fuel Model

Temperature °K	1400	1500	1600	1700	1800	1900	2000
$N_e \times 10^{15}$ m^{-3}	0.5	1.7	5.3	14	35	73	146
Attenuation (dB m^{-1})	0.23	0.82	2.45	6.49	15.4	32.4	60.0

Table 6.3: Attenuation table [a]

[a] Attenuation Taken at mid-band $\sim$ 600MHz Data used: Plant Type - Eucalyptus Diversicolor (K 0.9%, Ca 0.82%, Mg 0.28% see Appendix), Small Scale fuel (N_{fuel} = 6mol m^{-3}), Bushfire Conditions (ρ_s = 0.049m s^{-1}, F_L = 2.68kg m^{-2}, M_{fuel} = 0.13kg)[42] , Collision Frequency ($\nu_{eff} = 1 \times 10^{11}$), Pyrolysis Conversion ($\Pi_K = 100\%, \Pi_{Ca} = 20\%, \Pi_{Mg} = 40\%$)

to encapsulate the major features of the underlying electron distribution. Where possible, electron densities will be given as they are seen as the physical cause for attenuation.

Propagation characteristics for each temperature profile will be explored by varying the maximum temperature. In some profiles, scaled temperatures are used that may seem excessive. This accentuation is simply used to study and understand the mechanisms and does not represent the temperature in a real fire. In addition, maximum electron densities will be given on the line of sight from transmitter to receiver.

Table 6.3 summarises the relationship between the maximum electron density and the temperature. This table also includes an estimate of the attenuation caused by such a plasma. As can be seen, the temperature controls the electron density created by the presence of ionisable material. The various fuel parameters have been chosen to represent the conditions of fire in our small scale experiments. In the first instance, a mathematical model of the temperature profile is used. Following this, a more realistic model based on an FDS fire simulation is given. For both temperature profiles the fuel heap has been removed. By doing this we can separate the plasma effects from the fuel heap interactions. We consider their joint effect in the following section.

Parameters	MMTP 1	MMTP 2	MMTP 3	MMTP 4
Scaled Temp.	1300°K	1500°K	1700°K	2000°K
$N_{e_{max}}$ m^{-3}	5.1×10^{15}	7.5×10^{16}	6.0×10^{17}	1.4×10^{18}
$N_{e_{max}}$ Height	4m	4m	4m	4m
$N_{e_{max}}$ at 2m	7.9×10^{13}	1.7×10^{15}	1.8×10^{16}	2.8×10^{17}
ν_{eff} (Hz)	10^{11}	10^{11}	10^{11}	10^{10}
μ_x	10	10	10	10
μ_y	5	5	5	5
μ_z	5	5	5	5
$\sigma_{x,y}$	2	2	2	2
σ_z	6.6	6.6	6.6	6.6
θ_{flare}	20	20	20	20
Loss at 2m 180MHz	0.01dB	1.17dB	4.49dB	11.7dB
Loss at 2m 450MHz	0.08dB	0.96dB	1.74dB	3.20dB
Loss at 2m 950MHz	0.01dB	0.59dB	3.22dB	4.27dB

Table 6.4: Mathematical Model Flame Temperature Plasma Profile

6.3.3 Mathematical Temperature Model

The mathematical model is a temperature profile that is abstracted from FDS data for a small scale fire. It consists of a log-normal function in the Z direction and gaussian functions in the X and Y directions. For more information review the mathematical model in Section 3.4.

Parameters for each Mathematical Model Temperature Profile (MMTP) have been summarised in Table 6.4. Included in the table is the maximum electron density for the entire volume and transmit and receiver height ($Z = 2m$). A series of plots of the three dimensional simulation volume have been provided in Figures 6.27 - 6.30. Surface contours have been taken at electron densities of 1×10^{15}m^{-3} ,5×10^{15}m^{-3} ,1×10^{16}m^{-3} ,5×10^{16}m^{-3} ,1×10^{17}m^{-3} .

The mathematical flame profile has a more complex variation in height compared to the column profile. As seen previously with the column profile, the gap between the ground and the start of the electron density will introduce a strong propagation path via

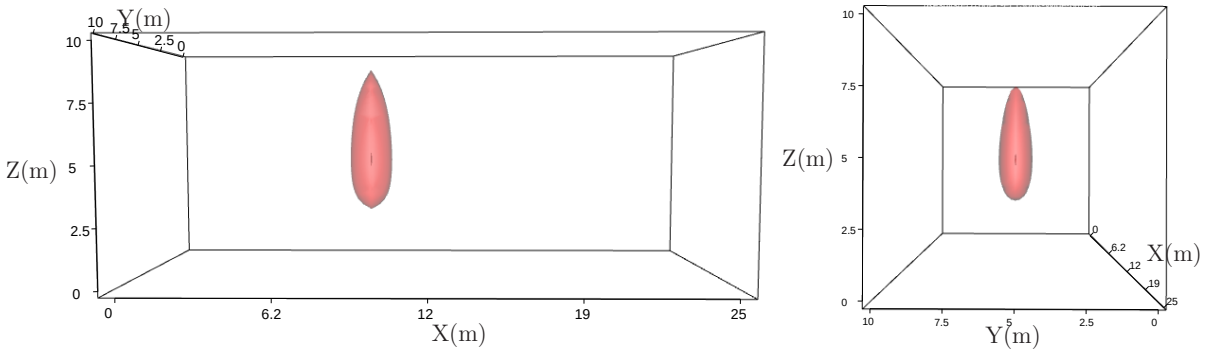

(a) 1300°K X-Z (b) 1300°K Y-Z

Figure 6.27: Electron Density - Mathematical Flame Profile 1300°K [a]

[a]Surface contours at densities $1 \times 10^{15}\mathrm{m}^{-3}$,$5 \times 10^{15}\mathrm{m}^{-3}$,$1 \times 10^{16}\mathrm{m}^{-3}$,$5 \times 10^{16}\mathrm{m}^{-3}$,$1 \times 10^{17}\mathrm{m}^{-3}$

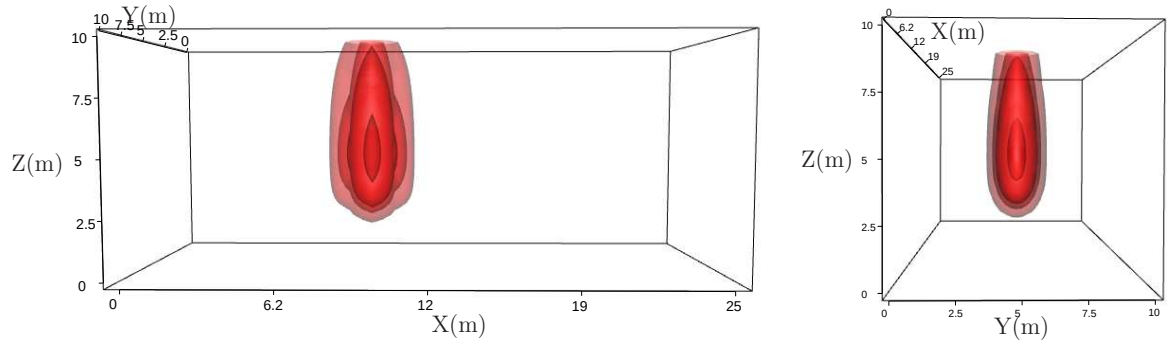

(a) 1500°K X-Z (b) 1500°K Y-Z

Figure 6.28: Electron Density - Mathematical Flame Profile 1500°K [a]

[a]Surface contours at densities $1 \times 10^{15}\mathrm{m}^{-3}$,$5 \times 10^{15}\mathrm{m}^{-3}$,$1 \times 10^{16}\mathrm{m}^{-3}$,$5 \times 10^{16}\mathrm{m}^{-3}$,$1 \times 10^{17}\mathrm{m}^{-3}$

ground reflection. Therefore, little attenuation is expected at the antenna height despite the fact that reasonable electron densities are present.

There is a great deal of similarity between Figures 6.31 - 6.33, for the mathematical temperature model, and Figures 6.20 - 6.22 for the plasma column with varying beginning height. As the starting height of the column moves closer toward the ground, the attenuation increases. For the mathematical flame profile this increase in attenuation is dependent on the scaled temperature. This demonstrates that by increasing the scaled temperature, the plasma volume increases and also blocks more of the ground reflection path. The encroachment on the ground reflection path is further illustrated in the

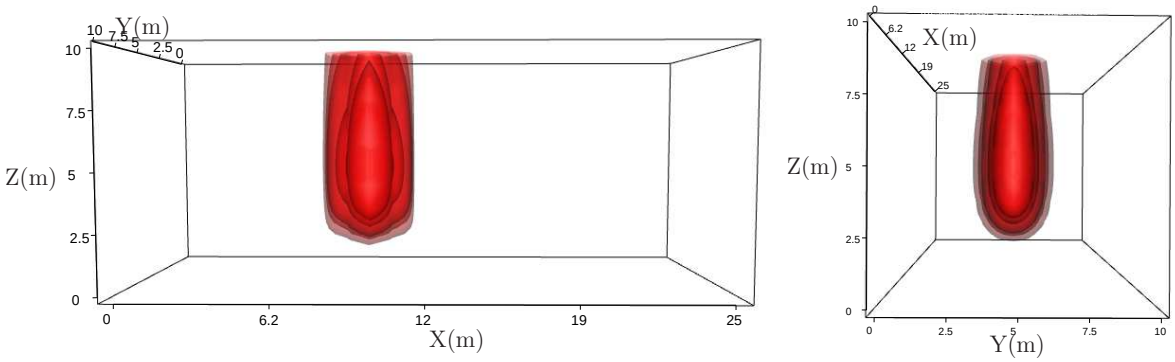

(a) 1700°K X-Z (b) 1700°K Y-Z

Figure 6.29: Electron Density - Mathematical Flame Profile 1700°K [a]

[a]Surface contours at densities $1 \times 10^{15}\mathrm{m}^{-3}$,$5 \times 10^{15}\mathrm{m}^{-3}$,$1 \times 10^{16}\mathrm{m}^{-3}$,$5 \times 10^{16}\mathrm{m}^{-3}$,$1 \times 10^{17}\mathrm{m}^{-3}$

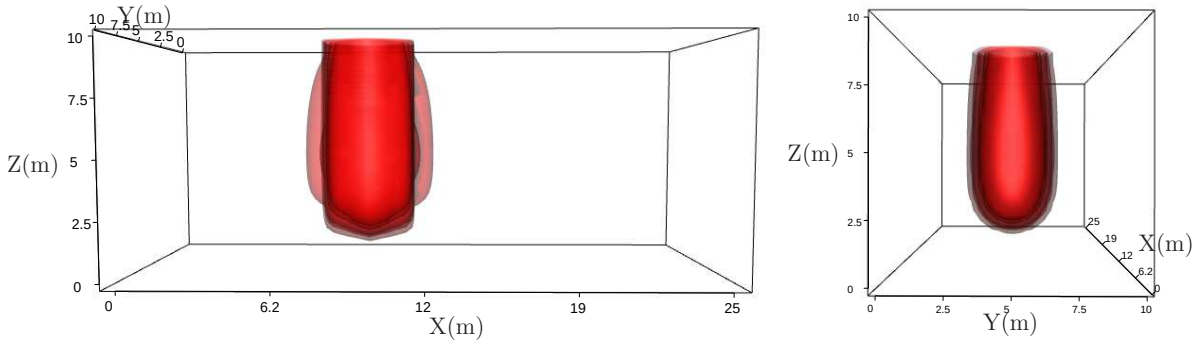

(a) 2000°K X-Z (b) 2000°K Y-Z

Figure 6.30: Mathematical Flame Profile 2000°K [a]

[a]Surface contours at densities $1 \times 10^{15}\mathrm{m}^{-3}$,$5 \times 10^{15}\mathrm{m}^{-3}$,$1 \times 10^{16}\mathrm{m}^{-3}$,$5 \times 10^{16}\mathrm{m}^{-3}$,$1 \times 10^{17}\mathrm{m}^{-3}$

movement of the position of reconstructive nulls in the pattern. The comparison with the plasma column shows that the strength of the electron density is not necessarily as important as the size of the ionised volume.

6.3.4 FDS Temperature Model

The FDS Temperature model utilises simulated data taken from a small scale fire that is defined on a mesh. Temperature data is collected on various surfaces at all time samples until 6 minutes after ignition. The data is then averaged and interpolated over

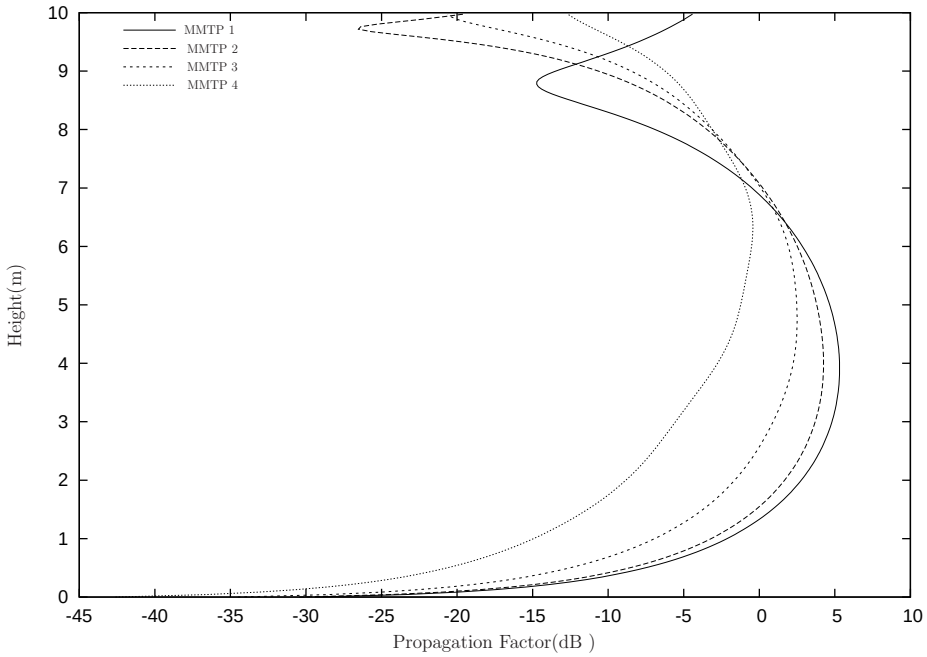

Figure 6.31: Propagation Factor using Mathematical Flame Profile (See Table 6.4) - 180MHz (20m from transmitter)

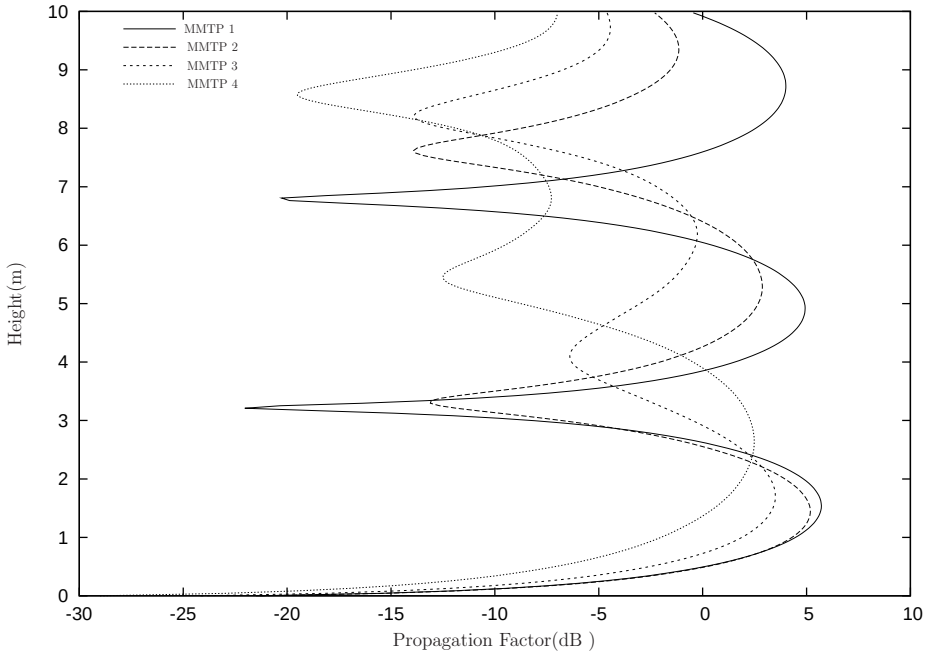

Figure 6.32: Propagation Factor using Mathematical Flame Profile (See Table 6.4) - 450MHz (20m from transmitter)

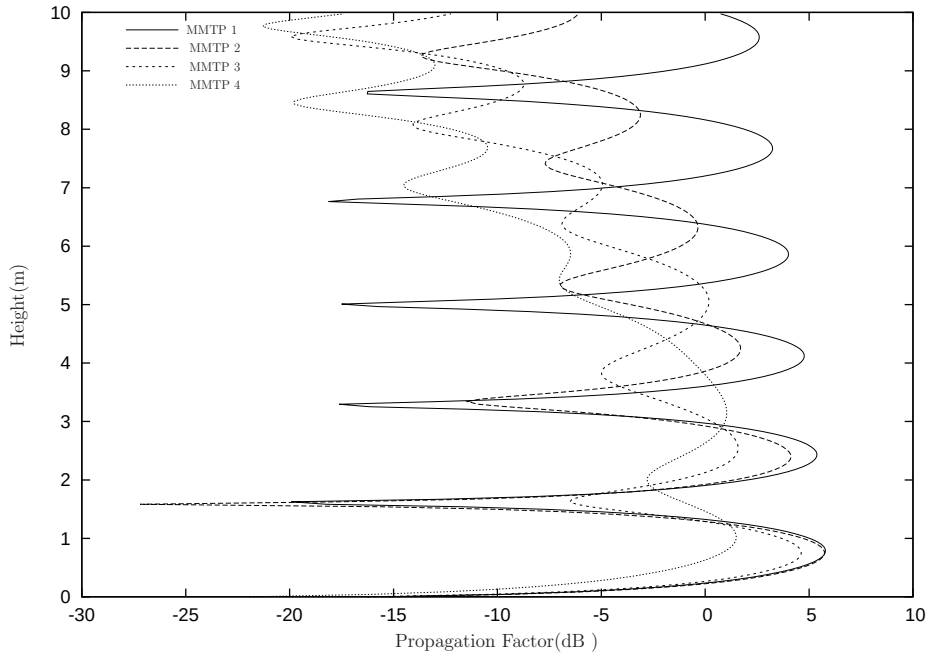

Figure 6.33: Propagation Factor using Mathematical Flame Profile (See Table 6.4) - 950MHz (20m from transmitter)

the FDTD simulation volume. The temperature profile is then scaled to the maximum temperature. Three FDS temperature profiles are considered with parameters outlined in Table 6.5. These profiles are representative of the different stages in the development of a fire. Figures 6.34 - 6.37 are three dimensional depictions of the electron density profile as the temperature is scaled. Contour surfaces have been provided for the electron densities $1 \times 10^{15}\mathrm{m}^{-3}$, $5 \times 10^{15}\mathrm{m}^{-3}$, $1 \times 10^{16}\mathrm{m}^{-3}$, $5 \times 10^{16}\mathrm{m}^{-3}$, $1 \times 10^{17}\mathrm{m}^{-3}$.

As can be seen for the electron density profiles, the strong concentration occurs in the region above the fuel heap. For the associated propagation simulations, similar to the idealistic mathematical model, a strong ground path is also present for the FDS profile.

A deliberate difference between the FDS temperature model and the ideal mathematical model is the location of the maximum temperature. This occurs at 9.6m for the FDS temperature model compared to 4m for the mathematical model. This will allow a comparison to be made for a change in the height of the maximum temperature. Inspecting Figures 6.34 - 6.37, the FDS profile yields a much larger volume of electron density at low heights compared to the mathematical model.

Parameters	FDS 1	FDS 2	FDS 3
Scaled T_{max}	1500°K	1700°K	2000°K
$N_{e_{max}}$ m^{-3}	5.8×10^{16}	4.5×10^{17}	4.75×10^{18}
$N_{e_{max}}$ Height	9.6m	9.6m	9.6m
$N_{e_{max}}$ at 2m	3.1×10^{15}	3.1×10^{16}	4.32×10^{17}
ν_{eff} (Hz)	10^{11}	10^{11}	10^{11}
Loss at 2m 180MHz	0.66dB	4.02dB	15.3dB
Loss at 2m 450MHz	0.47dB	2.77dB	7.21dB
Loss at 2m 950MHz	0.21dB	2.52dB	5.53dB

Table 6.5: FDS Temperature Plasma Profile

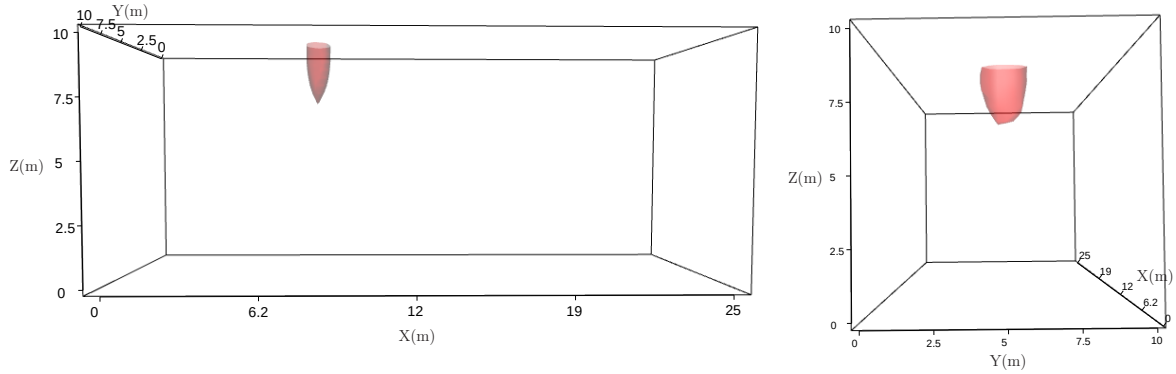

(a) 1300°K X-Z (b) 1300°K Y-Z

Figure 6.34: Electron Density - 1300°K FDS Profile [a]

[a]Surface contours at densities 1×10^{15}m^{-3} , 5×10^{15}m^{-3} , 1×10^{16}m^{-3} , 5×10^{16}m^{-3} , 1×10^{17}m^{-3}

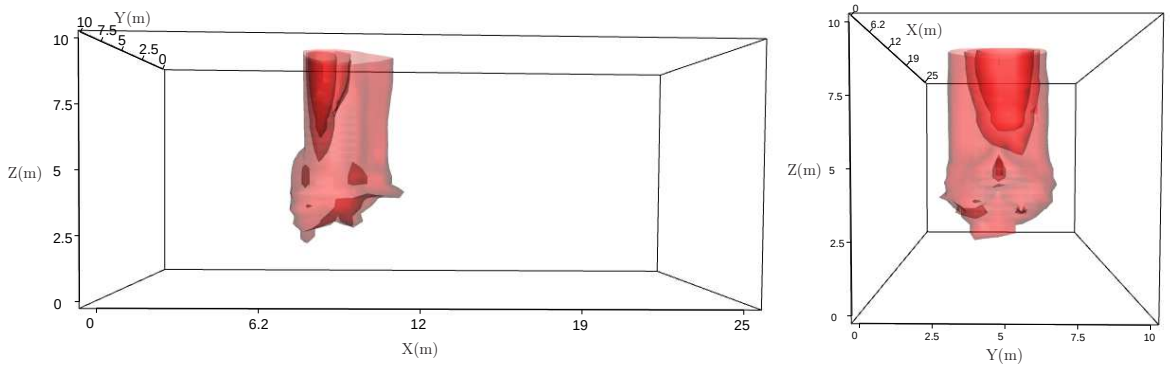

(a) 1500°K X-Z (b) 1500°K Y-Z

Figure 6.35: Electron Density - 1500°K FDS Profile [a]

[a]Surface contours at densities 1×10^{15}m^{-3} , 5×10^{15}m^{-3} , 1×10^{16}m^{-3} , 5×10^{16}m^{-3} , 1×10^{17}m^{-3}

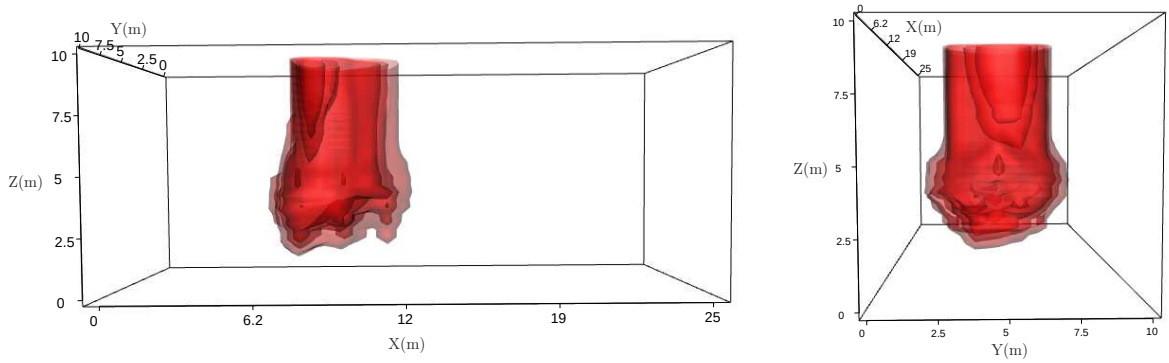

(a) 1700°K X-Z (b) 1700°K Y-Z

Figure 6.36: Electron Density - 1700°K FDS Profile[a]

[a]Surface contours at densities $1 \times 10^{15}\text{m}^{-3}$, $5 \times 10^{15}\text{m}^{-3}$, $1 \times 10^{16}\text{m}^{-3}$, $5 \times 10^{16}\text{m}^{-3}$, $1 \times 10^{17}\text{m}^{-3}$

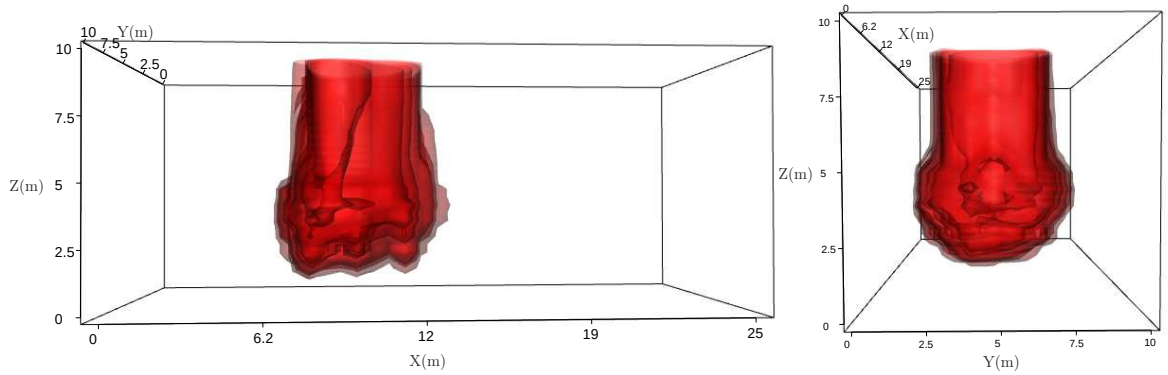

(a) 2000°K X-Z (b) 2000°K Y-Z

Figure 6.37: Electron Density - 2000°K FDS Profile[a]

[a]Surface contours at densities $1 \times 10^{15}\text{m}^{-3}$, $5 \times 10^{15}\text{m}^{-3}$, $1 \times 10^{16}\text{m}^{-3}$, $5 \times 10^{16}\text{m}^{-3}$, $1 \times 10^{17}\text{m}^{-3}$

From the various 3D profiles we see small pockets of high electron density. At low heights, the electron concentration present is small and a strong propagation path will exist due to ground reflection.

Propagation through the FDS temperature model exhibits similar behaviour to the mathematical model and the column profile with varying height. There is very little attenuation at low heights, but very large attenuation being observed above 4m . Due to the maximum electron densities being found at 9.6m , the larger attenuation is observed at heights around this region compared to the mathematical model. It should be noted,

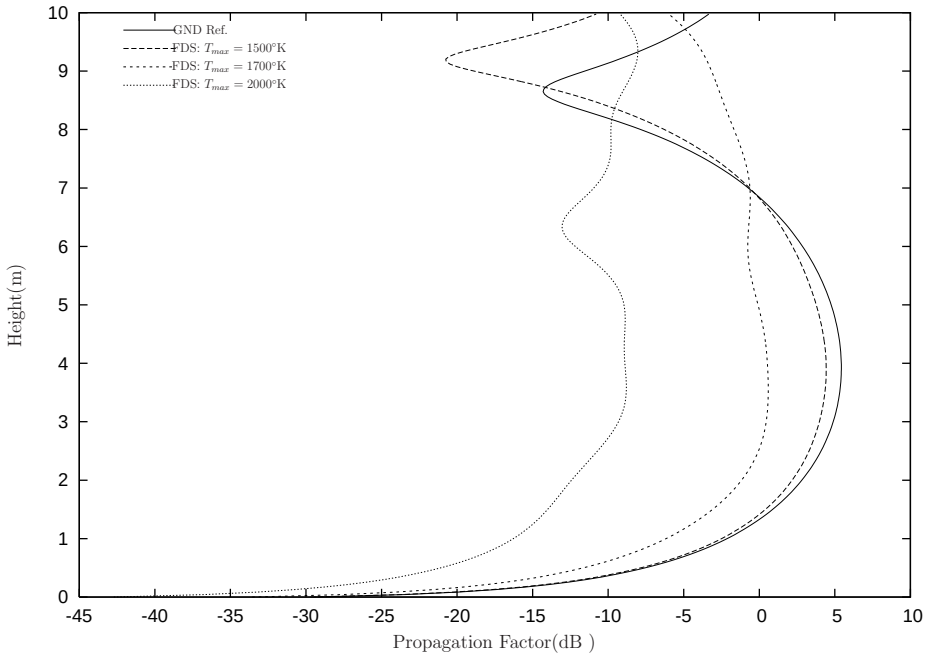

Figure 6.38: Propagation Factor for various FDS Profiles (See Table 6.5) - 180MHz (20m from transmitter)

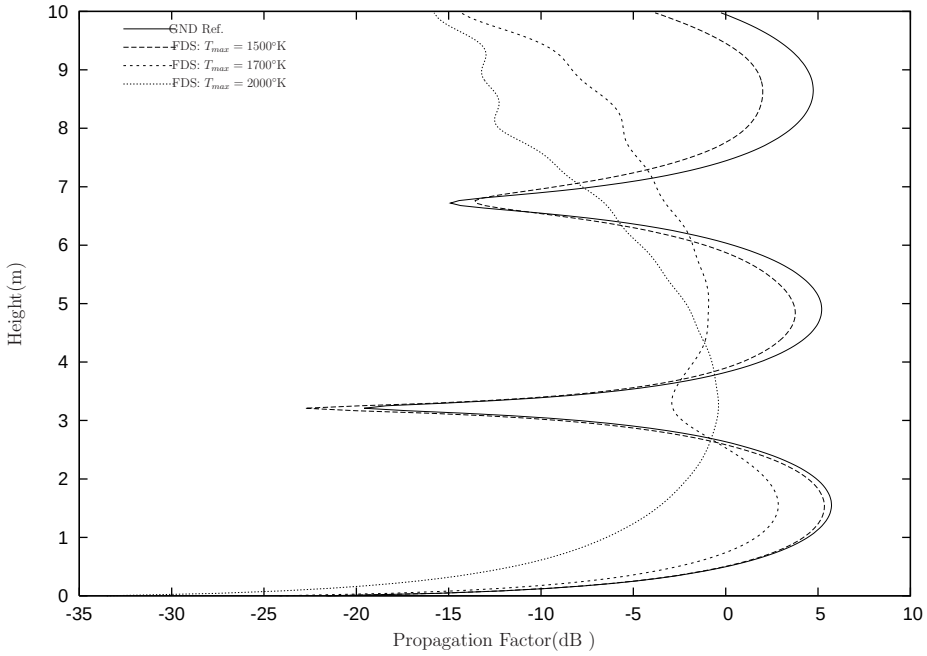

Figure 6.39: Propagation Factor for various FDS Profiles (See Table 6.5) - 450MHz (20m from transmitter)

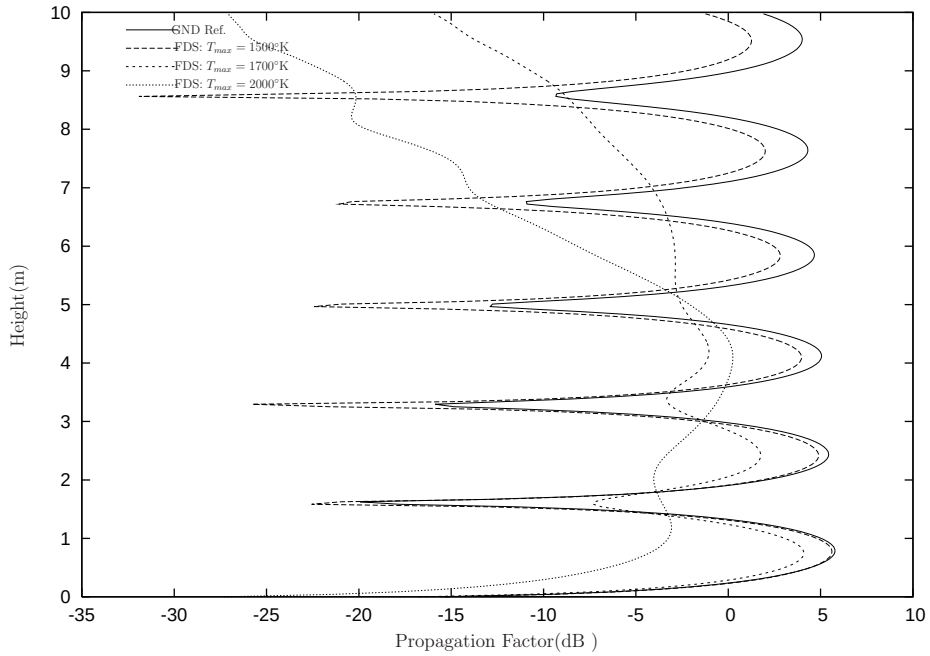

Figure 6.40: Propagation Factor for various FDS Profiles (See Table 6.5) - 950MHz (20m from transmitter)

that the mathematical model profiles produce similar results at the receiver height for temperatures that are scaled by 200°K more than the FDS profile.

This section has explored the effect of a combustion induced plasma upon radio wave propagation. It has been shown that attenuation can exist at low heights, in agreement with experimental results. The work has shown that the plasma itself does not completely explain propagation observations and the height of the fuel heap can be important since it can allow a ground reflection path that can dominate propagation. In addition, the work has shown that it is important to have a model of the plasma that encapsulates the important features.

6.4 Fuel and Plasma Dynamics

In this section we bring both the plasma and fuel heap together to study their combined effect. Previously, we considered separately the effects of the fuel heap and plasma upon propagation. It has been highlighted that the temperature profiles in the section above have variation in their height. One of the implications of this height variation is its effect

on propagation at low heights by introducing a ground reflection path. With the inclusion of the fuel heap, the ground reflection path is obstructed.

The propagation results have been generated by considering the fuel heap with a FDS generated temperature profile. Parameters for each simulation are summarised in Table 6.6. Propagation factor plots have been included in Figures 6.41 - 6.43. There is strong attenuation at the higher heights and this increases with temperature and electron density. With the fuel heap now present, attenuation exists at lower heights due to the dominant ground reflection path being obstructed by the fuel heap. In addition, diffraction propagation over the fuel heap has been diminished by the presence of the plasma. Both factors contribute to reduce the signal at low receiving heights. The loss calculated in Table 6.6 is relative to a fuel heap of 3m with no plasma present. The loss for all frequencies has greatly increased, showing the contribution of both the fuel heap and the combustion induced plasma are important. As the temperature increases, the greatest attenuation moves from 180MHz to 450MHz and finally 950MHz .

Parameter	**FH-FDS 1**	**FH-FDS 2**	**FH-FDS 3**
Scaled T_{max}	1500°K	1600°K	1700°K
Fuel Height	3m	3m	3m
Loss[a] at 2m 180MHz	6.1dB	21dB	9.3dB
Loss at 2m 450MHz	5.72dB	24dB	11.83dB
Loss at 2m 950MHz	4.0dB	15dB	19dB

Table 6.6: Excess Loss for a Fuel Heap with FDS Plasma Model

[a]This is relative to the Fuel Heap Simulation of 3m with no plasma present

The progression from profile FH-FDS 1 to FH-FDS 3 represents a period where the fuel heap height is constant. It represents the period where a fire is ignited and builds in intensity. Over this period, as the temperature increases, the attenuation progressively worsens at all heights.

It is evident that combustion induced plasma, and fuel heap, both contribute towards attenuation. It is now important to consider the dynamic of the fuel heap deteriorating. Profile FH-FDS 2 is used from Table 6.6 but with the fuel heap height reduced in 0.5m steps. Propagation plots are shown in Figures 6.44-6.46. A trace of the fuel heap at 3.0m with no plasma has been included as a reference when the fire or plasma is not

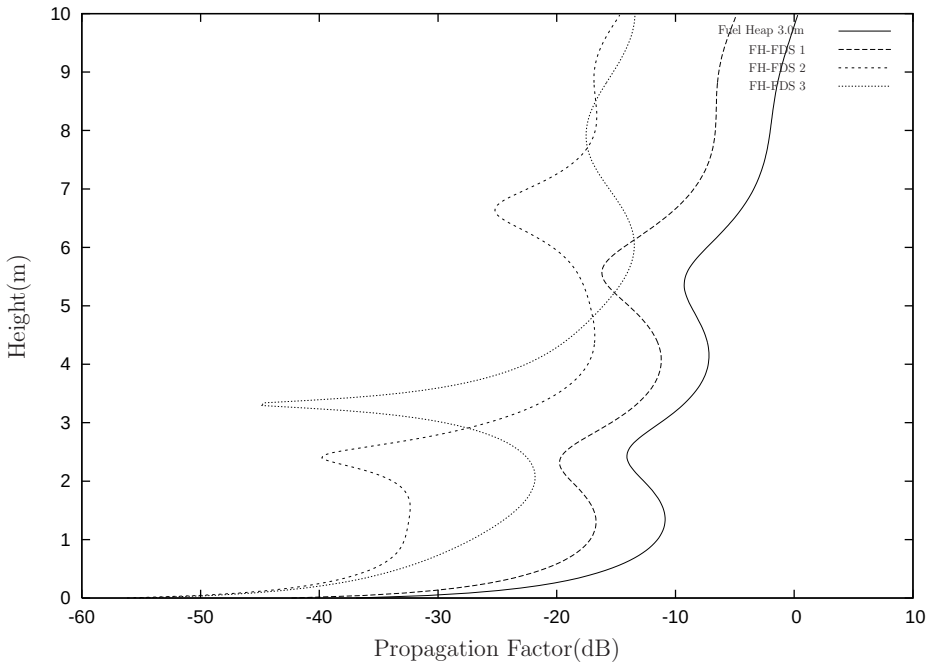

Figure 6.41: Propagation factor for varying Fuel Heap using a FDS temperature model - 180MHz . See Table 6.6 for profile parameters, 20m from transmitter

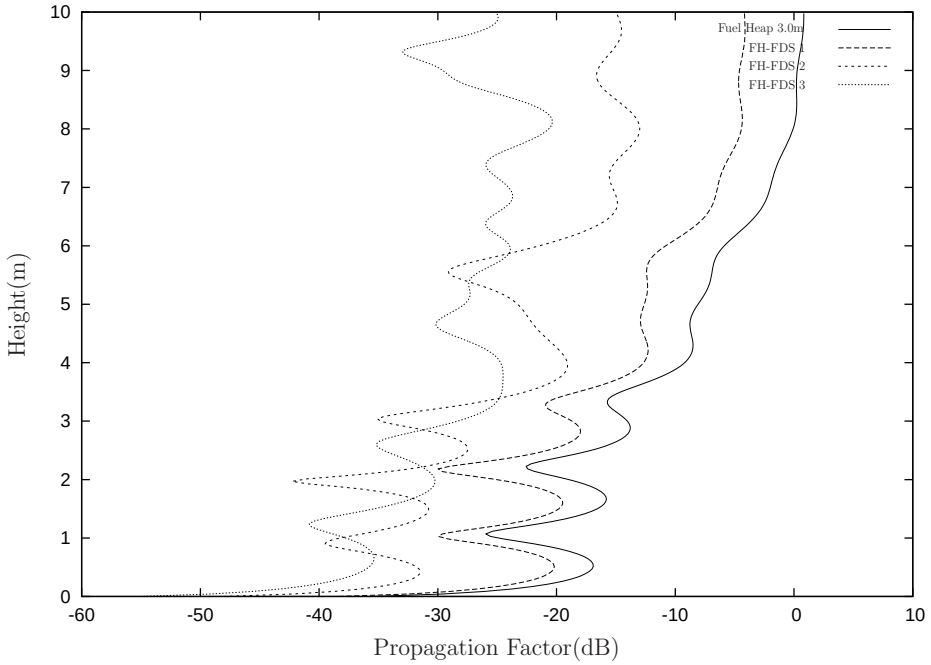

Figure 6.42: Propagation factor for varying Fuel Heap using a FDS temperature model - 450MHz . See Table 6.6 for profile parameters, 20m from transmitter

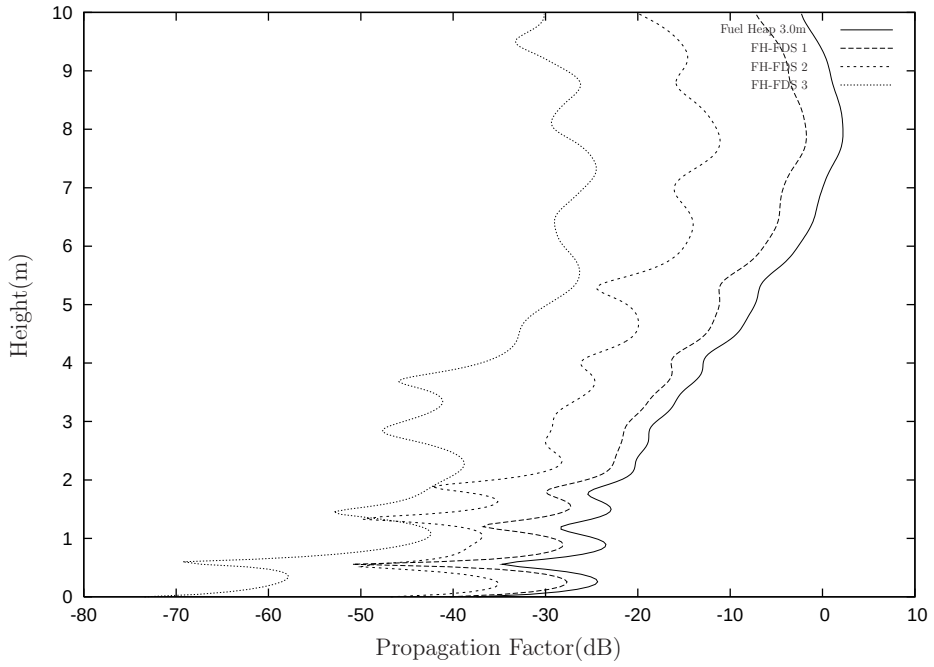

Figure 6.43: Propagation factor for varying Fuel Heap using a FDS temperature model - 950MHz . See Table 6.6 for profile parameters, 20m from transmitter

present ('pre-ignition'). To ensure that only the fuel heap dynamic is investigated we do not alter the parameters for the plasma. We are assuming that the fire's intensity is constant and plasma profile is not diminishing as the fuel heap collapses. The experimental work shows there is a stage where the fire increases or sustains constant intensity while the fuel heap is deteriorating; this development is what is being examined at this stage. The response seen in propagation depends on the frequency. Inspecting the 950MHz plot, a change of the fuel heap height by 0.5m results in a return to pre-ignition signal levels at the antenna height. This return in the signal means that only a little change in the fuel heap height is required before the effect of the plasma becomes masked and insignificant at that frequency. Each drop in the fuel heap results in a further increase in the signal strength even with the plasma intensity being strong. At higher observation heights, above 6m , the attenuation remains relatively constant, which is expected due to the peak of the electron density in the FDS profile at 9.6m . This indicates a large sensitivity to the fuel heap height and variation in the plasma profile at higher frequencies.

A trend is set further down in frequency with the 450MHz plot (Figure 6.45) showing a drop of 1m in the fuel height is required to return to 'pre-ignition' signal levels and 180MHz showing a change of 2.5m is required. These results provide an explanation

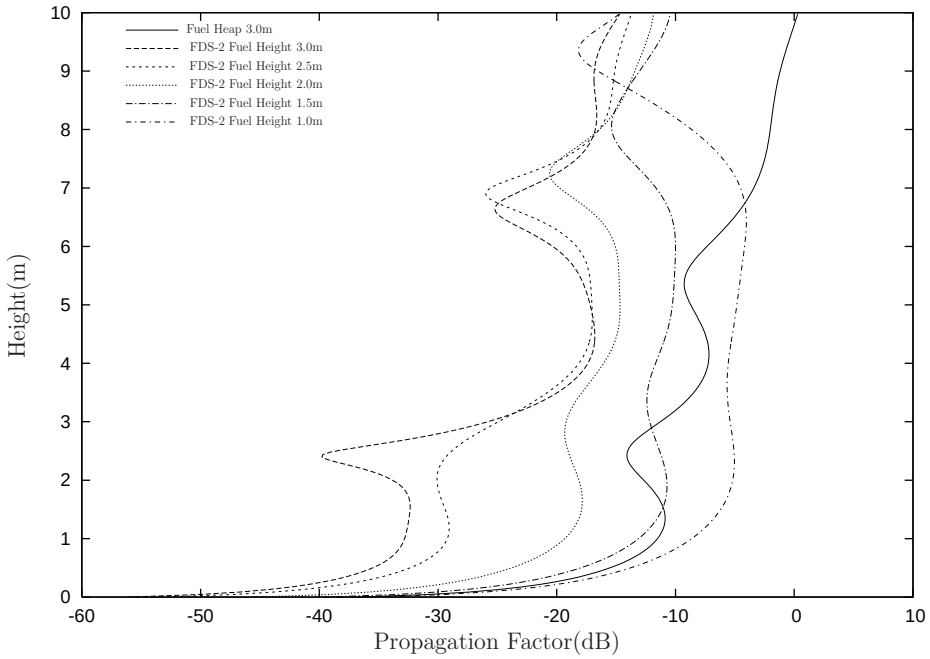

Figure 6.44: Propagation Factor with varying Fuel Heap Height with FDS plasma present - 180MHz (20m from Transmitter), See Table 6.6 for profile parameters

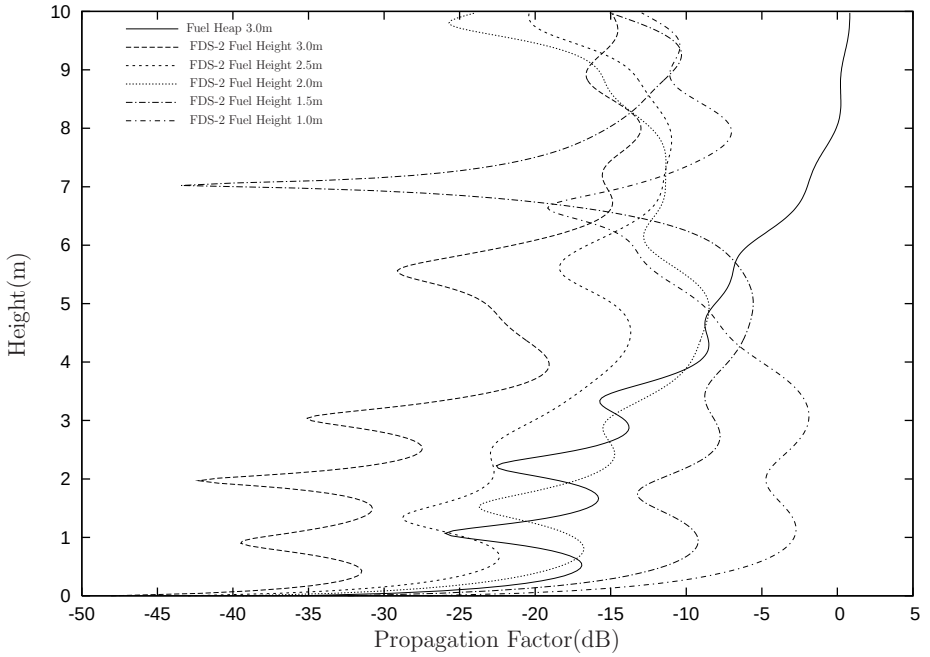

Figure 6.45: Propagation Factor with varying Fuel Heap Height with FDS plasma present - 450MHz (20m from Transmitter), See Table 6.6 for profile parameters

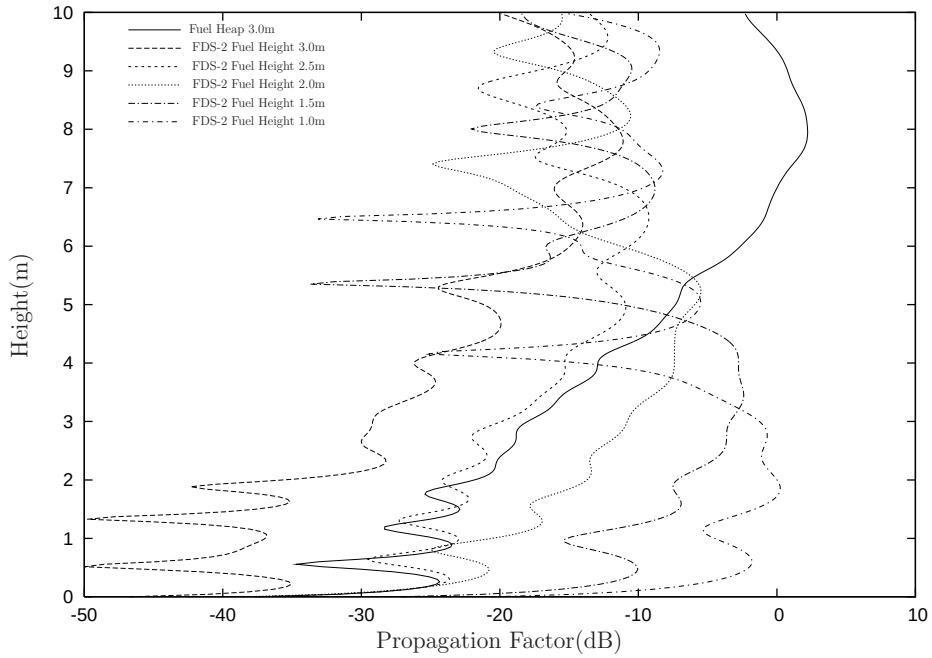

Figure 6.46: Propagation Factor with varying Fuel Heap Height with FDS plasma present - 950MHz (20m from Transmitter), See Table 6.6 for profile parameters

of the differing amount of time it takes each frequency band to return to pre-ignition signal levels in the small scale experiments. Regardless of the strength of the combustion induced plasma, the dynamic of the fuel heap size will cause the signal levels of each frequency to return to 'pre-ignition' levels at different rates. Mobile bands will return quite promptly, followed by the UHF band, and lastly the VHF band. Experimentally this trend is confirmed by revisiting Table 2.3.

In the discussion of the experimental chapter (see Section 2.2.5) the idea of the fuel heap 'masking' the effects of the plasma was introduced. Here we can further clarify what is meant by 'masking'. The fuel heap interaction that was seen in Figures 6.44 - 6.46 only occurs at the lower heights, where the fuel heap is present. Combustion induced plasma effects are still present in the propagation of energy, particularly at heights above 6m . The collection of data being limited to a single antenna located at one point in space can hide the true state of the propagation environment.

A similar behaviour is seen when using an electron density column profile instead of the more realistic fire profile. The profile used is 'CEP 1' of Table 6.1. Propagation plots for the column profile are shown in Figures 6.47 - 6.49. The 950MHz (Figure 6.49)

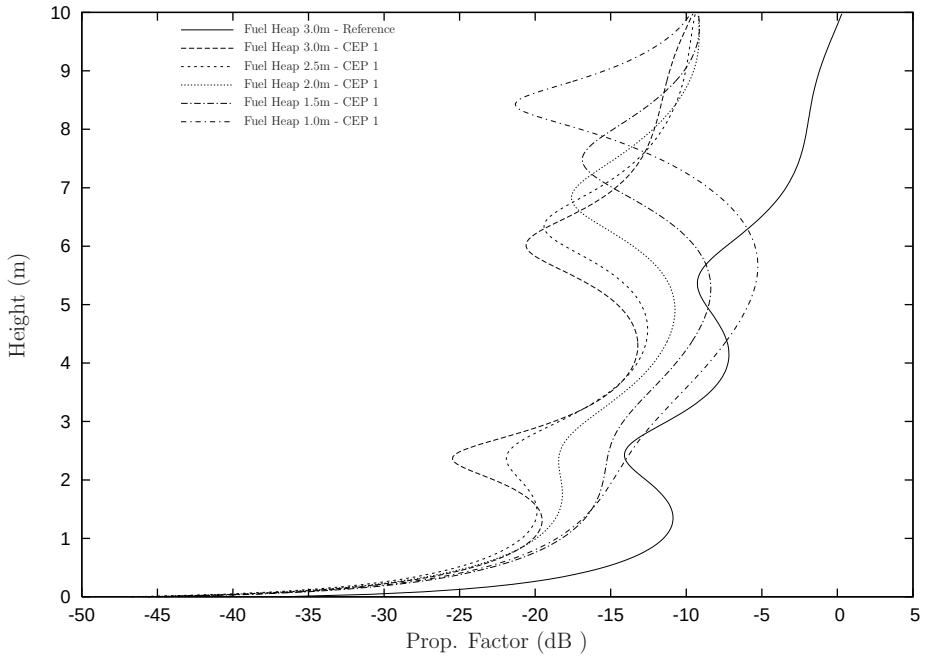

Figure 6.47: Propagation Factor with varying Fuel Heap Height using Column Plasma - 180MHz (20m from Transmitter). See Table 6.1 for profile parameters

reaches the pre-ignition when the fuel heap height reduces to 2.0m , 450MHz when the height is 1.5m and 180MHz when the height is 1.0m .

Collision Frequency variation

As well as providing temperature information, the FDS simulation also provides data concerning the atmospheric constituent gases in the flames. This allows one to include collision frequency information throughout the entire simulation volume. The collision frequency model is from Section 3.3.5. A varying collision frequency is included for the 'FH-FDS 2' profile and in Figures 6.50 - 6.52, label 'FDS CFXX' designates this simulation.

The FDS simulations show that in the centre of the fire the collision frequency increases. This is due to the higher pressure and presence of high collision gases (water, carbon dioxide). As the collision frequency increases, the overall attenuation reduces because less electromagnetic energy is coupled into the plasma. The minimum collision frequency is 1×10^{11}Hz outside the fire and a maximum of 4.5×10^{11}Hz inside the fire. These results are contrary to the work of Mphale and Heron[81], which predicts a much

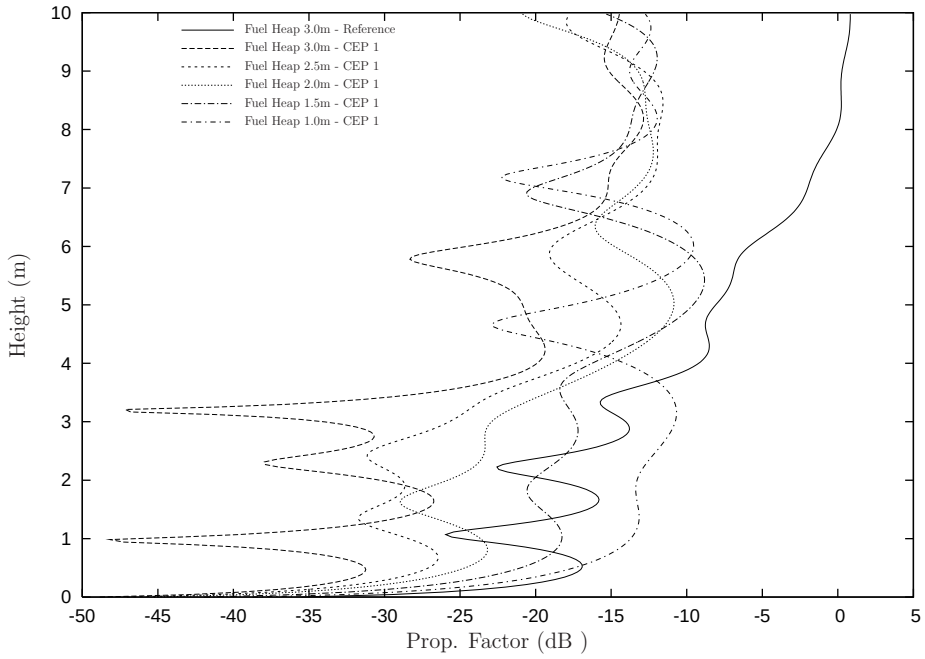

Figure 6.48: Propagation Factor with varying Fuel Heap Height using Column Plasma - 450MHz (20m from Transmitter). See Table 6.1 for profile parameters

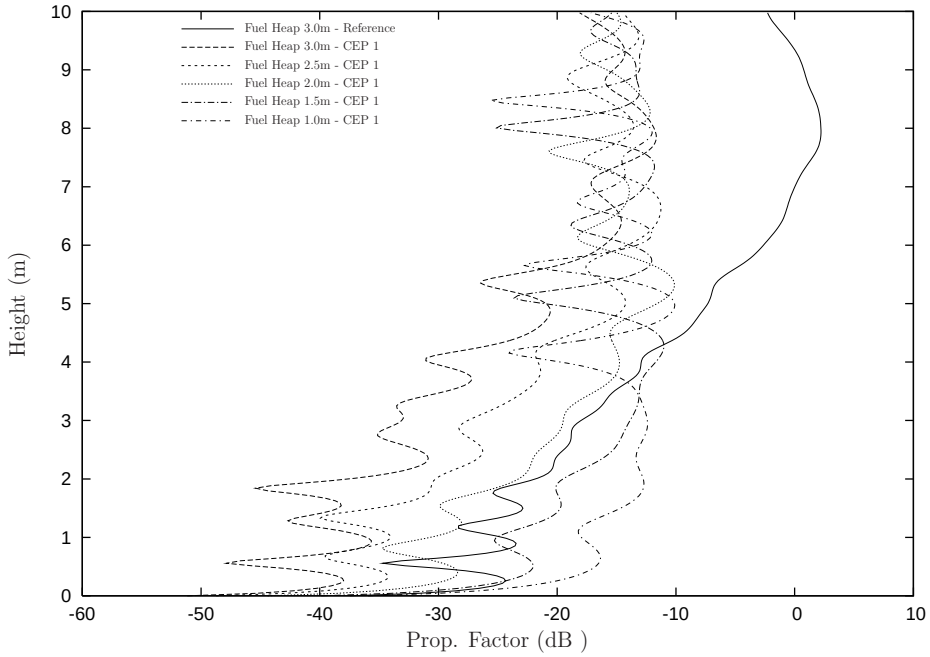

Figure 6.49: Propagation Factor with varying Fuel Heap Height using Column Plasma - 950MHz (20m from Transmitter). See Table 6.1 for profile parameters

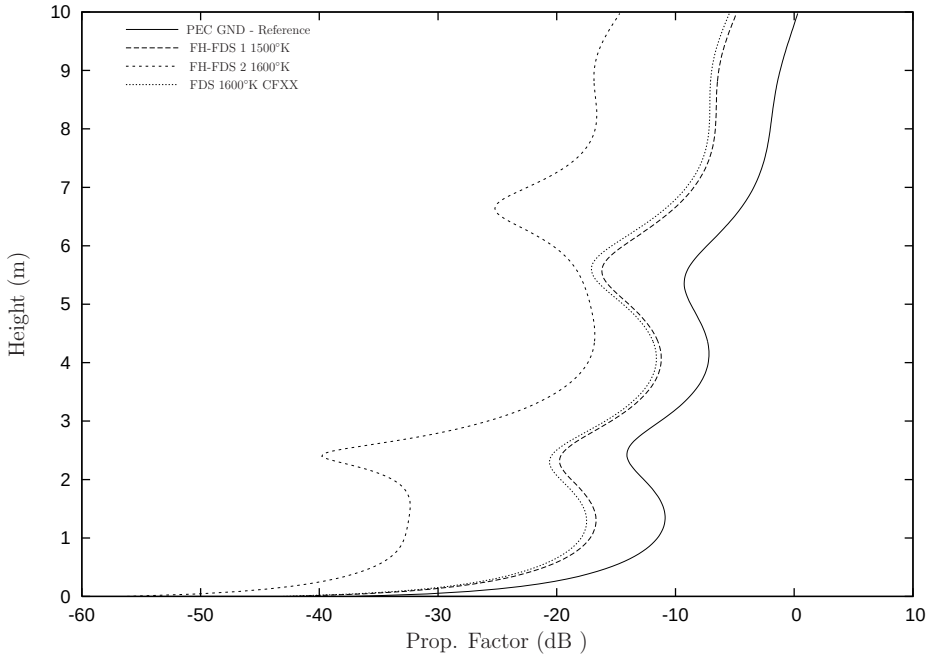

Figure 6.50: Propagation Factor with FDS Collision Frequency simulation - 180MHz (20m from Transmitter). See Table 6.6 for profile parameters, 'CFXX' denotes FDS calculated collision frequency

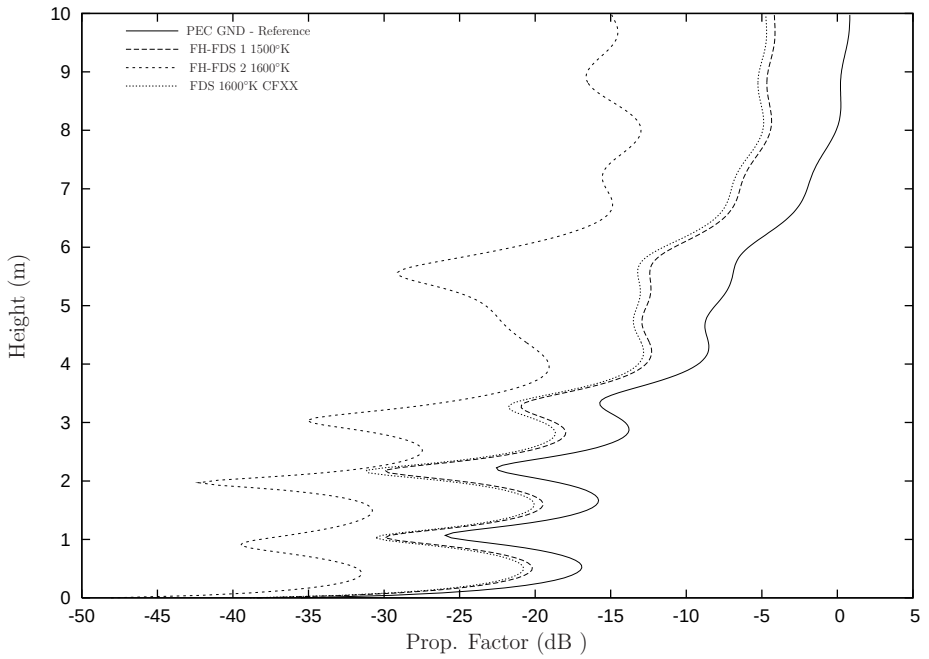

Figure 6.51: Propagation Factor with FDS Collision Frequency simulation - 450MHz (20m from Transmitter). See Table 6.6 for profile parameters, 'CFXX' denotes FDS calculated collision frequency

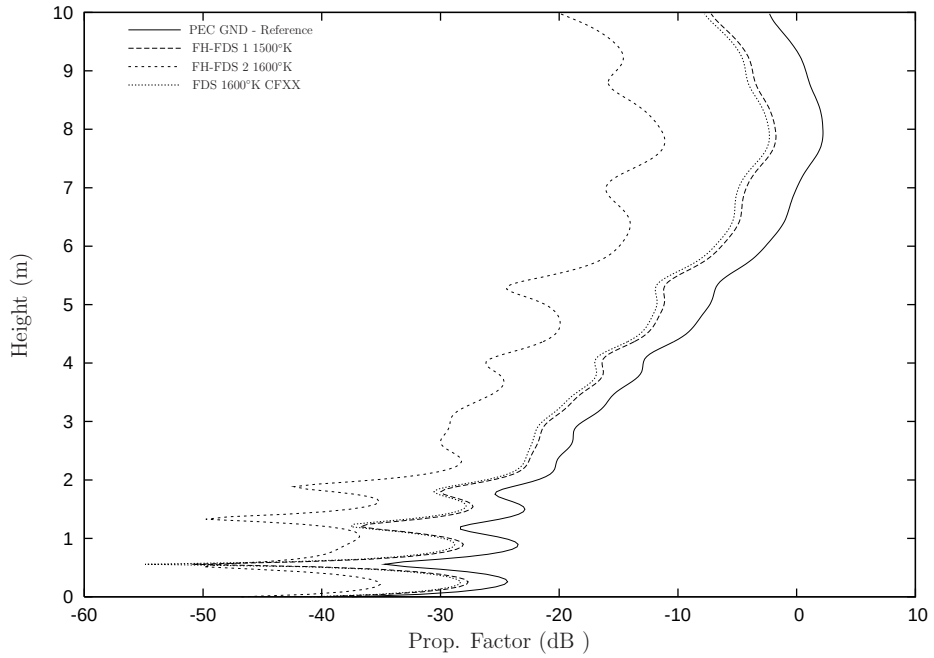

Figure 6.52: Propagation Factor with FDS Collision Frequency simulation - 950MHz (20m from Transmitter). See Table 6.6 for profile parameters, 'CFXX' denotes FDS calculated collision frequency

lower collision frequency (around $3 - 5 \times 10^{10}$) and a depreciation in the collision in the fire because the temperature increases. Changes in the pressure and gas constituents have not been considered in their work and our results indicate that they are important.

The inclusion of the collision frequency reduces the severity of attenuation caused by the plasma. The electron density needs to be approximately double to reach the same level of attenuation.

Small Scale Experiments

To complete this chapter, a representative time progression of the small scale fire experiments has been included. The fire has been broken into three stages, pre-burn, a period where the fire intensity increases, and a period where the fuel heap is deteriorating and undergoes collapse. Table 6.7 is a collation of the various simulations, stages and parameters. The temperature profile uses FDS data.

Number	Fire Stage	Scaled T_{max}	Fuel Height
1-3	Pre-burn	300°K	3m
4	Fire	1500°K	3m
5	Fire	1600°K	3m
6	Fire	1700°K	3m
7	Fire	1600°K	3m
8	Fuel Heap	1600°K	2.5m
9	Fuel Heap	1600°K	2.0m
10	Fuel Heap	1600°K	1.5m
11	Fuel Heap	1600°K	1.0m
12	Fuel Heap	1500°K	1.0m

Table 6.7: Progressive fire simulations

Each number in Table 6.7 is a single point displayed in Figure 6.53. For each trace on the plot the communication band is averaged over the frequency range of the band concerned and the power value is referenced to the 'pre-burn' stage. This follows the same procedure for the physical experiments found in Section 2.

Considering Figure 6.53 as a progression of the fire over time, there are important features in common with experimental data. Some of these are: strong attenuation on the UHF communication band, the duration of attenuation for each band and the recovery to pre-burn signal levels in the order of Mobile, followed by UHF and a drawn out recovery for VHF. Also, the differences in the pre-burn and post-burn levels are also visible at profile step 12.

For the mobile band, its shorter wavelength makes it more susceptible to small scale changes in the propagation region. In particular the fluctuations and turbulence that can occur in a real fire.

The VHF band has a much larger wavelength and propagation for this band is sensitive to larger variations in the propagation medium. Large changes in the fuel heap are required to mask the effect of the combustion induced plasma. Conversely, small variations in the plasma profile, such as small pockets of temperature variation, will not affect propagation substantially in this frequency band.

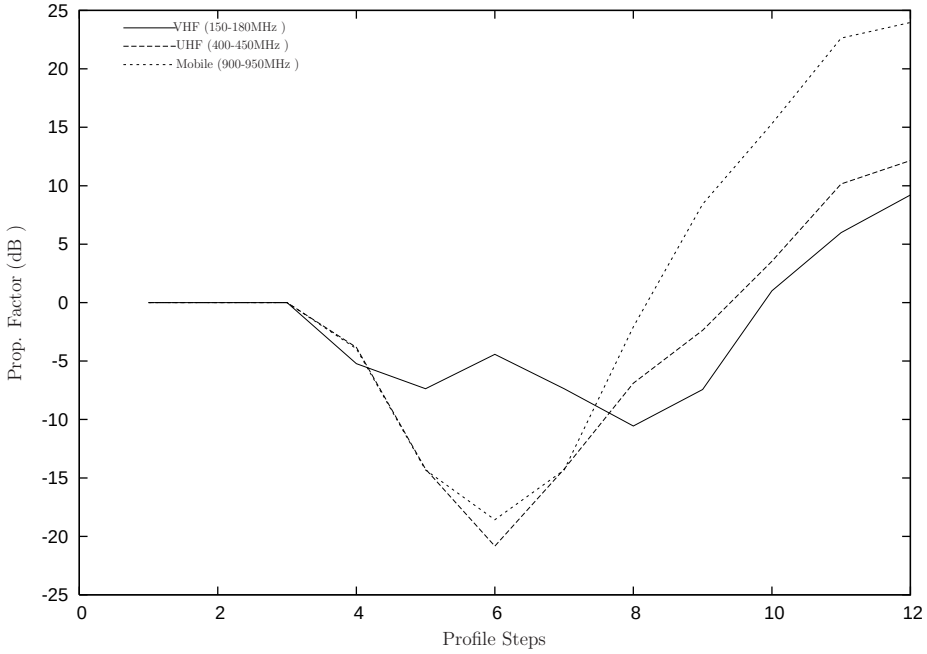

Figure 6.53: Simulated Fire stage progression for Small Scale Fires (20m from transmitter), using FDS temperature data with hemi-spherical fuel heap of varying height. See Table 6.7

The UHF band has a large enough wavelength to not be sensitive to small variations in the environment but is affected by changes to the environment more so than VHF. As shown in the experimental data and the simulations, it is a portion of frequencies that are most affected by the combustion induced plasma and its physical size in the small scale experiments.

The results of this chapter help to explain our observations of a small scale fire. In particular, frequency dependence on propagation has been shown to be a combination of both combustion induced plasma effects and fuel heap interactions.

There are a number of implications of this work to the radio communications. Fire induces a plasma that attenuates all radio signals over the currently used communication frequency range. Frequency dependence occurs in these environments because of the geometric changes in the environment, brought about by the fire and the combustion induced plasma. The contribution of the environment can lead to situations where the radio signal is diminished, such as the introduction of the fuel heap to the temperature profiles lead to a huge reduction in signal strength at low heights. It can also provide

multiple paths of propagation that enhance signal strength at a particular location, this is seen with the destruction of the fuel heap on higher frequencies.

Particular bands are problematic to communication through a fire environment. Frequencies around 400-450MHz have been shown to be sensitive to the fire and are unaided by diffraction. Frequencies around 180MHz are also attenuated in the presence of a fire with a lack of sensitivity to the environment but are aided by diffraction, allowing better communication in these environments compared to UHF frequencies.

This page is blank

SECTION 7

Large Scale Fire Numerical Experiments

In this chapter we build on our understanding to examine propagation on a much larger scale. The tools and models that have been developed will be used to investigate various scenarios. A two dimensional Finite Difference Time Domain (FDTD) code has been developed that allows cold plasma modelling and a moving propagation window for long range propagation. The aim is to demonstrate the usefulness of the code in studying extensive bushfire environments at a range of frequencies.

The first scenario will concentrate on exploring refractive index effects caused by the fire's atmosphere. From previous studies refractive effects are thought to be one of the major contributors to propagation in large scale fire environments. The main aim in this section will be to quantitatively ascertain the contribution of refractive effects. A comparison between propagation factors resulting from the atmosphere and a combustion induced plasma will be considered.

The second scenario considers a situation where a fire is located well away from both receive and transmit, but still causes propagation problems. It includes radio propagation into the shadow region of a hill with a fire located on the hill's peak. This scenario represents a class of problems where a combustion induced plasma, not located on the line of sight, can still cause communication problems.

7.1 Refractive Index Effects

The Euroka experiment [124] and various other studies [48] [45] have stated a significant factor that affects radio propagation through fire environments is due to changes to the refractive index. Sub-refractive conditions in the atmosphere surrounding a fire are known to redistribute radio energy upwards away from ground based communications. Up till now, we have only considered short distances in the small scale fire experiments where refractive effects would be negligible. As the propagation distance becomes larger it is prudent to consider refractive effects.

In this scenario propagation effects due to changes in the refractive index for a fire atmosphere will be examined. A two dimensional FDS model of a simple forest fire has been created with uniformly distributed trees. This fire simulation will provide a representation of the atmospheric gases and temperature as the forest burns. The fire geometry is shown in Figure 7.1. The output data from FDS includes profiles of each gas (N_2, O_2, H_2O, CO_2, CO), temperature and density that varies over time.

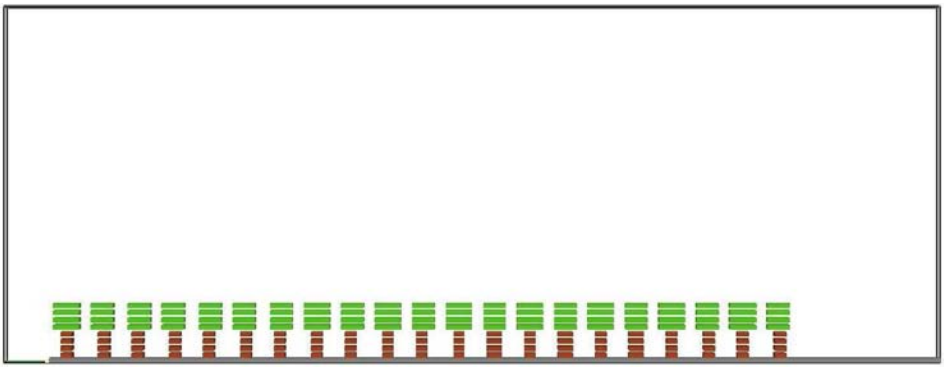

Figure 7.1: FDS Model of forest

The FDS data is then averaged to remove time varying information and used to develop a representation of the refractive index using the method outlined in Section 3.2. The resulting refractivity profile is shown in Figure 7.2, where $N_r = (n_r - 1) \times 10^6$.

The refractive index is a minimum at the regions of high temperature in and around the tree line and reaches its maximum at normal atmospheric conditions outside the main fire plume. The difference in N_r between the minimum and maximum is about 180 refractivity units. This is a substantial change in the refractive index compared to natural changes in the troposphere. In the troposphere ducting conditions occur when

the change in the refractivity is of the order of 30 units. However, for ducting to occur, these conditions are sustained over many kilometers and affect much higher frequencies (above 1GHz) [68].

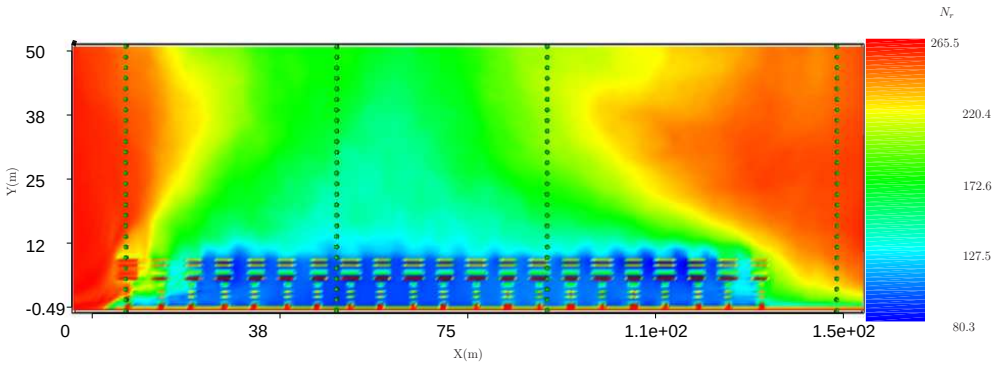

Figure 7.2: Refractive Index Profile - N_r

Once the refractive profile has been generated an electromagnetic simulation can be performed. A 2D TE_z implementation of the Finite Difference Time Domain code is used, with the propagation window modification to enable simulation over large distances. It should be noted that with 2D simulations there is symmetry involved, refer to Figure 5.4. In this situation the symmetry infers that objects are present in and out of the page. The simulated environment is excited with a time domain gaussian pulse similar to the small scale fire simulations. The spatial excitation represents a plane wave and is implemented as a vertical line that is vertically polarised (field E_y).

Time domain data is collected for the E_y field at all heights at distances 50m, 90m, and 145m as shown by a series of vertical dots in Figure 7.2. Three frequencies of interest have been displayed at each location (50m, 90m, 145m). These are shown in Figure 7.3, 7.4 and 7.5.

As is expected with refractive effects, the higher frequencies are affected most. From the plots it can be seen that as the frequency increases the effect of the refractive index upon propagation increases. The trace at 950MHz is clearly the most affected of the three displayed frequencies.

Secondly, the difference in propagation increases over distance. The attenuation for 950MHz increases from 0.6dB at 50m to 2dB at 145m . This is indicative of refractive problems, energy is slowly redistributed and accumulates over distance. More importantly,

the severity of attenuation is a function of the frequency and the distance over which the adverse refractive conditions are sustained.

Thirdly, the redistribution of energy is upwards. The attenuated region begins very close to the ground and widens in height as the distance increases. This confirms the proposition that sub-refractive atmospheric conditions occur in fire environments and cause the propagation to be bent upwards.

Lastly, the effect of the refractive index over the distances examined here is very small. As we consider the lower frequencies we see that the refractive conditions play an almost insignificant role in the overall propagation.

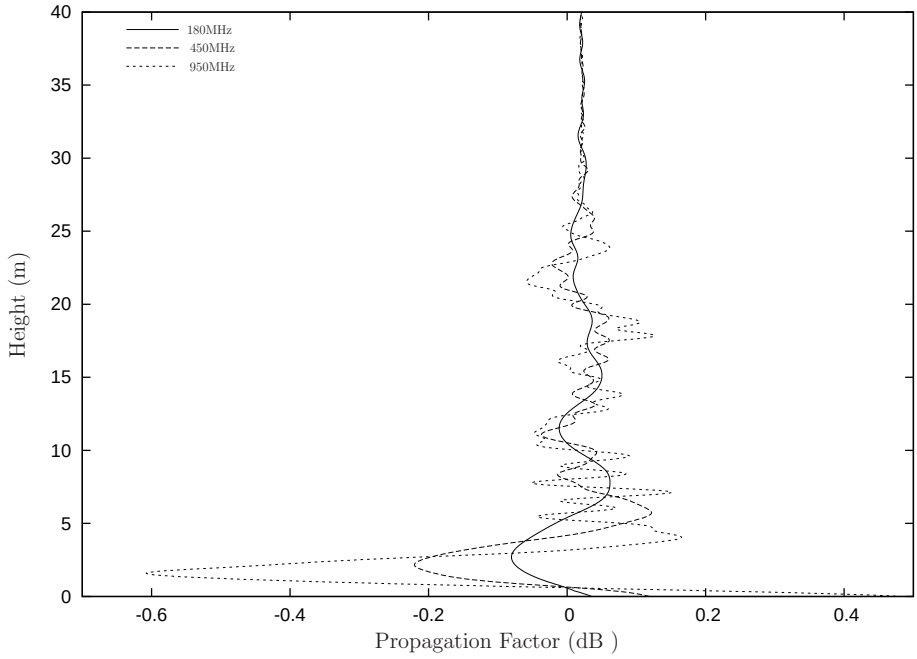

Figure 7.3: Refractive Index Effects at 50m

A final figure (see Figure 7.6) examines the refractive index effects 145m from the source and a height of 2m over all frequencies. Once again, from the figure, it is evident that the contribution to propagation from the fire atmosphere increases with frequency.

In summary, for frequencies below 400MHz the effect of the refractive index is insignificant. For frequencies above 400MHz a change in the propagation may be observed even in regions where the fire atmosphere is extremely subrefractive. From the simulation above it is shown that over approximately 100m there is 1dB in loss experienced on frequencies around 1GHz . In addition it has be seen that refractive index problems need

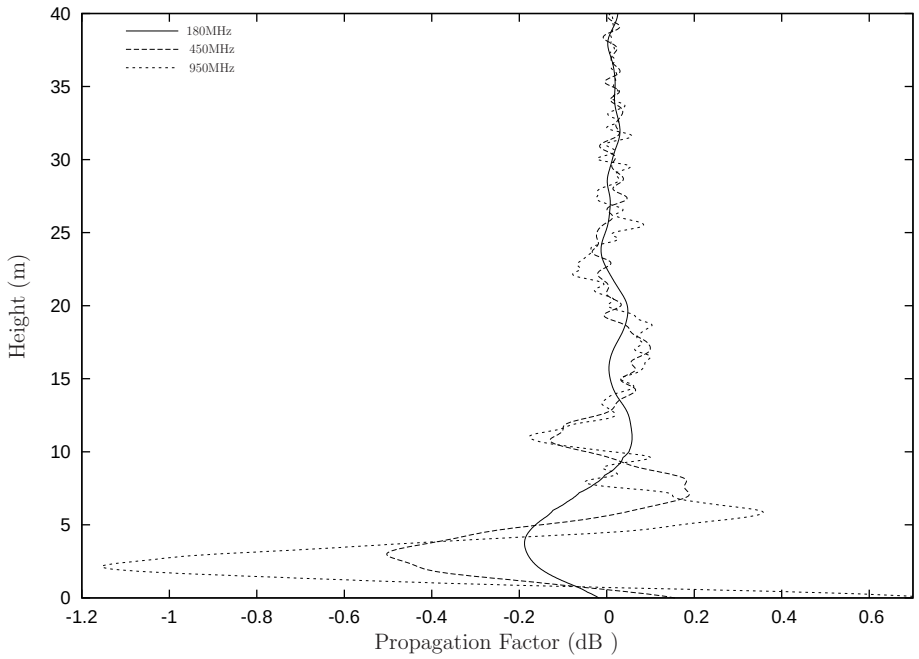

Figure 7.4: Refractive Index Effects at 90m

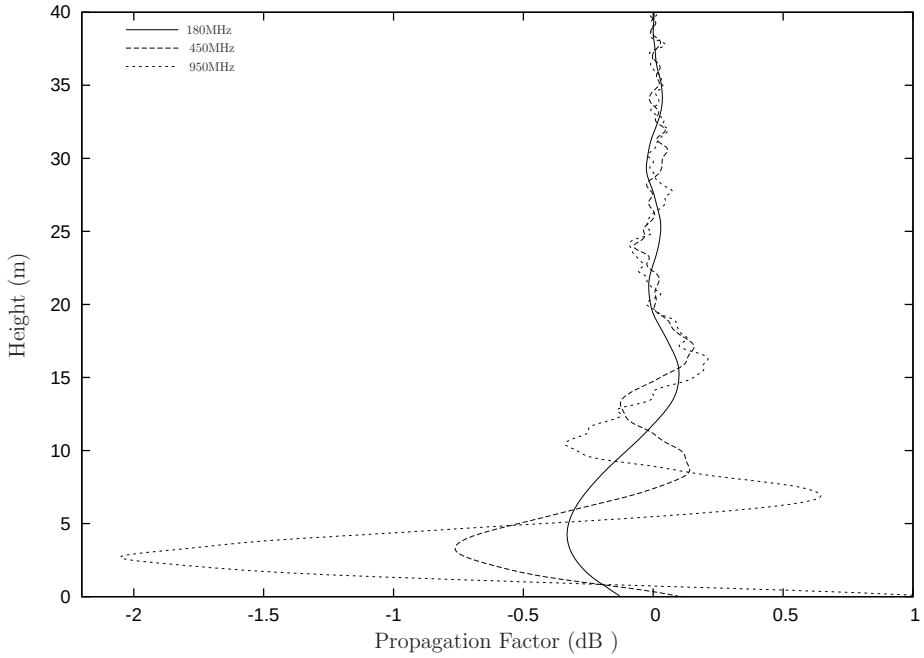

Figure 7.5: Refractive Index Effects at 145m

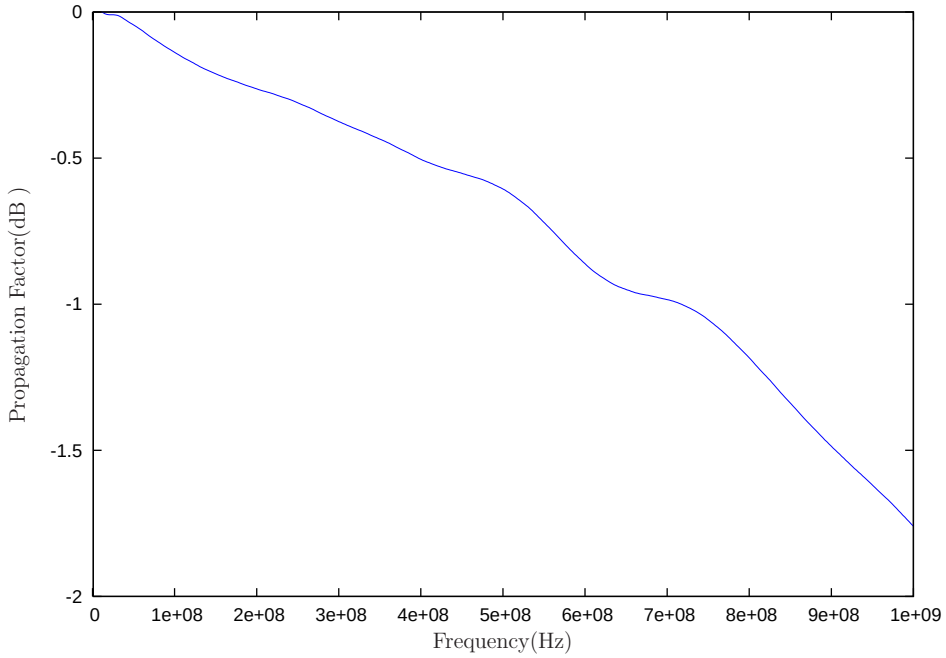

Figure 7.6: Fire Atmosphere contribution at height 2m

distance to accumulate and will only become problematic when extreme sub-refractive conditions are sustained over large regions.

Having treated the refractive effects of the fire atmosphere in an isolated manner, we now make a comparison of refractive effects with the combustion induced plasma. Using the same FDS data as the fire atmosphere we use the bushfire combustion plasma model developed in Section 3.3 to examine the plasma effects. A number of plots have been prepared at distances 50m, 90m and 145m which, are shown in Figures 7.7- 7.9.

With the inclusion of combustion plasma effects the difference in propagation increases. In these figures the energy attenuation occurs at the regions of high temperature along the tree height. This is slightly higher than the refractive effects. Additionally, the amount of attenuation is substantially larger, of the order of 10-14dB .

A variation in the propagation factor with frequency is shown in Figure 7.10. Interestingly, this plot shows the maximum attenuation occurs in the 400MHz to 450MHz frequency range and remains relatively constant for higher frequencies. As the frequency increases, propagation will become more complex and symmetry breaks down resulting in a more complex propagation scenario is expected than that shown here. In particular, there can be diffractive propagation around the fire.

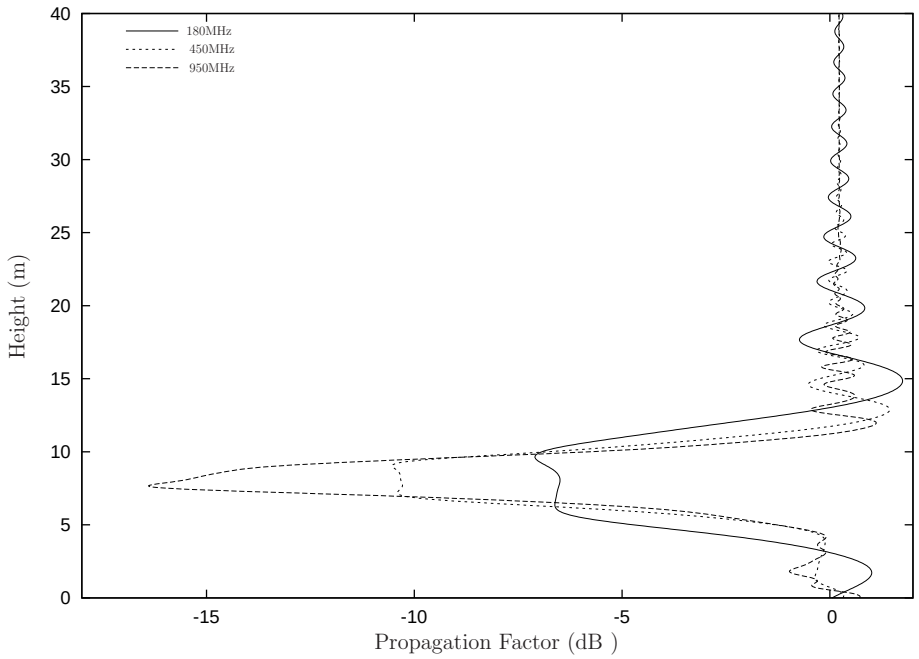

Figure 7.7: Plasma Effects at 50m

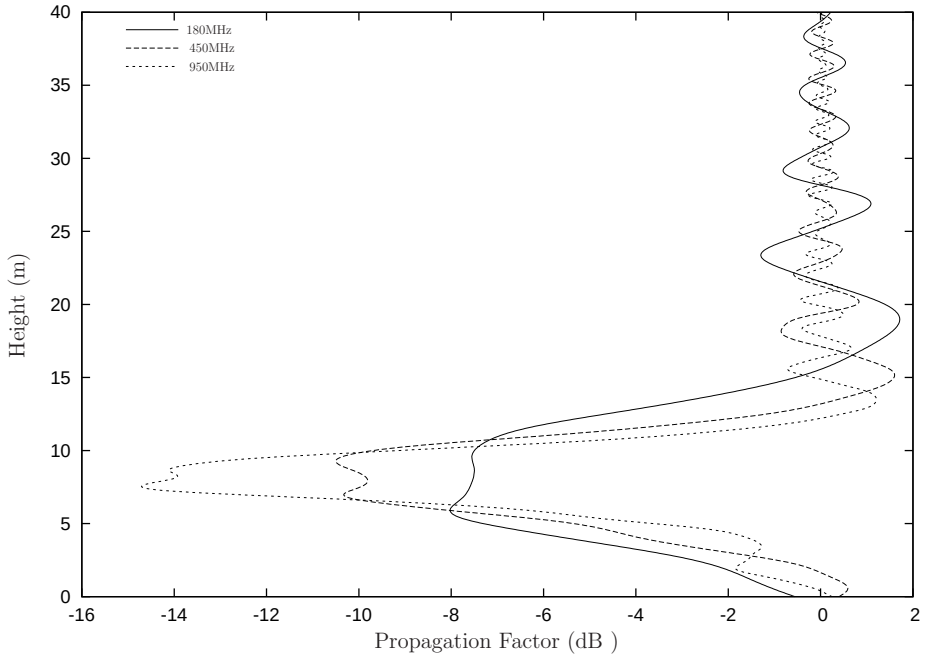

Figure 7.8: Plasma Effects at 90m

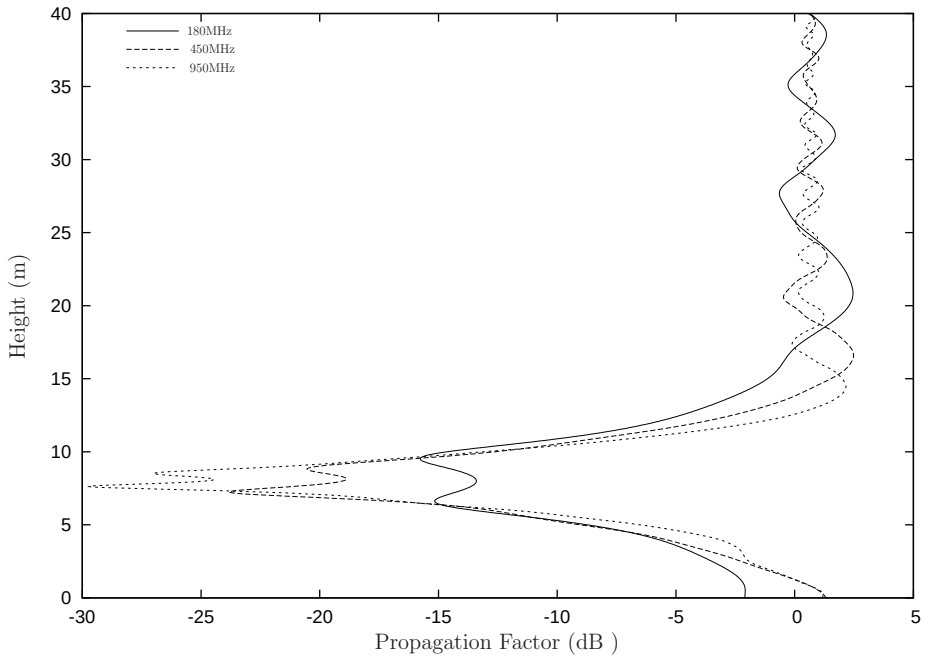

Figure 7.9: Plasma Effects at 145m

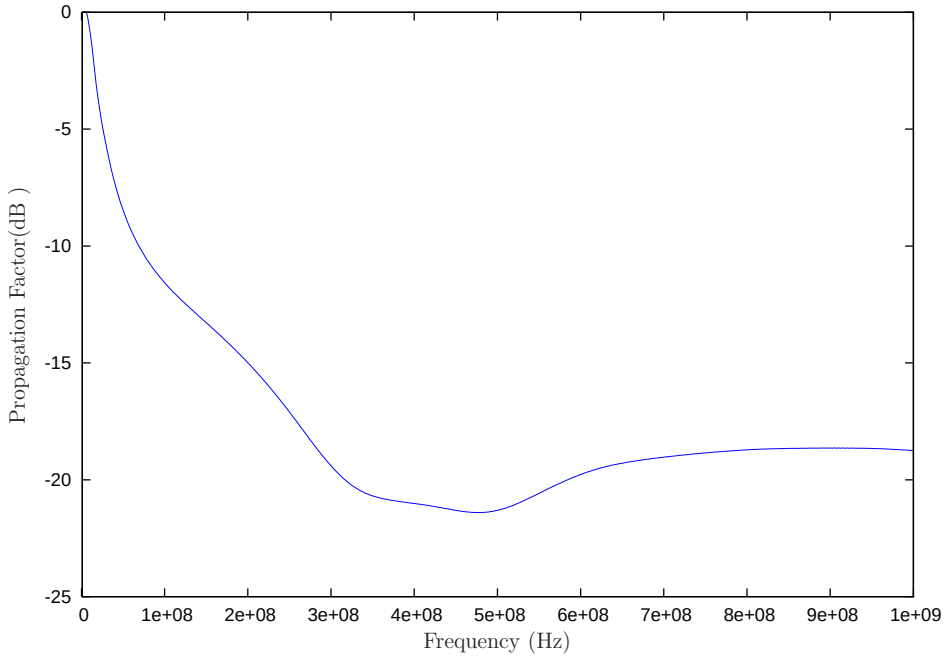

Figure 7.10: Combustion Contribution over frequency at height 7m

Compared to the refractive index effects there is no accumulation of propagation effects over distance. This leads to a strong difference in the propagation phenomena. Refractive effects are small but accumulate over distance and have their maximum attenuation closest to the ground. The combustion effects are very dramatic but are more localised to the regions of strong temperature and ionisable fuels. In this example this is the tree top line. At heights closer to ground level the attenuation is much less.

7.2 Diffraction Problems

Communication problems and the underlying propagation is dependent on the environment. So far we've considered propagation where a fire is directly on the line of sight propagation path. There are however, a number situations where the main propagation path is not necessarily line of sight.

In this section we consider radio propagation into the shadow region of a hill. Communications in the shadow of the hill is mainly by diffraction. This is a good example of non-line of sight propagation. In this case a fire that is not within proximity of fire personnel but located on the peak of a hill can still cause propagation and communication problems. This simulation is not exhaustive, but it is here to illustrate the need to look beyond the proximity of a fire to personnel and consider the overall propagation scenario.

A representative background environment has been created using a gaussian shaped hill that is 15m high and is a perfectly electrical conductor. A representation of the geometry is shown in Figure 7.11. This background environment provides a reference solution which, the other simulations will be related.

Added to the background environment is a fire, located on the peak of the hill. The fire temperature profile is described using the mathematical model developed in to Section 3.4 and the parameters used are shown in Table 7.1.

The fuel description is encompassed in the bushfire model (See Section 3.3). It consists of a Jarrah forest with fuel loading using data from forrest fires. At this point we are less concerned with the plasma model but are concentrating on the geometry and propagation exploration.

A representation of the geometry that includes the fire is shown in Figure 7.12.

Parameter	Value
Collision Frequency (ν_{eff})	1×10^{11}
μ_y	8m
σ_y	20m
σ_x	8m
Flare Angle (θ_{fl})	20 deg
Position X	25m
Position Y	11m

Table 7.1: Flame Parameters

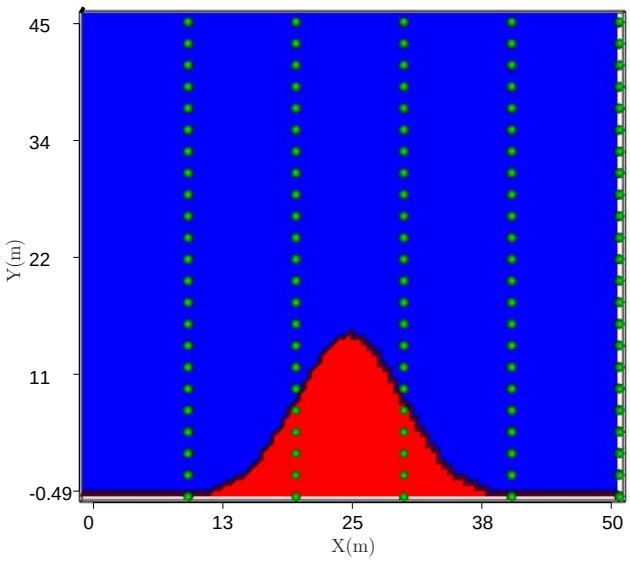

Figure 7.11: Hill Profile

The source excitation is similar to that of the refractive effect scenario and includes a time domain gaussian pulse that is excited spatially as a plane wave.

Three plots have been included in Figures 7.13 - 7.15. Each figure investigates one of the frequencies of interest (180MHz , 450MHz , 950MHz) with varying maximum profile temperature. The results are displayed in power relative to that with the hill present but no fire.

For example, considering Figure 7.13 at 180MHz the change in power due to the addition of a fire for a receiver at height 5m is a reduction by 5dB for maximum temperature of 1500°K and a reduction by approximately 18dB for a temperature of 1700°K . The main mechanism of propagation in the shadow region of the hill is by diffraction and because of this the fire has the effect of increasing the effective height of the hill and hence affects all propagation below the height of the hill. The strength of the fire (related to the maximum temperature in this model) has direct influence on the radio power received in this shadow region.

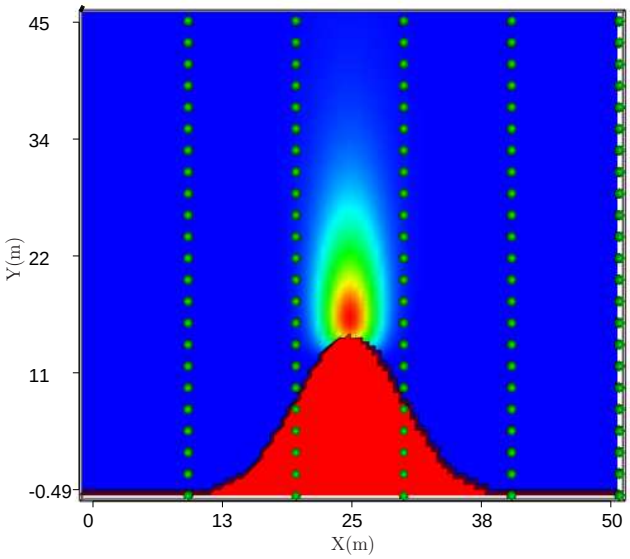

Figure 7.12: Hill and Fire Profile

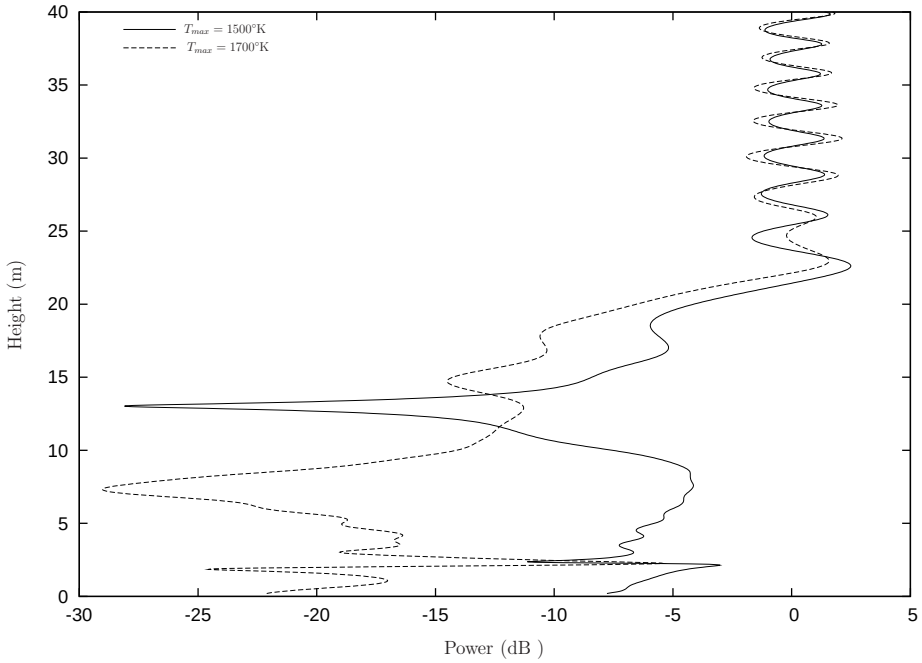

Figure 7.13: Hill top fire -180MHz

These results are also consistent for the 450MHz frequency in Figure 7.14. In this case more attenuation is experienced for a temperature of 1500°K and is closer to 10dB , compared to 5dB for 180MHz .

For the higher band at 950MHz (see Figure 7.15) the results start to deviate. Attenuation is shown at the height of fire and its intense regions at heights around 15m . At the lower heights, deep in the shadow of the hill, the relative signal power fluctuates dramatically below 10m . At this frequency such a low amount of energy is diffracted into the shadow region that the presence of the fire is not registered. As a consequence, results in terms of a relative power distribution must be treated with caution.

At frequencies where diffractive energy would allow communication, for example at 180MHz and 450MHz , the effect of the fire is substantial in the shadow region of the hill.

7.2.1 Summary

A much larger area of radio propagation research has been opened through these two examples. The refractive scenario has shown that refractive effects in the near vicinity of a fire are dramatic but are insufficient to destroy a communication link. By comparison,

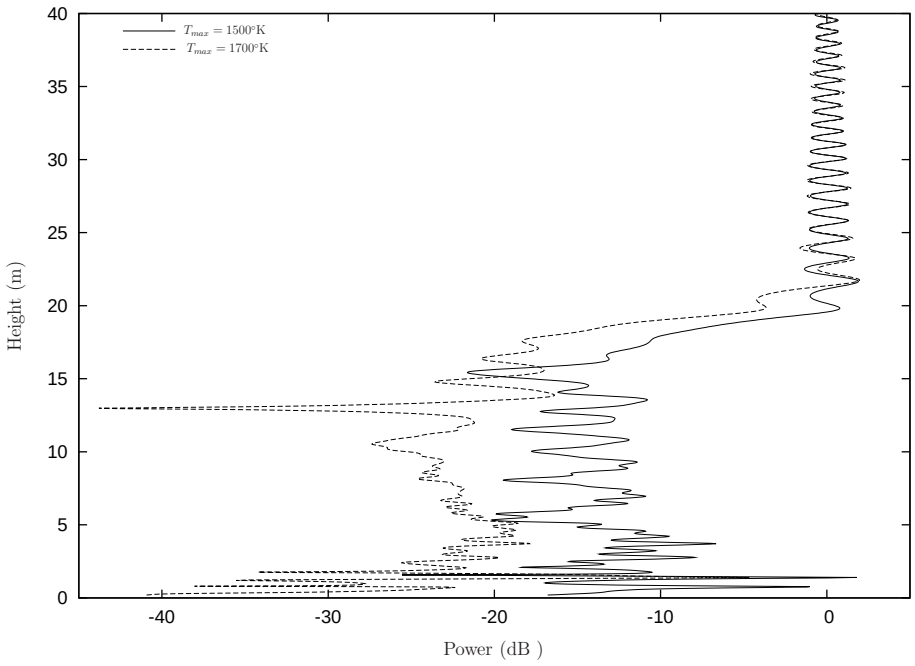

Figure 7.14: Hill top fire - 450MHz

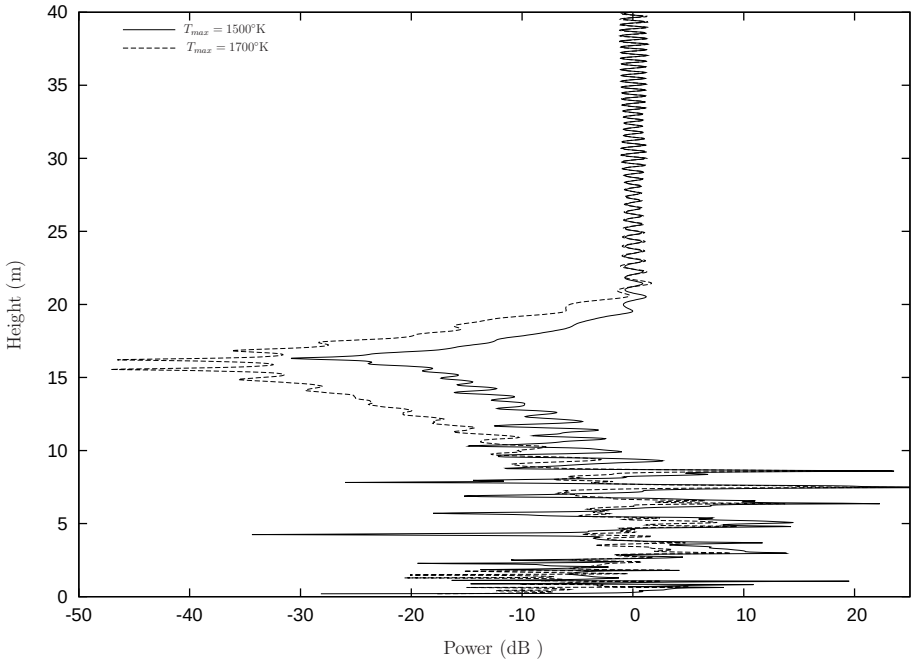

Figure 7.15: Hill top fire - 950MHz

plasma effects are a dominant factor in propagation. Over a long communication link, however, refractive effects can accumulate and become a significant factor. The scenarios in this chapter serve as a warning of the possible effect that fire can have over a wide area.

SECTION 8

Conclusions and Comments

This work began with the hope of providing a scientific framework to study radio communications in fire environments. Its intention was to address the concern of fire fighters, with regards to reliability of radio devices in extreme fire environments, and provide understanding to the scientific community.

In the pursuit of such a goal the initial undertaking was to establish experimentally a propagation problem. Broadband radio propagation experiments with small scale fires demonstrated a number of propagation effects are present. These experiments have clearly demonstrated that attenuation of radio energy occurs when a fire is present. The amount of attenuation has been found to be dependent on the frequency band used and the presence of a fire on the line of sight propagation path. Correlation with a fire's intensity and size have been demonstrated, showing combustion involving plant life is sufficient to cause communication problems and artificial additives can further exacerbate problems.

Literature and previous studies involving flames stipulate that a combustion induced plasma exists in flames. Simple propagation theory and modelling has shown the presence of a combustion induced plasma causes broadband attenuation of radio waves. Utilising more complex propagation modelling, it was found that frequency dependent attenuation is produced, not from the plasma alone, but from the combination of three dimensional geometry and broadband plasma attenuation. Furthermore, as the frequency increases radio propagation grows in complexity. This inhibits the predictive power of modelling techniques to accurately predict radio propagation.

8.1 Summary of Findings

The experimental portion of this work has established a number of important points. Radio propagation through a fire is disrupted resulting in a change in signal characteristics which, has been verified over a number of fires of different size and fuel. Signal's below 600MHz were observed to have a reduction in signal strength in the presence of fire. Signal's above 600MHz were observed to have either an enhancement or reduction in signal strength depending on the fuel characteristics and propagation environment.

Throughout the experimentation it was found that different communication bands vary in their response to the presence of fire in the environment. Communication from 400MHz - 450MHz (common to modern UHF Emergency services radio transmission) were found to be very strongly attenuated. For a bonfire, typical power reduction was measured to be from 10dB to 15dB . This has been highlighted throughout this work as a significant problem, which will contribute to major communication problems. Lower communication bands from 100MHz - 180MHz (common to modern VHF radio transmission) were observed to have a typical power reduction of 3dB to 6dB . It has been shown that, although power loss is not desirable, this band has other propagation factors (longer wavelength and diffraction) which will aid in sustaining communication in problematic environments.

From the literature it was identified that combustion induced plasma is the cause of variation in a signal's characteristics. A theoretical framework was developed to investigate the effects of the refractive index in the fire's surrounding atmosphere and modelling of the combustion plasma using cold plasma physics.

The refractive index model considered a chemically stable representation of the atmosphere with varying constituent gases. It was found that the refractive index variation has a relatively small effect on radio propagation throughout the frequency range of interest (100MHz - 1GHz). Simulations showed that refractive effects are small in nature and require a reasonable distance to accumulate and be problematic.

In this work the combustion induced plasma has been modelled using a thermal ionisation cold plasma model. Variations in temperature, fuel and fire characteristics all contribute to form a volume of free ionised electrons in the combustion and flame regions. Special attention has been paid to calculating the collision frequency in fire environments.

The collision frequency has been found to be relatively high and dominates the plasma behaviour resulting in broadband attenuation characteristics. The electron density, which is a function of the fuel and its alkali mass, contributes to the level of attenuation with larger ionised populations greatly increasing the attenuation upon radio propagation. All of the above depends on having a good characterisation of the chemistry and dynamics of the fire. It is a hallmark of the current studies that we have adopted existing modelling of the physics of fire to provide us with a realistic picture of the these aspects.

By utilising a three dimensional Finite Difference Time Domain electromagnetic propagation algorithm it was demonstrated that combustion plasma interactions and diffraction were the key propagation mechanisms involved in the fire experiments. The combustion plasma causes frequency independent attenuation as a radio waves propagates through fire. By introducing three dimensional geometry, a frequency variation results which is caused by more complex electromagnetic propagation and indicates diffraction recovery of the signal. Recognising the importance of three dimensional geometry to this problem, further exploration of fuel heap interactions was possible. It was demonstrated that as the fuel heap deteriorates, and collapses, greater sensitivity to these changes was experienced at higher frequencies. Understanding this sensitivity with relation to frequency added to our understanding of the fire experiments and their development over time. Higher frequencies recover to pre-burn signal power levels quicker due to greater sensitivity to the fuel heap. We can now see that the problematic band of frequencies (400MHz - 450MHz) is affected by the attenuation of the fire and the lack of diffraction recovery. The combination of these two factors leads to a dangerous scenario for modern communication in these bands.

8.2 Future Work

The main direction of future work is towards extending the fire environment from small scale fires to larger bushfire scenarios and to include the effects of fluctuations (turbulence) in the fire.

8.2.1 Experimental Work

The experimental work performed in this research has extended our knowledge of interactions with electromagnetic energy and flames, taking our knowledge from the small scale flames in the laboratory to larger propagation distances (10m-20m) with flame diameters on the scale of meters. This has been a important step to allow a transfer of knowledge from scientific laboratory work to bonfires and ultimately large scale bushfires.

Greater exploration and experimentation is required to extend our understanding into much more complex propagation scenarios involving bushfire. Bridging the current gap in knowledge and providing greater understanding in these environments is the prime aim of this research. A possible means to experiment in these environments has been proposed through the use of single frequency transmitters and receivers which, allow one to monitor multiple propagation paths simultaneously has already been developed. Higher resolution propagation data in time would also be highlighted as an important feature. The current method has helped in understanding the overall effects of the fire upon propagation but to properly model and predict communication channel conditions greater time resolution is required. Importantly, we need to understand the effect of turbulence upon the radio signal. This will cause Doppler and range spreading to the signal, resulting in degradation in the quality of the communication channel.

Aside from the propagation aspect there is a greater need for gathering fire characteristics in bushfire environments. Measurements of temperature and fuel analysis is necessary to refine and further improve the modelling based on this experimental work.

8.2.2 Modelling

There is substantial room for improvement on the modelling side of this work. A more accurate and reliable ionisation model should be used, particularly the inclusion of chemi-ionisation and its contribution to the electron population. Further improvement can be made in the understanding of fuel transport and the chemical change that occurs in plant life as it moves from solid to gaseous states.

As the work moves into understanding propagation on a much larger scale, other environmental factors should be explored. The understanding of a fire atmosphere with

inclusion of inversion layers should be considered. Additionally, scattering effects have been mentioned in this work but not rigorously modelled and should become more important as turbulence or smoke plume dynamics have a greater influence over a larger propagation environment.

8.2.3 Propagation Simulation

The numerical Finite Difference Time Domain simulation method presented here has been adequate to investigate propagation for small scale fires. For very large propagation scenarios it is a very inefficient means to study propagation. As the work moves to consider much larger propagation scenarios for single frequency operation a more efficient method should be considered, such as a three dimensional Parabolic Equation method or a three dimensional Kirchoff integral method that has already been applied to this work[23].

As our understanding of propagation in these environments increases more emphasis should be placed on the communication channel and developing stochastic models more in line with the current communication literature. A semi-empirical propagation model could easily be developed with the use of higher resolution propagation data.

This page is blank

APPENDIX A

Chemical Data

A.1 Collision Frequency Data

Temp. °C	100	200	300	400	500	1000	1500
H_2O	158.000	107.000	84.900	71.500	62.300	39.300	29.300
CO_2	10.100	10.140	10.100	9.960	9.760	8.040	6.450
CO	0.532	0.712	0.950	1.210	1.480	2.790	3.990
CH_4	1.510	0.987	0.719	0.568	0.480	0.396	0.486
O_2	0.123	0.237	0.335	0.425	0.512	0.956	1.410
N_2O	33.620	3.620	3.620	3.610	3.600	3.570	3.610
NO	0.589	0.528	0.566	0.673	0.859	2.730	4.880
H	3.440	4.850	5.890	6.720	7.420	9.810	11.300
He	0.448	0.654	0.820	0.963	1.090	1.620	2.050
O	0.081	0.138	0.192	0.245	0.297	0.551	0.800
Ne	0.037	0.063	0.088	0.114	0.139	0.258	0.368
Ar	0.341	0.293	0.243	0.203	0.173	0.110	0.126
Kr	2.040	2.010	1.840	1.650	1.470	0.885	0.621
Xe	6.420	6.130	5.510	4.890	4.330	2.520	1.670
Cs	83.000	73.700	69.500	84.500	123.000	360.000	397.000
Hg	1.870	2.470	3.750	6.450	10.300	29.400	39.600
H_2	0.686	1.060	1.390	1.700	199.000	3.270	4.400
N_2	0.255	0.491	0.723	0.948	1.170	2.110	2.860
NH_3	75.200	57.700	46.800	39.300	33.800	20.500	15.300

Table A.1: Effective Collision Frequency < 2000°C [54]

Temp. °C	2000	2500	3000	3500	4000	4500	5000
H_2O	23.700	20.100	17.600	15.800	14.500	13.400	12.500
CO_2	5.340	4.610	4.140	3.860	3.710	3.680	3.740
CO	5.180	6.410	7.660	8.840	9.880	10.800	11.500
CH_4	0.636	0.822	1.040	1.290	1.580	1.910	2.260
O_2	1.870	2.320	2.730	3.080	3.400	3.680	3.920
N_2O	3.770	4.080	4.540	5.130	5.780	6.460	7.130
NO	6.460	7.490	8.130	8.540	8.790	8.940	9.060
H	12.200	12.900	13.400	13.800	14.100	14.300	14.500
He	2.410	2.740	3.030	3.300	3.550	3.780	4.000
O	1.040	1.280	1.410	1.730	1.940	2.140	2.340
Ne	0.468	0.561	0.648	0.728	0.805	0.876	0.945
Ar	0.185	0.272	0.379	0.504	0.643	0.795	0.960
Kr	0.517	0.504	0.556	0.658	0.802	0.984	1.200
Xe	1.290	1.180	1.250	1.450	1.760	2.180	2.640
Cs	350.000	292.000	242.000	202.000	171.000	147.000	128.000
Hg	44.400	46.700	47.800	48.100	48.100	47.900	47.600
H_2	5.410	6.330	7.160	7.920	8.610	9.250	9.830
N_2	3.490	4.080	4.720	5.440	6.230	7.080	7.960
NH_3	12.600	11.000	9.830	8.990	8.340	7.810	7.380

Table A.2: Effective Collision Data > 2000°C , $< \nu_{eff} > \times 10^{-14} sec^{-1} m^{-3}$ [54]

A.2 JANAF-NIST Thermo-chemical Data

JANAF-NIST thermochemical data for different elements of interest.

$$\frac{n_{X^+}n_{e^-}}{n_X} = \frac{2}{\Lambda^3}\frac{IPF_{X^+}}{IPF_X}\exp\left[\frac{-c_2 IP_X}{T}\right] \tag{A.1}$$

where IPF_X is the Internal Partition Function of a element X and IP_X is the ionisation potential for element X.

$$\Lambda = \sqrt{\frac{h^2}{2\pi m_e k_B T}} \tag{A.2}$$

Internal Partition Function

$$IPF = \sum_{i=1}^{n} g_i \exp\left(\frac{-c_2\epsilon_i}{T}\right) \tag{A.3}$$

where $c_2 = 1.43879 \times 10^{-2}$ is the second radiation constant.

A.2.1 Ca Chemical Data

Ionisation Potential = 4930595 $A_r = 40.078$

State	$\epsilon_i\ cm^{-1}$	g_i
1	0.0	1
2	1515790.1	1
3	1521006.3	3
4	1531594.3	5

A.2.2 Ca^+ Chemical Data

Ionisation Potential = 9575187 $A_r = 40.078$

State	$\epsilon_i\ cm^{-1}$	g_i
1	0.0	2
2	1365010.0	4
3	1371080.0	6
4	2519150.0	2
5	2541440.0	4

A.2.3 Cl Chemical Data

Ionisation Potential = 10459100 $A_r = 35.453$

State	$\epsilon_i\ cm^{-1}$	g_i
1	0.0	4
2	88236.0	2

A.2.4 Cl^- Chemical Data

$A_r = 35.453$

State	$\epsilon_i\ cm^{-1}$	g_i
1	0.0	1

A.2.5 Cl^+ Chemical Data

Ionisation Potential = 19207000 $A_r = 35.343$

State	$\epsilon_i\ cm^{-1}$	g_i
1	0.0	5
2	69610.0	3
3	99640.0	1
4	1165350.0	5
5	2787780.0	1

A.2.6 K Chemical Data

Ionisation Potential = 3500978 $A_r = 39.098$

State	$\epsilon_i\ cm^{-1}$	g_i
1	0.0	2
2	1298517.0	2
3	1304287.6	4
4	2102655.1	2
5	3499120.0	4

A.2.7 K^+ Chemical Data

Ionisation Potential = 3500978 $A_r = 39.098$

State	$\epsilon_i\ cm^{-1}$	g_i
1	0.0	1

A.2.8 Mg Chemical Data

Ionisation Potential = 6167102 $A_r = 24.305$

State	$\epsilon_i\ cm^{-1}$	g_i
1	0.0	1
2	2185040.5	1
3	2187046.4	3
4	2191117.8	5
5	3505126.4	3

A.2.9 Mg^+ Chemical Data

Ionisation Potentail = 12126761 $A_r = 24.305$

State	$\epsilon_i\ cm^{-1}$	g_i
1	0.0	2
2	3566931.0	2
3	3576088.0	4

A.2.10 O Chemical Data

Ionisation Potential = 10983702 $A_r = 16.000$

State	$\epsilon_i\ cm^{-1}$	g_i
1	0.0	5
2	15826.5	3
3	22697.7	1
4	1586786.2	5
5	3379258.3	1

A.2.11 O^- Chemical Data

$A_r = 16.000$

State	$\epsilon_i\ cm^{-1}$	g_i
1	0.0	4
2	17708.0	2

A.2.12 O^+ Chemical Data

Ionisation Potential = 28324000 $A_r = 16.000$

State	$\epsilon_i\ cm^{-1}$	g_i
1	0.0	4
2	2681070.0	6
3	2683050.0	4
4	4046690.0	4
5	4046840.0	2

A.3 Refractive Index Data

Below is a set of refractive elements for a pure gas under conditions 15°C and pressure of 101.3kPa .

A.3.1 O_2 refractive

$$n_{O_2} = 1 + 10^{-8}\left(k_0 + \frac{k_1}{k_2 - \sigma^2}\right) \tag{A.4}$$

k_0 20564.8

k_1 24.80899

k_2 4.09×10^9

Where $k_0 = 20564.8$, $k_1 = 24.80899$, $k_2 = 4.09 \times 10^9$, $\sigma = 1/\lambda$ where λ is in cm

$$F_k = K_0 + K_1\sigma^2 + K_2\sigma^2 \tag{A.5}$$

K_0 1.096

K_1 1.385×10^{-11}

K_2 1.448×10^{-20}

where $K_0 = 1.096$, $K_1 = 1.385 \times 10^{-11}$, $K_2 = 1.448 \times 10^{-20}$. Data taken from [108].

A.3.2 CO refractive

$$n_{CO_2} = 1 + 10^{-8} \left(k_0 + \frac{k_1}{k_2 - \sigma^2} \right) \tag{A.6}$$

where $k_0 = 22851$, $k_1 = 0.456 \times 10^{12}$, $k_2 = 71427^2$.

k_0 22851

k_1 0.456×10^{12}

k_2 71427^2

Data taken from [108].

A.3.3 CO_2 refractive

$$n_{CO_2} = 1 + 10^{-3} k_0 \left(\frac{k_1}{k_2 - \sigma^2} + \frac{k_3}{k_4 - \sigma^2} + \frac{k_5}{k_6 - \sigma^2} + \frac{k_7}{k_8 - \sigma^2} + \frac{k_9}{k_{10} - \sigma^2} \right) \tag{A.7}$$

k_0 1.1427×10^6

k_1 5799.25

k_2 128908.9^2

k_3 120.05

k_4 89223.8^2

k_5 5.3334

k_6 75037.5^2

k_7 4.3244

k_8 67837.7^2

k_9 0.1218145×10^{-4}

k_{10} 2418.136^2

At 15°C , pressure $101325Pa$. Data taken from [108].

A.3.4 N_2 refractive

$$n_{N_2} = 1 + 10^{-8}\left(k_0 + \frac{k_1}{k_2 - \sigma^2}\right) \tag{A.8}$$

k_0 6498.2

k_1 307.43305×10^{12} Data taken from [108].

k_2 14.4×10^9

A.3.5 Ar refractive

$$n_{Ar} = 1 + 10^{-8}\left(k_0 + \frac{k_1}{k_2 - \sigma^2}\right) \tag{A.9}$$

k_0 6432.135

k_1 286.06021×10^{12} Data taken from [108].

k_2 14.4×10^9

A.3.6 CH_4 refractive

$$n_{CH_4} = 1 + 10^{-8}\left(k_0 + k_1\sigma^2\right) \tag{A.10}$$

k_0 46662

k_1 4.02×10^{-6}

Data taken from [108].

A.3.7 N_2O refractive

$$n_{N_2O} = 1 + 10^{-8}\left(k_0 + k_1\sigma^2\right) \tag{A.11}$$

k_0 46890

k_1 4.12×10^{-6}

Data taken from [108].

A.3.8 SF_6 refractive

$$n_{SF_6} = 1 + 10^{-8}\left(k_0 + k_1\sigma^2\right) \tag{A.12}$$

k_0 71517

k_1 4.996×10^{-6}

Data taken from [108].

A.3.9 Dry Air Refractive

$$n_{as} = 1 + \frac{k_1}{k_0 - \sigma^2} + \frac{k_3}{k_2 - \sigma^2} \tag{A.13}$$

$$n_a = 1 + (n_{as} - 1)\left(1 + 0.53 \times 10^{-6}\left(X_c - 450\right)\right) \tag{A.14}$$

k_0 238.0185

k_1 5792105

k_2 57.362

k_3 167917

At 15°C , 101324 Pa, 0% humidity , 450ppm CO_2. Data taken from [20].

A.3.10 H_2O refractive

$$n_{H_2O} = 1 + 1.022 \times 10^{-8}\left(k_0 + k_1\sigma^2 + k_2\sigma^4 + k_3\sigma^6\right) \tag{A.15}$$

k_0 $295.235\mu m^{-2}$

k_1 $2.6422\mu m^{-2}$

k_2 $-0.032380\mu m^{-4}$

k_3 $0.004028\mu m^{-6}$

At 293.15°K pressure is $1333Pa$. Data taken from [20].

APPENDIX B

Plant Data

B.1 Ash Analysis

Below are tables with a breakdown of ash. These tables are helpful when considering the alkali concentration in various plants.

NOTE:
This table is included on page 179
of the print copy of the thesis held in
the University of Adelaide Library.

Table B.1: Ash Analysis taken from [71]

Ash Analysis	Pine	Oak	Spruce	Redwood
SiO_2	39.0	11.1	32.0	14.3
Fe_2O_3	3.0	3.3	6.4	3.5
TiO_3	0.2	0.1	0.8	0.3
Al_2O_3	14.0	0.1	11.0	4.0
Mn_3O_4	Trace	Trace	1.5	0.1
CaO	25.5	64.4	25.3	6
MgO	6.5	1.2	4.1	6.6
Na_2O	1.3	8.9	8.0	18.0
K_2O	6	0.2	2.4	10.6
SO_3	0.3	2.0	2.1	7.4
Cl	Trace	Trace	Trace	18.4

Table B.2: Ash Analysis (%) taken from [116]

B.2 Eucalypt Alaki Breakdown

Below are tables for the Alkali breakdown in Eucalypts.

		K			Ca	
Eucalypts	H[a]	S[b]	B[c]	H	S	B
E.cameronii	0.002	0.037	0.529	0.003	0.0024	0.58
E. campuanulata	0.003	0.016	0.410	0.002	0.006	5.25
E. oleosa	0.054	0.160	0.625	0.270	0.160	2.00
E. saligna	0.004	0.100	0.970	0.010	0.050	0.65
E. saligna	0.006	0.075	0.440	0.025	0.064	3.88
E. maculata	0.022	0.080	0.190	0.237	0.124	2.93
E. diversicolor	0.018	0.105	0.145	0.018	0.064	0.31
E. sieberi	0.016	0.090	0.070	0.075	0.095	0.1
E. grandis	0.020	0.125	0.175	0.075	0.065	3.15
E. viminalis	0.007	0.115	0.160	0.020	0.073	2.24
E. obliqua	0.001	0.065	0.090	0.002	0.051	0.1
E. obliqua	0.006	0.059	0.266	0.008	0.022	0.43
E. diversicolor	0.009	0.12	0.35	-	0.069	2.08
E. calophylla	0.05	0.10	0.32	-	0.14	0.47
E. marginata	0.023	0.051	0.234	0.007	0.024	0.43
Other Species						
Tristania conferta	0.105	0.105	0.220	0.175	0.080	0.67
Syncarpia glomulifera	0.004	0.095	0.016	0.013	0.060	0.13
Acacia aneura	0.002	0.059	0.191	0.580	0.250	2.35
Ackama paniculata	0.210	0.110	0.265	0.049	0.061	0.32
Ceratopetalum apetalum	0.170	0.120	0.100	0.270	0.260	0.48
Tarreita actinophylla	0.090	0.290	0.166	0.075	0.076	0.88
Pinus radiata	0.028	0.094	0.073	0.115	0.090	0.56

Table B.3: Eucalypt data (%) taken from [4] (p. 96)

[a] Heartwood
[b] Sapwood
[c] Bark

Ratio of retention: uptake (Retention is the annual accumulation of nutrients in the stand; uptake is retention plus the amount of nutrient in the biogeochemical cycle.

Name	P	K	Ca
Pines	0.19	0.19	0.16
Other Conifers	0.18	0.30	0.16
Hardwoods	0.42	0.35	0.40
E. obliqua	0.34	0.23	0.17

Table B.4: Ratio of Retention [4](p. 99)

Name	Foliage	Bark	Branch	Wood
Forest				
E. diversicolor				
K	0.61-1.28	0.29-0.41	0.29-0.30	0.033-0.056
Ca	0.82-1.68	2.06-2.09	0.59-0.68	0.065-0.073
Mg	0.22-0.31	0.24-0.29	0.18-0.20	0.030-0.042
E. obliqua				
K	0.32-0.45	0.04-0.27	0.06-0.21	0.015-0.175
Ca	0.39-0.66	0.07-0.37	0.13-0.66	0.018-0.158
Plantation				
E. grandis				
K	0.53-1.43	0.24-0.53	0.32-0.57	0.13
Ca	0.38-1.38	0.77-1.94	0.22-1.06	0.15
Mg	0.15-0.44	0.16-0.25	0.04-0.21	0.03
E. saligna				
K	0.22-1.8	0.17-0.65	0.22-0.49	0.045-0.15
Ca	0.22-1.60	0.83-5.50	0.44-2.14	0.050-0.160
Mg	0.05-0.40	0.19-0.45	0.12-0.28	0.010-0.030

Table B.5: Range of measure concentrations of macro-nutrients in various components of eucalypts [4](p.136)

APPENDIX C

Modelling Input Files

C.1 Fire Dynamics Simulator - Small Scale Fires

```
 &HEAD CHID='bonwood5',TITLE='Pipers Creek Cube Fire Model for FDS vers.5 '/
&MESH IJK = 60,30,100, XB=-10.0,10.0,-10.0,10.0,0.0,60.0/
&TIME TWFIN=360.0/ Run simulation a long time to see long term effects and average
&DUMP NFRAMES=600/


Define the Reaction Types
&REAC ID='WOOD'
      FYI='Ritchie, et al., 5th IAFSS, C_3.4 H_6.2 O_2.5'
      SOOT_YIELD = 0.01
      O=2.5
      C=3.4
      H=6.2
      HEAT_OF_COMBUSTION = 11020. /

&MATL ID = 'TREE'
N_REACTIONS = 1
       NU_FUEL = 0.97
NU_WATER = 0.01
```

```
CONDUCTIVITY = 0.17
SPECIFIC_HEAT = 2.45
DENSITY = 600.0
REFERENCE_TEMPERATURE = 300.0
HEAT_OF_REACTION = 300.0/



For the leave surface model we may need to create another matl model for the moisture co
&MATL ID = 'WET_TREE'
        N_REACTIONS = 1
       NU_FUEL = 0.87
NU_WATER = 0.1
CONDUCTIVITY = 0.17
SPECIFIC_HEAT = 2.45
DENSITY = 200.0
REFERENCE_TEMPERATURE = 200.0
HEAT_OF_REACTION = 200.0/


&SURF ID='TRUNK'
COLOR = 'BROWN'
        BURN_AWAY            = .TRUE.
MATL_ID       = 'TREE'
        THICKNESS            = 0.028
        BACKING              = 'EXPOSED'/

&SURF ID='LEAVE'
COLOR = 'GREEN'
MATL_ID      = 'WET_TREE'
THICKNESS      = 0.028
BURN_AWAY      = .TRUE.
        BACKING              = 'EXPOSED'/
```

```
&SURF ID='GRASS'
RGB                  = 0.0,1.0,0.1
        BURN_AWAY            = .FALSE.
MATL_ID      = 'WET_TREE'
THICKNESS      = 0.028
        BACKING              = 'INSULATED'/

&SURF ID='FIRE',HRRPUA=15000.0,COLOR = 'RED' /

NOT USED !! But included to simulate a wind in the atmosphere
CSURF ID='WIND',VEL=0.0, PROFILE='ATMOSPHERIC',Z0=27.0,PLE = 0.15/
CSURF ID='WIND',VEL=-1.0, PROFILE='ATMOSPHERIC',Z0=27.0,PLE = 0.15/
CSURF ID='WIND',VEL=-3.0, PROFILE='ATMOSPHERIC',Z0=27.0,PLE = 0.15/
CSURF ID='WIND',VEL=-5.0, PROFILE='ATMOSPHERIC',Z0=27.0,PLE = 0.15/

&VENT MB='XMIN' ,SURF_ID='OPEN' / All open boundaries
&VENT MB='XMAX' ,SURF_ID='OPEN' /
&VENT MB='ZMAX' ,SURF_ID='OPEN' /
CCVENT MB='ZMIN' ,SURF_ID='INERT' /
&VENT MB='YMIN' ,SURF_ID='OPEN' /
&VENT MB='YMAX' ,SURF_ID='OPEN' /


model for a rapidly spreading fire over a rectangular area

&SURF ID = 'bushfire', HRRPUA=2500.0, RAMP_Q='fireramp',COLOR='RED'/
&RAMP ID = 'fireramp',T=0.0,F=0.0/
&RAMP ID = 'fireramp',T=1.0,F=1.0/
&RAMP ID = 'fireramp',T=30.0,F=1.0/
&RAMP ID = 'fireramp',T=31.0,F=0.0/
VENT XB = -2.0,2.0,-2.5,2.5,0.0,0.0, SURF_ID='bushfire',XYZ=0.5,1.0,0.0,SPREAD_RATE
end of model of rapidly spreading fire
```

```
OBST XB=-1.5,1.5,-1.2,1.2,2.51,3.7,SURF_ID='FIRE',DEVC_ID='time_fire'/ Trying a pilot fl

&VENT XB=-2.5,-1.5,-1.5,1.5,0.0,0.0, SURF_ID='FIRE', DEVC_ID = 'time_fire' /


&DEVC XYZ=0.1,0.1,0.1, ID='time_fire', SETPOINT= 35.0, QUANTITY='TIME', INITIAL_STATE=.T

Data to save !!
&SLCF PBY=0.0,QUANTITY='TEMPERATURE'/
&SLCF PBY=0.0,QUANTITY='oxygen'/
&SLCF PBY=0.0,QUANTITY='water vapor'/
&SLCF PBY=0.0,QUANTITY='nitrogen'/
&SLCF PBY=0.0,QUANTITY='carbon dioxide',VECTOR=.TRUE./
&SLCF PBY=0.0,QUANTITY='fuel',VECTOR=.TRUE./
&SLCF PBY=0.0,QUANTITY='DENSITY'/
&SLCF PBY=0.0,QUANTITY='carbon monoxide'/
&SLCF PBY=0.0,QUANTITY='soot volume fraction'/
&SLCF PBY=0.0,QUANTITY='soot density'/
PL3D DTSAM=TWFIN/5,QUANTITIES='TEMPERATURE','U-VELOCITY','V-VELOCITY','W-VELOCITY','HRRP


Main Fuel Block
&OBST XB=-3.5,3.5,-3.5,3.5,0.5,4.5,SURF_ID='TRUNK'/

Hole generation by HoleGen3D
Thickness: 0.1\nX(-4,4) - Y(-4,4) - Z(0.5,4.5) \n
&HOLE XB = -3.95 ,-3.85 , -4.00 ,  4.00 ,  0.50 ,  4.50 /
&HOLE XB = -3.55 ,-3.45 , -4.00 ,  4.00 ,  0.50 ,  4.50 /
&HOLE XB = -3.15 ,-3.05 , -4.00 ,  4.00 ,  0.50 ,  4.50 /
&HOLE XB = -2.75 ,-2.65 , -4.00 ,  4.00 ,  0.50 ,  4.50 /
&HOLE XB = -2.35 ,-2.25 , -4.00 ,  4.00 ,  0.50 ,  4.50 /
&HOLE XB = -1.95 ,-1.85 , -4.00 ,  4.00 ,  0.50 ,  4.50 /
```

```
&HOLE XB = -1.55 ,-1.45 , -4.00 ,  4.00 ,  0.50 ,  4.50 /
&HOLE XB = -1.15 ,-1.05 , -4.00 ,  4.00 ,  0.50 ,  4.50 /
&HOLE XB = -0.75 ,-0.65 , -4.00 ,  4.00 ,  0.50 ,  4.50 /
&HOLE XB = -0.35 ,-0.25 , -4.00 ,  4.00 ,  0.50 ,  4.50 /
&HOLE XB =  0.05 , 0.15 , -4.00 ,  4.00 ,  0.50 ,  4.50 /
&HOLE XB =  0.45 , 0.55 , -4.00 ,  4.00 ,  0.50 ,  4.50 /
&HOLE XB =  0.85 , 0.95 , -4.00 ,  4.00 ,  0.50 ,  4.50 /
&HOLE XB =  1.25 , 1.35 , -4.00 ,  4.00 ,  0.50 ,  4.50 /
&HOLE XB =  1.65 , 1.75 , -4.00 ,  4.00 ,  0.50 ,  4.50 /
&HOLE XB =  2.05 , 2.15 , -4.00 ,  4.00 ,  0.50 ,  4.50 /
&HOLE XB =  2.45 , 2.55 , -4.00 ,  4.00 ,  0.50 ,  4.50 /
&HOLE XB =  2.85 , 2.95 , -4.00 ,  4.00 ,  0.50 ,  4.50 /
&HOLE XB =  3.25 , 3.35 , -4.00 ,  4.00 ,  0.50 ,  4.50 /
&HOLE XB =  3.65 , 3.75 , -4.00 ,  4.00 ,  0.50 ,  4.50 /
&HOLE XB = -4.00 ,  4.00 , -4.00 ,  4.00 , 0.55 ,  0.65 /
&HOLE XB = -4.00 ,  4.00 , -4.00 ,  4.00 , 0.95 ,  1.05 /
&HOLE XB = -4.00 ,  4.00 , -4.00 ,  4.00 , 1.35 ,  1.45 /
&HOLE XB = -4.00 ,  4.00 , -4.00 ,  4.00 , 1.75 ,  1.85 /
&HOLE XB = -4.00 ,  4.00 , -4.00 ,  4.00 , 2.15 ,  2.25 /
&HOLE XB = -4.00 ,  4.00 , -4.00 ,  4.00 , 2.55 ,  2.65 /
&HOLE XB = -4.00 ,  4.00 , -4.00 ,  4.00 , 2.95 ,  3.05 /
&HOLE XB = -4.00 ,  4.00 , -4.00 ,  4.00 , 3.35 ,  3.45 /
&HOLE XB = -4.00 ,  4.00 , -4.00 ,  4.00 , 3.75 ,  3.85 /
&HOLE XB = -4.00 ,  4.00 , -4.00 ,  4.00 , 4.15 ,  4.25 /
&HOLE XB = -4.00 ,  4.00 , -3.95 , -3.85 , 0.50 ,  4.50 /
&HOLE XB = -4.00 ,  4.00 , -3.55 , -3.45 , 0.50 ,  4.50 /
&HOLE XB = -4.00 ,  4.00 , -3.15 , -3.05 , 0.50 ,  4.50 /
&HOLE XB = -4.00 ,  4.00 , -2.75 , -2.65 , 0.50 ,  4.50 /
&HOLE XB = -4.00 ,  4.00 , -2.35 , -2.25 , 0.50 ,  4.50 /
&HOLE XB = -4.00 ,  4.00 , -1.95 , -1.85 , 0.50 ,  4.50 /
&HOLE XB = -4.00 ,  4.00 , -1.55 , -1.45 , 0.50 ,  4.50 /
&HOLE XB = -4.00 ,  4.00 , -1.15 , -1.05 , 0.50 ,  4.50 /
&HOLE XB = -4.00 ,  4.00 , -0.75 , -0.65 , 0.50 ,  4.50 /
&HOLE XB = -4.00 ,  4.00 , -0.35 , -0.25 , 0.50 ,  4.50 /
```

```
&HOLE XB = -4.00 ,  4.00 ,  0.05 ,  0.15 , 0.50 ,  4.50 /
&HOLE XB = -4.00 ,  4.00 ,  0.45 ,  0.55 , 0.50 ,  4.50 /
&HOLE XB = -4.00 ,  4.00 ,  0.85 ,  0.95 , 0.50 ,  4.50 /
&HOLE XB = -4.00 ,  4.00 ,  1.25 ,  1.35 , 0.50 ,  4.50 /
&HOLE XB = -4.00 ,  4.00 ,  1.65 ,  1.75 , 0.50 ,  4.50 /
&HOLE XB = -4.00 ,  4.00 ,  2.05 ,  2.15 , 0.50 ,  4.50 /
&HOLE XB = -4.00 ,  4.00 ,  2.45 ,  2.55 , 0.50 ,  4.50 /
&HOLE XB = -4.00 ,  4.00 ,  2.85 ,  2.95 , 0.50 ,  4.50 /
&HOLE XB = -4.00 ,  4.00 ,  3.25 ,  3.35 , 0.50 ,  4.50 /
&HOLE XB = -4.00 ,  4.00 ,  3.65 ,  3.75 , 0.50 ,  4.50 /
```

BIBLIOGRAPHY

[1] F. Akleman and L. Sevgi. A novel finite-difference time-domain wave propagator. *IEEE Transactions on Antennas and Propagation*, 48(3):839, March 2000.

[2] F. Akleman and L. Sevgi. Realistic surface modeling for a finite-difference time-domain wave propagator. *IEEE Transactions on Antennas and Propagation*, 51(7):1675, July 2003.

[3] K. C. Allen and H. J. Liebe. Tropospheric absorption and dispersion for terrestrial or earth-satellite path. *IEEE Transactions on Antennas and Propagation*, 31(1):221, 1983.

[4] Peter M. Attiwill and Mark A. Adams. *Nutrition of Eucalypts*. CSIRO, 1996.

[5] L. P. Bayvel and A. R. Jones. *Electromagnetic scattering and its applications*. London, Applied Science Publishers, 1981. 303 p., 1981.

[6] H. Belcher and T. M. Sugden. Studies on the ionization produced by metallic salts in flames i. the determination of collision frequency of electrons in coal-gas/air flames. *Proceedings of the Royal Society of London, Series A*, 201:480–488, 1949.

[7] H. Belcher and T.M. Sugden. Studies on the ionization produced by metallic salts in flames ii. reactions governed by ionic equilibria in coal-gas/air flames containing alkali metal salts. *Proceedings of the Royal Society of London, Series A*, 202:17–39, 1949.

[8] J. P. Berenger. A perfectly matched layer for the absorption of electromagnetic waves. *Journal Computational Physics*, October 1994.

[9] H. C. Bolton and I. G. McWilliam. Ionization in flames: current-voltage relationships for the flame ionization detector. *Proceedings of the Royal Society of London, Series A*, 321:361–380, 1971.

[10] A. J. Borgers. On the application of the high frequency resonance method in the analysis of flame ionization. *10th Symposium on Combustion*, pages 627–637, 1965.

[11] Max Born and Emil Wolf. *Principles of Optics: Electromagnetic Theory of Propagation, Interference and Diffraction of Light*. Pergamon, 1970.

[12] M. Q. Brewster and T. Kunitomo. The optical constants of coal, char and limestone. *Journal of Heat Transfer*, 106:678, 1984.

[13] K. G. Budden. *The propagation of radio waves*. Cambridge University Press, 1985.

[14] H. F. Calcote. Mechanisms for the formation of ions in flames. *Combustion and Flame*, 1:385, 1957.

[15] H. F. Calcote. Ion and electron profiles in flames. *Ninth Symposium on Combustion*, 1963.

[16] Cantera. Cantera: Open source object oriented software for reacting flows. *http://www.cantera.org/*.

[17] CFA. Reducing the risk of entrapment in wildfires - a case stud of the linton fire. Technical report, Country Fire Association, Victoria, July 1999 1999.

[18] M.W. Chase. NIST-JANAF thermochemical tables. *Journal of Physical and Chemical Reference Data, Monograph 9*, 1998.

[19] Philip E. Ciddor. Refractive index of air: new equations for the visible and near infrared. *Applied Optics*, 35(9):1566, 1996.

[20] Philip E. Ciddor. Refractive index of air: 3. the roles of CO2, H2O, and refractivity virials. *Applied Optics*, 41(12):2292, 2002.

[21] Philip E. Ciddor and Reginald J. Hill. Refractive index of air. 2. group index. *Applied Optics*, 38(9):1663, 1999.

[22] Terry L Clark, Mary Ann Jenkins, Janice Coln, and David Packham. A coupled atmosphere - fire model: Convective feedback on fire-line dynamics. *Journal of Applied Meteorology*, 35(June):875 – 901, 1996.

[23] C. J. Coleman and J. A. Boan. A kirchoff integral approach to radio wave propagation in fire. *IEEE Antennas and Propagation Symposium, Hawaii, Honolulu*, 2007.

[24] Chris J. Coleman. A kirchoff integral approach to estimating propagation in an environment with nonhomogeneous atmosphere and complex boundaries. *IEEE Transactions on Antennas and Propagation*, 53(10):3174, October 2005.

[25] G. Cox. Turbulent closure and the modelling of fire by using computational fluid dynamics. *Philosophical Transactions of The Royal Society London A*, 356:2835–2854, 1998.

[26] S. A. Cummer. An analysis of new and existing FDTD methods for isotropic cold plasma and a method for improving their accuracy. *IEEE Transactions on Antennas and Propagation*, 45(3):392, March 1997.

[27] S. J. Melinek D. Boothman, J. Lawton and F. Weinberg. Rates of ion generation in flames. *12th International Symposium on Combustion*, page 969, 1969.

[28] Richard J. French David C. Dayton and Thomas A. Milne. Direct observation of alkali vapor release during biomass combustion and gasification. 1. applicaiton of molecular beam/mass spectrometry to switchgrass combustion. *Energy and Fuels*, 1995.

[29] R. S. Davis. Equation for the determination of the density of moist air (1981/91). *Metrologia*, 29:67–70, 1992.

[30] D. Dence and T. Tamir. Radio loss of lateral waves in forest environments. *Radio Science*, 4(4):307, 1969.

[31] M. A. El-Rayes and F. T. Ulaby. Microwave dielectric spectrum of vegetation - part 1: Experimental observations. *IEEE Transactions on Geoscience Electronics*, 25(5):541, September 1987.

[32] D.C. Dayton et al. Release of inorganic constituents from leached biomass during thermal conversion. *Energy and Fuels*, 13:860–870, 1999.

[33] H. J. Liebe et al. Propagation modeling of moist air and suspended water/ice particles at frequencies below 1000ghz. *AGARD*, pages 3/1–10, May 1993.

[34] Jiayuan Fang and Zhonghua Wu. Numerical implementation and performance of perfectly matched layer boundary condition for waveguide structures. *IEEE Transactions on Microwave Theory and Techniques*, 43(12):2767, 1995.

[35] Jiayuan Fang and Zhonghua Wu. Generalized perfectly matched layer for the absorption of propagating and evanescent waves in lossless and lossy media. *IEEE Transactions on Microwave Theory and Techniques*, 44(12):2216, 1996. Generalized PML for all media, uses stretched coordinates.

[36] Jiayuan Fang and Zhonghua Wu. High performance PML algorithms. *IEEE Microwave and Guided Wave Letters*, 6(9):335, 1996.

[37] FDS. Fire dynamics simulator. *http://www.fds-smv.net*.

[38] P. J. Foster and c. R. Howarth. Optical constants of carbons and coals in the infrared. *Carbon*, 6(5):436–447, 1968.

[39] L. S. Frost. Conductivity of seeded atmospheric pressure plasmas. *Journal of Applied Physics*, 32(10):2029, October 1961.

[40] M. Fusco. FDTD algorithm in curvilinear coordinates. *IEEE Transactions on Antennas and Propagation*, 38(1):76, January 1990.

[41] A. G. Gaydon and H. G. Wolfhard. *Flames: Their structure, radiation and temperature*. Chapman and Hall, 4th edition, 1979.

[42] C. D. Grant, J. M. Koch, D. T. Bell, and W. A. Loneragan. Tree species response to prescribed burns in rehabilitated bauxite mines in Western Australia. *Australian Forestry*, 60(2):84–89, 1997.

[43] C. D. Grant, W. A. Loneragan, J. M. Koch, and D. T. Bell. Fuel characteristics, vegetation structure and fire behaviour of 11-15 year-old rehabilitated bauxite mines in Western Australia. *Australian Forestry*, 60(3):147–157, 1997.

[44] J. A. Green and T. M. Sugden. Some observations on the mechanism of ionization in flames containing hydrocarbons. *Ninth Symposium on Combustion*, 1963.

[45] Ben Griffiths and Doug Booth. The Effects of Fire and Smoke on VHF Radio Communications. Technical Report COMM-REP-038-1, Country Fire Association, March 2001.

[46] A. N. Hayhurst and H. R. N. Jones. Chemi-ionization in oxyacetylene flames. *Nature*, 296, 1983.

[47] A. N. Hayhurst and D. B. Kittelson. Ionization of alkaline earth additives in hydrogen flames. ii. hydrogen atom concentrations and ion stabilities. *Proceedings of the Royal Society London A*, 338(1613):155–173, Jun 1974.

[48] M.L. Heron and K. Mphale. Radio wave attenuation in bushfires, tropical cyclones and other severe atmospheric conditions. Final Report on EMA Project 60/2001 Final Report, James Cook University, April 2004 2004.

[49] G. Heskestad. Dynamics of the fire plume. *Philosophical Transactions of The Royal Society London A*, 356:2815–2833, 1998.

[50] D. A. Hill. HF ground wave propagation over forested and built-up terrain. Technical Report "NTIA Report 82-114", "U.S. Department of Commerce", 1982.

[51] R. Holland. Finite-difference solution of maxwells equations in generalized nonorthogonal coordinates. *IEEE Transactions on Nuclear Science*, 30(6):4589–4591, 1983. Times Cited: 105 Article English Cited References Count: 3 Rz801.

[52] R. Holland. Threds - A finite-difference time-domain EMP code in 3D spherical coordinates. *IEEE Transactions on Nuclear Science*, 30(6):4592–4595, 1983. Times Cited: 21 Article English Cited References Count: 7 Rz801.

[53] P. C. F. Eggers I. Z. Kovacs and K. Olesen. Radio channel characterization for forest environments in the vhf and uhf frequency bands. *IEEE 50th Vehicular Technology Conference, Amsterdam*, 1999.

[54] Yukikazu Itikawa. Effective collision frequency of electrons in gases. *The Physics of Fluids*, 16(6):831, 1973.

[55] Ulf Jaglid John G. Olsson and Jan B. C. Pettersson. Alkali metal emission during pyrolysis of biomass. *Energy and Fuels*, 11:779–784, 1997.

[56] A. R. Jones. Electromagnetic wave scattering by assemblies of particles in the rayleigh approximation. *Proceedings of the Royal Society London A*, 366:111–127, 1979.

[57] A. R. Jones. Scattering efficiency factors for agglomerates of small spheres. *Journal of Physics D: Applied Physics*, 12:1661, 1979.

[58] J. S. Juntunen and T. D. Tsiboukis. Reduction of numberical dispersion in fdtd method through articial anisotropy. *IEEE Transactions on Microwave Theory and Techniques*, 48(4):582, 2000.

[59] M. Heron K. Mphale and T. Verma. Effect of wildfire-induced thermal bubble on radio communication. *Progress In Electromagnetics Research*, PIER 68:197–228, 2007.

[60] B.J. Stojkova K. O. Davidsson and J.B.C. Pettersson. Alkali emission from birch-wood particles during rapid pyrolysis. *Energy and Fuelds*, 16:1033–1039, 2002.

[61] Mohan Jacob Mal Heron Kgakgamatso Mphale. Prediction and measurement of electron density and collision frequency in a weakly ionised pine fire. *International Journal of Infrared and Millimetre Waves*, 28:251–262, 2007.

[62] R. F. Klemm and A. T. Blades. Ionization in hydrocarbon flames. *Nature*, 212:920, 1966.

[63] J.B.C Pettersson K.O. Davidsson, J.G. Korsgren and U. Jaglid. The effects of fuel washing techniques on alkali release from biomass. *Fuel*, 81:137–142, 2002.

[64] Michael Krumpholz and Linda P. B. Katehi. MRTD: new time-domain schemes based on multiresolution analysis. *IEEE Transactions on Microwave Theory and Techniques*, 44(4):555, April 1996.

[65] D. J. Latham. Space charge generated by wind tunnel fires. *Atmospheric Research*, 51:267–278, 1999.

[66] J. Lawton, P.J. Mayo, and F.J. Weinberg. Electrical control of gas flows in combustion processes. *Proceedings of the Royal Society of London, Series A*, 303:275–298, 1968.

[67] J. Lawton and F. J. Weinberg. Maximum ion currents from flames and the maximum practical effects of applied electric fields. *Proceedings of the Royal Society London A*, 277(1371):468–497, 1964.

[68] Mireille Levy. *Parabolic equation methods for electromagnetic wave propagation*. The Insitution of Electrical Engineers, 2000.

[69] H. J. Liebe. Modeling attenuation and phase of radio wave in air at frequencies below 1000ghz. *Radio Science*, 16(6):1183, 1981.

[70] Gang Liu and S. D. Gedney. Perfectly matched layer media for an unconditionally stable three-dimensional adi-fdtd method. *IEEE Microwave and Guided Wave Letters*, 10(7):261, July 2000.

[71] Sjaak van Loo and Jaap Koppejan. *Handbook of Biomass Combustion and Co-Firing*. Twente University Press, 2002.

[72] L.W. Li et al. Analysis of radiowave propagation in a four-layered anisotropic forest environment. *IEEE Transactions on Antennas and Propagation*, 37(4):1967, July 1999.

[73] Gates D. M. Water relations of forest trees. *IEEE Transactions on Geoscience and Remote Sensing*, 29, 1991.

[74] M. V. Smith M. Fusco and L. W. Gordon. A three-dimensional FDTD algorithm in curvilinear coordinates. *IEEE Transactions on Antennas and Propagation*, 39(10):1463, October 1991.

[75] F. Akleman M. O. Ozyalcin and L. Sevgi. A novel TLM-based time-domain wave propagator. *IEEE Transactions on Antennas and Propagation*, 51(7):1680, July 2003.

[76] E. Maouhoub, H. Coitout, and M. J. Parizet. Excitation temperature measurements in an argon-co2 thermal plasma. *IEEE Transactions on Plasma Science*, 27(5):1469, 1999.

[77] H. Margenau. Conduction and dispersion of ionzed gases at high frequencies. *Physical Review*, 69(9):May 1 1949, 1946.

[78] P.J. Mayo and F.J. Weinberg. On the size, charge and number-rate of formation of carbon particles in flames subjected to electric fields. *Proceedings of the Royal Society of London, Series A*, 319:351–371, 1970.

[79] Ron McLeod. Inquiry into the Operational Response to the January 2003 bushfires in the ACT.

[80] K.W. Morton and D. F. Mayers. *Numerical Solution of Partial Differential Equations*. Cambridge University Press, 1994.

[81] K. Mphale and M. Heron. Ray tracing radio waves in wildfire environments. *Progress In Electromagnetics Research*, PIER 67:153–172, 2007.

[82] Kgakgamatso Mphale and Mal Heron. Microwave measuremnt of electron density and collision frequency of a pine fire. *Journal of Physics D: Applied Physics*, 40:2818–2825, 2007.

[83] G. Mur. *Computation of Electromagnetic Fields in Inhomogeneous media: Scattering and Guiding Properties*. PhD thesis, 24 May 1978.

[84] R. H. Lang N. S. Chauhan and K. J. Ranson. Radar modeling of a boreal forest. *IEEE Transactions on Geoscience and Remote Sensing*, 29(4), 1991.

[85] Takefumi Namiki. A new FDTD algorithm based on alternating-direction implicit method. *IEEE Transactions on Microwave Theory and Techniques*, 1999.

[86] L. J. Nickisch and P. M. Franke. Finite-difference time-domain solution of maxwell's equations of the dispersive ionosphere. *IEEE Antennas and Propagation Magazine*, 34(5):33, 1992.

[87] James C. Owens. Optical refractive index of air: Dependence on pressure, temperature and composition. *Applied Optics*, 6(1):51, 1967.

[88] M. Stenholm P. A. Jensen and P. Hald. Deposition investigation in straw-fired boilers. *Energy and Fuels*, 11:1048–1055, 1997.

[89] K.G. Payne and F. J. Weinberg. A preliminary investigation of field-induced ion movement in flame gases and its applications. *Proceedings of the Royal Society of London, Series A*, 250:316–336, 1958.

[90] Richard M. Lucas, Mahta Moghaddam, and Natasha Cronin. Microwave scattering from mixed-species forests,queensland, australia. *IEEE Transactions on Geoscience Electronics*, 42(10):2142, October 2004.

[91] D. M. Roessler and F. F. Faxvog. Opacity of black smoke: Calculated variation with particle size and refractive index. *Applied Optics*, 18(9), May 1979.

[92] R. R. Rogers and W. O. J. Brown. Radar observations of a major industrial fire. *Bulletin of the American Meteorological Society*, 78(5):803–814, 1997. Times Cited: 7 Article English Cited References Count: 14 Xd572.

[93] J. M. Rueger. International association of geodesy, report of the ad-hoc working party on refractive indices of light, infrared and radio waves in the atmosphere of the IAG special commission SC3 - fundamental constants (SCFC). 1999.

[94] Jean M. Rueger. Refractive index formulae for radio waves. Technical report, International Congress, April 19-26 2002 2002. Very Good and Exhaustive references.

[95] Simon R. Saunders. *Antennas and Propagation for Wireless Communication Systems*. John Wiley and Sons, 1999.

[96] Jurgen Schneider and F. W. Hofmann. Absorption and dispersion of microwaves in flames. *Physical Review*, 116(2):244, 1959.

[97] K. Schofield and T. M. Sugden. Some observations on the ionization of alkali and alkaline-earth elements in hydrogen flames. *10th Symposium on Combustion*, 1965.

[98] S. Seker and A. Schneider. Stochastic model for pulsed radio transmission through stratified forests. *"IEE Proc. Microwave, Antennas, Propagation"*, 141(5), October 1994.

[99] S.S. Seker. Radio pulse transmission along mixed paths in a stratified forest. *"IEE Proc. Microwave, Antennas, Propagation"*, 136(1):13, Febuary 1989.

[100] S.S. Seker. Multicomponents discrete propagation model of forest. *"IEE Proc. Microwave, Antennas, Propagation"*, 142(3):201, June 1995.

[101] E. S. Semenov and A. S. Sokolik. Thermal and chemical ionization in flames. *Combustion, Explosion and Shock Waves*, 6(1):37, 1970.

[102] T. B. A. Senior and J. L. Volakis. *Approximate boundary conditions in electromagnetics*, volume 41 of *IEE Electromagnetic waves Series*. 1995. Oct 2004 UniSA - Mawson Lakes Collection.

[103] Levent Sevgi. *Complex Electromagnetic Problems and Numerical Simulation Approaches*. IEEE Press, 2003.

[104] A. C. Simmons. The refractive index and Lorentz-Lorenz functions of propane, nitrogen and carbon-dioxide in the spectral range 15803-22002cm-1 and 944cm-1. *Optics Communications*, 52(2):211, 1978.

[105] H. Smith and T. M. Sugden. Studies on the ionzation produced by metallic salts in flames. iii. ionic equilibria in hydrogen/air flames containing alkali metal salts. *Proceedings of the Royal Society of London, Series A*, 211(1104):31–58, 1952.

[106] H. Smith and T.M. Sugden. Studies on the ionization produced by metallic salts in flames. iii. ionic equilibria in hydrogen/air flames containing alkali metal salts. *Proceedings of the Royal Society London A*, 211(1104), 1952.

[107] H. Smith and T.M. Sugden. Studies on the ionization produced by metallic salts in flames. iv. the stability of gaseous alkali hydroxides in flames. *Proceedings of the Royal Society London A*, 211(1104), 1952.

[108] Maarten Sneep and Wim Ubachs. Direct measurement of the rayleigh scattering cross section in various gases. *Journal of Quantitative Spectroscopy and Radiative Transfer*, 92:293–310, 2005.

[109] STANJAN. Standford JANAF tables.

[110] W. L. Stutzman and G. A. Thiele. *Antenna Theory and Design*. John Wiley and Sons, 2 edition, 1998.

[111] W. Yu T. Su and R. Mittra. A new look at FDTD excitation. *IEEE Microwave and Optical Technology Letters*, 45(3):203, May 2005.

[112] A. Taflove. *Finite Differrence Time Domain Methods for Electrodynamic Analyses*. NY: Artech House, May 1995.

[113] Allen Taflove. *Computational Electromagnetics: The Finite-Difference Time-Domain Method*. Boston, MA Artech House, 1995.

[114] Allen Taflove and Morris E. Brodwin. Numerical solution of steady-state electromagnetic scatttering problems using the time-dependent maxwell's equations. *IEEE Transactions on Microwave Theory and Techniques*, 23(8):623 – 630, 1975. The first FDTD Algorithm. Taflove the father of FDTD.

[115] T. Tamir. On Radio-wave propagation in forest environments. *IEEE Transactions on Antennas and Propagation*, 15(6), 1967.

[116] David A. Tillman, Amadeo J. Rossi, and William D. Kitto. *Wood Combustion : Principles, Processes, and Economics*. Academic Press, 1981.

[117] Chirag Sathe Tsutomu Okuno Nozomu Sonoyama Jun-ichiro Hayashi Chun-Zun Li and Tadatoshi Chiba. Primary release of alkali and alkaline earth metallic species during the pyrolysis of pulverized biomass. *Energy and Fuels*, 19:2164–2171, 2005.

[118] F. T. Ulaby and M. A. El-Rayes. Microwave dielectric spectrum of vegetation - part 2: Dual-dispersion model. *IEEE Transactions on Geoscience Electronics*, 25(5):550, September 1987.

[119] Robert J. Vidmar. On the use of atmospheric pressure plasmas as electromagnetic reflectors and absorbers. *IEEE Transactions on Plasma Science*, 18(4):733, 1990.

[120] Domingos Xavier Viegas. Forest fire propagation. *Philosophical Transactions of The Royal Soceity London A*, 356:2907–2928, 1998.

[121] C. L. Wagner and J. B. Schneider. Divergent fields, charge, and capacitance in fdtd simulations. *IEEE Transactions on Microwave Theory and Techniques*, 46(12):2131, December 1998.

[122] WIA. Australian amateur radio band plans. *Wireless Institute of Australia*, 2007.

[123] P. Wiart and P. Maunder. The January 2003 Canberra bushfires. *Aon Re Update*, 2003.

[124] Williams, D. W. and Adams, J.S. and Batten, J. J. and Whitty, G. F. and Richardson, G.F. Operation Euroka - An Australian Mass Fire Experiment. Technical Report Report 386, Department of Supply, 1970.

[125] H. A. Wilson. On the electrical conductivity of flames containing salt vapours. *Philosophical Transactions of the Royal Society London A*, 192:499, 1899.

[126] Kane S. Yee. Numerical solution of initial boundary value problems involving maxwell's equations in isotropic media. *IEEE Transactions on Antennas and Propagation*, 14(3):302– 307, 1966. The first and readily quoted article on the FDTD Method, Yee Cell.

[127] J. L. Young. A full finite difference time domain implementation for radio wave propagation in a plasma. *Radio Science*, 29(6):1513, 1994.

[128] J. L. Young and R. Adams. Excitation and detection of waves in the fdtd analysis of n-port networks. *Progress In Electromagnetics Research*, PIER 53:249–269, 2005.

[129] Jeffrey L. Young and Ronald O. Nelson. A summary and systematic analysis of fdtd algorithms for linearly dispersive media. *IEEE Antennas and Propagation Magazine*, 43(1):61, 2001.

[130] A. P. Zhao. Rigorous analysis of the influence of the aspect ratio of yee's unit cell on the numerical dispersion property of the 2-d and 3-d fdtd methods. *IEEE Transactions on Antennas and Propagation*, 52(7):1630, July 2004.

[131] T. T. Zygiridis and T. D. Tsiboukis. Higher-order finite-difference schemes with reduced dispersion errors for accurate time-domain electromagnetic simulations. *International Journal of Numerical Modelling: Electronic Networks, Devices and Fields*, 17:461–486, 2004.